Blood velocity and viscosity in bifurcating microchannels

Joseph M. Sherwood

Thesis submitted for the degree of

Doctor of Philosophy

to

University College London

Department of Mechanical Engineering

University College London

July 2013

I, Joseph Michael Sherwood confirm that the work presented in this thesis is my own. Where information has been derived from other sources, I confirm that this has been indicated in the thesis.

‘A fool you know, is a man who never tried an experiment in his life’

Erasmus Darwin

Abstract

Blood is a complex fluid comprised of predominantly red blood cells (RBCs) suspended in a continuous, Newtonian phase, the plasma. Blood viscosity is highly dependent on the RBC concentration (haematocrit) and also displays shear thinning properties, as a result of RBC deformation and aggregation at high and low shear rates, respectively. However, these two phenomena also lead to uneven haematocrit distributions, which are exacerbated in microvascular bifurcations. In the present study, multifaceted experiments of human blood, perfused through bifurcating microchannels, are used to further elucidate the relationship between haematocrit, velocity and viscosity.

A custom pressure based perfusion system was developed and was coupled with image acquisition for velocity measurement with μPIV and further processing. The acquired data was analysed in order to investigate the flow characteristics of human blood in two different idealised bifurcation geometries. The 'cell-depleted layer' (CDL), a region of reduced haematocrit which occurs near the walls of the channel, and the continuous haematocrit distribution were experimentally measured. Analytical and numerical approaches were used to extract further information on the effect of flow rate, flow ratio and the presence of aggregation on microhaemodynamics.

In the parent branch of the bifurcation, RBC aggregation was observed to increase the radial migration of RBCs away from the vessel wall. This enhanced the non-uniformity of the haematocrit downstream of the bifurcation and altered the relative velocity between the RBCs and the suspending medium.

A skewed distribution of cells was observed downstream of the bifurcation, which resulted in skewed velocity profiles, which were also captured in the analytical and computational approaches. The geometry of the bifurcation was observed to influence the results and RBC aggregation quite significantly modified the haemodynamic characteristics even at high flow rates.

Acknowledgements

Undertaking this thesis has been an excellent experience, but has at times been challenging. I would sincerely like to thank my supervisor, Dr. Stavroula Balabani for her support, enthusiasm, guidance and patience.

I must also thank those other academics who have provided input into papers, presentations and research methods: Professor Mihalis Yianneskis, Dr. Efstathios Kaliviotis, Dr. Jon Dusting and Dr. David Holmes.

I am grateful also to Mona, who showed me that perhaps a fool is a man who has never tried a simulation in his life.

The unsung heroes of engineering research, the technicians, more than deserve a mention. Julian Greenberg and Sean Wooton at King's College, and Peter Kelly at UCL, thank you. Thanks also go to Urmilla Mefsut and Sarndra Clarke for training me as a phlebotomist.

My appreciation also goes to all of the volunteers who donated blood for the research.

Finally, I must thank those outside of my world of work, all encompassing though it has been, for being there when I needed it.

Contents

Nomenclature

Roman Symbols

HB	Haematocrit profile bluntness index (-)
HS	Haematocrit profile skewness index (-)
A	Cross sectional area (m^2)
B, *VB*	Velocity bluntness index (-)
B^*	Velocity bluntness index relative to that for a Newtonian fluid (-)
B_N	Value of the bluntness index B for a Newtonian fluid (-)
D	Cylindrical conduit diameter or hydraulic diameter for square channel (m)
E, F	Empirical parameters in the diameter-viscosity relationship of Pries et al. (1992b) (-)
F^*	Flux ratio, proportion of RBC flux entering a daughter branch from the parent branch (-)
F_d	Daughter branch RBC flux ($kg\ s^{-1}$)
F_p	Parent branch RBC flux ($kg\ s^{-1}$)
G, J, T	Empirical parameters in the model of Pries et al. (1989)
H	Haematocrit (-)
H_C	Channel haematocrit (-)
H_D	Discharge haematocrit (-)

H_F	Feed haematocrit (-)
H_p	Parent branch haematocrit distribution (-)
H_s	Symmetric parent branch haematocrit distribution (-)
H_z	z-direction haematocrit distribution (-)
I	Pixel intensity (-)
I^*	Normalised pixel intensity (-)
I_{max}	Maximum pixel intensity (-)
K	Bluntness index for flow in a cylindrical conduit (-)
L	Length a cylindrical conduit (m)
M	Key derived term in two phase model. Equal to τ_δ^* (-)
M_t	Total system magnification (-)
N	Number of images in a data set (-)
P	P-value for Pearson's or Spearman's correlation coefficient (-)
Q	Flow rate ($m^3\ s^{-1}$)
Q^*	Flow ratio, proportion of flow entering a daughter branch from the parent branch (-)
Q_0^*	Critical flow ratio below which no cells enter a branch (-)
Q_d	Daughter branch flow rate ($m^3\ s^{-1}$)
Q_p	Parent branch flow rate ($m^3\ s^{-1}$)
Q_{rbc}	Red blood cell volumetric flow rate ($m^3\ s^{-1}$)
Q_{tot}	Total blood volumetric flow rate ($m^3\ s^{-1}$)
R	Radius of a cylindrical conduit (m)
S^*	Skewness of the velocity profiles as a percentage ($\%$)

U^*	Velocity normalised by mean value (-)
U_0	A given velocity vector component, either u or v ($m\ s^{-1}$)
U_c	Velocity of top plate in Couette flow ($m\ s^{-1}$)
U_m	Median of vectors surrounding a given vector, U_0 ($m\ s^{-1}$)
U^*_{max}	Velocity magnitude normalised by maximum velocity (-)
U_{rbc}	Red blood cell velocity ($m\ s^{-1}$)
U_{rel}	Difference in velocity between the RBC and SM ($m\ s^{-1}$)
U_{sm}	Suspending medium velocity ($m\ s^{-1}$)
U_{tot}	Total blood velocity ($m\ s^{-1}$)
$\overline{U}$	Average velocity ($m\ s^{-1}$)
VS	Velocity skewness index (-): Chapters 5 and 6
$\vec{V}$	Velocity vector ($m\ s^{-1}$)
V^*	Normalised velocity in channel diameters per second (s^{-1})
a	Saturation fitting parameter for haematocrit against normalised image intensity (-) : Chapter 5
b	Nonlinearity fitting parameter for haematocrit against normalised image intensity (-) : Chapter 5
d_p	Seeding particle diameteter (m)
dt	The time between two successive images in a PIV image pairs (S)
e	Error in mass conservation ($\%$)
e_1, e_2	Exposure of first and second image frames (s)
e_s	Microstrobe pulse width (s)
f	Frequency (Hz)

$f^{\#}$	Focal number (-)
h	Height of a Couette or microchannel geometry (m)
h_1, h_2	Height of the daughter branch reservoir fluid levels (m)
h_i	Height of the inlet reservoir fluid level (m)
k	Intrinsic viscosity for Quemada model (-)
k_0	Intrinsic viscosity at zero shear for Quemada model (-)
k_∞	Intrinsic viscosity at infinite shear for Quemada model (-)
n	Index term in summation (-)
p	Pressure (Pa)
r_0'	Normalised residual for a given vector, U_0 ($m\ s^{-1}$)
r_m	The median of the difference between U_0 and U_m for the surrounding vectors ($m\ s^{-1}$)
t_d	Delay between camera trigger and shutter opening (s)
t_f	Time shutter camera closes between frames (s)
t_{l1},t_{l2}	Delay between trigger and firing the two laser pulses (s)
u	x-component of Cartesian velocity vector or axial component of cylindrical velocity vector ($m\ s^{-1}$)
u_{max}	Maximum value in a velocity profile ($m\ s^{-1}$)
v	y-component of velocity in Cartesian coordinates ($m\ s^{-1}$)
w	Width of a rectangular channel (m)
x^*	x coordinate normalised by channel width (-)
y^*	y coordinate normalised by channel width (-)
z^*	z coordinate normalised by channel height (-)

z_{corr} μPIV depth of correlation (m)

Greek Symbols

α Constant of proportionality indicating deviation of RBCs from streamlines (-)

β Constant of proportionality between normalised image intensity and haematocrit (-)

δ Cell-depleted layer width (m)

δ^* Normalised cell-depleted layer width (-)

Δp Pressure drop over a distance L (Pa)

$\Delta p_1, \Delta p_2$ Pressure drop between the inlet reservoir and daughter branch reservoirs (Pa)

Δ^* Normalised CDL width averaged axially (-)

$\overline{\Delta^*}$ Normalised CDL width, averaged axially and laterally (-)

ϵ Minimum normalisation in normalised residual test ($m\ s^{-1}$)

ε Distance of influence along optical axis in derivation of z_{corr} (m)

$\dot{\gamma}$ Shear rate (s^{-1})

γ_c Critical shear rate for Quemada model (s^{-1})

γ_r Shear rate normalised by critical shear rate for Quemada model (s^{-1})

$\overline{\gamma_a}$ Average shear rate (s^{-1})

$\overline{\gamma}$ Pseudoshear rate (s^{-1})

λ Wavelength of light (m)

μ Dynamic viscosity ($Pa\ s$)

μ_0 Plasma or other suspending medium viscosity ($Pa\ s$)

μ_a	Relative apparent viscosity (-)
μ_c	Viscosity of the RBC core in two-phase model ($Pa\ s$)
μ_h	Relative apparent viscosity for for CFDH data (Pa)
μ_r	Relative viscosity (-)
μ_r'	Modified relative viscosity in Quemada model (-)
μ_u	Relative apparent viscosity for for CFDU data (Pa)
μ_δ	Viscosity of CDL in two-phase model ($Pa\ s$)
μ_{app}	Apparent viscosity ($Pa\ s$)
ρ_c	Spearman's correlation coefficient (-)
r_c	Pearson's correlation coefficient (-)
$\overline{\sigma^*}$	Temporal standard deviation of the normalised CDL width, averaged axially (-)
σ^*	Temporal standard deviation of the normalised CDL width (-)
σ_A^*	Image contrast based aggregation index (-)
σ_I	Standard deviation of pixel intensity (-)
ρ	Density ($kg\ m^{-3}$)
τ	Shear stress (Pa)
τ_h	Wall shear stress for CFDH data (Pa)
τ_u	Wall shear stress for CFDU data (Pa)
τ_w	Wall shear stress (Pa)
τ_δ^*	Normalised wall shear stress in the CDL for the two phase model (-)
τ_c^*	Normalised wall shear stress in the CRBC core for the two phase model (-)

Abbreviations

CCD	Charge-coupled device
CDL	Cell-depleted layer
CFD	Computational fluid dynamics
CFDH	Computational fluid dynamics case with non-uniform experimental haematocrit distribution
CFDU	Computational fluid dynamics case with uniform haematocrit distribution
CFL	Cell-free layer
CMOS	Complementary metal oxide semiconductor
DAQ	Data acquisition
EDTA	Ethylene-diamine-tetra-acetic acid
ESL	Endothelial surface layer
IMAQ	Image acquisition
IW	PIV interrogation window
μPIV	Micro particle image velocimetry
MCFS	Microfluidic Flow Control System
NA	Numerical aperture
PBS	Phosphate buffered saline
PDMS	Polydimethylsiloxane
PIV	Particle Image Velocimetry
PTV	Particle tracking velocimetry
RBC	Red blood cell
ROI	Region of interest
SD	Standard deviation

SM	Suspending medium
VI	Virtual instrument (LabVIEW)
WBC	White blood cell
WSS	Wall shear stress
WSSR	Wall shear stress ratio

.

List of Figures

List of Tables

Chapter 1

Introduction

1.1 Background

Blood is a fascinating and complex fluid. The human body contains 5-6 litres of blood which is constantly recycled, with new red blood cells (RBCs) being created at a rate of 3 million per second and living for around 120 days before being broken down and recycled. Blood has three functions: transportation (gases, nutrients, waste products etc.), regulation (pH, temperature, cell water content) and protection (clotting, immune responses) (Tortora & Grabowski, 2001). Irregularities in the blood can either be a cause or a marker of a large number of pathological states and thus detailed understanding of its functions and behaviour is of fundamental importance to the field of medicine. Furthermore, due to the unique flow properties of blood, it is of considerable interest to fluid dynamicists.

Blood is a two-phase fluid, made up of plasma and formed elements. The plasma consists of around 91.5% water and 7% plasma proteins, such as albumins and fibrinogen, with the remaining 1.5% being made up of nutrients, vitamins and other solutes. The formed elements consist of red blood cells, white blood cells (WBCs) and platelets. A single μl of blood contains approximately 5×10^6 RBCs, $1.5 - 4 \times 10^5$ platelets and $5 - 10 \times 10^3$ WBCs. The main function of the RBCs is to transport oxygen, while WBCs form a key part of the immune system and platelets are involved in haemostasis (clotting in response to vessel damage) (Tortora & Grabowski, 2001; Martini, 2004).

The vascular circulation is a closed loop fluid system, with around 10^{11} vessels in humans (Schmid-Schönbein, 1999) and pressure provided predominantly by a single pump: the heart. Deoxygenated blood is pumped from the right side of the heart to

the lungs, where it absorbs oxygen, returns to the left side of the heart and is pumped around the body. With the exception of the pulmonary arteries and veins, the large vessels carrying oxygenated blood away from the heart are termed arteries, while those returning deoxygenated blood to the heart are termed veins. In between the arteries and veins lies the microvasculature, where the delivery of oxygen to cells is carried out and about 80% of the pressure drop in the vasculature occurs (Popel & Johnson, 2005).

Blood flow in the arteries and veins is often considered to be Newtonian (Fung, 1990)[†], thus the viscosity is independent of the shear rate. However, in the microvasculature the viscosity is affected by a large number of parameters, many of which are interdependent. The properties of the RBCs and their concentration, as well as the fluid dynamic environment result in viscosity which can change by orders of magnitude. RBCs deform under the influence of shear forces and align with the flow. Under low shear conditions, RBCs have a propensity to aggregate, and the non-Newtonian properties of microvascular blood flow have been largely attributed to these phenomena. RBC aggregation occurs in physiological conditions, but is elevated in pathological ones. However, it is present in athletic but not sedentary species, implying some potential benefit. It is still not clear whether aggregation is a positive or negative phenomenon, and thus further investigation is required to fully elucidate how and why it occurs (Meiselman, 2009).

Another important consideration regarding microvascular blood flow is that the distribution of cells within individuals vessels and across microvascular networks is strongly heterogeneous, both spatially and temporally, mainly as a result of cell migration and phase separation at arteriolar bifurcations. The parameters affecting the phase separation have been investigated, but more information is still required as current mathematical models are only capable of accurately predicting the distribution of cells on a network scale (i.e. not on the scale of individual vessels) (Cokelet, 1999). Furthermore, detailed quantitative descriptions of local cell distributions have not yet been reported.

The local and bulk viscosity characteristics of blood have a great impact on the function of the body in both health and disease, and hence understanding the parameters which most affect blood viscosity is of great importance. *In vitro* experimental measurements in long straight tubes and viscometers over the past century have provided a

[†]This is not to say that this assumption is valid, but that it is commonly made.

large amount of data on blood flow characteristics, but the simplified geometries limit the application of such results. *In vivo* data is invaluable in understanding the importance of relative phenomena, but the lack of control of the parameter space leads to highly scattered and often contradictory data. *In silico* models of varying degrees of complexity can provide highly detailed information, but require accurate experimental data for verification.

Recent advances in technology, particularly the fluid velocity measurement technique known as Particle Image Velocimetry (PIV) and soft-lithography for microfabrication, provide the opportunity to acquire increasingly accurate and detailed experimental data on microscale blood flow phenomena. The present study will make use of these methodologies, in combination with image processing, mathematical modelling and computational fluid dynamics (CFD) in order to provide new insight into microscale blood velocity and viscosity relationships.

It seems prudent to first describe the fundamental properties of blood and the system in which it operates, in order to provide context to the present work. Consequently, the remainder of this chapter is concerned at first with a brief description of the functions and properties of the components of the circulatory system, before continuing with a review of the present haemodynamics literature relevant to the present study.

1.2 The circulatory system

This section will describe the biological and mechanical characteristics of the constituent parts of the circulation: the vessels and the blood[†]. The former will be kept to a minimum, owing to the fact that the present study is concerned with *in vitro* models, which cannot take many of the structural characteristics into account at present.

1.2.1 Vessel structure and topology

Oxygenated blood is ejected from the left ventricle of the heart via the aorta, which branches into a number of arteries. These bifurcate sequentially with decreasing diameter at each generation. The microvasculature is defined for vessel diameters below $\approx 100\mu m$[‡]. In the microvasculature, mass transfer functions are carried out, and the

[†]The lymphatic system is also an important part of the circulatory system, but will not be considered here.

[‡]Or up to $300\mu m$, depending on the source.

blood then flows into the veins, which transport the deoxygenated blood back to the right ventricle of the heart.

The vessels of the circulatory system are made up of multiple layers comprising collagen and elastic fibres, smooth muscle cells, connective tissue and the endothelial cells which line the lumen (the space inside the vessel in which blood flows) (Martini, 2004). The relative proportions of each of the layers varies between vessels, depending on their size, function and the pressure under which they operate. For example, arteries have a high proportion of elastic membrane due to the high internal pressure conditions therein. Conversely, the pressure in veins is very low and thus in limbs, flaps of the intimal layer form valves which present reperfusion into the microvasculature.

The microvasculature essentially consists of three types of vessel: arterioles, capillaries and venules. The blood from arteries feeds into arterioles, with diameter approximately $10 - 125\mu m$ (Fung, 1997), and these vessels bifurcate into sequentially smaller vessels leading to the capillary bed. Arterioles have multiple layers of smooth muscle cells which allow the diameter of the vessels to contract or expand significantly (up to 50% (Johnson, 2008) or 300% in a conjunctival arteriole (Jung, 2010)), which allows control over capillary perfusion. This control occurs predominantly in the smaller arterioles with diameters less than $40\mu m$ (Pries et al., 1996), which is also the region of the vasculature where the greatest pressure gradient is found. In skeletal muscle, the pressure drop in the arterioles accounts for $50 - 60\%$ of the total pressure drop across the vasculature (Fronek & Zweifach, 1975).

The smallest vessels of the microvasculature are capillaries ($4 - 7\mu m$ (Levick, 2009)), wherein the main goal of the vascular system is carried out; the exchange of oxygen and nutrients for waste products and carbon dioxide via diffusion, although some molecular diffusion does occur in the venules and arterioles (Popel & Johnson, 2005). Approximately 15% of the total pressure drop occurs in the capillary bed (Fronek & Zweifach, 1975). Capillaries are spread throughout organs and muscles, accessing the majority of cells within the body and cover a surface area of $\approx 70m^2$ in humans (Popel & Johnson, 2005). Structurally they essentially consist of endothelial cells held together by a thin basal lamina. This allows diffusion of water, small solutes and lipid-soluble materials but inhibits loss of blood cells and plasma proteins (Martini, 2004). Although the flow in arterioles and venules is relatively constant, capillary flow oscillates around every 5

seconds as a result of contraction and dilation of the capillary sphincter, the last smooth muscle cell present in the arteriolar system: this is known as vasomotion. Thus the blood flow in the capillary bed can take different paths depending on the phase of the oscillation. Under a state of rest, only 25% of the vessels in a capillary bed have flow (Martini, 2004). Capillaries also provide some degree of control of vascular resistance under increased flow via a narrowing of the glycocalyx, which is located on the luminal side of the endothelial cells (Pries et al., 1997).

Venules collect the flow from the capillary bed, converging to form sequentially larger vessels in the range from 8 to $100\mu m$ (Fung, 1997). Structurally, they consist of an endothelial tube with a tunica externa, although the smaller ones closely resemble capillaries. It is within the post-capillary venules of diameter up to approximately $50\mu m$ that the migration of WBCs through the vessel walls occurs (transmigration), which allows them to access the damaged tissue (Ohashi et al., 1996). The movement of WBCs towards the vessel wall is known as leukocyte margination and is of considerable interest to the medical community. Additionally, the shear rates in venules are the lowest in the vasculature, and hence it is within these vessels that RBC aggregation most commonly occurs (Popel & Johnson, 2005).

On the luminal side of the endothelial cells, there exists a layer of glycoproteins, proteoglycans and glycosaminoglycans which make up the glycocalyx, which is tens of nm thick (Pries et al., 2000). However, there is evidence of a thicker layer of $0.5 - 1\mu m$, known as the endothelial glycocalyx layer or endothelial surface layer (ESL) which has a considerable hydrodynamic effect (Pries et al., 2000). The properties of this layer are discussed in depth in a number of reviews (VanTeefelen et al., 2007; Pries et al., 2000; Weinbaum et al., 2007). As there is almost no plasma velocity observed in the ESL (Savery & Damiano, 2008; Smith et al., 2003) the shear stress acting on the endothelial cell plasma membrane is very small. Shear stress is instead transmitted to the endothelial cell by translating the drag force on the ESL fibres into a torque acting on the endothelial cell cytoskeleton (Weinbaum et al., 2007). Mechanotransduction, the chemical response to mechanical stimuli, is a key part of the flow regulation in the microvasculature. For example, nitric oxide, which is a vasodilator, is released by endothelial cells in response to elevated wall shear stress levels. This causes smooth muscle cells to relax, increasing the diameter and thus reducing the flow resistance of

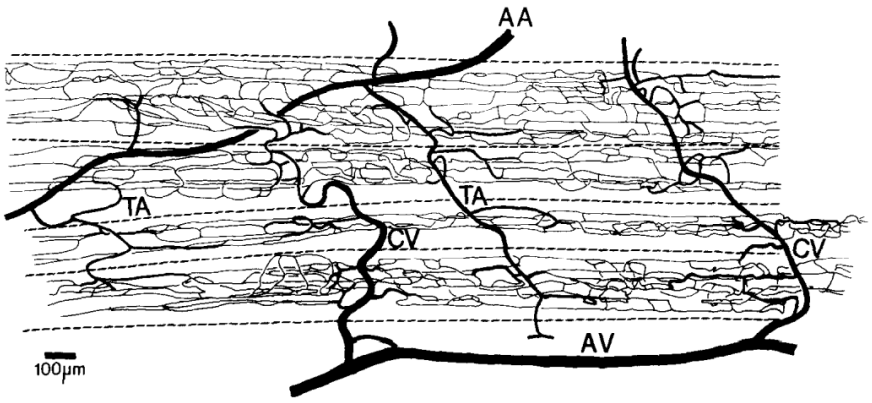

Figure 1.1: Schematic of a section of microvascular network of rat spinotrapezius (Skalak & Schmid-Schönbein, 1986).

the network. The absence of the endothelial cells *in vitro* is of concern and may account for some of the contradictions with *in vivo* work. The seeding of channels with endothelial cells shows potential in resolving this (Rosano et al., 2009; Fiddes et al., 2010), however, there is some doubt as to whether such cell culturing approaches are able to produce a physiologically relevant ESL (Potter & Damiano, 2008; Potter et al., 2009).

Although microvascular network topology is specialised within individual organs and skeletal tissue, some features are generally present. In the arteriolar network, an arcade arrangement is often found in vessels larger than $25\mu m$, while a sequential branching structure is more common in smaller vessels (Fung, 1997). A similar structure is found in venules, although individual sections have larger diameter and shorter length and the total number of vessels is greater. In skeletal muscle, capillaries are bundled, such that each terminal arteriole feeds two separate capillary networks, which in turn feed into two collecting venules, each of which receives the fluid from two such capillary bundles. Figure 1.1 shows a schematic of a section of microvascular network in the rat spinotrapezius muscle. The arcade arteriole (AA) feeds into a number of branching terminal arterioles (TA), which feed the capillary network bundles, separated by the dashed lines in the figure. The branched collecting venules (CV) collect the blood from the capillaries and feed into the arcade venule (Schmid-Schönbein, 1999). It should be noted that the bifurcations show a wide range of angles.

The general structure as a whole can take different forms. For example, a serial arrangement is sometimes observed, wherein a single artery feeds a network which is collected

by a single vein. Parallel networks also exist, in which there are multiple points of connection between the arterial and venous networks. Finally, it should be noted that, although vascular networks are generally three-dimensional, certain muscles, such as the spinotrapezius shown in Figure 1.1, have an approximately two-dimensional structure.

1.2.2 Blood Constituents

Plasma

Blood plasma is a solution of proteins and other solutes in water ($90 - 92\%$ (Caro et al., 2012)). The proteins are large enough so that they do not, under normal conditions, diffuse through the endothelial barrier, and thus remain in the circulatory system. The main plasma proteins can be split into three categories; albumins, globulins and fibrinogen, which make up 60, 35 and 4% of the total protein content respectively. Albumins contribute greatly to the osmotic pressure and are important in the transport of hormones and fatty acids, while globulins have immune and transport properties. Fibrinogen is important in haemostasis (clotting). Upon damage to a vessel wall, a complicated cascade of reactions results in the enzyme thrombin, which converts the dissolved fibrinogen into strands of insoluble fibrin, in which platelets and RBCs are trapped, causing a clot (Tortora & Grabowski, 2001; Martini, 2004). In addition to the aforementioned functions, plasma proteins are an important factor in the plasma, and thus blood, viscosity. Plasma viscosity has long been used as a diagnostic tool: elevated viscosity implies pathology. Additionally, plasma proteins are a key component in the RBC aggregation process, which will be discussed further later in this section. From a fluid dynamics point of view, plasma is a Newtonian fluid and has a viscosity of $1.15 - 1.35mPas$ at physiological temperature of 37 degrees centigrade (Lowe, 1988).

Red blood cells

RBCs constitute approximately 45% of the blood by volume and thus they dominate the mechanical characteristics of the blood. The structure of the RBC is very simple; they have no nucleus or organelles and are essentially a flexible membrane surrounding a mixture of cytosol and haemoglobin, to which oxygen binds. The lack of mitochondria means that none of the oxygen bound to the haemoglobin is used by the RBC,

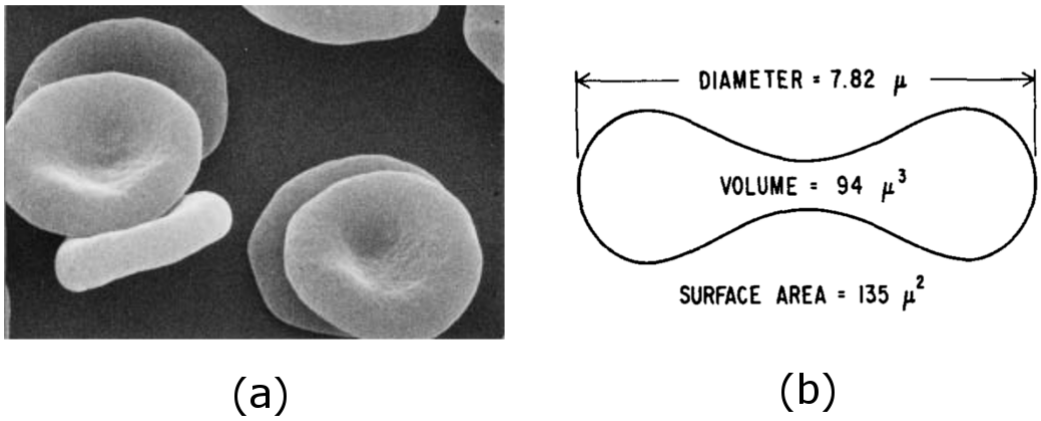

Figure 1.2: RBC shape. (a) Scanning Electron Micrograph at pH 7.1 (Cicha et al., 2003), (b) RBC shape in isotonic buffer derived microscopic holography (Evans & Fung, 1972).

thus their form is patently specialised for the purpose of oxygen delivery. However, their specialisation is not only biochemical; their mechanical properties are unique and complex.

The RBC membrane consists of three layers: an extracellular glycocalyx layer, a lipid bilayer plasma membrane and an elastic two dimensional network of skeletal proteins, the latter of which are connected via transmembrane proteins (Yazdanbakhsh et al., 2000). This structure results in a highly elastic membrane which can deform easily, with linear deformations of up to 250%, but is very resistant to changes in surface area. The elastic, bending and isotropic area dilation moduli have been reported to be $6\mu N/m$, $1.8 \times 10^{-6}\mu N/m$ and $0.5N/m$ respectively (Evans, 1983). If the cell membrane surface area increases by $3-4\%$, then cell lysis will ensue, i.e. its membrane will break and its contents will be released (Mohandas & Gallagher, 2008).

Under stasis in an isotonic suspending medium, RBCs have a biconcave disc shape with a diameter and thickness of approximately 8 and $2\mu m$ respectively, as shown in Figure 1.2, which results in a zero-stress state on the membrane and a zero transmembrane pressure (Fung, 1993).

Under flow conditions in confined spaces, RBCs deform significantly and can fit through passages significantly smaller than their dimensions under static conditions: as low as $2.8\mu m$ (Halpern & Secomb, 1992). The characteristic time for the deformation has been reported to be $0.06s$ (Cokelet, 1980). Figure 1.3 shows RBCs deforming

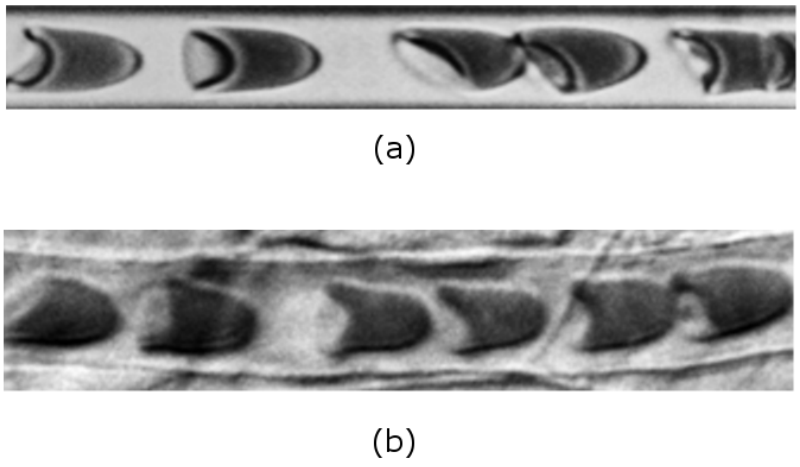

Figure 1.3: Erythrocytes deforming in 7 μm wide channel. (a) *In vitro* (glass tube), (b) *In vivo* (rat mesentery) (Pries & Secomb, 2008).

in $7\mu m$ channels *in vitro* and *in vivo*. It can be seen that the cells have a structure which has been described as 'bullet-shaped' or 'parachute-shaped'.

In larger vessels, their deformability allows the erythrocytes to align with the flow and the membrane has been observed to rotate around the cell interior, in a process known as tank treading (Abkarian et al., 2007). This reduces viscous dissipation and thus the viscosity of the fluid. Any pathological changes in erythrocyte deformability can thus result in significant changes in the fluid dynamics of the vasculature (Lowe, 1988).

Under low flow conditions, RBCs have a propensity to aggregate, forming either clumps or stacks termed rouleaux (Lipowsky, 2005). The rouleaux can connect to each other to form a three dimensional network, as shown in Figure 1.4.

There are two contradictory theories describing the mechanism under which aggregation occurs; bridging and depletion, both of which involve RBC surface charge properties and either long chain proteins such as fibrinogen or polymers, such as high molecular weight Dextran. Under both proposed mechanisms, the extent of aggregation is dependent on the relationship between the attractive, electrostatic, mechanical shear and membrane bending forces acting on the cell (Chien & Jan, 1973).

The bridging model suggests that the macromolecules accumulate on the cell surface and form a bridge between two aggregating cells, holding them together (Chien & Jan, 1973; Maeda & Shiga, 1985). However, Armstrong et al. (1999) have provided

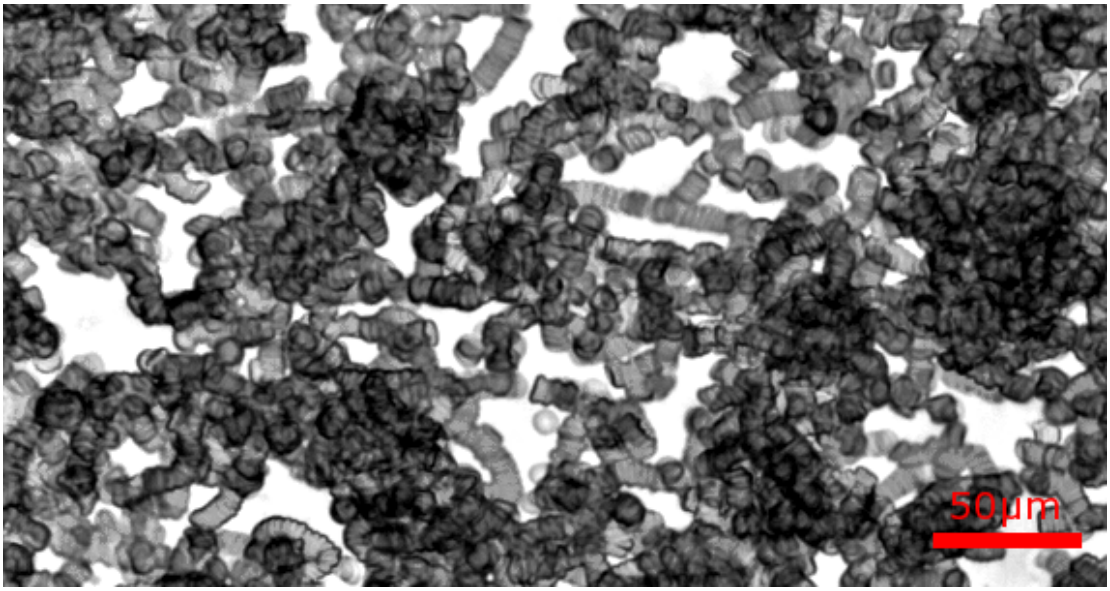

Figure 1.4: RBC aggregate network in a microchannel. Contrast is enhanced for clarity.

evidence to the contrary. In their study, they covalently bonded polyethylene oxide, which strongly aggregates RBCs, to the surface of the cells. If the bridging theory was correct, this would result in increased aggregation, but their experiments showed the opposite.

The alternative depletion model suggests that a lower localised concentration of macromolecules occurs near the cell surface (depletion layer). This generates an osmotic pressure gradient and fluid moves away from the region between the cells, in order to reduce the free energy of the system, which generates an attractive force (Neu & Meiselman, 2002; Meiselman, 2009). It should be noted that Bronkhorst et al. (1997) suggest that perhaps both bridging and depletion mechanisms are active, in that depletion plays a role in bringing aggregates sufficiently close for cross-bridging to occur. Nonetheless, the depletion theory is generally accepted as the best explanation for the phenomenon of aggregation, particularly for RBC aggregation induced by Dextrans (Meiselman, 2009).

Disaggregation occurs mainly as a result of shear stress acting on the aggregates (Popel & Johnson, 2005). The range of magnitudes of the shear stresses and shear rates required for disaggregation reported in the literature is wide. Snabre et al. (1987) state critical shear rates ranging from $120s^{-1}$ to $13s^{-1}$ and critical shear stresses ranging from $0.219 - 0.281N/m^2$ in a Couette flow as haematocrit increased from 15 to 75%.

Chien et al. (1977) found the shear stress required for disaggregating two cells in a channel to be $0.05 - 0.1N/m^2$, while Rampling et al. (2004) cite shear rates of $20 - 40s^{-1}$ for disaggregation. However, it should be noted that for blood flow in vessels, the shear rates are not uniform and aggregation has been observed at pseudoshear rates† exceeding $70s^{-1}$ in venules (Bishop et al., 2004) and $100s^{-1}$ in arterioles (Ong et al., 2010). Pseudoshear rates in humans have been estimated to be $< 40s^{-1}$ (Bishop et al., 2001a; Whitmore, 1968), indicating that aggregation is likely to be present throughout a large portion of the human vasculature. Additionally, for shear rates $< 1s^{-1}$, the greater the flow, the more frequent the cell-cell interactions, thus aggregation is increased (Cokelet, 1980).

The extent of aggregation is dependent on extrinsic factors, such as aggregating agents and shear, and intrinsic factors, such as cell type, deformability, age etc. (Kim et al., 2009), the latter of which are defined by Baskurt & Meiselman (2008) as 'aggregability'. Summaries of the influence of these factors have been recently reviewed by Rampling et al. (2004) and Meiselman (2009). Aggregation has been found to increase with decreasing temperature (Schmid-Schönbein et al., 1972), increasing fibrinogen concentration up to $4 \times 10^{-3}kg/L$ (Falcó et al., 2005), increasing haematocrit (Schmid-Schönbein et al., 1972) and increasing Dextran concentration up to a point, before rapidly decreasing (Chien & Jan, 1973).

Decreasing the deformability of the cells was found to decrease the amount of aggregation (Jovtchev et al., 2000; Maeda et al., 1983). However, the simulations of Bagchi et al. (2005) suggested that aggregates were more stable if the cytoplasm was more viscous and the membrane more rigid.

Cokelet (1980) reports aggregation time of the order of $5 - 7$ seconds after rapid reduction of shear, although this value is increased under pathological conditions and is dependent on a range of other factors.

Initially, after reduction from a high to a low shear rate, RBC aggregation undergoes a rapid increase with a time scale of the order of 1 second (Kaliviotis & Yianneskis, 2008). A steady aggregation state has been shown in a parallel plate optical shearing

†Pseudoshear rate is defined as the mean velocity divided by the diameter in round channels/vessels or the mean velocity divided by the height in flow between two plates. The term will be discussed in detail later.

microscope viscometer to reach a steady state in approximately $15 - 20$ seconds, although the time was found to be shear rate and haematocrit dependent (Kaliviotis et al., 2011). A peak in viscosity was observed to occur after $2 - 3$ seconds, which decreased as networks formed at low shear rates ($\leq 2s^{-1}$).

Aggregation measurement is generally carried out separately to flow experiments in rotational geometries, with the extent of aggregation measured as a function of light transmission or back scattering of laser light (Baskurt et al., 2009b). Multiple indices tend to be defined based on transient responses and threshold shear rates. However, as aggregation is shear and time dependent, the data collected from such systems is not directly applicable to channel flow, as the shear distribution and characteristic times in such systems will be significantly different. Shin et al. (2006) developed a method based on laser back-scattering in a disposable microchannel. The effects of aggregation on blood flow will be described in more detail in §1.4.8.

Finally, it should be mentioned that the density of plasma and RBCs have been reported to be 1025 and 1125 kg/m^3 respectively (Jäggi et al., 2007; Kenner, 1989). As a result, RBCs sediment in plasma. This effect is enhanced under aggregating conditions (Alonso et al., 1995) due to the larger mass to surface area ratio of the aggregates compared to individual cells. In horizontal tube flow, the sedimentation rate is proportional to the fourth power of the haematocrit and the square of the particle diameter (Baskurt et al., 2012).

White blood cells

Leukocytes, or white blood cells, are part of the immune system and also remove waste substances, toxins and damaged cells from the body. Unlike red blood cells, they contain a nucleus and organelles. There are five types of leukocyte: neutrophils, basophils, eosinophils, monocytes and lymphocytes, each of which carry out different functions. They are approximately spherical in shape with a diameter of $7 - 8\mu m$ and are deformable (Lowe, 1988) and exist in very low concentrations compared to the RBCs ($< 1\%$). Due to inflammation or the presence of an antigen, leukocytes become activated and their physical structure and properties change significantly (Popel & Johnson, 2005). Under such conditions, leukocytes have been observed to block capillaries, significantly increasing capillary network resistance (Eppiheimer & Lipowsky, 1996).

This effect has also been observed *in vitro* (Thomson et al., 1989), wherein the RBCs form 'trains' behind a relatively larger and less deformable leukocyte. When flowing through capillaries, leukocytes conform to a cylindrical shape, and tend towards the vessel centre, flowing with a velocity lower than that of the RBC. In the post-capillary venules, interactions with the RBCs deflect the leukocytes towards the wall, wherein they start to roll along, and subsequently adhere to, the endothelium. This effect has been observed to be increased by RBC aggregation (Pearson & Lipowsky, 2004).

Platelets

Platelets have a flattened disc shape of approximately $4\mu m$ diameter and $1\mu m$ depth. Functionally, they comprise a significant portion of the process of thrombosis. Due to their low volume concentration ($0.2 - 0.5\%$), they have negligible effect on the mechanical flow properties of blood (Lowe, 1988), except when involved in coagulation. Additionally, they have been used in a number of studies as flow tracers by labelling them with fluorescent dye (Tangelder et al., 1985; Tangelder et al., 1986).

1.3 Approaches to haemodynamics research

Due to the large number of variables which affect blood flow in the vasculature, *in vivo* (lit. in life) experiments provide the most realistic environment for analyses of the flow characteristics, as it is not possible to account for all such variables in model experiments. However, the inability to accurately control many of the variables, and thus to study individual parameters with a high degree of accuracy, requires simplified models to be utilised. *In vitro* (lit. in glass) and *in silico* (computer simulations) approaches each provide their own advantages and disadvantages. In this section, a brief explanation of each of these approaches will be given.

1.3.1 *In silico*

In silico studies allow for a large number of variables to be considered and can provide highly detailed data which is not possible to acquire experimentally. Furthermore, if computational models are able to predict experimental measured results, it indicates that the understanding of the phenomena of interest is accurate. Arterial and venous blood flow is often modelled assuming the blood to be a continuous, Newtonian fluid (Cebral et al., 2005; Fung, 1997; Taylor et al., 1999; Tse et al., 2011); although

some non-Newtonian models are commonly utilised (Gijsen et al., 1999; Soulis et al., 2008). Blood flow in large vessels is characterised by high Reynolds and Womersley numbers[†] and thus the effects of viscosity are small and the inertial and pulsatile nature of the flow caused by the cardiac cycle are of greatest significance (Fung, 1997). Thus, in such simulations, the unsteady flow (Liu et al., 2001), turbulence (Varghese & Frankel, 2003), flow separation (Seo et al., 2005), wall shear stress (Migliavacca & Dubini, 2005) and other such aspects of classical fluid dynamics are considered. Advances in medical imaging have allowed for simulations in patient-specific geometries reconstructed from magnetic resonance imaging, computed-tomography and ultrasound as reviewed by Steinman (2002).

Microvascular blood flow is characterised by Reynolds numbers which are much less than one and thus the flow is dominated by viscous effects (Fung, 1997). Additionally, as the vessel dimensions approach the scale of the suspended cells, the two phase nature of the flow becomes increasingly significant. If only bulk flow properties are required, then continuum models can be applicable for some situations. Approaches include fitting empirical equations based on experimental data (Pries et al., 1994) and modelling the flow as two regions of Newtonian fluid with different viscosities (Fenton et al., 1985; Sharan & Popel, 2001). If more detailed information is required, such as on the cell-cell interaction, cell-wall interaction, RBC aggregation or deformability, then more complex multi-cell flow methods must be utilised. These include the lattice-Boltzman (Hyakutake et al., 2006; Zhang et al., 2008) and immersed boundary methods (Bagchi, 2007; Eggleton & Popel, 1998).

Capillary blood flow is generally modelled taking into account the deformation of the cells, the interaction with the vessel wall and the coupling between the flow in the cell interior and the flow exterior to the cell (Freund & Orescanin, 2011; Lee & Smith, 2008; Pozridikis, 2005).

In arterioles and venules, the continuum approach is considered a reasonable assumption for vessels larger than $20 - 50\mu m$ (Cokelet, 1999; Popel & Johnson, 2005). However, if aggregation or cell deformability is of interest, then such models may not be

[†]These are dimensionless fluid dynamics parameters. The Reynolds number relates the relative importance of the inertial to viscous forces. The Womersley number relates the transient inertial force and its frequency to the viscous forces.

sufficient. Historically, due to the large number of cells involved, the computational cost of multi-cell models has precluded them as a feasible methodology in flow on this scale. However, recent advances have allowed small scale modelling of microvascular bifurcations (Chesnutt & Marshall, 2009; Hyakutake et al., 2006; Secomb et al., 2007) and the effects of aggregation (Bagchi et al., 2005; Chesnutt & Marshall, 2010; Zhang et al., 2008). The most advanced computer models consider individual RBCs to be comprised of many interconnected springs (Fedosov et al., 2010a; 2010b; Imai et al., 2010; 2011). These models provide very detailed information on the flow of RBCs and suspending medium, but have a high computational cost. Such approaches provide perhaps the best potential for further modelling of microvascular blood flows, but still require accurate experimental measurements in order to verify the results.

1.3.2 *In vitro*

In vitro studies have provided a large amount of information on the basic parameters which affect the flow of blood in the microvasculature. Through these studies, concepts such as the Fåhraeus and Fåhraeus-Lindqvist effects and the Zweifach-Fung bifurcation law have been developed and the importance of geometrical and fluid parameters have been investigated. Initial studies of blood flow were carried out in glass capillary tubes by pioneers such as Fåhraeus (1929) and have continued to provide useful information with important studies on sedimentation, aggregation, velocity profiles and apparent viscosity. However, the large length to diameter ratio of these tubes changes the balance in the complicated interactions between various phenomena, giving results which do not quantitatively match *in vivo* results, and in some cases even contradict them.

Viscometric studies of blood flow using Couette (Chien & Jan, 1973), parallel plate (Kaliviotis & Yianneskis, 2008) and cone and plate viscometry (Schmid-Schönbein et al., 1968) have provided useful information on blood viscosity and aggregation characteristics by allowing for accurate control of shear forces and thus the response of RBCs and aggregates to these forces. While these studies have provided invaluable data on the mechanisms involved in aggregation and its response to certain conditions, the shear force and RBC concentration distributions which occur *in vivo* are far more complex, and thus experiments in more realistic geometries and a range of flow conditions are required to improve understanding of the phenomenon. Individual and sequen-

tial bifurcating geometries, relative and absolute branch sizes as well as suspending medium, flow rate, flow proportions, the influence of the flow pulsations etc. are all likely to have an impact on the occurrence of RBC aggregation *in vivo* and should be investigated.

A number of experimentalists have modelled the flow of blood in bifurcations using plastic channels (Carr & Wickham, 1990; Chien et al., 1985; Dellimore et al., 1983; Fenton et al., 1985; Perkkiö et al., 1987; Yen & Fung, 1978). These experiments provided valuable information on the importance of various parameters on phase separation observed in bifurcations and will be described further in §1.4.9. However, in these studies the analysis was carried out only on bulk measurements and detailed information on the flow field around such bifurcations is still required. Accurate modelling (in terms of the geometry) of microvascular networks is difficult due to the technical requirements of constructing microchannels. While straight channels and simple bifurcations can be achieved by casting using wires (Fenton et al., 1985; Lima et al., 2009b), more sophisticated methods are required for detailed geometries. With the rapid increase in microfluidic research over the last decade, advanced fabrication methods have become available. The most common of which for use in biological studies is soft-lithography using polydimethylsiloxane (PDMS), and a number of reviews on the subject are available (Sia & Whitesides, 2003; Xia & Whitesides, 1998). PDMS microchannels have been used to study a bifurcating and then converging junction (Ishikawa et al., 2011) and a stenosis (Fujiwara et al., 2009) and have also been used to create a large number of devices for blood analysis (Faivre et al., 2006; Jäggi et al., 2007; Kersaudy-Kerhoas et al., 2010; Sollier et al., 2009; Zheng et al., 2008). Recently, a few examples of microchannels representing entire microvascular networks have been produced (Prabhakarpandian et al., 2008; Rosano et al., 2009; Shevkoplyas et al., 2003), although the analysis of the flow in these networks was limited. While synthetic microvascular networks represent a better approximation of the microcirculation, the difficulty of creating different depths and the fact that the cross sectional shape in these devices is rectangular reduce their applicability. The latter issue was overcome by Fiddes et al. (2010) who converted a channel fabricated using standard methodologies to have a circular cross section by injecting silicon oligomer into the channel then infusing nitrogen, and varying the pressure to control the diameter of the final channel.

A further development of these systems was the seeding of endothelial cells inside the channel (Fiddes et al., 2010; Rosano et al., 2009) which should produce conditions closer to those found *in vivo* than has previously been possible.

1.3.3 *In vivo*

The aim of *in vitro* and *in silico* studies is ultimately to be able to understand the flow of blood in the microvasculature and thus, to be able to predict the flow of blood *in vivo*. In addition to the lack of control of variables mentioned previously, *in vivo* studies are also made more challenging due to the considerable difficulty in accessing appropriate tissue and acquiring the required data. Nuclear magnetic resonance imaging and ultrasound techniques can be used to measure blood flow in vessels deep within the body, but have limited spatial resolution due to the wavelengths used in the techniques and are thus not suitable for microvascular measurement (Vennemann et al., 2007). Particle Tracking Velocimetry (PTV) and Particle Image Velocimetry (PIV) provide high spatial resolution data, but require optical access, which limits the range of use. In humans, microvascular networks are generally inaccessible, with the exception of the eye which has received recent research attention (Makita et al., 2011; Shahidi et al., 2010; Yu et al., 2010). Additionally, microvascular networks are generally three dimensional, which makes it very difficult to obtain data with optical methods, although confocal PTV can be used if optical access is sufficient (Kamoun et al., 2010). Specific microvascular beds which are approximately two-dimensional such as the mesentery of rabbit (Tangelder et al., 1986), cat (Lipowsky & Zweifach, 1974) or rat (Sugii et al., 2002), rat spinotrapezius (Das et al., 2007), cat sartorius (Dodd & Johnson, 1991) and hamster cremaster (Klitzman et al., 1983) are used in conjunction with intravital microscopy. Dual-slit and videophotometric methods are commonly used for measurement of the velocity, often with labelled RBCs. *In vivo* studies have provided information on all aspects of the microcirculation including cell-free layer (Kim et al., 2007; Ong et al., 2010), RBC aggregation (Bishop et al., 2001c; Soutani et al., 1995), vessel and network flow resistances (Lipowsky et al., 1980; Pries et al., 1994; Pries & Secomb, 2005), radial migration (Bishop et al., 2001c), cell deformability, haematocrit distribution and the ESL (Smith et al., 2003). However, the data in such experiments generally has a relatively large amount of scatter and there are many reported contradictory results.

1.4 Dynamics of blood flow

Blood flow is dominated by the interaction between the RBCs, suspending medium and the boundaries of the system. This section will provide an introduction to the most relevant aspects of haemodynamics for the analysis of the results reported in the present study.

1.4.1 Fundamental flow models

The fundamental equations of fluid dynamics are the Navier-Stokes equations and the continuity equation. The former provide a description of the conservation of momentum in each coordinate axis and the continuity equation describes the conservation of mass.

$$\rho\left(\frac{\partial\vec{V}}{\partial t}+\vec{V}.\nabla\vec{V}\right)=-\nabla p+\mu\nabla^2\vec{V} \tag{1.1}$$

$$\nabla.\vec{V}=0 \tag{1.2}$$

These non-linear, partial differential equations are analytically soluble for only a few idealised systems. Two of these have particular relevance in haemodynamics, namely the flow between two parallel plates, which approximately represents that found in parallel-plate, cone and plate and Couette viscometers, and Poiseuille flow, which describes the flow in a long straight cylindrical channel. These solutions will be introduced in the following section. For more complex problems, the equations above can be solved using CFD, by discretising the geometric domain and solving the equations numerically.

Flow between parallel plates

Plate-plate viscometers have been widely used in rheology, the study of viscosity, and have provided a large amount of haemorheological data (Chien & Jan, 1973; Dufaux et al., 1980; Kaliviotis & Yianneskis, 2009; Kaliviotis et al., 2011). The plate-plate viscometer is based on Couette flow, in which a Newtonian fluid (one for which the viscosity is independent of shear), flows steadily between two flat, infinite plates. The lower plate is fixed and the upper plate moves with a velocity U. The no-slip condition (arising from the fact that fluid particles in direct contact with the wall must have the same velocity as the wall) implies that the velocity of the fluid at the stationary plate

will be zero, and at the moving plate will be U. Solving the Navier-stokes equations under these conditions yields the velocity profile

$$u\left(y\right) = \frac{Uy}{h} \tag{1.3}$$

where the distance between the two plates is given by h. Hence the fluid velocity varies linearly between the two plates. As a result, the shear rate

$$\dot{\gamma} = \frac{du\left(y\right)}{dy} = \frac{U}{h} \tag{1.4}$$

is a constant. In plate-plate viscometers, two circular plates are used in order to provide a continuous region in which to apply this flow. The torque required to rotate the plate gives a measure of the fluid viscosity for a *single* shear rate. In this case, the average shear is $\overline{\gamma}_a = \frac{U}{h}$†.

Poiseuille flow

As a first approximation, the flow in a blood vessel can be modelled by assuming flow of a Newtonian fluid through a long, rigid cylindrical tube of uniform cross section. Under the assumptions of laminar, incompressible, fully developed flow, Equations 1.1 and 1.2 yield the following equation for the axial velocity at a given radius as

$$u(r) = \frac{1}{4\mu}\frac{\partial p}{\partial x}\left(r^2 - R^2\right) \tag{1.5}$$

where $u(r)$ is the axial velocity at radius r, μ is the viscosity, $\partial p/\partial x$ is the axial pressure gradient and R is the tube radius. Assuming that the pressure drop is constant along the length L ($\Delta p/L = -\partial p/\partial x$), and integrating the velocity profile, Equation 1.5 can be written as

$$\Delta p = \frac{8\mu LQ}{\pi R^4} \tag{1.6}$$

which is known as the Hagen-Poiseuille equation or law. Although the majority of the assumptions made in the derivation are inaccurate for the vessels in the vasculature, the equation nonetheless provides a useful benchmark and indicates certain relationships. Importantly, it shows that the pressure drop is inversely proportional to the fourth power

†The subscript a is used to as to distinguish between the average shear rate $\overline{\gamma}_a$ and the pseudoshear rate $\overline{\gamma}$

of the vessel diameter. This has a large impact on the flow in the vasculature, particularly in the arterioles where vasodilation and vasoconstriction are used to maintain a constant pressure in the capillary bed (Fung, 1997).

Given that $Q = \pi R^2 \overline{U}$, Equation 1.5 can be written in terms of the mean velocity as

$$u(r) = 2\overline{U}\left(1 - \frac{r^2}{R^2}\right) \tag{1.7}$$

hence the shear rate is described by

$$\frac{du(r)}{dr} = \frac{4\overline{U}r}{R^2} \tag{1.8}$$

The shear rate in Poiseuille flow is thus linearly related to the radial position. At the wall, $r = R$ and the shear rate is $4\overline{U}/R = 8\overline{U}/D$. In the vessel centre the shear rate is zero.

In the study of the shear-dependent characteristics of blood, a singular representative value for the shear rate, termed the 'pseudoshear rate' is commonly used to describe the flow environment. In many cases, the Couette definition is used for blood vessels, and the pseudoshear rate, ($\overline{\gamma}$) is defined according to $\overline{\gamma} = \overline{U}/D$ (Bishop et al., 2001a; Ong et al., 2010; Reinke et al., 1987). This is equivalent to a normalised velocity, measuring the number of channel diameters per second (Cokelet & Goldsmith, 1991). However, the value should not be used to directly compare shear dependent characteristics with those acquired in plate-plate viscometers. The mean shear for Poiseuille flow is found by integrating the shear profile across the channel, yielding

$$\overline{\gamma}_a = \frac{16}{3}\frac{\overline{U}}{D} \tag{1.9}$$

Flow in rectangular channels

In vitro studies in PDMS channels generally have a rectangular cross sectional area. In this case, the velocity profile is given by Bruus (2008) as

$$u(y,z) = \frac{4h^2\Delta p}{\pi^3 \mu L}\sum_{n,odd}^{\infty}\frac{1}{n^3}\left[1 - \frac{cosh\left(n\pi\frac{y}{h}\right)}{cosh\left(n\pi\frac{w}{2h}\right)}\right] sin\left(n\pi\frac{z}{h}\right) \tag{1.10}$$

where the channel height is in the z direction ranging from 0 and h and the width is in the y direction between $\pm 0.5w$. The flow rate is given by

$$Q = \frac{h^3 w \Delta p}{12 \mu L} \left[1 - \sum_{n,odd}^{\infty} \frac{1}{n^5} \frac{192}{\pi^5} \frac{h}{w} \tanh\left(n\pi \frac{w}{2h} \right) \right] \tag{1.11}$$

For a channel with a square cross section, the hydraulic diameter $D = 2hw/(h+w) = h = w$. Hence in this case, the average shear is close to that for a cylindrical pipe. For high aspect ratio channels, the Couette definition based on the channel height is most suitable.

1.4.2 Effect of suspended elements

These idealised flow situations provide a frame of reference against which blood flow characteristics can be compared. However, blood is not a Newtonian fluid as a result of the high quantity of RBCs suspended in the plasma. To consider how these particles behave, let us first consider Poiseuille flow at low velocities with dilute suspensions of increasingly complex particles. The following concepts have been reviewed in some depth by, for example (Caro et al., 2012; Goldsmith et al., 1989; Karnis et al., 1963), and will be briefly summarised in the following.

The velocity in Poiseuille flow is zero at the wall and at a maximum in the channel centre, and the shear stress is zero at the channel centre and increases linearly towards the wall. However, if a rigid spherical particle is within the flow, the fluid velocity at the surface of the particle will be zero (relative to the particle) and the shear rate, and hence shear stress acting on the particle will be greater towards the centre of the channel (wherein the velocity is greatest). As a result the particle will rotate toward the vessel wall such that the side closest to the wall rotates in the direction opposite to the flow, but will follow fluid streamlines. The resultant stresses on the rigid particle are compressive along an axis which approximately aligns with the shear gradient, and extensive in the orthogonal direction. If the sphere is deformable, such as would be the case for a liquid drop or an RBC, it will deform according to these forces, but continue to rotate around its centre. As a result of interactions between the flow field of the fluid around the deformable particle and the channel wall, the particle will migrate towards the centre of the channel. For RBCs, Cokelet (2011) describes the phenomenon as occurring due to the distortion of the flow field of the suspending medium around the cell, both when it is near the wall and when it deforms and elongates due to the stresses acting on the cell membrane. The rate of this migration increases as the droplet deformability increases,

and as the shear gradient across the droplet increases; either due to increasing flow rate or decreasing ratio of particle to channel diameter. Rods and disks tend to tumble, as the forces acting on either side are dependent on the inclination angle of the object in relation to the flow. Deformable rods or disks will migrate radially, but rigid ones will not. Finally it should be mentioned that, as the particle concentration increases, particle-particle interactions will oppose the radial migration to some extent. Red blood cells are deformable disks, and their aggregates akin to deformable rods. The way in which they affect fluid flow can be similar to droplets, disks or rods, depending on the relative size of the channel to the RBC, the deformability of the RBCs and the flow rate.

In vessels which are large enough for the RBCs to move freely, their behaviour is dependent on flow rate. At low flow rates, they act like disks, tumbling with a periodic rotational velocity. At high flow rates, RBCs deform similarly to liquid droplets, but their membrane rotates freely about the liquid centre in what is known as a tank-treading motion (Abkarian et al., 2007). This reduces viscous dissipation and thus the relative viscosity of the fluid. Hence, if deformability of the RBCs is decreased, the radial migration will be decreased also. Furthermore, RBC aggregation results in rouleaux which are equivalent to flexible rods. Aggregation also forms clumps, which act as large diameter deformable particles. The relative size of both rouleaux and clumps is larger than that of individual RBCs and hence radial migration is enhanced in the presence of aggregation (Alonso et al., 1995; Reinke et al., 1987).

1.4.3 The cell-depleted layer

As a result of radial migration, a non-uniform distribution of RBCs, which can be termed a haematocrit profile, is generated. In a long straight channel/vessel, where the forces inducing radial migration are in equilibrium with the particle-particle collision forces, the profile will have a maximum cell concentration in the channel centre and a minimum concentration at the channel walls. However, the details of this distribution are often overlooked, and blood is considered as two immiscible fluids: the RBC core (with constant haematocrit) and the cell-free layer (CFL) at the channel wall (with zero haematocrit). The cell-free layer has received a lot of research attention and has been reviewed by Kim et al. (2009). The term ‘cell-free layer’ is often disputed, for the rea-

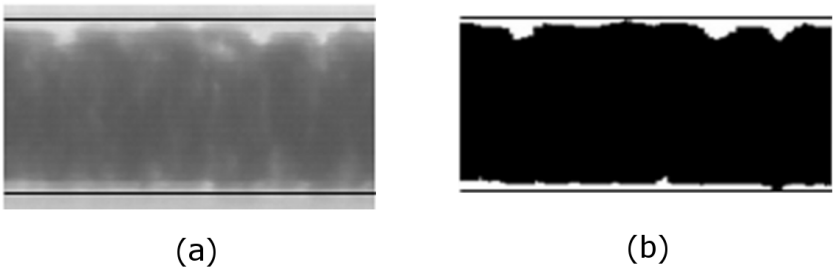

Figure 1.5: (a) Image of the CDL *in vivo*, (b) Approximated binary image for CDL width and roughness calculation (Kim et al., 2006). Black lines represent vessel wall boundaries. Channel width $\approx 40\mu m$ (not stated explicitly in the reference).

son that the region (if defined spatially) will rarely be entirely cell free (Baskurt et al., 2012). Instead, the interactions between neighbouring RBCs cause cells to impinge on the layer. To account for this fact, the term cell-depleted layer (CDL) (Reinke et al., 1986) is sometimes used. For the present study, the term CDL is preferred, although CFL is used for regions through which no cells ever pass.

Measurement of the CDL is commonly carried out based on thresholding microscopic images of the vessel. Figure 1.5a shows a microscopic image of a vessel with the walls marked by black lines. Figure 1.5b shows a binary approximation calculated by thresholding using the Otsu method, from which CDL width and roughness can be calculated (Kim et al., 2006).

It can be seen in Figure 1.5a, that there are regions which are notably lighter near the edge of the CDL. This is because the local haematocrit is reduced in that location, supporting the assertion that the CDL is in fact part of a continuous haematocrit profile. Nonetheless, it is a useful simplification which can be analysed with relative ease *in vivo* (Kim et al., 2007; Namgung et al., 2010; Ong et al., 2011a; Yalcin et al., 2011).

The width of the CDL is dependent on RBC concentration, aggregation and deformability, the diameter of the vessel, the flow rate and the presence of the ESL (Alonso et al., 1995; Kim et al., 2007; Pries et al., 1994). If flow rates in a vessel are sufficiently high so that aggregation is absent, then the CDL width increases with flow rate; however, the presence of aggregation inverts this relationship, as reducing flow rate increases aggregation (Kim et al., 2009). The aforementioned studies were carried out in straight vessel sections or capillary tubes; however, Ong et al. (2012) recently reported details on the CDL distribution in an arteriolar bifurcation and found that the flow ratio

also had an influence on the RBC distribution.

1.4.4 Velocity profiles

By changing the RBC distribution, radial migration also alters the shape of velocity profiles, as the viscosity distribution is dependent on local RBC concentration. For a continuum fluid at a given channel location, if the viscosity increases, the velocity will decrease due to increased resistance between shear layers in the fluid. For blood flow, the presence of RBCs disrupts local fluid streamlines leading to increased local viscosity which scales with the RBC concentration. Due to the low haematocrit near the wall resulting from radial migration of RBCs, the velocity near the channel wall is increased due to the relative reduction in viscosity. Moreover, in the channel centre, where the haematocrit concentration is highest, the viscosity is increased and the velocity decreases. The result is a 'blunted' velocity profile and has been observed, *in vivo* (Bishop et al., 2001a) and *in vitro* (Reinke et al., 1987). Given that the maximum velocity occurs at $r = 0$, the maximum velocity for Poiseuille flow is given by (see Equation 1.5)[†]

$$u_{max} = \frac{-R^2}{4\mu}\frac{\partial p}{\partial x} \tag{1.12}$$

Noting that $u_{max} = 2\overline{U}$, equation 1.7 can thus be written as

$$u(r) = u_{max}\left(1 - \left(\frac{r}{R}\right)^2\right) \tag{1.13}$$

In the microcirculation, particularly in the presence of aggregation, blunted velocity profiles have been observed. This is often empirically accounted for by applying an exponent K, such that

$$u(r) = u_{max}\left(1 - \left(\frac{r}{R}\right)^K\right) \tag{1.14}$$

Bishop et al. (2001a) found $K = 1.7$ and 2.1 for normal and slow flow respectively in a venule of a rat spinotrapezius muscle. When they induced RBC aggregation through infusion of Dextran 500, these values changed to 2.3 and 3.8 respectively.

[†]note that the minus sign is present because the fluid will flow in the direction opposite to the pressure gradient.

1.4.5 Viscosity

Blood viscosity, or haemorheology, is very complex due to the two-phase nature of the blood, as described above. The viscosity of blood is mainly dependent on the haematocrit and shear rate.

Blood plasma is Newtonian (Lowe, 1988), and hence behaves very much like water, albeit with a higher viscosity resulting from the suspended plasma proteins. The presence of RBCs results in an increase in viscosity, by disrupting streamlines and increasing viscous dissipation. However, as the majority of the flow resistance in any pressure driven flow through a channel is a result of the friction at the wall, the low viscosity CDL results in a decrease in the flow resistance of the vessel compared to that which would be observed for a uniform distribution of RBCs. This reduction in flow resistance becomes more pronounced for larger CDL widths.

A common way of describing the flow resistance is the 'apparent viscosity'. Also termed the effective viscosity, the apparent viscosity μ_{app}, is used to describe the bulk viscosity based on the flow rate generated by a given pressure drop (or the pressure drop for a given flow rate) if the fluid was Newtonian. For blood flow, the Poiseuille flow assumption is often adopted, for which the apparent viscosity is calculated according to

$$\mu_{app} = \frac{\pi R^4}{8L}\frac{\Delta p}{Q} \tag{1.15}$$

where the first term is related to the geometry of the system and the second is related to the flow (Cokelet, 1999). For blood flow, it is common to normalise the viscosity with that of the of the Newtonian phase (the plasma or other suspending medium), so as to clearly indicate the influence of the suspended elements on the viscosity, giving the relative viscosity

$$\mu_r = \frac{\mu}{\mu_0} \tag{1.16}$$

This apparent viscosity can be normalised similarly to give the relative apparent viscosity

$$\mu_a = \frac{\mu_r}{\mu_0} \tag{1.17}$$

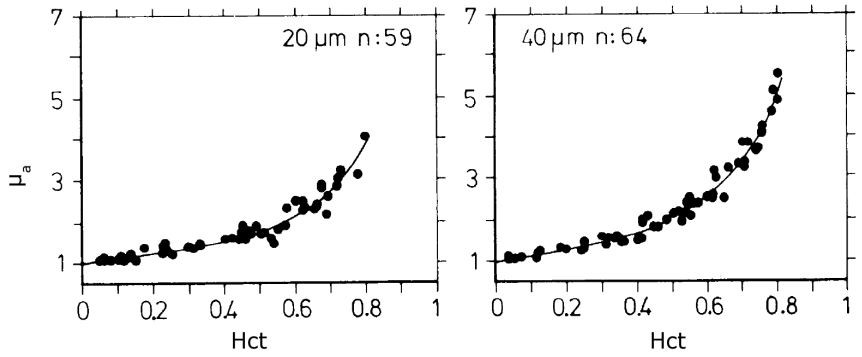

Figure 1.6: Relative apparent viscosity dependence on haematocrit in two different diameter capillary tubes (Pries et al., 1992b).

where μ_0 is the viscosity of the plasma (or other suspending medium for *in vitro* experiments).

For a Newtonian fluid, the shear stress a shear rate are related according to $\tau = \mu\dot{\gamma}$. However, suspensions of RBCs are non-Newtonian, in that the viscosity of blood is a function of the applied shear rate: as the shear increases, the viscosity decreases. Hence blood is a shear thinning fluid. Furthermore, RBC aggregation results in blood having a yield-stress: in fluid dynamics terminology, it acts as a Bingham plastic. In order to account for both properties, a number of constitutive models for blood viscosity have been developed. In the present study, the Carreau-Yasuda and Quemada models will be considered, but a detailed review of the derivation of these models is beyond the scope of this thesis.

The majority of these models have been considered using Couette viscometry, in which the shear rate and haematocrit are (relatively) constant, allowing for experiments to consider individual parameters. However, due to the additional complexities of the RBC suspension introduced by geometric constraints and transient characteristics of RBC radial migration and aggregation, an alternative approach is to acquire empirical data in, for example capillary tubes, and fit curves to the data, as done by Pries et al. (1992b). They made their own measurements and compiled data on the apparent viscosity of blood in capillary tubes of various diameters at a range of haematocrits.

As can be seen in Figure 1.6, the relationship between the apparent viscosity and the haematocrit is relatively linear below systemic haematocrit ($\approx 45\%$) and increases exponentially thereafter. In their paper, Pries et al. (1992b) defined an equation with

empirically derived parameters:

$$\mu_r = 1 + E\left((1 - H_D)^F + 1\right) \tag{1.18}$$

where H_D is the discharge haematocrit. The E parameter defines the slope of the viscosity-haematocrit relationship and the F parameter defines the non-linearity for a given tube diameter. Values of E and F were compiled for various studies and used to define an equation for relative viscosity in tube flow based on a bulk haematocrit and the diameter of the tube.

Pries et al. (1992b) showed the strong dependence of blood viscosity on haematocrit in tubes, which has also been shown for Couette viscometers (Chien, 1970) and in the rat mesentery (Lipowsky et al., 1980). However, the effect of local haematocrit distributions on both the local viscosity profile and the apparent viscosity in geometries such as a bifurcation is not understood and requires further investigation.

1.4.6 Wall shear stress

The wall shear stress (WSS) plays an important role in physiological regulation of blood flow. Endothelial and vascular smooth muscle cells are capable of sensing different levels of WSS (and pressure), and are responsible for controling vascular physiology (Hahn & Schwartz, 2009). Furthermore, changes in wall shear stress have been associated with altered gene expression in atherosclerosis (Reneman et al., 2006; Katritsis et al., 2007). Wall shear stress also regulates the production of nitric oxide, a vasodilator, from endothelial cells which dynamically reduces flow resistance (Ong et al., 2011c).

The wall shear stress is defined according to

$$\tau_w = \mu\dot{\gamma} \tag{1.19}$$

Where μ is the fluid viscosity at the wall and $\dot{\gamma}$ is the wall shear rate, i.e. du/dr in Poiseuille flow. For Poiseuille flow, differentiating Equation 1.13 with respect to r yields

$$\dot{\gamma} = \frac{du}{dr} = u_{max}\left(\frac{2r}{R^2}\right) \tag{1.20}$$

which evaluated at $r = R$, gives $2u_{max}/R$ (equivalent to $4\overline{U}/R$). However, as described previously, blood velocity profiles tend to be blunted. For a velocity profile described by Equation 1.14, the shear rate is given by

$$\dot{\gamma} = \frac{du}{dr} = u_{max} K \left(\frac{r^{K-1}}{R^K} \right) \tag{1.21}$$

which at at $r = R$ yields Ku_{max}/R. Hence, as the bluntness increases, so does the wall shear rate. Indeed, at low flow rates, the average values of K calculated by Bishop et al. (2001a) suggest wall shear rates of $3.8u_{max}/R$ and $2.3u_{max}/R$ for aggregating and non-aggregating cases respectively; an increase of 65% as a result of RBC aggregation. Further complexity is added to the calculation of τ_w for blood due to the difficulty in accurately defining the viscosity of the fluid at the wall. For a uniform haematocrit distribution, the viscosity is still dependent on shear rate, although this could be accounted for using an empirical non-Newtonian viscosity model.

In large vessels, the whole-blood viscosity is commonly used, on the assumption that the haematocrit distribution is uniform (Liu et al., 2011; Katritsis et al., 2007; Poelma et al., 2009). For arteriolar scale flow, the ostensible presence of the cell-free layer allows the assumption that the viscosity at the wall is equal to that of the plasma (Reneman et al., 2006). Namgung et al. (2011) estimated wall shear stresses by assuming that the the CDL viscosity was that of the suspending medium and that the velocity between the wall and the CDL edge varied linearly, as in Couette flow. They found that this resulted in an underestimation of the wall shear stress and proposed a multiplication by a factor of 1.22 to account for additional viscous dissipation caused by the roughness of the interface. Sharan & Popel (2001) numerically modelled blood flow in a similar manner and their results suggested that the effective viscosity of the CDL was higher than that of the plasma (or other suspending medium) as the roughness of the interface between the CDL and the RBC dense core increases energy dissipation. However, such results are also consistent with the idea that the CDL is part of a continuous haematocrit distribution, hence the cell concentration and thus viscosity would be greater than that of the suspending medium.

Damiano et al. (2004) developed a microviscometry approach which enabled them to estimate viscosity profiles from velocity profiles measured with micro particle image velocimetry (μPIV) in round vessels for shear rates $> 50s^{-1}$. This allows a more

accurate estimation of wall shear stress, but only in fully developed symmetric flow at high flow rates. Further work is required to understand how wall shear varies in complex geometries.

1.4.7 Fåhraeus and Fåhraeus-Lindqvist effects

As a result of radial migration, the average RBC velocity, U_{rbc} is higher than the velocity of the blood as a whole, or total blood velocity, U_{tot}. Thus the transit time of an RBC through a particular segment will be smaller than the blood as a whole and, in order for the discharge haematocrit, H_D, to equal the feed haematocrit H_F, the channel haematocrit, H_C, must be reduced (Goldsmith et al., 1989; Lipowsky, 2005). The discharge haematocrit must be equal to the ratio of the flow rate of the RBCs (Q_{rbc}) to the whole blood (Q_{tot}) (Pries & Secomb, 2008), thus

$$H_D = \frac{Q_{rbc}}{Q_{tot}} = \frac{H_T U_{rbc} A}{U_{tot} A} \tag{1.22}$$

where A is the cross sectional area of the cylindrical conduit and therefore

$$H_R = \frac{H_T}{H_D} = \frac{U_{rbc}}{U_{tot}} \tag{1.23}$$

Ultimately, this results in a reduction in haematocrit as a function of vessel diameter and is known as the Fåhraeus effect. Figure 1.7a shows the relative haematocrit, H_R, against the feed haematocrit for a range of tube diameters. It can be seen that as the tube diameter decreases, the influence of feed haematocrit increases. Figure 1.7b shows data collected from a cat mesentery, which shows the dependence of haematocrit on vessel diameter *in vivo*.

It can be seen that the minimum haematocrit occurs in the post-capillary venules, but the haematocrit is reduced throughout the microvasculature. In general, as the haematocrit increases, the apparent viscosity increases as more viscous dissipation arises from elevated fluid stresses and more frequent cell-cell and cell-wall interactions. Conversely, as the haematocrit decreases as a result of the Fåhraeus effect, the apparent viscosity decreases (due the the increased CDL width). In addition, at higher velocities (generally correlating with larger vessels), RBCs deform to a greater extent and align with the flow, which further reduces viscosity. This reduction in viscosity with vessel diameter is known as the Fåhraeus-Lindqvist effect. Figure 1.8 shows data from a num-

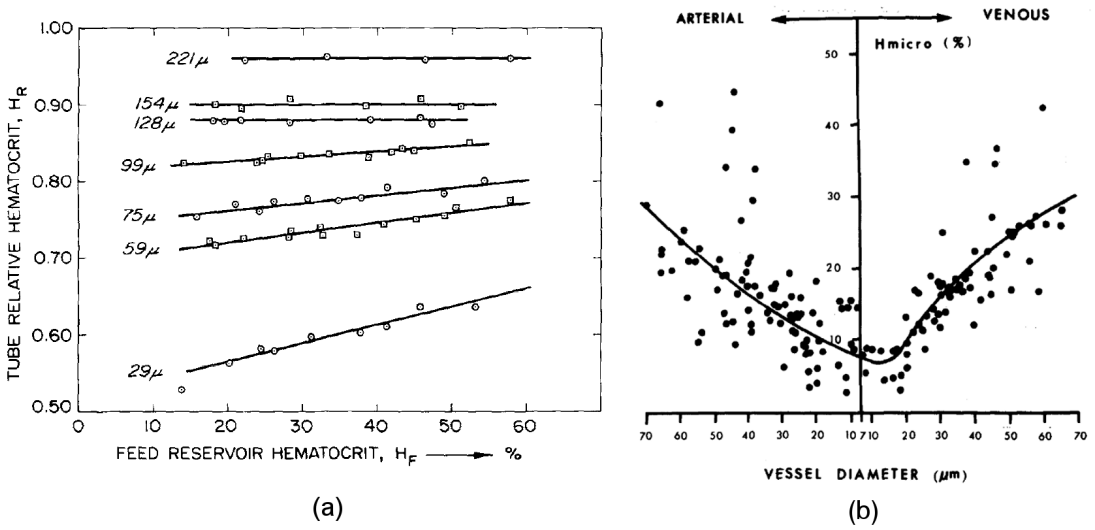

Figure 1.7: (a) Fåhraeus effect *in vitro* (Barbee & Cokelet, 1971), (b) Haematocrit measurements in the cat mesentery (Lipowsky et al., 1980).

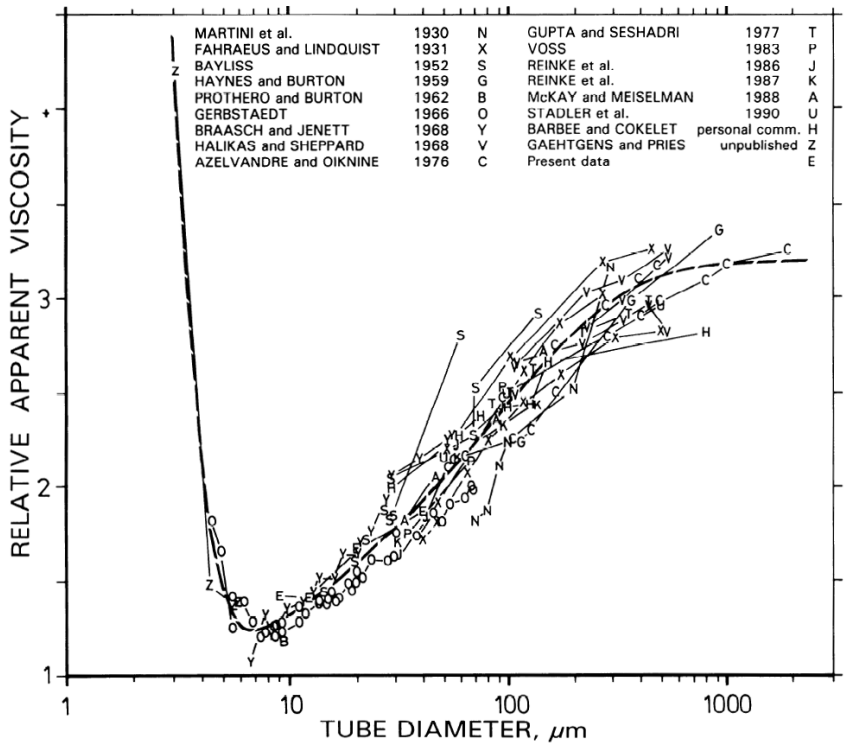

Figure 1.8: Compilation of data showing the Fåhraeus-Lindqvist effect (Pries et al., 1992a).

ber of sources compiled by Pries et al. (1992b) (in which the flow rates were too high for RBC aggregation).

As the tube diameter decreases from 1000 to $7\mu m$, the relative apparent viscosity of the blood decreases. Below $7\mu m$, the effect is inverted as the RBC deformation required in order for the cell to fit through vessels smaller than their equilibrium shape requires

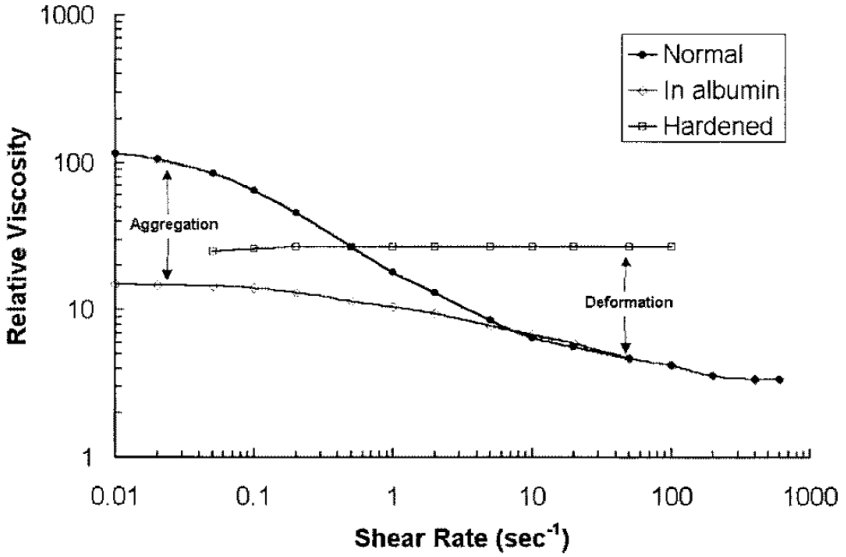

Figure 1.9: Relative importance of deformability and aggregation (Chien, 1970).

energy, and thus increases the apparent viscosity. Cokelet (1999) examined the available data and concluded, tentatively, that the Fåhraeus effect explains the Fåhraeus-Lindqvist for tube diameters down to about $20\mu m$, where a continuum model will suitably predict the flow characteristics.

1.4.8 Effects of aggregation on flow

RBC aggregation is a multifaceted phenomenon, both in its mechanisms and its effect on the flow of the blood. An interesting *in vitro* study by Chien (1970) highlighted the importance of aggregation on the shear-thinning behaviour of blood, with 75% of the decrease in viscosity at high shear resulting from aggregation, while 25% was a result of the RBC deformation, as indicated in Figure 1.9. It can be seen that the viscosity of the blood with hardened cells shows almost no shear dependence, while aggregation significantly increases the viscosity at low shear rates ($< 5s^{-1}$) and deformability decreases it at higher shear rates ($> 5s^{-1}$).

As described in §1.2.2, RBC aggregation has a significant effect on the viscosity of blood. However, the overall effect depends largely on the system in which aggregation is analysed. Viscometric studies show increased relative viscosity with increased aggregation (Chien & Jan, 1973; Kaliviotis & Yianneskis, 2008), due to the increased viscous dissipation, although at very high aggregation levels, network formation can reduce viscosity.

However, *in vitro* experiments in vertical glass capillaries show either an independence of viscosity on aggregation (Reinke et al., 1986) or a decrease in relative viscosity (Reinke et al., 1987). Cokelet & Goldsmith (1991) found that the flow resistance (comparable to relative viscosity) increased with pseudoshear rates decreasing from 50 to $2s^{-1}$, and then decreased as the pseudoshear rate was lowered further. This has been attributed to the enhanced radial migration under aggregating conditions at low shear rates (Reinke et al., 1987; Cokelet & Goldsmith, 1991), with CDL widths as large as 40% of the tube diameter (Reinke et al., 1987).

The literature on the effect of RBC aggregation on *in vivo* vascular network resistance shows conflicting results. A number of studies (Baskurt et al., 1999; Charansonney et al., 1993) found that flow resistance decreased with aggregation, while Gustafsson et al. (1981) found viscosity to be independent of aggregation. Conversely, some researchers have found aggregation to increase flow resistance (Bishop et al., 2001a; Cabel et al., 1997; Soutani et al., 1995). Vicaut (1995) suggested that this was a result of the relationship between the viscosity reducing CDL formation, and the added flow resistance resulting from aggregates entering capillaries. Furthermore, the CDL formation, and hence flow resistance, is dependent on vascular conditions, particularly geometry and flow rate (Bishop et al., 2001c).

Within the venules, where the majority of aggregation is reported to occur due to the lower shear rates, the topology consists of converging vessels. When two vessels meet, the converging flow streams deflect each other towards the vessel walls, counteracting the effects of radial migration and attenuating the CDL (Bishop et al., 2001b). It has been reported that aggregation will only decrease viscosity if there is sufficient time for aggregates to form, increase radial migration and generate a significant CDL between junctions. A number of studies have suggested that, as the characteristic time for radial migration to occur is considerably longer than that of aggregation and the residence times of vessels in individual sections, under physiological flow rates, significant CDL layers will not have time to form and will thus not affect the flow (Alonso et al., 1995; Bishop et al., 2001b)[†]. However, under pathological conditions such as ischemia/reperfusion or sepsis, the influence of aggregation may be increased (Bishop

[†]Although it is likely that the haematocrit gradients are present, and hence aggregation may still have an effect.

et al., 2001b). Ong et al. (2010) found that the CDL width in arterioles increased with aggregation, although only at reduced flow rates, while Kim et al. (2006) found a similar response in venules. Bishop et al. (2001b) identified a degree of radial migration, but did not observe a CDL, although the aggregation tendency of the blood in their study was below that of normal human blood.

Bishop et al. (2001c) measured radial migration of cells under aggregating and non-aggregating conditions in a venule and found that the radial movement per unit length increased slightly with increased aggregation, although in the vicinity of the converging vessel a large radial movement occurred due to infusion of the additional flow stream.

The increasing viscous dissipation which offsets the reduction in flow resistance due to CDL formation has a number of causes. Generally, this results from the modified shape of the RBC aggregates, which deflect the streamlines from those which would occur if the blood was in a dispersed state, particularly as they tumble along the wall (Kim et al., 2005). Further viscous dissipation occurs as a result of the blunting of the velocity profile which has been reported for aggregating flows (Bishop et al., 2001a; Gaehtgens et al., 1970; Reinke et al., 1986; Tangelder et al., 1986; Zhang et al., 2009).

Bishop et al. (2002) have also studied the effect of aggregation on temporal variations in velocity and radial position for labelled RBCs in rat venules. They found that aggregation had no discernible effect on deviations in radial positions, but that it attenuated velocity fluctuations. However, it should be noted that their data had a considerable amount of scatter and the differences between the aggregating and non-aggregating cases was small.

Leukocyte margination, which is an important part of the body's immunological response has been found to be significantly increased by RBC aggregation (Goldsmith et al., 1999; Pearson & Lipowsky, 2000; Pearson & Lipowsky, 2004). Platelet distribution has been found to be characterised by an increased density near the wall under non-aggregating conditions (Aarts et al., 1988), with a more extreme distribution in the presence of RBC aggregation (Goldsmith et al., 1999; Perkkiö et al., 1987). Both of these effects occur as a result of the RBC dense core forcing the platelets towards the vessel wall, and thus the effects also increase with increasing haematocrit. Platelet aggregation, a part of the haemostasis process, was found to be independent of RBC

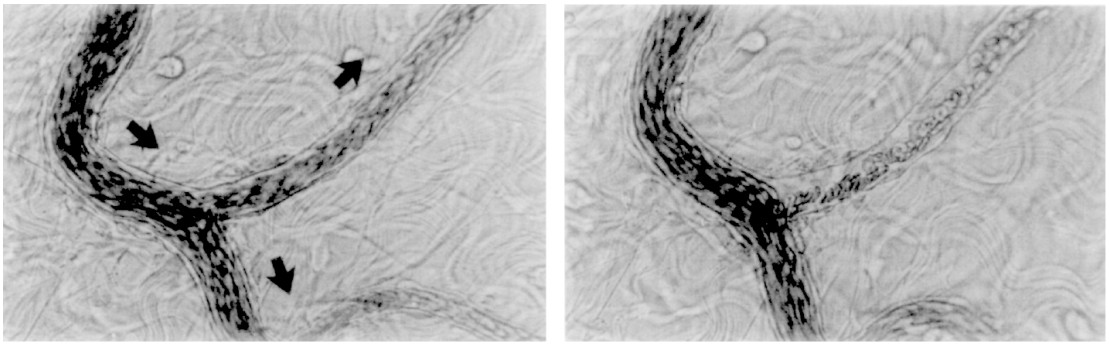

Figure 1.10: Plasma skimming in a rat mesentery (Pries et al., 1989). (a) Bifurcation under normal conditions, arrows indicate flow direction, (b) shows the same vessel after the side branch has been occluded to reduce the flow down that branch. A non-uniform haematocrit distribution can be observed.

aggregation (Ott et al., 2010).

1.4.9 Bifurcations and plasma skimming

The bulk distribution of cells (the average haematocrit in each vessel) in the microvasculature is strongly heterogeneous. This is largely a result of phase separation at arteriolar bifurcations (Pries et al., 1996). For the general case of a parent branch bifurcating into two daughter branches with different flow rates, the higher flow rate branch receives disproportionately more cells. This is known as the Zweifach-Fung or Bifurcation law. A significant factor in this phenomenon is the presence of a CDL in the parent vessel. An example of the occurence of this phenomenon *in vivo* is shown in Figure 1.10.

This effect has been termed 'plasma skimming' and in extremis, can result in entirely plasmatic vessels (Popel & Johnson, 2005). In general, cell and suspending medium streamlines coincide, so that a separating surface, or flow divider, can be defined, for which cells on either side will always enter one of the daughter branches. If the fluid entering one of the daughter branches has a lower flow rate, the separating surface will be positioned such that a larger proportion of the fluid entering this branch will have been part of the CDL in the parent branch and the daughter branch haematocrit thus will be lower than that in the parent branch. The high flow rate daughter branch will thus have increased haematocrit for the same reason (Fenton et al., 1985).

Cells which lie on the separating surface will be drawn down one of the branches as a result of the hydrodynamic forces acting upon them. This effect will become rela-

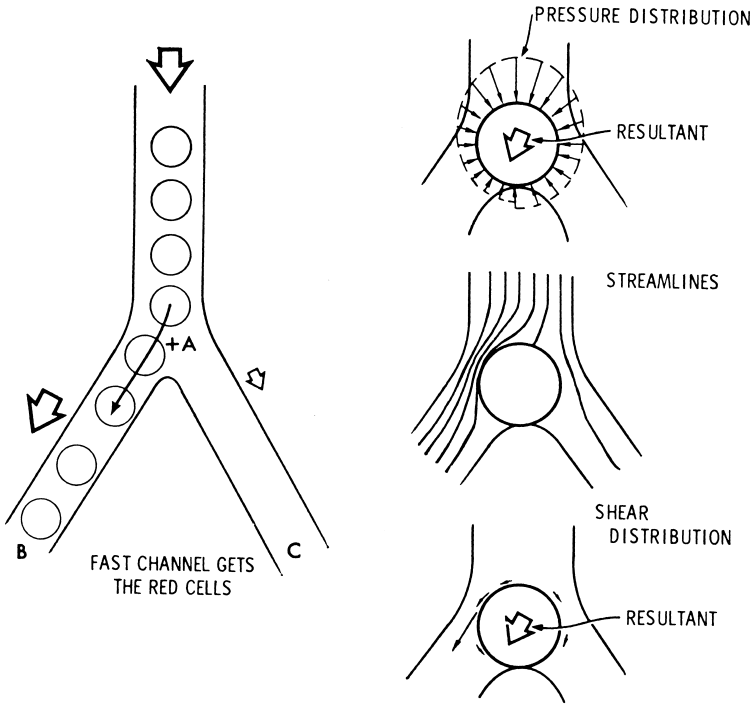

Figure 1.11: Classic theory of plasma skimming - An attraction towards the high flow branch (Fung, 1973).

tively more important with decreasing vessel diameter, as a larger proportion of cells will lie on the separating surface. An attraction towards the high-flow rate branch has been described (Fung, 1973; Yang et al., 2006; Kersaudy-Kerhoas et al., 2010). The reasoning behind this was provided by Fung (1973) and is illustrated in Figure 1.11.

Fung (1973) explains the mechanism behind the attraction towards the high-flow rate branch in terms of the resultant forces from the pressure and shear acting on a particle entering a bifurcation. Assuming that the flow rate into the left hand branch is higher than that into the right, the pressure will thus be lower in the left branch. This will generate a greater pressure gradient between the parent vessel and the higher flow rate right branch, leading to a resultant force directing the particle into the left hand branch. Similarly, the shear forces acting on the left hand side of the particle will be greater than those on the right as a result of the higher velocity and thus the resultant force will also point towards the left branch. Thus, the attraction is always towards the higher flow rate branch. Although Fung's description is for a vessel with of similar length scale to the red cells, Yang et al. (2006) provide a similar argument for larger vessels.

However, recently Barber et al. (2008) and subsequently Doyeux et al. (2011) have pro-

vided an opposing conclusion, suggesting that there is in fact an attraction towards the lower flow rate branch under certain conditions. Doyeux et al. (2011) compared a number of results reported in the literature with predicted values based on the assumption of no attraction and carried out simulations and experiments with rigid spheres. They concluded that, while in most cases in the literature the higher flow-rate branch does receive disproportionately more particles/cells, this is due solely to the distribution of particles/cells in the parent branch as a result of radial migration or the depletion effect (particles cannot be closer to the vessel wall than their radius). Figure 1.12a shows a schematic of the attraction towards the low flow branch, while Figure 1.12b shows the attraction towards the high flow branch. Both occur as a result of a lower pressure on one side of the particle, but the magnitude of these pressures is different at different points in the bifurcation. At the entrance to the bifurcation, the pressure drop is inversely proportional to flow rate, and thus the attraction is towards the low flow rate branch. Within the bifurcation but closer to the far wall, the particle will be attracted towards the high flow rate branch, along similar lines of reasoning to Fung (1973), in that the pressure in the high flow branch is lower than the low flow branch. However, in the context of blood flow on the scale of arterioles, the deformability of the cells and resulting radial migration will limit the attraction towards the low flow rate branch, as will the small size of the RBCs relative to the channel compared to capillary size bifurcations.

Plasma skimming is generally described in terms of the flow ratio, $Q^* = Q_d/Q_p$ and the RBC flux ratio, $F^* = F_d/F_p$, where the subscripts d and p refer to the daughter and parent branches respectively. In the absence of plasma skimming the relationship between Q^* and F^* would be linear, but it has been shown in many studies to deviate significantly from the linear response (Audet & Olbricht, 1987; Carr & Wickham, 1990; Chesnutt & Marshall, 2009; Chien et al., 1985; Dellimore et al., 1983; El-Kareh & Secomb, 2000; Fenton et al., 1985; Yen & Fung, 1978). These studies have provided valuable information on the important parameters, such as vessel diameter, velocities, flow ratio, bifurcation angle/configuration, parent vessel haematocrit, haematocrit distribution and RBC deformability and aggregation. Fenton et al. (1985) concluded that the most important parameters were the parent vessel haematocrit, the tube diameter and the flow ratio, and subsequent studies have not contradicted this.

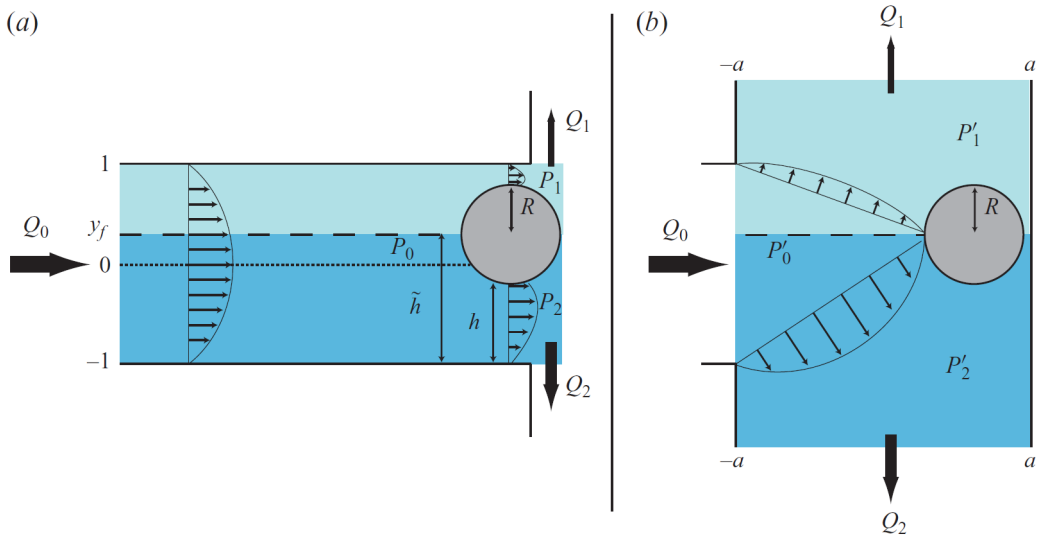

Figure 1.12: Alternative theory of plasma skimming - an attraction towards the low flow branch (Doyeux et al., 2011). Schematic shows a bifurcation (daughter branches on the right hand side). Light blue fluid enters the low flow branch (p_1, Q_1). Profiles show velocity of the suspending medium. (a) Flow field characteristics at the entrance to the bifurcation. $p_1 < p_2$ indicating an attraction towards the low flow branch, (b) The flow characteristics at the far wall of the bifurcation. Here, $p_1 > p_2$, resulting in an attraction towards the high flow branch.

As the feed haematocrit increases, the amount of plasma skimming decreases, i.e. the F^* vs. Q^* plot becomes more linear; additionally, the scatter increases (Dellimore et al., 1983; Fenton et al., 1985; Yen & Fung, 1978). In general, it has been found that decreasing vessel diameter increases plasma skimming (Fenton et al., 1985; Yen & Fung, 1978). Pries et al. (1989) found the same trend *in vivo*, with little plasma skimming occurring for vessel diameters greater than $40\mu m$, although Dellimore et al. (1983) identified plasma skimming in relatively large channel ($180\mu m$) *in vitro*. Relative parent to daughter branch diameters were found by Carr & Wickham (1990) to be of little importance *in vitro*, although it was found that, for different daughter branch sizes, the smaller branch receives more cells *in silico* (Barber et al., 2008) and *in vivo* (Pries et al., 1989).

It is generally accepted that, due to the low Reynolds numbers found in microvascular flows, local geometry has only minor influence on the plasma skimming. Fenton et al. (1985) investigated the filleting angle in a T-junction bifurcation and found that this parameter did not have a significant effect, and it has been reported that the angle of bifurcation is relatively unimportant (Barber et al., 2008; Fenton et al., 1985; Pries

et al., 1989). Fenton et al. (1985) also found that changes in parent vessel flow rate and cell distensibility had little effect on plasma skimming.

The low radial dispersivity of RBCs ($\approx 10^{-7} mm^2/s$ (Cokelet, 1999)) means that between bifurcations the haematocrit profile may not have sufficient time to become symmetric. A few studies have investigated the effect of serial bifurcations, due to the importance of the upstream haematocrit distribution *in vitro* using particles (Roberts & Olbricht, 2006) or RBCs (Carr & Wickham, 1991) and *in vivo* (Pries et al., 1989). Pries et al. (1989) reported that if the distance between bifurcations was more than $10D$, then the haematocrit distribution would have recovered symmetry and thus the upstream bifurcation would not influence the downstream one. Bishop et al. (2001c) identified an average ratio of 3.5:1 (vessel length to diameter) between bifurcations in venules, although larger values between 8:1 and 30:1 have been reported elsewhere (House & Johnson, 1986). Carr & Wickham (1991) reported that the key parameter is the ratio of the distance between bifurcations to the flow rate. For 25 and $50\mu m$ tubes, they found that the critical value of this parameter for which symmetry would be achieved were 50 and $200 s/mm^2$ respectively, indicating that both distance between bifurcations and the local flow rates are of importance. However, more experimental data is required in order to better understand how microhaemodynamic phenomena, particularly RBC aggregation, affect the recovery of symmetry in both haematocrit and velocity distributions.

In a recent *in silico* study, Chesnutt & Marshall (2009) modelled blood flow through a bifurcation, including cell interactions and aggregation. They concluded that aggregation had little effect on plasma skimming. However, their study used a low haematocrit ($0.05 - 0.15$) and they only analysed results for a single Q^* value (0.1). Perkkiö et al. (1987) studied plasma and platelet skimming in channels of $200\mu m$ with a $100\mu m$ side branch. They found that for non-aggregating blood, there was no discernible plasma skimming, but for aggregating blood, the plasma skimming effect was considerable. Furthermore, Gelin (1963) and Gaehtgens et al. (1978) also found that aggregation increased the extent of plasma skimming. This might be expected, as aggregation increases CDL width, and thus the main factor in the phenomenon of plasma skimming, as described above. However, the relationship between plasma skimming and RBC aggregation requires more in depth analysis. It should be noted that while the working

fluids in the studies of Fenton et al. (1985) and Dellimore et al. (1983) would have allowed for aggregation to occur, the flow rates in these studies were sufficiently high that disaggregative forces would dominate, and thus no effect of aggregation was observed. It is worth noting that the experimental studies reported above generally reported bulk effects, such as average velocities, vessel haematocrit and mean cell free layer width. In order to fully understand why each of the above effects is important, more detailed information is required on local velocity, haematocrit and aggregation. This is part of the focus of the present research.

1.5 Practical aspects of microscale blood flow analysis

This section will provide some information on the importance of understanding the characteristics of microvascular blood flow. First the role of microvascular blood viscosity in pathology will be outlined. A description of some diagnostic devices based on hydrodynamic phenomena will follow.

1.5.1 Importance of blood flow in pathology

Microvascular blood viscosity and its associated phenomena have great significance in a large number of diseases. Pries et al. (2008) identified the coronary microcirculation as complicit in myocardial ischemia (restriction of blood supply to the heart). Barabino et al. (2010) reported that, in sickle cell disease, increased plasma protein concentration leads to increased aggregation, which increases viscosity. Additionally, reduced RBC deformability enhances the effect. Jain (1988) reported significantly increased aggregation in cancer patients compared to healthy controls, with higher levels in the deceased than in survivors. Diabetic patients have increased levels of RBC aggregation and decreased cell deformability (Babu & Singh, 2004). Hypoxia (deprivation of oxygen to a tissue) can be caused by RBC aggregation (Dintenfass, 1985). In malaria and sickle cell disease, adhesion of infected/damaged RBC to the endothelium can increase flow resistance and, in the extreme, result in complete occlusion of vessels (Rogerson et al., 2004; Yedgar et al., 2008).

It is evident that there is some connection between increased blood viscosity and pathological states, but the details of the relationship remain unclear. It has generally been assumed that increased blood viscosity necessarily has negative implications. However,

recent reports have suggested that this may not be the case and that increased blood viscosity may be a compensatory mechanism to regulate peripheral resistance and perfusion in pathological states (Forconi & Gori, 2009; Intaglietta, 2009). Furthermore, some athletes deliberately increase their haematocrit (and thus viscosity) through erythropoietin doping, and their performance is improved while many long-distance runners are carriers of sickle cell trait and thus have an associated hyperviscosity syndrome (Forconi & Gori, 2009). The corollary is that increased viscosity must not necessarily be causing significant deleterious consequences.

1.5.2 Applications to biomedical microdevices

Blood plasma contains a large number of proteins and other solutes and is widely used in diagnostic medicine to derive information on a patient's condition. In order to perform these analyses, the plasma needs to be separated from the cells due to chemical and optical properties of the cells which can affect results (Jäggi et al., 2007). Typically, this has been done via centrifugation of a sample of blood, but this requires a large sample size and has considerable labour, time and cost implications (Jäggi et al., 2007). In some surgical procedures, it is beneficial to be able to continuously analyse the contents of the blood, which cannot be achieved via centrifugation (Yang et al., 2006). Microfluidics offer a new approach which can be utilised to carry out blood analyses in 'lab on a chip' or 'micro total analysis systems'.

Faivre et al. (2006) used a rapid contraction then expansion geometry to enhance the CDL width, taking advantage of the low dispersivity of RBC. They reported extraction of 24% of the plasma (plasma yield) for a haematocrit of 16% at $200\mu l/hr$, with a purity of 100%, (i.e. the extracted plasma contained no cells). Sollier et al. (2009) used a similar approach but achieved a higher throughput of $6ml/hr$, although they used a lower haematocrit of 5% and only achieved 10.7% plasma yield with 99% purity. Yang et al. (2006) designed a device for continuous separation based on plasma skimming and found that plasma yield improved from $10 - 35\%$ as they increased haematocrit from $2 - 10\%$ at $180 - 240\mu l/hr$ with a purity of almost 100%. Zheng et al. (2008) achieved 97% efficiency of leukocyte extraction in their device utilising plasma skimming in multiple branches but at a low haematocrit of 1% and a throughput rate of $60\mu l/hr$. Kersaudy-Kerhoas et al. (2010) used the combination of CDL enhancement

and plasma skimming to achieve 40% plasma yield, although with a purity of only 53% at $10ml/hr$.

This list of devices is by no means exhaustive, but is provided to give the reader a brief introduction to the range of designs which have been reported in the field, and also to highlight that the haematocrit used in the testing of these devices was generally very low and that the flow inside these devices was not rigorously examined, as could be done using μPIV approaches, described in §2.4. The influence of aggregation is not mentioned in any of these studies, but in practical use may significantly affect the device if used with untreated human blood due to the low flow rates involved.

1.6 Image-based blood flow measurement

There have been a large number of reports on the use of μPIV to measure blood flow, which are summarised in this section. The details of the technique will be described in §2.4. μPIV has been used *in vivo* with intravital microscopy or *in vitro* with glass tubes or PDMS microchannels. The latter allow for more complex and realistic geometries to be constructed, significantly improving the scope and applicability of *in vitro* studies. The following is a brief review of the literature on application of the particle image-based velocity measurement approaches, μPIV and μPTV, to blood flow measurement.

A number of studies have reported the use of PIV and PTV methods in the context of blood flow. In some of these studies, the flow is seeded with fluorescent particles which yields velocity fields for the suspending medium. However, in some cases, the RBC themselves can be used as tracer particles.

Using fluorescent liposomes, which are bio-inert, as tracers, Vennemann et al. (2006) measured the velocity of blood in the outflow tract of an embryonic chicken heart. Other *in vivo* studies using fluorescent particles include the flow in a mosquito proboscis (Lee et al., 2009) and a hamster cremaster muscle arteriole (Savery & Damiano, 2008). In the latter, the high resolution of the data allowed them to identify the effect of the ESL throughout the cardiac cycle, which, by effectively retarding plasma flow, reduced the shear stress acting on the endothelial cells to almost zero. The same group have also analysed the effect of haemodilution on shear distribution in microvessels, using their 'microviscometric' approach (Long et al., 2004) in which they calculate local viscosity profiles from μPIV data (Damiano et al., 2004).

A number of *in vitro* studies have been carried out, using tracer particles seeded in blood, providing information on viscosity (Ji & Lee, 2008) and the effect of bulk haematocrit on velocity profiles (Lima et al., 2007). The latter study found that increasing haematocrit up to 17% did not change the shape of the time averaged profile, but increased velocity fluctuations. Their data implied an importance of instantaneous measurements in order to capture velocity fluctuations due to the two phase nature of the flow, despite the steady, laminar flow commonly found in microfluidic environments. The same group used their confocal system to attain three dimensional velocity profiles in square microchannels (Lima et al., 2006; 2008b). Saadatmand et al. (2011) studied the dispersion of tracer particles in tube flow and showed that increasing haematocrit up to 20% linearly enhanced particle dispersion (above the levels of Brownian motion). Lima et al. (2008a; 2009b) used their confocal setup with labelled RBC, using PTV methodologies to quantify the radial dispersion of RBC in channel flow. They found that there was little dispersion in the regions next to the wall and in the channel centre, with significant dispersion in the region between. The amount of dispersion increased with increasing diameter and haematocrit, up to about 25%. Ishikawa et al. (2011) used particle tracking of both tracer particles (for water) or labelled cells to analyse the flow of RBCs and cancer cells in a bifurcating and converging microchannel. They found that the CDL was absent at the junction point in the bifurcation, at which point cancer cells were found to adhere to the wall, but was enhanced on the outer walls of the daughter branches, although only qualitatively. It was pointed out that this could influence dispersion of large molecules and platelets in the flow in the vicinity of bifurcations. Dusting et al. (2009) used RBC as tracers in aggregating blood in a Couette flow and found that the aggregated cells gave more accurate PIV data.

Using RBCs as tracers for PIV evaluation, Nakano et al. (2003) measured cell velocities in an arteriolar bifurcation *in vivo* and found that the velocity profiles in the daughter branches were skewed towards the outer walls. Additionally, they captured the profiles at different stages in the cardiac cycle and found that the bluntness parameter K (see Equation 1.14) ranged between 2.6 and 3.2, with maximum values occurring at the phases of both the minimum and maximum average ensemble velocities. Other *in vivo* studies using RBC as tracers include the rat mesentery, accounting for movement of the tissue (Sugii et al., 2002), a chicken embryo (Lee et al., 2007) and the important

study by Hove et al. (2003) who highlighted the importance of haemodynamic forces on embryonic cardiogenesis (growth of the heart) in a zebrafish embryo.

All of the aforementioned studies considered the velocity by measuring either the RBCs or the suspending medium (using fluorescent tracer particles). Poelma et al. (2012) investigated the difference between the two measurement approaches and concluded that they were equivalent for low magnification lenses ($10\times$), whereas for high magnifications, the RBC data would be underestimated to a greater extent than the fluorescent tracer data. However, this analysis was based on the tacit assumption that both data acquisition approaches should provide the same information: for a two-phase fluid this is not necessarily the case.

Sugii et al. (2005) used fluorescent particles and labelled cells with a different emission wavelength to capture both suspending medium and cell velocities. However, they reported that both displayed Poiseuillean profiles, which they attributed to relatively high velocities and low haematocrits. A quantitative experimental description of the difference between RBC and suspending medium velocities is yet to be reported, perhaps due to the additional requirement of describing the local concentrations in order to properly discriminate between the two phases.

1.7 Main Findings

It is clear from the preceding review of the literature that, while a considerable amount of research has been done in the field of microvascular blood flow, the literature is rife with contradictory reports on the effects of various parameters. Recent advances in experimental techniques have provided researchers with hitherto unachievable levels of accuracy and resolution. Nonetheless, the application of these techniques in the literature is still relatively limited and there is more that needs to be done in order to improve the state of understanding and ultimately, clinical approaches to diagnostics and care in a large number of pathological states.

The microvascular environment is highly complicated and even the most advanced experimental models cannot recreate *in vivo* conditions. Computational models are making significant advances, but still require experimental data for purposes of verification. There are many parameters which *in vitro* models cannot account for, such as the flexibility and active control of the vessel wall, the biochemical interactions between the

cells, the endothelium and other chemicals in the blood and the network nature of the system. Nevertheless, they are able to provide detailed information on specific parameters which cannot be acquired *in vivo* due to technical difficulties. Furthermore, there are ethical considerations regarding the use of animals for *in vivo* experimental research.

RBC aggregation has been studied in depth using the different approaches described in §1.3. However, results between the different methods, and even between *in vivo* studies, are often contradictory. This is largely a result of the different environments affecting the complex biochemical, geometric, fluid dynamic and temporal relationships which define the overall effect of aggregation on blood flow. The *in vitro* environment has the advantage of being able to provide repeatable conditions, in which aggregation can be studied in a repeatable manner. Additionally, the many parameters involved in the phenomenon of plasma skimming have been studied in depth, but the flow field around the bifurcation regions still lacks in-depth characterisation and the influence of aggregation and local haematocrit distribution have not been rigorously examined.

1.8 Objectives of the present research

The aim of the present study is to improve the understanding of microscale haemodynamics, with a particular focus on RBC aggregation, which is often overlooked.

The present work will take advantage of advances in μPIV and fabrication techniques in SU8 and PDMS to acquire high resolution data on human blood samples *in vitro*.

In order to achieve this aim, the following objectives can be defined:

1. Develop experimental tools to study microscale blood flows in the presence of aggregation.

2. Resolve the flow field in idealised bifurcating geometries using μPIV. Analyse the velocity profiles and their characteristics parametrically.

3. Investigate the cell-depleted layer and its relationship to the velocity profiles. Use an analytical model to infer data on viscosity and wall shear stress.

4. Study the RBC distribution as continuous one-dimensional profiles. Analyse the effect of the haematocrit distribution on velocity and viscosity.

5. Discriminate between RBC and suspending medium velocity with simultaneous measurements in order to gain insight on the multiphase nature of the blood.

6. Utilise experimental data to develop hybrid numerical approaches to investigate the effect of haematocrit distribution on velocity, wall shear stress and apparent viscosity.

The parameter space will include flow ratio, parent branch flow rate, the geometrical configuration and the presence or absence of RBC aggregation.

1.9 Outline of the thesis

In Chapter 2 the details of the experimental setups used in the present study, which were custom built for the purpose will be described. Information on hardware, software and processing methodologies will be provided. In the subsequent four chapters, the results of the following four experimental investigations shall be described.

In Chapter 3, the region of low RBC concentration which occurs close to channel (and microvessel) walls, the cell-depleted layer, are analysed. Aggregating and non-aggregating samples are considered at a range of flow ratios. A new CDL identification technique is developed to provide detailed spatio-temporal data on its distribution. A simple mathematical model based on two constant viscosity phases is derived and used to assist in analysis of the results.

In Chapter 4, a methodology for extracting continuous haematocrit profiles is described. The profiles are combined with an empirical model for blood viscosity and used in conjunction with CFD to predict velocity profiles, which are compared to the experimental data. The independent parameters in this study are the flow ratio and presence or absence of RBC aggregation.

Chapter 5 uses a further development of the acquisition system which allows velocity measurements of both phases of the blood quasi-simultaneously. Combining this with a refinement of the methodology described in Chapter 4, based on planar symmetry and an aspect ratio of one, phase discrimination is possible. This chapter discusses the haematocrit and velocity distributions of blood as a multiphase fluid. Furthermore, in addition to the independent parameters considered in the previous chapters, data are reported for a range of parent branch flow rates.

In Chapter 6, the data from Chapter 5 are combined with a haematocrit and shear dependent viscosity model to provide full three-dimensional simulations of the blood flow using a hybrid approach. The model is validated against the experimental velocity data and used to analyse the influence of various parameters on the wall shear stress and apparent viscosity.

The thesis is concluded with an outline of the main findings of the research and recommendations for further work.

Chapter 2

Experimental Methods †

The present research requires sophisticated measurement techniques in order to account for the many experimental obstacles which arise from the scales to be investigated and the multiphase nature of blood flow on the microscale. A significant effort was expended on developing such tools and these are described in this chapter. The details of the working fluids will be given, followed by descriptions of the two different microchannels used. Accurate control of blood flow on the microscale is non-trivial, and further complicated by RBC aggregation, and therefore a custom perfusion system was developed and is described in detail. A description of the imaging system and data acquisition approaches will follow. An explanation of the image preprocessing methodologies used for the acquired images will the given, followed by a discussion of the errors in the measurements. The chapter concludes with an initial investigation into the aggregation time of blood in a microchannel.

2.1 Blood sample preparation

The experiments were carried out using human blood acquired from healthy volunteers, under ethics approval granted by the South East London Research Ethics Committee (ref:10/H0804/21). Blood was extracted from volunteers by venepuncture and collected into vacutainers (Beckton Dickinson, UK) preloaded with $1.8mg/ml$ ethylenediaminetetraacetic acid (EDTA) to prevent coagulation. The samples were centrifuged at $3,600rpm$ in order to separate the constituent parts of the blood. The plasma and buffy coat (containing leukocytes and platelets) were aspirated and discarded and the

†The data presented in §2.8 was presented at *'British Microcirculation Society 61st Annual conference'*, April $18^{th} - 19^{th}$ 2011, London, UK.

RBCs were washed twice via centrifugation in phosphate buffered saline (PBS). To achieve the required haematocrit for the experiments, RBCs were then suspended in PBS at fixed volumes. For Chapters 3 and 4, a volume fraction (haematocrit) of 0.25 was used. For Chapter 5, calibration experiments using haematocrits in the range of $0.05 - 0.3$ were carried out. The main experiments for Chapters 5 and 6 was carried out with feed haematocrit of 0.2. Although systemic haematocrit in humans is ≈ 0.45, due to the Fåhraeus effect, in vessels on the scale of the channels used for these experiments, a haematocrit of $0.15 - 0.25$ is within the physiological range.

For aggregating cases, Dextran 2000 was added at a concentration of $5g/L$. This value was selected to give as little change as possible to the viscosity of the suspending medium (SM) while inducing moderate aggregation (Chien & Jan, 1973). For the rest of the thesis, the terms Dextran case and PBS case will be considered synonymous with aggregating and non-aggregating conditions.

Using a Couette rheometer, the viscosity of the PBS was measured to be $1mPa\ s$, while for the Dextran solution, it was found to be $1.3mPa\ s$ at room temperature. However, the densities of both fluids were found to be negligibly different from water (at room temperature).

For fluorescent PIV data, $1\mu m$ diameter rhodamine dyed polystyrene microspheres (Invitrogen, UK), were washed via centrifugation and resuspended in PBS. The peak absorption and emission wavelengths for these particles are $535nm$ and $575nm$ respectively, and are hence ideal for illumination with an Nd:YAG laser (wavelength $532nm$). The particles were than added to the SM at a volume concentration of 0.1%.

All experiments were carried out at room temperature. After extraction, all samples were used within four hours, or refrigerated. Refrigerated samples were allowed to reach room temperature before use and used within the same time constraints, following the haemorheological guidelines (Baskurt et al., 2009a).

2.2 Microchannels

The microchannels used in Chapters 3 and 4 were purchased from Epigem (UK) and were made with soft lithography using SU8 photoresist. Both upper and lower sections of the channel were made from SU8 and were irreversibly bonded. The channels featured a long straight section of approximately $40mm$ followed by a bifurcation, as

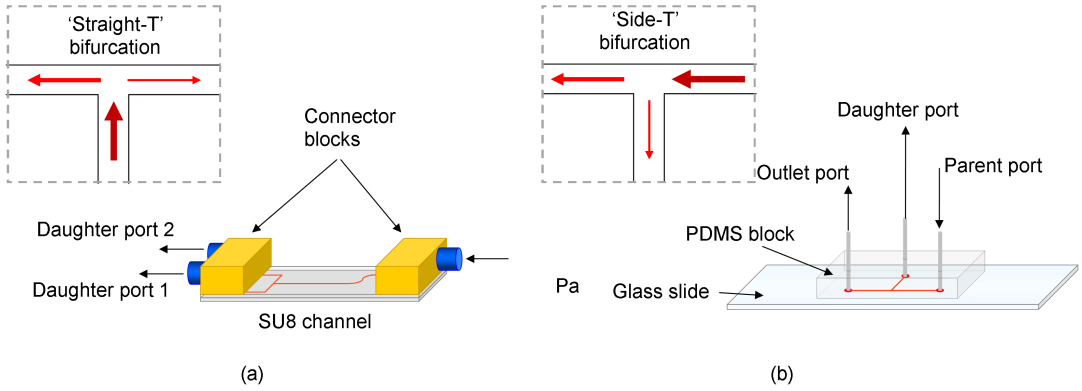

Figure 2.1: The two microchannels used. (a) Epigem SU8 microchannel with aspect ratio of 5:2 and a 'straight-T' configuration. Inset shows the flow configuration: thicker arrows indicate parent branch, (b) Custom made PDMS microchannel mounted on a glass slide. Aspect ratio is 1:1 and the 'Side-T' configuration is used.

shown in Figure 2.1a.

The cross section was $100 \times 40\mu m$ in all branches, giving an aspect ratio of 5:2. Although this geometry is not physiological, the large width and small depth provide optimum conditions for the data considered in Chapter 3 and 4. In these experiments, the flow configuration is that of the 'straight-T' bifurcation', as shown in the dashed box in Figure 2.1a. The tubing was connected to the channel using standard HPLC fittings via the connector blocks.

The channel used for Chapters 5 and 6 was made from polydimethylsiloxane (PDMS) via photolithography using standard methods at the cleanroom facilities of London Centre for Nanotechnology. Briefly, the photoresist S1818 was spin coated onto a silicon wafer and exposed to UV light through a quartz photomask (JD photo tools, UK). The mask was developed and then etched with deep-resistive ion etching to generate a master with a depth of $50\mu m$. PDMS prepolymer was mixed with the curing agent at a ratio of $10:1$ and poured onto the master. After baking overnight at $65°C$, the PDMS was removed and cut to the required size. Inlet and outlet ports were created using a biopsy punch. The channel was rinsed with isopropyl alcohol and its surface was plasma treated using a handheld corona. The channel was then bonded to an untreated glass microscope slide and baked overnight at $65°C$. Connections to the channel were achieved using $\approx 20mm$ lengths of hypodermic needle, which were connected to the

tubing with a push fit.

The channels consisted of a long straight inlet section ($\approx 2mm$) followed by a T bifurcation at a 90 degree angle, in the 'side-T' configuration, as shown in Figure 2.1b. The outlet branch (downstream of the bifurcation) was also $\approx 2mm$. All branches were $50\mu m \times 50\mu m$, giving an aspect ratio of 1:1.

2.3 Perfusion system

2.3.1 Design Requirements

In the present study the aim was to measure aggregating blood on a microvascular scale. This presents two main challenges: the effect of aggregation on the flow system and achieving rapid and accurate flow control at sufficiently low flow rates for aggregation to occur.

In the literature, the most common method of flow control is with a syringe pump (Dellimore et al., 1983; Fujiwara et al., 2009; Lima et al., 2009b) or a peristaltic pump with a bypass circuit (Fenton et al., 1985). Syringe pumps operate using stepper motors to guide the syringe shaft along a linear rail, by rotating a lead screw, thus infusing or withdrawing fluid. However, the use of stepper motors generates two unwanted frequency responses, one at the stepping rate of the motor and the other at the rate of rotation of the lead screw due to inevitable deviations from perfect axial motion. The specific frequencies at which the noise sources occur is dependent on the syringe internal diameter and the selected flow rate. The flow oscillations induced by these changes can be as much as $\pm 50\%$ of the mean flow rate. Even more problematic for the current application is that when using flow control, the compliance of the system, predominantly in the tubing, introduces a long time constant which tends to be of the order of minutes. Thus, in the present study, where the presence of RBC aggregation greatly constrains acquisition times, flow control by means of a syringe pump was not suitable.

Instead, a pressure control system was required. An advantage of pressure control is that the compliance in the system becomes unimportant as equilibrium is reached almost instantaneously under an applied pressure. However, controlling the perfusion using pressure rather than flow rate is more unpredictable, as the flow generated by the applied pressure gradient is dependent on the fluid viscosity, the length and diameter of

each section of tubing and the channel itself. Furthermore, when using blood, the shear-thinning, thixotropic and multiphase aspects of the fluid further add to the complexity of the system. A number of recent studies have reported the use of measurements using pressure control. Doyeux et al. (2011) used gravity driven flow, i.e. by setting reservoir heights accurately one can use the hydrostatic pressure to accurately prescribe a given systemic pressure drop. However, two drawbacks of this method are that it is not practical to change the pressure significantly with high temporal resolution[†] and that the applied pressure is limited by the height of the reservoirs (e.g. 1 metre of water is required to perfuse a $50\mu m$ capillary tube of $100mm$ length at $1\mu L/min$).

An alternative approach is to seal the inlet reservoir, and regulate the pressure of the gas above the fluid. Quinn et al. (2010) used sealed reservoirs and pneumatic solenoid valves to control their flow in experiments on RBC deformation. A commercial system based on a similar principle is available from Fluigent (France).

The system must contain an inlet reservoir, two outlet reservoirs, the microchannel and a certain amount of tubing to provide connections. It should be noted that the microchannel is necessarily the narrowest part of the system, i.e. it has the smallest cross sectional area. Thus, due to continuity, for a given velocity in the microchannel, the velocities and thus shear rates in the connecting tubes and reservoirs (herein termed the external flow system) will be considerably lower. Given that aggregation is a shear dependent phenomenon, the degree of aggregation in the external flow system will thus always be greater than that within the channel. Furthermore, as described in the introduction, due to their larger density compared to the SM, RBCs sediment. This results in an uneven haematocrit distribution, which will in turn result in an uneven (temporally and spatially) viscosity distribution throughout the system and hence fluctuating flow. Through preliminary experiments, it was deemed that the system needed to be run at very high flow rate until the time of acquisition. After reducing the flow to the desired level, uniform flow rate and haematocrit were observed for around 60 seconds after which the system became unpredictable.

[†]If the working fluid was, for example, water, then a switching T-junction could be used to rapidly change between high and low pressures. For blood flow, however, there would be static fluid in the dead space in the switch and the tube that was not in use. This would introduce further problems as a result of sedimentation and aggregation.

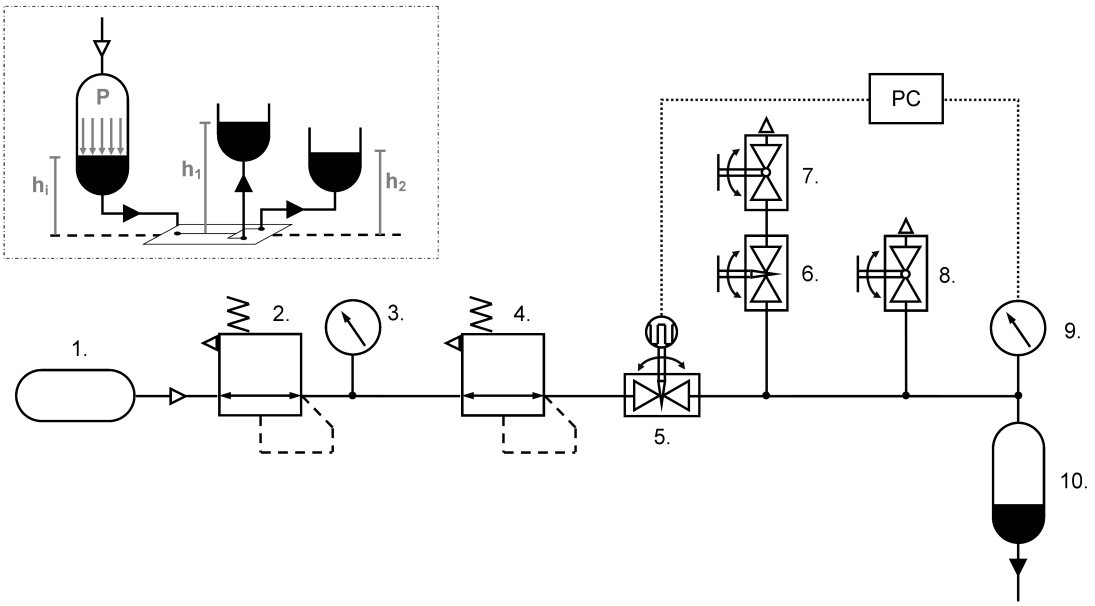

Figure 2.2: Pneumatic flow diagram of the control system. 1: Compressed nitrogen cylinder, White arrow indicates direction of gas flow. 2: Pressure regulator. 3: Pressure gauge. 4: Low pressure regulator. 5: Stepper motor controlled needle valve. 6: Manual needle valve. 7: Ball valve, Triangle indicates vent to atmosphere. Open under normal operating conditions. 8: Ball valve, Triangle indicates vent to atmosphere. Closed under normal operating conditions. 9: Pressure transducer. 10: Inlet reservoir. Black arrow indicates direction of liquid flow. Inset shows the liquid system.

2.3.2 System Description

The system developed for these experiments and used in Chapters 3 and 4 involved using a compressed nitrogen cylinder connected via a series of valves to the inlet reservoir. A block diagram of the flow path is shown in Figure 2.2

The pressure source is a compressed nitrogen cylinder. A standard pressure regulator and gauge (BOC, UK) are used in series with a low pressure regulator (Norgren, UK: Maximum output pressure $50kPa$). This is connected to a Swagelok (UK) SS-SS2, high precision needle valve. The needle valve was coupled to a stepper motor (Nanotec, Germany: ST2818S) via a custom coupling as shown in Figure 2.3. The coupling consists of two hollow cylinders, the largest of which is rigidly fixed to the stepper motor shaft with a grub screw. Inside this cylinder fits a smaller one, with a peg perpendicular to the axis which can slide along slots in the large cylinder. The needle stem attaches rigidly to a hole in the base of the small cylinder. This setup allows for the travel of the needle stem as the valve rotates (up to 10 times, travelling approximately $1mm$ per

rotation). By controlling the stepper motor, the position of the needle changes, modifying the resistance to flow of the nitrogen and hence modifying the pressure applied to the working fluid. Downstream of the actuated needle valve, a T-junction (Swagelok, UK) splits the flow pathway, with one branch connected to a manual needle valve followed by a ball valve. With the ball valve open, the manual needle valve serves as a leak valve, allowing rapid reduction of pressure in the system which would otherwise not be possible. Closing the ball valve greatly increases the system pressure without the need to modify either needle valve, which is useful for purging the microchannel. The other branch of the T-junction is connected to a second T-junction, which is in turn connected to a ball valve, open at one end to atmospheric pressure. When this valve is open, the system pressure will rapidly drop to atmospheric pressure, which is useful when adjusting the hydrostatic pressures, as will be discussed later. The other branch of the second T-junction is connected to a sealed reservoir which contains the working fluid and the pressure of the gas above the working fluid is monitored with a pressure transducer (Omega,UK: PX243A, Range $\pm 20kPa$). The stepper motor is controlled via a stepper motor control board (Nanotec, Germany: SMC11) connected to the data acquisition (DAQ) card and controlled using LabVIEW (National Instruments, UK). The pressure transducer is used as an input to the control system.

Setting up the system requires the following steps: with the actuated valve fully open and the ball valves closed, the low pressure regulator is set to a given pressure, e.g. $40kPa$. The ball valve connected to the manual needle valve is then opened, and the manual needle valve is adjusted so that the pressure reaches a lower value, such as $15kPa$. Then via control of the actuated needle valve, the system can regulate the pressure between 0 and $15kPa$, at a stable level with a resolution of around $10Pa$[†].

The system provides a temporal response of the order of seconds (i.e. the pressure reaches equilibrium in this time),[‡] and excellent stability: an RMS variation of only 1% was observed for flow rates of $5\mu l/hr$ (data not shown for brevity).

Figure 2.4 shows the custom setup used for Chapter 3 (which is also shown schemati-

[†]This limit is only imposed by the choice pressure transducer, and a larger range or higher resolution could be achieved as required by using different transducers.

[‡]This value is quoted for a Newtonian fluid, such as water. For aggregating blood, the change in fluid viscosity as aggregation increases alters the pressure as described in §2.8.

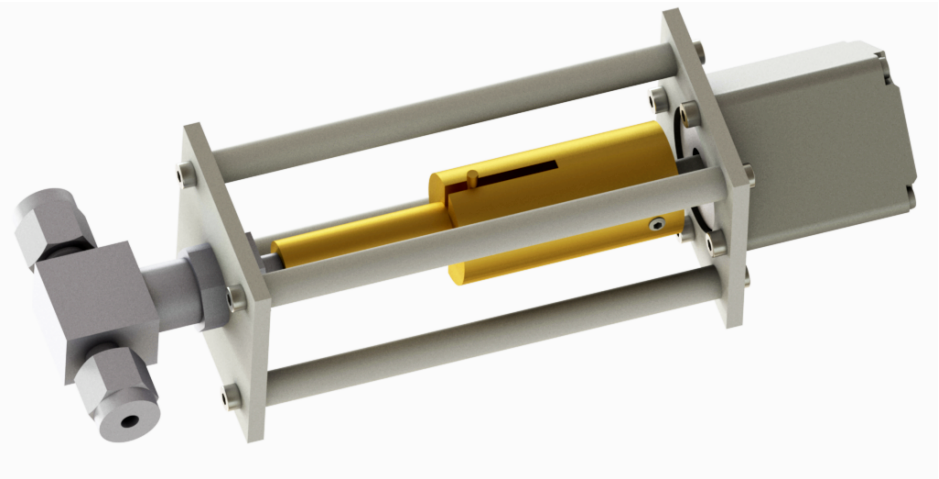

Figure 2.3: Computer-aided design model of the coupling used to connect the stepper motor to the needle valve.

cally in the inset of Figure 2.2). The same fluid control system, but a different optical configuration, was used in Chapter 4. The microchannel is placed on an inverted microscope (Leica, Germany: DM ILM). It can be seen that the outlet of each of the daughter branches of the bifurcation is connected to a large diameter syringe (Beckton Dickinson, UK: $60ml$ Plastic syringe, diameter $26.7mm$), which is cut at the top to act as a water filled reservoir, open to atmospheric pressure. Each reservoir is mounted on a micrometer stage, allowing very accurate control of the height of each reservoir, and hence hydrostatic pressure, which controls the proportion of flow entering each branch. Considering the inset in Figure 2.2, it can be seen that the pressure drop for each branch is given by

$$\Delta p_1 = p + \rho g \left(h_i - h_1 \right) \tag{2.1}$$

and

$$\Delta p_2 = p + \rho g \left(h_i - h_2 \right) \tag{2.2}$$

For a given inlet pressure, altering the two outlet reservoirs by the same amount in opposing directions modifies the flow split without significantly affecting the parent branch flow rate. The large diameter syringes are used for the outlet reservoirs in order to reduce the effect of changing volume (from perfused fluid) on the hydrostatic pressure relative to the inlet reservoir (i.e. h_1, h_2 do not change with time significantly).

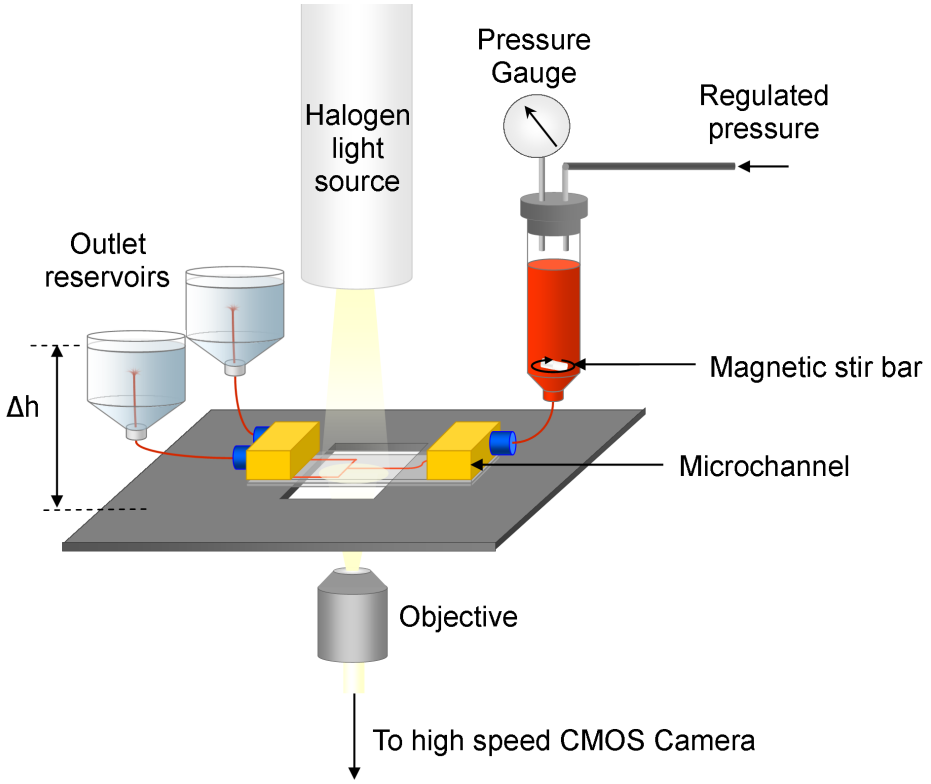

Figure 2.4: Schematic of the experimental setup used for Chapter 3. Regulated pressure provided by system described in Figure 2.2. Halogen illumination with high-speed CMOS camera. See text for details.

The use of water in the outlet reservoirs removes the pressure pulse induced by droplets forming at the end of the tubing and causes lysis of the RBCs, which prevents blockage. In the inlet reservoir, the limited sample size precluded using a large reservoir, so a smaller diameter syringe was used (Beckton Dickinson, UK: $5ml$ plastic syringe, diameter $12.06mm$). The reduction in h_i and hence the applied pressure drop was accounted for by adjusting the applied pressure P or reducing both h_1 and h_2.

A magnetic stirrer was used to mix the fluid in the inlet reservoir, in order to allay the effects of sedimentation and aggregation. Additionally, the length of the tubing connecting the inlet reservoir to the microchannel was kept to a minimum (a total of less than $300mm$). However, these changes alone are not sufficient to ensure uniform haematocrit distribution in the channel for a long period of time. Even with these considerations, only around 60 seconds was available for acquisition before the flow became unstable. In order to account for this, a high flow rate is applied between acquisitions, which disaggregates and redistributes the RBCs. In order to acquire data,

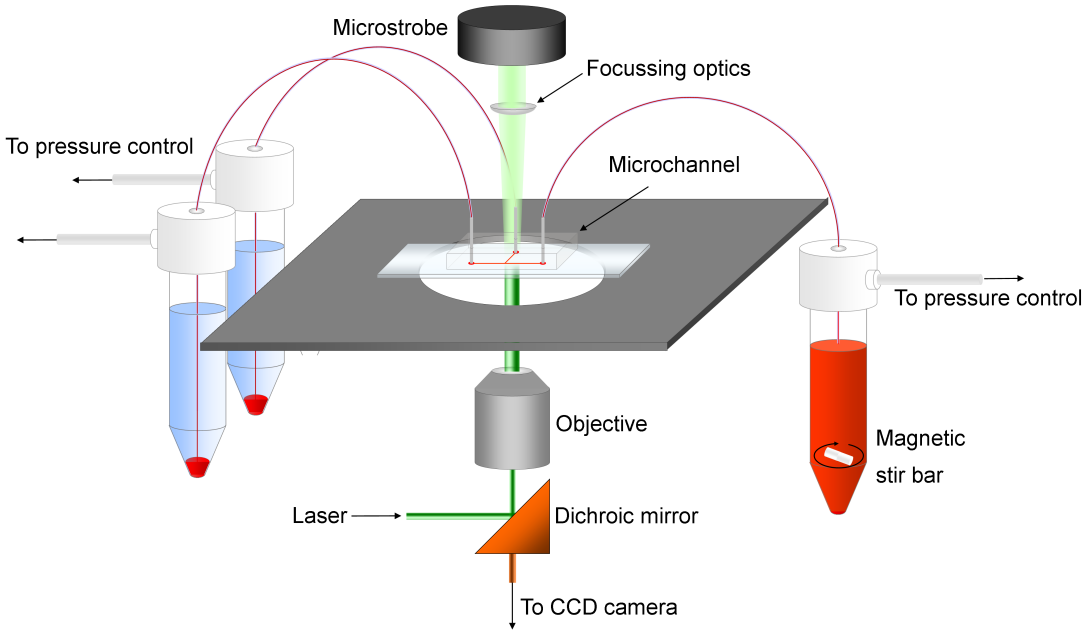

Figure 2.5: Schematic of the experimental setup used for Chapter 5. Pressure control provided by Fluigent MCFS. Alternating microstrobe and laser illumination are utilised in conjunction with a dual-frame CCD camera. See text for details.

the pressure is then dropped from the high pressure to a target pressure over a fixed period ($5-10s$) and acquisition is triggered an appropriate time after the target pressure has been reached (to allow aggregation to reach a steady state). In order to quantify this time, a simple aggregation index was developed based on brightfield image of the RBCs, and will be described in §2.8. Twenty seconds was found to be a sufficient time for aggregation to reach a steady state under a range of flow rates.

For the measurements in Chapter 5, an alternative system was used for the control of pressure. A Fluigent MCFS (Microfluidic Flow Control System: Fluigent, UK) was utilised, as shown in Figure 2.5. Instead of using hydrostatic pressure to control the proportion of flow entering each branch, all reservoirs were sealed and controlled using the Fluigent system.

A final consideration is that using pressure control requires that the flow rates be measured. Flow rates in the present system cannot be measured via the travel of a meniscus in a glass tube, as described in the literature (Dellimore et al., 1983; Fenton et al., 1985), as the RBC aggregation would change the resistance (potentially blocking the tube) and thus produce unreproducible results. Use of micro flow meters may be pos-

sible, but the requirement for short tubing lengths makes this option less feasible, in addition to the large cost of these items. However, by using average velocities calculated with Particle Image Velocimetry (PIV) and comparing to the analytical profile (see Equation 1.11), flow rates can be approximated.

2.4 Particle Image Velocimetry Setup

2.4.1 Description of the technique

PIV is a commonly used technique in fluid dynamics for gathering high spatial resolution Eulerian velocity information. In essence, a flow is seeded with neutrally buoyant particles which are small enough to follow the streamlines and not affect the flow significantly. A laser sheet is passed through the flow and two images of the light reflected by the particles are acquired in quick succession. These two images are separated into interrogation windows (IW) and processed using image correlation to provide the most probable distance travelled by particles within the IW between the two images. By dividing this distance by the time between the images, dt, it is possible to generate a velocity field for the flow. Through the use of specialised cameras, allowing a small value for dt, and processing iteratively using progressively smaller windows and overlapping, it is possible to obtain high temporal and spatial resolution data, respectively. In order to resolve microscale flows, the technique was first extended by Santiago et al. (1998) into what is known as micro PIV (μPIV). Shortly after, Meinhart et al. (1999) reported near-wall velocity calculations with a spatial resolution of $0.45\mu m$. The main differences between 'macro-PIV' and μPIV are that in μPIV; (1) the sample is placed on a microscope, since the scales are significantly smaller; (2) volume illumination is used, as the characteristic scales of the flow are often comparable to that of a light sheet (Williams et al., 2010); (3) for the standard μPIV approach (herein termed fluorescent μPIV), instead of using reflected light, fluorescent microparticles are seeded in the flow, which are excited by the laser; (4) for particles of diameter less than $0.5\mu m$, the effect of Brownian motion becomes significant; and (5) particle density is often very low, and Brownian motion precludes particle tracking methods, thus ensemble or correlation averaging (Adrian & Westerweel, 2011) or image overlapping (Raffel et al., 1998) are used. An alternative to fluorescent μPIV is using images of RBCs which act as tracers for the correlation algorithm. These two approaches will be discussed further

in §2.4.2.

The volume illumination method means that the image plane is defined by the depth of focus of the objective as well as a number of other parameters. Olsen & Adrian (2000) define the depth of correlation for an air immersion lens using a small angle approximation as

$$z_{corr} = \left[\frac{(1-\sqrt{\varepsilon})}{\sqrt{\varepsilon}} \left(f^{\#2} d_p^2 + \frac{5.95\,(M_t+1)^2\,\lambda^2 f^{\#4}}{M_t^2} \right) \right]^{1/2} \tag{2.3}$$

Where M_t is the total magnification of the system, d_p is the particle diameter, λ is the wavelength of the light emitted by the particle and $f^{\#}$ is the focal number of the lens ($NA = 1/2f^{\#}$). ε is a parameter which defines the distance of influence along the optical axis, beyond which a particle will not contribute to the correlation function and is generally chosen to be 0.1. As an example, for a $10\times$ objective with $NA = 0.25$ and $1\mu m$ seeding particles, the depth of correlation is $2z_{corr} = 38.0\mu m$. Equation 2.3 will not give an accurate prediction of the depth of correlation in blood flows, due to the diffractive and absorbant properties of the RBCs, but can be used to provide an estimate.

The effect of having a finite depth of correlation is that out-of plane particles influence the measured velocity. If one considers the central plane of a microchannel, the result is an underestimation of the fluid velocity, as the maximum velocity occurs in the channel centre. Poelma et al. (2012), provided the first direct comparison of μPIV using RBCs or fluorescent particles as tracers. They found that, for low magnification lenses in microchannels/microvessels of depth around $50\mu m$, the depth of correlation is similar to the channel depth. Hence, the system is 'depth-saturated' and both fluorescent μPIV and RBC μPIV methods underestimate the velocity by approximately the same amount. For higher magnification lenses, RBC images have a larger depth of correlation, due mainly to the larger particle size (see Equation 2.3).

2.4.2 Alternative μPIV approaches

Figure 2.5 is a schematic of the system used for the measurements in Chapter 5, and shows the light path followed for the fluorescent μPIV approach (as well as the strobe illumination). This imaging approach was also used in Chapter 4, but with the flow

components shown in Figure 2.4.

The microchannel is placed on an inverted microscope and the sample is volume illuminated with a dual cavity Nd:YAG laser (ESI, Germany: New Wave Solo). The fluorescent rhodamine particles used to seed the flow are excited at $532nm$ (close to their peak absorbance of $535nm$) and emit light at $575nm$. The emitted light passes through the microscope objective and through a dichroic mirror which filters the light at $610nm$ with a $75nm$ bandwidth. The light passing through the dichroic mirror is collected on a high sensitivity CCD (charge-coupled device) camera (Hamamatsu, UK: C8484-05C).

An alternative approach, often used with blood flows is to use images of the RBCs instead of fluorescent particles, i.e. the RBCs act as a surrogate for the tracer particles[†]. Figure 2.4 shows this system, as used in the experiments in Chapter 3. The sample is illuminated with a halogen light source and the transmitted light is collected through the objective into a high speed CMOS (complementary metal oxide semiconductor) camera (IDT, USA: X3). Alternatively, illumination can be achieved with a microstrobe, as shown in Figure 2.5 and used in Chapter 5.

Each of these experimental approaches has advantages and disadvantages. In general, use of microparticles provides a smaller depth of correlation and higher spatial resolution, particularly near the wall (Vennemann et al., 2007). However, the method also requires either a very sensitive CCD camera, which tend to be slow, or a fast CMOS camera with an intensifier. Intensifiers are very expensive and add considerable noise to the acquired images. Using brightfield illumination, however, a fast CMOS camera can be used to capture very high temporal resolution images of the RBCs. An advantage of brightfield illumination is that the RBC images can be processed to provide additional information on the flow, such as aggregation quantification (Dusting et al., 2009) (also see §2.8) or RBC distribution (Chapters 3-5).

For the experiments in Chapters 4 and 5, the two approaches were combined. As shown

[†]Although images of the RBCs provide the data on which the correlation algorithm acts, they do not have the same characteristics as the Gaussian particles images acquired with fluorescent μPIV. When using PIV processing on RBC images, the approach acts as a well-refined image correlation algorithm, but its characteristics are different from those of fluorescent μPIV. However, given that the approach is commonly still termed PIV, this convention will be used herein.

in Figure 2.5, a microstrobe was mounted above the sample and focused using plano-convex lenses. The location of the focal point was positioned using X, Y, Z stages so as to be collocated with the imaging region and achieve a maximum intensity, minimising the required 'exposure time'. By alternately using laser or strobe illumination, both brightfield and fluorescent images could be acquired quasi-simultaneously. This system was used in Chapter 4 to acquire RBC images for evaluation of the haematocrit distribution along with fluorescent μPIV data. For Chapter 5, refinement of the technique allowed for double frame brightfield images, allowing for simultaneous use of both RBC and fluorescent μPIV methods. These provided information on both phases of the blood, which in conjunction with haematocrit distribution estimations via image processing of the RBC images, allowed for phase discrimination analysis, as will be shown in Chapter 5.

2.5 Data acquisition

Due to the complex nature of the fluid and associated control and acquisition requirements, a customised system was required, which was built in LabVIEW. The system provided flexibility in control, synchronisation and acquisition. This section will outline the hardware and software components of this system.

2.5.1 Hardware

The hardware for the control and acquisition system is shown schematically in Figure 2.6. Two PCI-cards were inserted into a PC running LabVIEW. A National Instruments (UK) PCIe-6353 multifunction DAQ card was used for synchronisation and control purposes. The strobe illumination, CCD camera triggering, stepper motor control and laser flashlamps and Q-switches were all controlled via 5 Volt pulses generated on the digital output port of the DAQ card. The pressure measurements were acquired using the built-in analog-to-digital converter in the PCIe-6353. Two National Instruments BNC2110 connector boxes were used for easy interfacing between the hardware and the DAQ card. Control of the settings and acquisition of the images was carried out via a National Instruments PCI-1426 card, using the LabVIEW IMAQ (image acquisition) library.

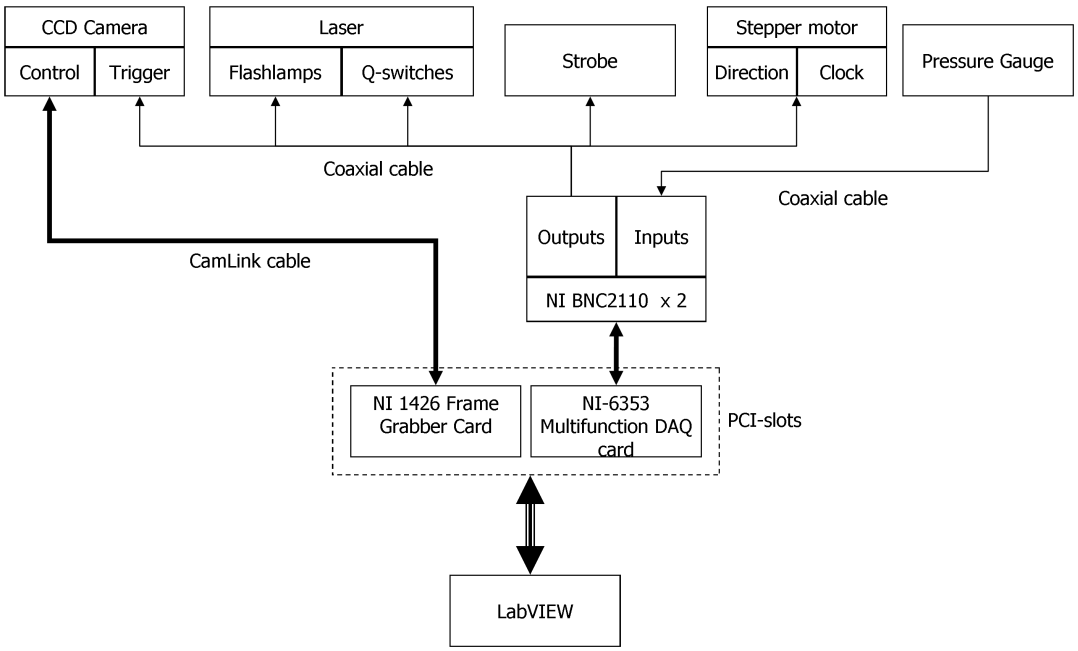

Figure 2.6: Flow diagram of the hardware used in the current setup.

2.5.2 Software

LabVIEW is a visual programming language which is specialised for control purposes. The main concept of the software is the use of VIs (virtual instruments), which are equivalent to functions for standard text based coding. LabVIEW code has two parts, a block diagram in which the program is coded, and an automatic GUI which can be customised by the user. All of the control in the present study, as well as some of the image processing, was carried out in LabVIEW using standard libraries as well as DAQmx (data acquisition) for input/output control, IMAQ for the camera control and Vision for image processing.

As mentioned previously, the μPIV setup was designed in such a way that alternate image pairs would contain fluorescent particle and brightfield images. A timing diagram is shown in Figure 2.7 which describes the synchronisation requirements of the system. The acquisition frequency of the Hamamatsu C8484-05C cooled CCD camera in normal mode is $12Hz$. However, the camera is specifically designed for μPIV, and can acquire image pairs $100ns$ apart, with a total frequency of $6Hz$ using double-frame mode. In this mode, the camera shutter opens twice in response to a single trigger, with exposure times of e_1 and e_2 respectively. The default values for e_1 and e_2 are provided in table 2.1. However, e_1 can be modified by altering the pulse width of the camera trig-

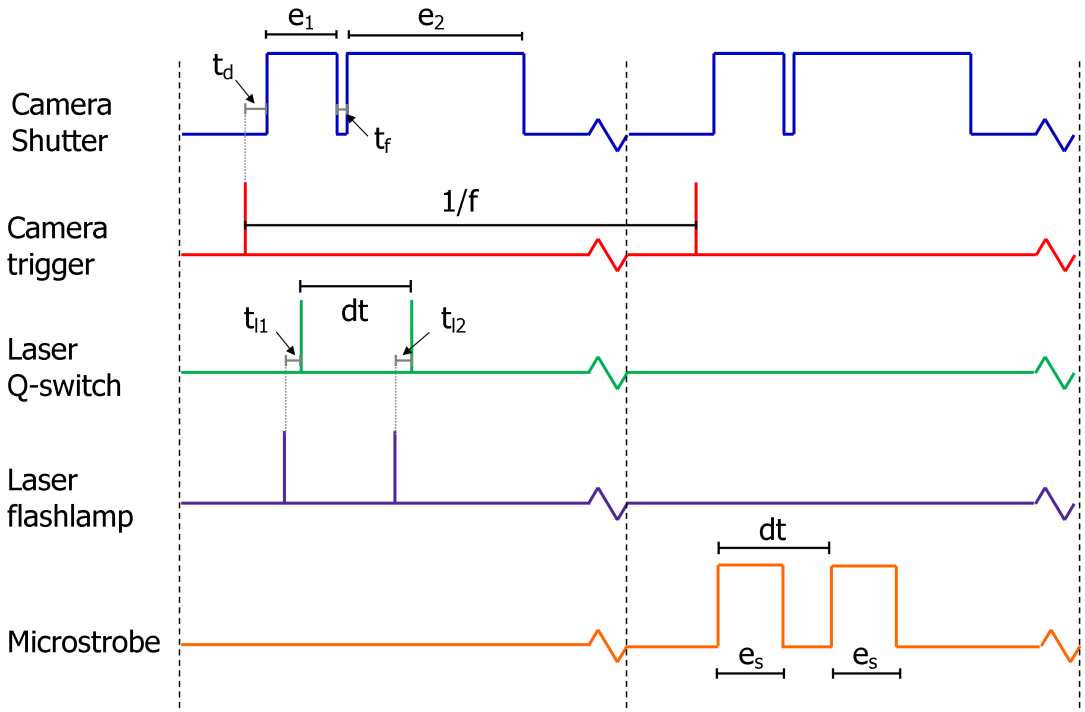

Figure 2.7: Timing diagram for the alternating laser and strobe illumination. Dashed lines separate image acquisition pairs. Timing details provided in Table 2.1.

ger pulse. The camera shutter opens at a time interval $t_d = 1.61\mu s$ after the falling edge of the camera trigger pulse. The timing between the two exposures is $t_f = 0.26\mu s$. For each laser pulse, the flashlamp must be fired, followed by the Q-switch with a delay of t_l, as listed in Table 2.1 for each of the cavities in the dual-cavity laser. The time interval between the two Q-switch pulses gives the time between the two images dt, which is used in the PIV processing. During the first phase of the acquisition, the strobe is not fired. After the image acquisition, the system must wait for the camera for the next acquisition. At the maximum speed of the camera ($6Hz$), the time between the dashed lines is $167ms$. In the second phase of the acquisition, the camera is fired in the same way, but instead of the laser, the strobe is triggered, with the illumination active for the pulse duration, e_s. The two pulses are timed such that the time between the two frames is the same as for the laser illumination. The pulse width, and hence the camera exposure time are defined so that sufficient light is collected during the strobe pulse to get a good contrast in the acquired image. The parameter dt is defined in order to achieve the optimum displacement of particles between images for the PIV algorithm. As alternating image pairs are used for each type of illumination, the frequency for the

Table 2.1: Typical parameters for the alternating laser and strobe illumination method.

Controllable				Fixed				
$f(Hz)$	$dt(ms)$	$e_s(ms)$	$e_1(\mu s)$	$e_2(\mu s)$	$t_d(\mu s)$	$t_f(\mu s)$	$t_{l1}(\mu s)$	$t_{l2}(\mu s)$
6	2	0.2	4.5	81.7	1.61	0.26	0.25	0.19

Table 2.2: Summary of the parameters and experimental setups used for each Chapter. Chapter 6 is purely computational but uses data from Chapter 5. AR - aspect ratio. Hct - haematocrit. Flow rate in $\mu l/hr$. Two ranges in flow ratio for Chapter 5 refer to daughter and outlet branches.

Chapter	μPIV	Channel	Feed Hct.	Flow rate	Flow ratio
3	Brightfield	'Straight-T', AR 5:2	0.25	2.5	0.1-1
4	Fluorescent	'Straight-T', AR 5:2	0.25	2.5	0.1-1
5	Microstrobe, Fluorescent	'Side-T', AR 1:1	0.20	5.4-72	0.1-0.5, 0.5-0.95

individual data sets is thus $f/2$.

The pressure control system and timing image acquisition are operated in parallel but not directly synchronised. Instead, at a specified time after the target pressure has been reached, an internal trigger starts the acquisition.

The control algorithm used for the valve is a basic incremental non-linear proportional control, wherein the rate and total angle turned by the stepper motor for each increment are proportional to the difference between the current and target pressures. After selection of optimal parameters, this has been shown to give a quick response to a pressure change with very little overshoot (the exact time depends on the specific settings and the pressure difference, but steady state is generally reached in approximately $2 - 10$ seconds).

The experimental parameters and setups used in the present study are summarised in Table 2.2. All experiments considered aggregating (Dextran) and non-aggregating (PBS) cases.

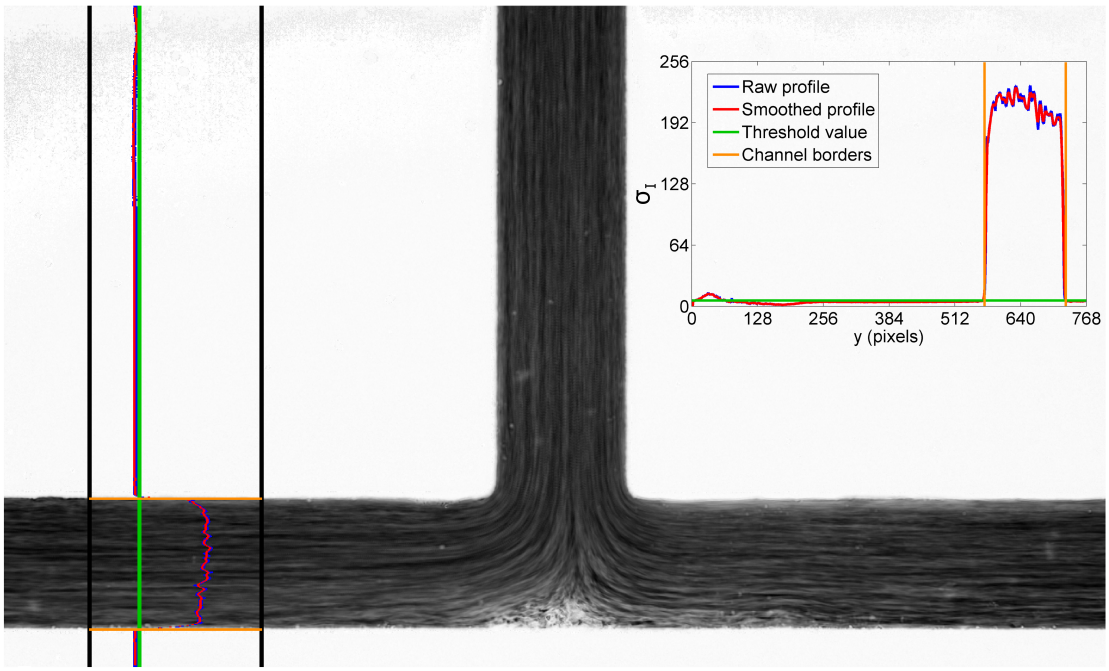

Figure 2.8: Image showing standard deviation at each pixel location, σ_I over a stack of images. Intensity is inverted for clarity. Overlaid lines show steps in the processing algorithm described in the text and colours correspond to the lines shown in the graph.

2.6 Data Processing

2.6.1 Image Pre-processing

In order to get velocity vectors evenly spaced within the channel, the images must be cropped and rescaled so that the width is a multiple of the final PIV IW. This process requires identifying the parent and daughter branch locations and scaling and cropping accordingly. The first stage is to identify the location of the channel in the images. This is non-trivial due to the diffraction observed next to the channel walls. Different approaches were used for the data in Chapters 3 and 4, and those in Chapter 5, which will be described separately. All image processing algorithms were developed and carried out using LabVIEW (National Instruments, UK) or Matlab (Mathworks, USA). Figure 2.8 shows the approach used for Chapter 3[†]. The standard deviation of the intensity at each pixel location, σ_I, was acquired for a set of images, from which regions in the images which are static, i.e. where there is no flow, can be identified (as the standard deviation will be very low, indicated by light areas in the figure). A vertical

[†]This is similar to the approach used in Chapter 4. However, the approach used in that Chapter is described therein.

strip of the standard deviation image which passes through one of the daughter branches was selected (black lines) and the average of each row was calculated to give a profile line of the standard deviation (blue line). This profile was smoothed using a moving average to remove noise (red line) and a minimum threshold was selected to account for any remaining noise (green line). The channel width and location on the image can be identified from the profile, as shown by the orange lines, from which the exact vertical channel position relative to the image can be calculated. The same process is carried out with a horizontal strip of the image to correctly locate the parent branch in the horizontal coordinate.

The channel width was used to calculate a rescaling factor, such that the modified channel width, D, will be a multiple of 8 (the final IW size used in the PIV processing). The image was then stretched using cubic spline interpolation and cropped so that only three 3.5 channel widths upstream of the bifurcation, and downstream along each daughter branch, are considered in subsequent processing.

For Chapter 5, a more advanced approach was utilised. In order to achieve sufficient illumination on the first frame, the strobe had to be focussed more strongly in order to maximise intensity and minimise the strobe pulse width. However, this resulted in uneven illumination of the image. Furthermore, with the custom built microchannels, it was not possible to easily align the channel accurately, and so correction for this was also required. The block diagram in Figure 2.9 shows the preprocessing steps used to prepare the images and correct for errors. After the steps described have been carried out, each instantaneous image is corrected for uneven illumination and rotation and cropped and scaled according to the values found for the mean image.

For the fluorescent particle images analysed in Chapters 4 and 5, the minimum intensity value of each pixel in a set of images is subtracted from each image, which removes background artefacts (Raffel et al., 1998). This approach is not suitable for the bright-field μPIV images, as it results in a loss of information, and therefore was not utilised.

2.6.2 Particle Image Velocimetry Processing

Processing of the images for velocity data was carried out using standard PIV processing methods (Raffel et al., 1998; Adrian & Westerweel, 2011) with freeware provided by Peter Vennemann, JPIV (www.vennemann-online.de/jpiv).

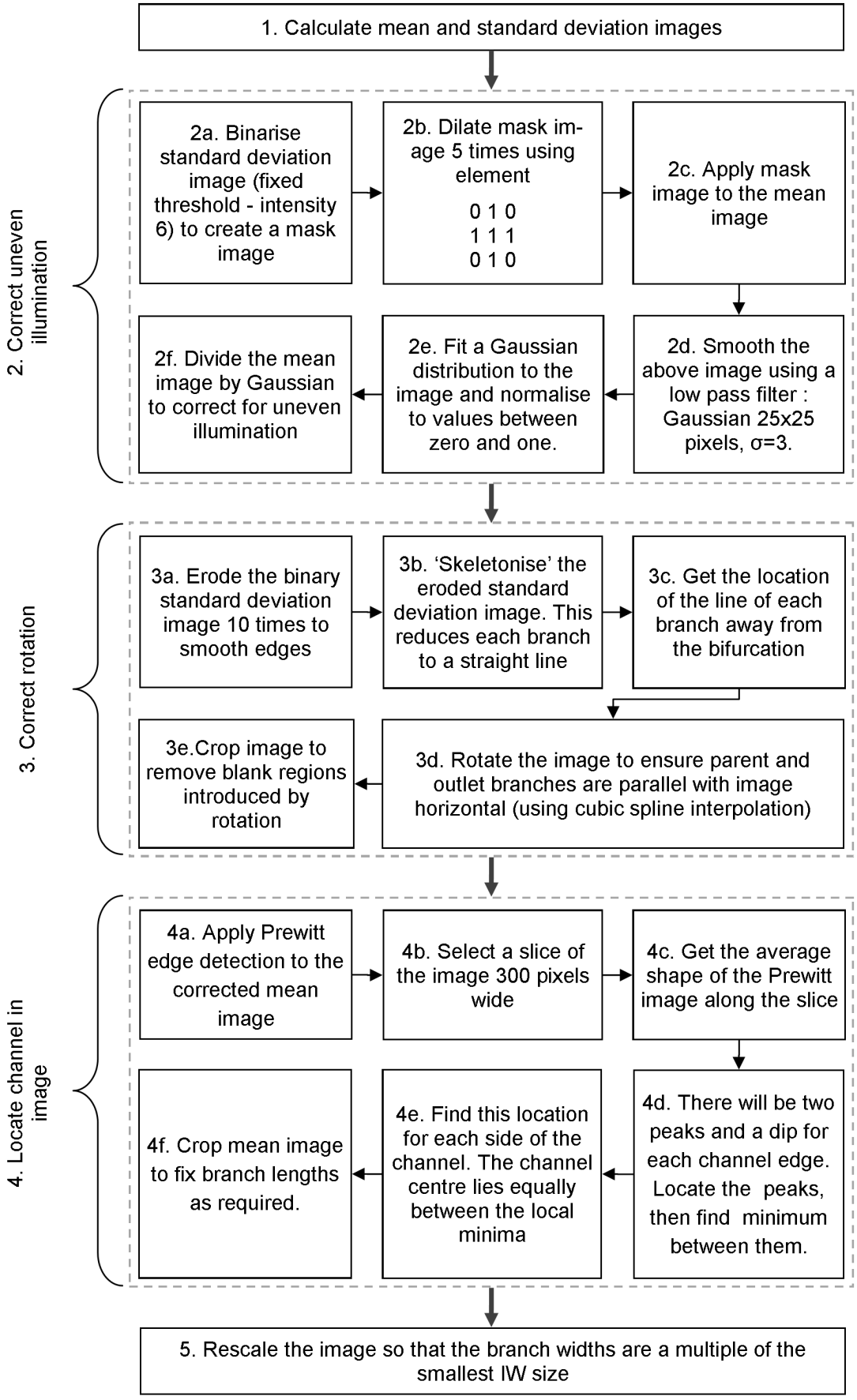

Figure 2.9: Block diagram showing the image preprocessing approach used in Chapter 5.

For fluorescent μPIV, a relatively low seeding density is required, as at high seeding densities, the fluorescence can saturate. However, using a low seeding density leads to IWs in each image pair which have insufficient number of particles to get a correct vector. Hence, it is generally necessary to perform time-averaging in order to get accurate flow fields. This can be done by processing each image pair separately and averaging the final vector fields. However, such an approach would give equal importance to erroneous vectors. Filtering the fields for erroneous vectors and omitting such data from the averaging process could improve the accuracy. When using multi-pass algorithms, which generally improve accuracy, this approach would be further limited to averaging the final pass and hence errors from preceding passes would propagate. An alternative approach is 'ensemble' or 'correlation' averaging. In this method, for each pass, the average correlation peak at each location is calculated, and this is used to define the vector for each IW. This method significantly reduces the number of erroneous vectors. Vennemann et al. (2006) found that for their data, the number of erroneous vectors reduced from just over 40% for a single image pair, to 10% for 5 image pairs and 0% for 50 image pairs.

For the present data, multi-pass (4 passes) ensemble averaging was used for all cases, with final IW sizes of 8×8 pixels and vector spacing of 4 pixels. The resolution of the images was $0.65 \mu m/pixel$, hence the interrogation windows were approximately 50% larger than the largest diameter of an RBC.

Final vector fields were analysed with the normalised median test (Westerweel & Scarano, 2005) and invalid vectors were replaced with the median of the surrounding vectors. In all cases, less than 0.1% of the vectors were replaced.

Due to diffraction, there were around 4 pixels at the channel walls which could not be used. Thus, for the final IW parameters utilised, the closest two vectors to the wall (at 4 and 8 pixels) were not valid. In order to estimate the whole velocity profile (for the purpose of calculating flow rates), spline interpolation is used to interpolate between the valid vectors and an assumed no-slip condition at the channel wall.

In Chapters 3 and 4, flow rates were estimated using the mean velocity scaled by a factor calculated according to Equation 1.10 relating the mean flow velocity in the middle plane compared to that mean velocity for the total profile (the scaling factor for a 5:2 aspect ratio is 0.6683). In Chapter 5, a more complicated approach is used, which

is described therein.

For Chapter 5, the acquired data was scaled based on the work of Poelma et al. (2012) (see §2.4). For a channel of depth $50\mu m$, their data suggests that the measured velocity will be 0.66 times the true velocity. Hence the PIV velocities were scaled by a factor of 1.5. This modification was not applied to the data in Chapters 3 and 4, as the work was performed and published prior to the publication of the aforementioned paper. However, as the flow rate in those cases was a fixed parameter, this should not effect the conclusions drawn.

2.7 Error estimation

The data acquired in the present study is based on processing images (including PIV processing), thus it is inherently difficult to estimate errors. This section comprises a discussion of error estimation approaches and corrections used for various parts of the data analysis.

2.7.1 Errors in PIV analysis

Particle image velocimetry processing is mathematically complex, and theoretical analyses of error estimation are based on the assumption of Gaussian particle images. For the analysis of vector fields from RBC images using PIV algorithms, such analyses are not suitable.

Ensemble averaging is used for all of the PIV data reported in Chapters 3-5. By using the averaged correlation at each location from a stack of 60 or more images, the number of invalid vectors, an indication of the accuracy of the processing is greatly reduced (Vennemann et al., 2006).

Post-processing of the vector fields using the normalised median test (Westerweel & Scarano, 2005) was used to identify spurious vectors. For a given vector U_0, the normalised residual r'_0 (indicating the difference between a given vector and those surrounding it), is given by

$$r'_0 = \frac{|U_0 - U_m|}{r_m + \epsilon} \tag{2.4}$$

where U_m is the median of the surrounding vectors and r_m is the median of each of the surrounding vectors minus U_m. ϵ is an additional term representing a minimum

normalisation level which prevents a zero denominator. r'_0 is calculated for both u and v velocity components and the magnitude of the two components of r'_0 is calculated. If the result exceeds a predefined threshold, then the vector is considered to be invalid. The recommended values of $\epsilon = 0.1$ and a threshold of 2 are utilised (Westerweel & Scarano, 2005). For all data sets reported in Chapters 3-5, the number of invalid vectors was calculated to be less than 0.1%. Invalid vectors were replaced with the median of the surrounding vectors.

For the fluorescent μPIV data, subtraction of the minimum image from a stack of images was used to remove background noise. However, further preprocessing methods were not found to reduce the number of spurious vectors. Given the high percentage of valid vectors calculated by the normalised median test, and the desire to keep the processing algorithms as similar as possible between the RBC and fluorescent μPIV data sets, no further error reduction techniques were adopted.

The use of bifurcating geometries, however, provided a very simple test of the accuracy of the measurements, as the conservation of mass (Equation 1.2) requires that

$$\rho_p Q_p = \rho_d Q_d + \rho_o Q_o \tag{2.5}$$

where the subscript p represents the parent branch and d and o refer to the two daughter branches (after the terminology used in Chapters 5 and 6). Q is the volumetric flow rate and ρ is the density. In the absence of full three-dimensional data sets, as in Chapters 3 and 4, it is assumed that the density is constant (for the densities of the SM and RBCs described in Chapter 1, the density of blood is expected to increase from 1025 to 1055 kg/m^3, for haematocrits of 0 to 0.3: a difference of less than 3%). Thus, an estimate of the error is given by

$$e = \frac{Q_p - Q_d - Q_o}{Q_p} \times 100\% \tag{2.6}$$

This gives a percentage error deviation from ideal mass conservation and the values are reported in each chapter. For the brightfield PIV data reported in Chapter 3, e was found to be 3.8 and 6.4% for the Dextran and PBS cases respectively. For the fluorescent μPIV data in Chapter 4, e was just 1.3 and 1.4% for the Dextran and PBS cases. For Chapter 5, a full three-dimensional haematocrit distribution is available, and

the approach is adapted accordingly. Details are reported therein.

In μPIV, the volume illumination leads to out of plane particles influencing the processing, and hence underestimating the measured velocity. As discussed in §2.4, the influence of out-of-plane particles is similar for RBC and fluorescent μPIV approaches at low magnification ($10\times$) but becomes significant for $25\times$ objectives (Poelma et al., 2012). All data in the present study, with the exception of the brightfield illuminated images in Chapters 3 and 4, are acquired with a $10\times$ objective. In Chapter 3, the RBC velocity is not directly compared to that of the SM, so the difference will only affect estimation of the absolute flow rate, which may be overestimated for all cases, but was not a control parameter. In Chapter 4, RBC velocity profiles are only compared to SM profiles in normalised form.

2.7.2 Errors in image processing

Image processing methods are very hard to verify. For Chapter 3, the CDL identification algorithm developed is tested by user verification, as reported in previous methods (Kim et al., 2007). Despite being slightly subjective, this approach is utilised in the absence of superior alternatives.

For the haematocrit distribution technique reported in Chapter 5, it was not possible to confirm the data by user verification. Analysis of the total flux of each component involved the haematocrit estimation technique, and hence low values of the percentage error in mass conservation indicated accurate velocity and haematocrit estimations. The ideal solution for verifying the bulk haematocrit would be to measure the haematocrit discharged from each branch. However, due to the influence of aggregating RBC and thus short acquisition times, the volumes of fluid collected for each experiment were too small to practically collect and assess for the present study.

2.7.3 Wall shear stress

As discussed in Chapter 1, estimation of wall shear stress commonly requires a number of assumptions to be made regarding the local shear rates and viscosities. In the present microchannel flows, RBC distributions and velocities vary greatly. Considering Chapter 3, wherein the CDL distribution is calculated, perhaps the most suitable approach to estimate the wall shear stress from the experimental data would be to extrapolate the measured velocity profiles to the wall and assume either SM viscosity in the CDL or a

bulk viscosity based on haematocrit in the absence of a CDL. For Chapters 4-6, given the calculated viscosity distribution, only extrapolation of the velocity vectors would be required.

However, the no-slip condition is not valid for RBCs, and hence such extrapolation would introduce significant errors (as measurement close to the wall was not possible as discussed above). Instead, in the present study, calculations of the wall shear stress were made from the numerical data generated for each set of measurements. In Chapter 3, an analytical model was used in conjunction with an empirical viscosity model (Pries et al., 1992b) to estimate wall shear stresses. In Chapters 4 and 6 (the latter presents numerical data based on Chapter 5), wall shear stresses were extracted directly from the computational models of the flow which were developed using experimental data as an input.

Using this approach, the estimated wall shear stresses are self-consistent, in that sources of error will be equivalent for all parameters (parent branch flow rate, flow split etc.), as may not be the case when trying to extract such data from the experimental measurements. This approach was preferred as the presence of observed trends is expected to be more reliable.

2.7.4 Statistical analysis

For some of the parametric investigation reported in Chapters 3, 5 and 6, statistical analysis was necessary in order to confirm whether observed trends were statistically significant.

In Chapter 3, the Pearson's correlation coefficient provided a simple measure of the linear correlation between two data sets. The accompanying P-value describes the likelihood that the observed trend is observed by chance. P-values were reported for each case, but the commonly adopted threshold value of $P = 0.05$ was used as a benchmark to verify significance or otherwise.

In Chapters 5 and 6, due to the larger parameter space and non-linear relationships, the Spearman's rank correlation coefficient was more appropriate. For this parameter, the data are 'ranked', i.e. put in numerical order and the Pearson's correlation coefficient is then calculated for the ranked variables. This provides a better estimation of significance in the absence of a linear relationship. However, the approach requires that the

relationship is monotonic. Where this was not the case, the data was split in two, based on prior knowledge, and the Pearson's rank correlation coefficient was calculated on each side of the supposed threshold value between the two data sets, as Spearman's rank correlation is less effective for smaller sample sizes.

2.8 Time-dependent state of the aggregation in a microchannel

Chapters 3, 4 and 5 contain descriptions of image processing methodologies for identifying the location of the CDL, and for developing one dimensional and three dimensional haematocrit distributions respectively. The details of these approaches will thus not be discussed here. However, in order to define how long it is necessary to leave the system at low flow rate before starting the acquisition, i.e. in order to understand what the aggregation time is in the microchannel, a simple approach to analyse the extent of aggregation in a microchannel was developed. A set of simple experiments was carried out in order to ascertain the time response of aggregation in microchannel flow at the haematocrits used in the present study.

Kaliviotis & Yianneskis (2008) described a method of quantifying aggregation based on 'plasma gaps' in images acquired using an optical shearing microscope. The area of such gaps is identified by thresholding the image at an appropriate level, and used to calculate an aggregation index using the known haematocrit (in Couette systems the haematocrit is uniform and the Fåhraeus effect is absent) . However, this method required that there was only a single layer of cells in the channel. In microchannels of depth 40 or $50\mu m$ (as used in this study), this would not be the case. Furthermore, the haematocrit varies spatially within the microchannel, as will be described in subsequent chapters. Hence, a different approach was required. It was proposed that, under equal feed haematocrit conditions, the image contrast gives an indication of the extent of aggregation. Figure 2.10 shows two images with different levels of aggregation and their corresponding histograms.

In Figure 2.10a, the RBCs are relatively uniformly distributed. It can be seen that the histogram of the image is a normal distribution, skewed towards lower pixel values. However, in Figure 2.10b, wherein the RBCs are clearly aggregated, the histogram is

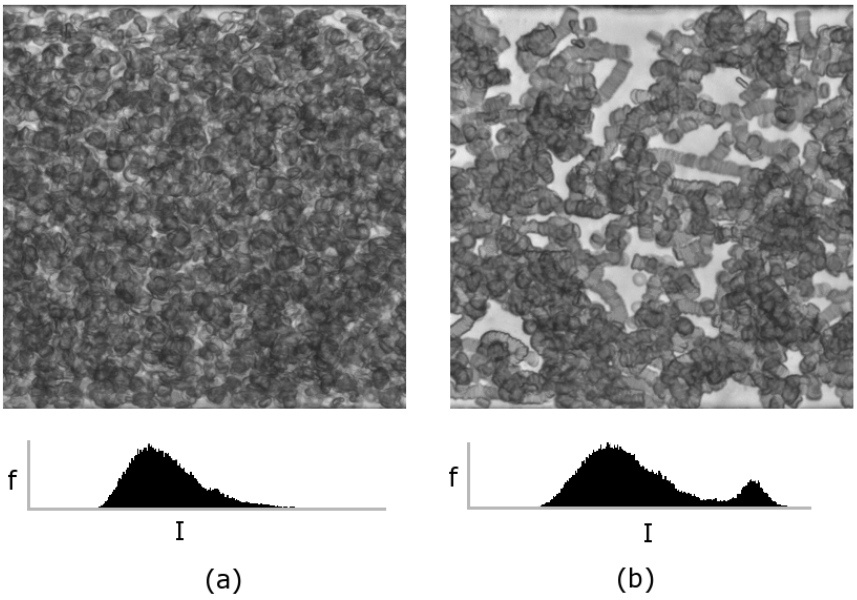

Figure 2.10: Images of Dextran samples with different levels of aggregation. Histograms of pixel intensity are shown underneath the images. f is frequency and I is pixel intensity. (a) Non-aggregated cells at high flow rate (average velocity $2.44mm/s$), (b) At very low flow rate (average velocity $0.03mm/s$), strong aggregation can be observed, with both linear rouleaux and clumps of RBCs.

bimodal in character, with a second peak at high intensity levels. The image contrast, as quantified using the standard deviation of the pixel intensities can thus provide a measure of the extent of aggregation present (although standard deviation is not an accurate statistical measure for the bimodal distribution, it nonetheless captures the range of values observed and is thus suitable for this usage).

In order to analyse this approach, a long straight section of a microchannel with dimensions $250 \times 50\mu m$ was used (Epigem, UK: other than the different cross section, the channel was the same as that described for use in Chapters 3 and 4). The flow rate was droped from a very high value to a low value, after which acquisition was triggered. Image acquisition was carried out in bursts of 200 images every two seconds for 60 seconds using the IDT X3 CMOS camera and halogen lamp illumination. The acquisition frequency was chosen depending on the velocity of the flow. Dextran (aggregating) and PBS (non-aggregating) cases were analysed at a range of average velocities $(0 - 2.5mm/s)$, and 3-pass ensemble averaged PIV with a final interrogation window of 16 pixels was used to analyse the velocity field.

The proposed aggregation index, σ_A^*, is defined as the standard deviation of all of the

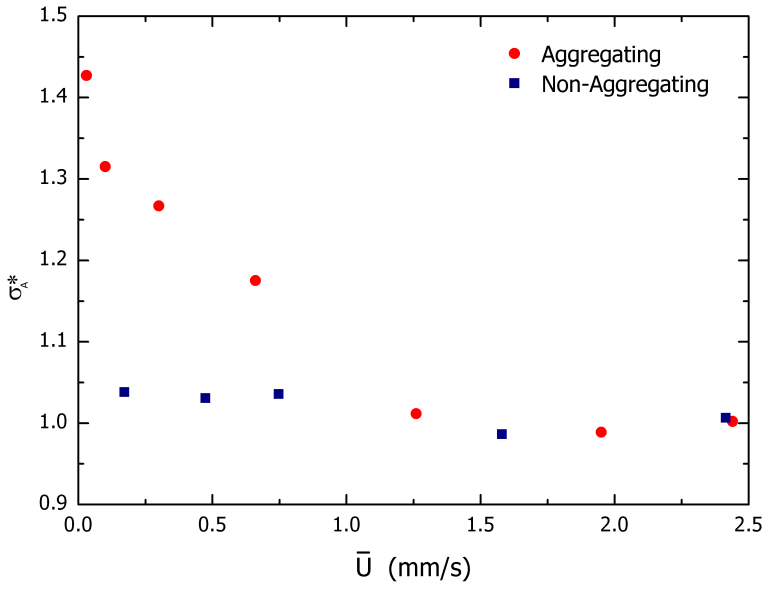

Figure 2.11: Image contrast based aggregation index against average velocity for aggregating and non-aggregating cases.

pixels in an image stack, normalised by the average value calculated for a PBS case, in which aggregation was absent.

Figure 2.11 shows the average value of σ_A^* over the last 10 seconds of acquisition against the mean channel velocity (estimated from the PIV based on equation 1.10). It can be seen that σ_A^* is approximately constant for the non-aggregating cases, varying between 1 and 1.05, which can be considered as an estimate of the sensitivity of the approach. For the aggregating cases, σ_A^* is 1.43 for almost static flow, and decreases with increasing flow rates. This trend is to be expected, as disaggregation occurs due to fluid shear stresses. For average velocities above $1.25mm/s$ (pseudoshear rate based on channel height of $25s^{-1}$), there is negligible aggregation indicated by σ_A^*, and the PBS and Dextran cases have the same value.

In Figure 2.12, σ_A^* is plotted over a period of 60 seconds after the pressure had been dropped to a low level. The black line shows the change in the standard deviation for a low velocity PBS case. It can be seen that there was no systematic change in the contrast during the acquisition, which justifies its choice as a normalisation parameter. The value for all PBS cases was approximately the same, and none showed a systematic change in time; hence only one case is shown on the figure. Conversely, for the aggregating cases, after the low flow rate is reached ($t = 0$), σ_A^* increases rapidly and

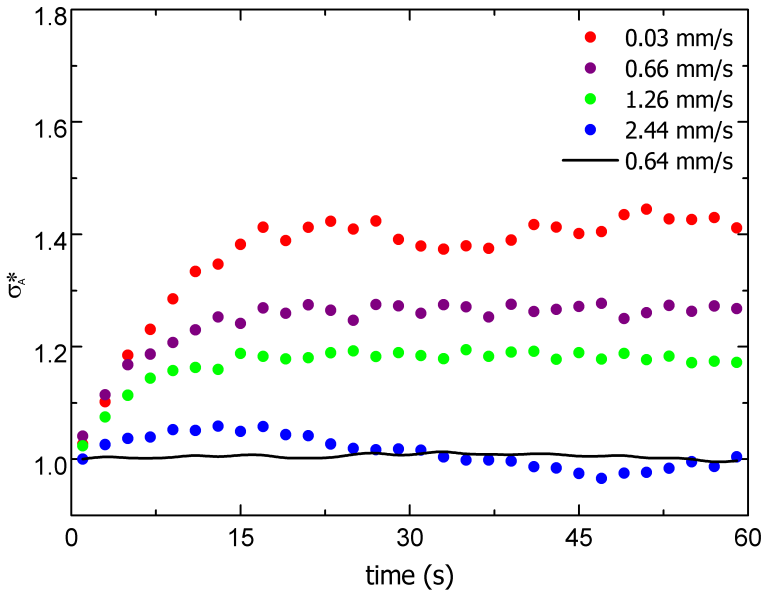

Figure 2.12: Image contrast based aggregation index against time for aggregating cases at different average velocities. Solid black line represents typical non-aggregating case.

reaches a steady state after 15 seconds. It can be seen that the lower the average velocity, the higher the steady state value of σ_A^*. Furthermore, even at almost zero flow (red dots, average velocity $0.03mm/s$), the time to reach steady state was similar to that at higher velocities.

The proposed method for quantifying aggregation is very simple, but from the evidence presented in Figures 2.11 and 2.12, it seems to be capable of estimating the state of aggregation. That is to say, the time response and response to shear which are expected are apparent in the data. The technique does not require any prior knowledge of the haematocrit, but provides a value which only has relevance relative to equivalent data sets in the absence of aggregation. By comparing Dextran cases with equivalent PBS cases, Figure 2.11 showed that the observed trends are not a result of the velocity of the blood. The major limitation of the approach, is that it assumes an approximately uniform haematocrit distribution. In the very high aspect ratio (5:1) channel used for these tests, this is a reasonable assumption, although there is a slight reduction in haematocrit near the upper channel walls visible in Figure 2.10. However, in the lower aspect ratio channels used in Chapters 3 and 4 (5:2) and Chapters 5 and 6 (1:1), a larger effect of haematocrit distribution would be expected. Furthermore, in the bifurcation region, RBC distributions will be highly heterogeneous as will be shown in subsequent

chapters. Hence, this approach will not be suitable for estimating aggregation states in the bifurcated microchannels. Instead, when considering aggregation in the following chapters, its influence will be inferred from measurements of RBC distribution and velocities, rather than trying to quantify it directly. Nonetheless, this brief experiment provides confidence that having reduced the flow from a high value (at which the RBCs are uniformly distributed and non-aggregated), to a low value, a steady aggregation state will be reached within 20 seconds and that it will remain so for at least 40 seconds afterwards.

2.9 Closure

In this Chapter the details of the experimental acquisition and image preprocessing stages have been described. The design requirements for the perfusion system were stated and a description of the system developed for the purpose was given. The system comprised a high pressure source connected via a series of valves, one of which was coupled to a stepper motor. This pressure control system was found to be very easily controlled and was very accurate. Multiple imaging approaches were utilised and these were described, along with the hardware and software requirements for the acquisition. The image preprocessing approaches that were used in the present study were described and errors were discussed. Finally, an initial investigation into aggregation characteristics and time response in a microchannel was carried out.

The next chapter presents the development of a technique for estimating the temporal and spatial characteristics of the CDL for blood flow in a bifurcating microchannel. The effects of RBC aggregation and flow ratio on the CDL distribution are considered and a simple mathematical model is derived to estimate the influence of the CDL on the observed velocity profiles, wall shear stress and apparent viscosity.

Chapter 3

Cell-depleted layer characteristics †

In this Chapter, a new technique for measuring the cell-depleted layer (CDL) is developed and used to analyse blood flow in a straight-T bifurcating microchannel. Velocity profiles of the RBCs are measured and skewed velocity profiles are observed. A simple two-fluid mathematical model is derived and used to investigate whether the CDL is sufficient to generate the observed skewness.

3.1 Introduction

As discussed in Chapter 1, in long straight channels/vessels there tends to be a region near the vessel wall where the local haematocrit is reduced, due to radial migration and, in the presence of aggregation, synaeresis. A large amount of research has aimed to understand what factors influence the size and distribution of this region and the effect that it has on flow characteristics, such as plasma skimming (Doyeux et al., 2011) and apparent viscosity (Reinke et al., 1986). Terminology regarding the layer varies, with cell-depleted layer (CDL) (Reinke et al., 1986) and cell-free layer (CFL) (Kim et al., 2009; Yalcin et al., 2011) being used interchangeably, although the latter seems to be the most common. In an instantaneous sense, there are regions which are 'cell-free', but over a finite length of time cells will inevitably impinge on the layer. Hence, there will

†The data presented in this Chapter has been published in 'Sherwood et al (2012) The effect of red blood cell aggregation on velocity and cell-depleted layer characteristics of blood in a bifurcating microchannel', *Biomicrofluidics* (Sherwood et al., 2012a). The work was also presented at *'Physiological Fluid Mechanics'*, July $14^{th} - 15^{th}$ 2011, London, UK (Poster), *'Micro and Nano Flows'*, August $22^{nd} - 24^{th}$ 2011, Thessaloniki, Greece and *'Bioengineering 2011'*, September $12^{th} - 13^{th}$ 2011, London, UK.

be very few regions in microvessels which are permanently cell-free. In this chapter, CDL will be used to describe a geometrical region, while CFL will apply to a region which is instantaneously devoid of cells.

The majority of quantitative CDL studies have been in straight vessel sections or straight capillary tubes, wherein the CDL is relatively symmetric. That is to say that the instantaneous shape may vary, but the average width of the layer is equal on either side of the conduit. RBC aggregation has been shown, in such circumstances, to enhance CDL formation by inducing synaeresis and increasing radial migration. However, it remains unclear how these parameters will affect local haemodynamics in geometries in which symmetry is not present. A recent paper by Ong et al. (2012) reported cell-free layer characteristics downstream of a bifurcation *in vivo*. They showed an increase in CDL width with decreasing flow ratio and a correlation between parent and daughter branch CDL widths. However, the effect of aggregation was not considered separately to non-aggregating samples and hence its influence could not be inferred from the data. What is more, *in vitro* data could provide a wider parametric analysis with a higher resolution. It has been reported that plasma skimming occurs due to the CDL (Doyeux et al., 2011), and is enhanced by aggregation (Gaehtgens et al., 1978; Gelin, 1963), but details of the local flow characteristics and their influence on each other require further elucidation.

One approach to investigating the effect of the CDL on fluid dynamics is to model the fluid as two-immiscible phases: the RBC core and a CFL (modelled as pure plasma). While simplistic, this approach has yielded some useful insight into the relationships between various parameters. However, this approach has not hitherto been reported for asymmetric CDL distributions.

The aim of this chapter is to investigate how microhaemodynamic parameters affect the CDL characteristics in bifurcating geometries. To this end, the flow of human blood in a microchannel with a simple T-bifurcation, as discussed in Chapter 2, is utilised. Images are acquired with brightfield illumination and a high speed CMOS camera. The reservoir haematocrit is fixed at 0.25, and the parent branch flow rate is regulated at around $3.6\mu l/hr$, which corresponds to an average velocity of $0.25mm/s$ in a channel with a cross sectional area of $100\mu m \times 40\mu m$.

Figure 3.1 shows the terminology relating to channel location superimposed on a sam-

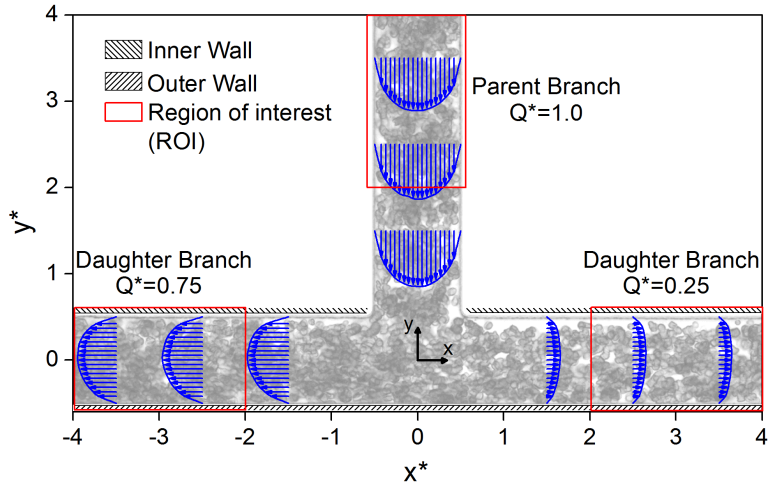

Figure 3.1: Sample image with terminology and ROI superimposed. Velocity profiles are also shown for a flow split of 25:75.

ple image. Experimental velocity profiles for a flow split of $25 : 75$ are also shown. The regions of interest (ROI), in which the velocity profiles considered later in the chapter are averaged, are indicated by the red boxes. The 'inner wall' and 'outer wall' of the daughter branches are indicated on the figure. The coordinate system is (x^*, y^*), defined as the (x,y) coordinate normalised by the channel width.

The effects of flow flow ratio (Q^*) are investigated by altering the pressure in the daughter branches. RBC aggregation is considered by the addition of Dextran 2000 at $5g/l$. The acquired images are processed using PIV algorithms in order to derive full flow field velocity information. The same images are then further processed using a newly developed technique to estimate the spatial and temporal CDL characteristics. In order to further understand the influence of the CDL under conditions of asymmetry, a two-fluid mathematical model is derived and utilised with experimentally derived parameters. The results are compared and inferences are made about the importance of RBC aggregation, the CDL and the limitations of considering blood flow in this manner.

3.2 Cell-Depleted Layer

Sample images of the RBCs in the bifurcation, illuminated with a 100 Watt halogen lamp, are shown for a PBS case in Figure 3.2a and a Dextran case in Figure 3.2b; the flow split for both cases is 80:20. In Figure 3.2a, the cells suspended in PBS are not

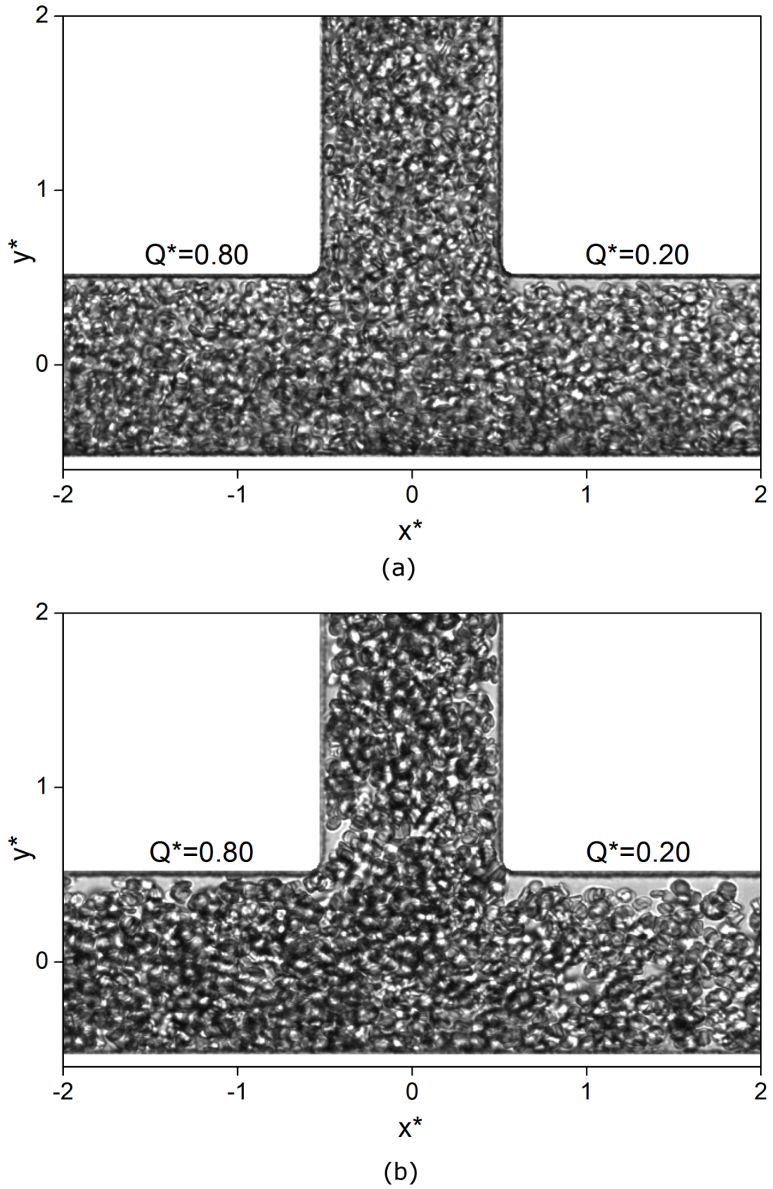

Figure 3.2: Sample brightfield illuminated images of RBCs in a microchannel bifurcation. Flow enters through the vertical branch. (a) PBS case, (b) Dextran case.

aggregated and are distributed fairly homogeneously throughout the channel. However, it can be seen that there are fewer cells at the inner wall compared to the outer wall, particularly in the low flow rate branch. Figure 3.2b shows an equivalent image for the Dextran case. There are clumps and linear rouleaux at various orientations visible throughout the domain. Through the analysis of videos of the Dextran samples travelling through the bifurcation, it was observed that aggregates exist in a range of sizes, from around 2 - 10 cells per aggregate. It can be seen that in addition to the increased size of the region without cells at the inner wall of the low flow rate branch, there are

similar regions in the parent branch and high flow daughter branch. Furthermore, there are a number of gaps - cell-free areas, within the channel, particularly in the low flow daughter branch. As discussed previously this represents a cell-free layer (CFL) in the temporal dimension, or a cell-depleted layer in the spatial dimension. The following section describes the development of an approach to quantify this layer and its variation in space and time.

3.2.1 Technique development

Considering Figure 3.2, it can be seen that the way in which the illumination affects the cells is not straightforward. Although in general the cells appear darker than the background, there are many regions of high intensity where cells are present. Furthermore, the diffraction at the walls of the channel forms a relatively large area (≈ 4 pixels) near the wall, where the intensity is low, whether there are cells in the vicinity or not. Comparing these images with the *in vivo* images of Kim et al. (2005) (Figure 1.5), it can be seen that the quality of the present images is much higher, a result of the easier experimental acquisition in *in vitro* conditions. The disadvantage of the use of microchannels with vertical channel walls parallel to the light transmission direction, is that they result in large areas of diffraction near the wall, which would be relatively less pronounced in a round channel or vessel. However, they also avoid the problems associated with different refractive indices inside and outside the channel. Given the specific qualities of the images shown in Figure 3.2, it is clear that a simple thresholding approach as used by other researchers (Kim et al., 2006; Namgung et al., 2010; Ong et al., 2011b) will not be sufficient. An example of this approach is shown in Figure 3.3a, where the Otsu thresholding method (Otsu, 1979) is applied to a sample RBC image. While the technique works in some regions, the near wall areas (which are clearly important) are unusable and there are regions where cell-edges are filtered out.

An alternative approach, termed the 'grayscale' method, has been used by some groups (Ong et al., 2011b; Yalcin et al., 2011) and uses the intensity gradient along the radial direction at a given axial position. However, this requires that the image is consistently darker in regions where there are cells than in those where there are not, which is not the case for the present data. It should be noted that in the aforementioned papers, this is not exactly how the approach was carried out. In those studies, an analysis line was set up to

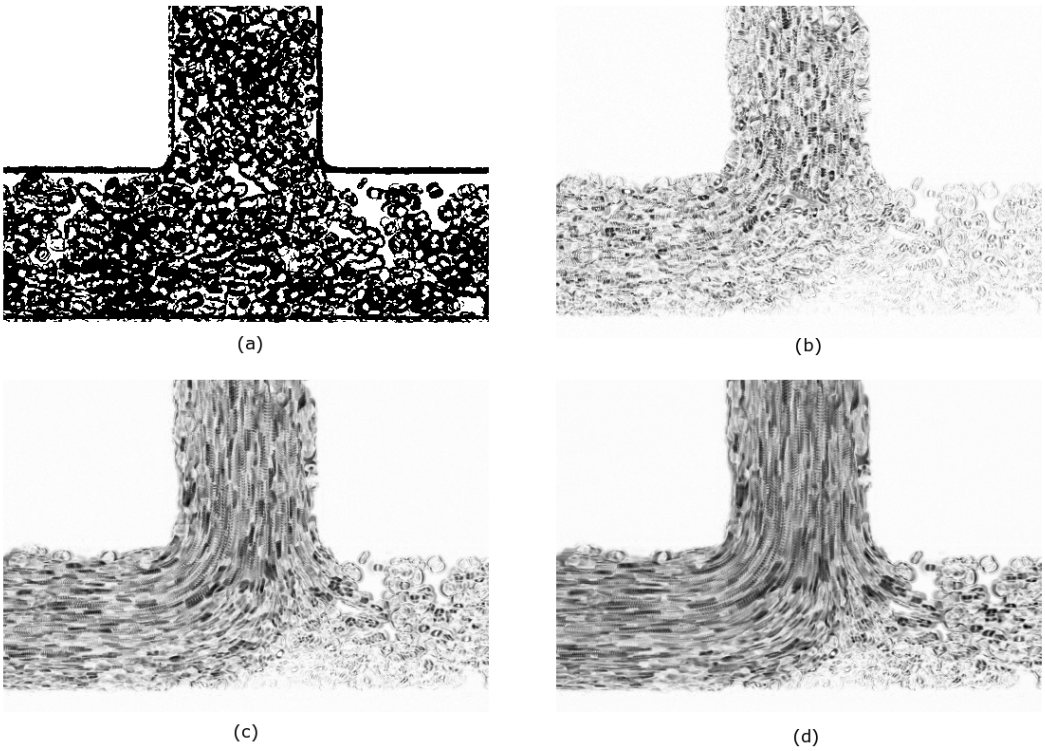

Figure 3.3: (a) Sample image thresholded using the Otsu approach. (b-d) Standard deviation images of a stack of different numbers of images. Grayscale values have been inverted for clarity, scale shows full 8-bit range (0-255). (b) 3, (c) 7, (d) 11. The case shown is a Dextran sample with an 80:20 flow split.

form an artificial image with a temporal axis at a given one dimensional location (line). The location of this line is chosen in an area where the vessel wall is clearly defined and the image contrast is high. While multiple lines can be set up, this is a limitation of these approaches, as it requires manual selection of such regions and limits the spatial resolution. Furthermore, this approach would not significantly improve the response shown in Figure 3.3a and for the present study a full field distribution is desired.

For the present data, a new technique was required. The proposed approach is based on the concept of motion detection. The basis of this idea is that in the regions where there are no cells, nothing will move between frames, including the channel walls. Hence, an image which shows motion rather than intensity could provide an alternate approach to CDL/CFL detection. One way in which this could be carried out is by finding the arithmetic difference between two images. This approach is limited to the use of two images, and is hence mono-directional in time (i.e. it can work either forwards or backwards). An alternative option is to use the standard deviation (SD) at each pixel

location across a stack of images. This can be applied in both directions, and over a number of images. The importance of the latter point is made clear by comparing Figure 3.3b, c and d, which show the SD images for three different size image stacks.

Firstly, it can be seen that the channel walls are absent, which means that the CDL can be measured close to the wall in a way which would not be possible using a standard thresholding approach (the wall location could still be identified from the original images). However, it can also be seen that the different image stack sizes are more or less effective in identifying the CDL in different branches. In the parent branch, wherein the cell velocity is greatest, Figure 3.3b shows the best result, as Figures 3.3c and d exhibit significant blurring in the parent branch due to the large displacement of individual cells across the increased image stack length. In the high flow daughter branch (left) the best result is observed in either Figures 3.3b or c. For the low flow daughter branch, Figures 3.3b and c have low contrast and poorly defined cell boundaries and Figure 3.3d seems to be most suitable. Considering these differences, it is clear that the technique will be optimal when the RBCs have a specific amount of motion between frames. Too much motion will induce blurring, while too little doesn't provide significant contrast in the SD image (this is analogous to PIV processing, where the time between frames is selected to optimise the displacement in terms of pixels). To account for this, the data in each branch are processed separately, and the image stack size in each branch is scaled to be inversely proportional to the flow ratio in that branch. In the parent branch a stack of 3 images (one image before and one image after the time step of interest) are used. For the daughter branches, the number of images scales with $1/Q^*$. In the case of Figures 3.2 and 3.3 where the flow split is 80:20, the low flow branch has 20 % of the flow from the parent branch. Hence the velocity is approximately 0.2 times that in the parent branch (due to the same cross sectional area). In this case $1/Q^* = 5$, so for an equivalent average RBC displacement (necessary for comparison of SD), 5 images each side of the time step of interest are used. In the high flow branch, the velocity is 0.8 times that in the parent branch, which gives $1/Q^* = 1.25$. It is not possible to use a fractional index of image, so the value is rounded to the nearest value. Hence, for $Q^* = 0.4 - 0.66$, 2 images on either side of the timestep of interest are used, for $Q^* = 0.28 - 0.4$, 3 images on each side are used etc.

The SD images are then thresholded to give a boundary for the CDL. Each histogram

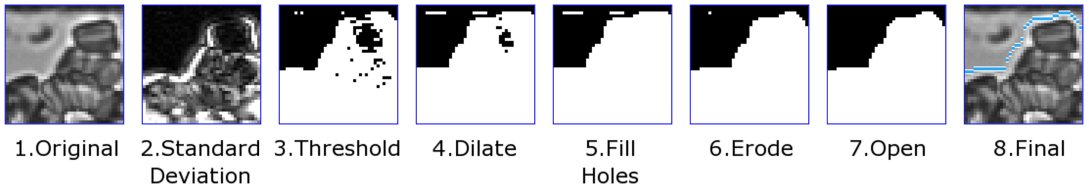

Figure 3.4: Stages in CDL identification. Details can be found in the text.

will have two peaks, one for the background (no cell movement) and one for the main image (where there is movement). It is necessary that the same threshold is applied to each case in order that the 'sensing' of the CDL edge is the same. The value was chosen by taking a histogram of 256 bins (8-bit images), and smoothing with a minimum filter of width three pixels. The location of the valley between the two peaks was noted. This was carried out for a large number of data sets and the modal value was chosen as the threshold. For the present data, the value was 5, but this is dependent on frame rate, illumination levels etc., and therefore it would need to be calibrated for other experiments.

Having applied the threshold, a number of morphological (binary) operations are applied to the image. The stages are summarised in Figure 3.4. A sample of the original image and the SD image are shown in panels 1 and 2. For features which are parallel to the flow direction (i.e. the edge of a cell), the SD may be low, forming a gap, as can be seen in Figure 3.4 panel 3. Basic morphological operations were used in order to resolve this problem. The SD image was dilated in the direction of the flow to 'bridge' the gap. Dilation is an operation in which each pixel which has a value of 1 is extended to adjacent pixels according to the structuring element, which is a 3×3 matrix, in this case

$$\begin{bmatrix} 0 & 0 & 0 \\ 1 & 1 & 1 \\ 0 & 0 & 0 \end{bmatrix}$$

assuming that the flow direction for the image is horizontal. The dilation operation was carried out twice to ensure all gaps were bridged (Figure 3.4, panel 4). A hole filling operation is then carried out using a LabVIEW VI (Figure 3.4, panel 5). The image is then eroded to counteract the dilation. This operation is identical to dilation but inverted, and operates on the pixels of value 0. Hence, carrying out two successive

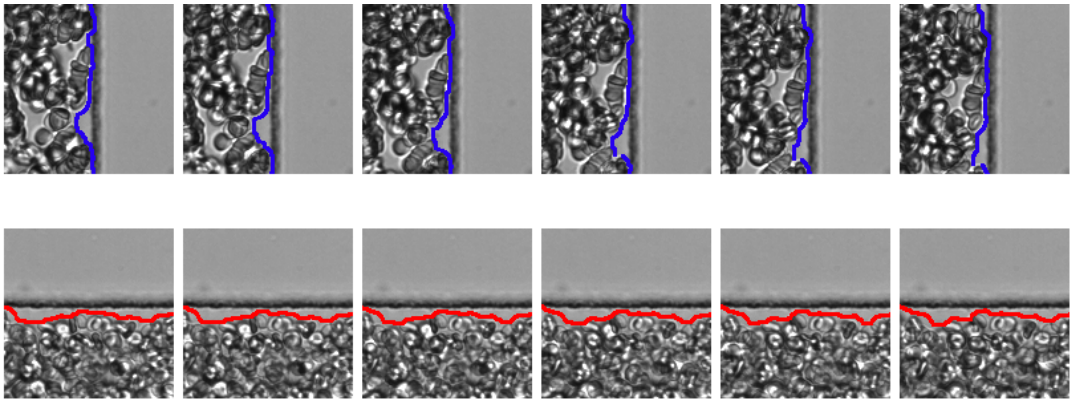

Figure 3.5: Sample images of the CDL at multiple moments in time. The top row is an aggregating case in the parent branch, the time between frames is $12ms$, flow from top to bottom. The bottom row is a PBS case for $Q^* = 0.1$, the time between frames is $28ms$, flow from left to right.

erosion operations reverses the dilation stages, but having filled the holes, the gaps are no longer present. A third iteration of erosion serves to counteract some of the blurring in the SD image due to the motion of the cells (Figure 3.4, panel 6). Finally, an opening function is applied. This is basically an erosion followed by a dilation and is used to remove noise in the image, such as the lone pixel visible at the top left corner of Figure 3.4, panel 6. The structuring element for the opening function was

$$\begin{bmatrix} 0 & 1 & 0 \\ 1 & 1 & 1 \\ 0 & 1 & 0 \end{bmatrix}$$

so has no preferential direction.

The distance between the channel wall and the CDL at each location perpendicular to the channel wall was then defined as the CDL width, as indicated by the blue line in Figure 3.4, panel 8.

In order to demonstrate the technique, a number of sample images with the estimated CDL superimposed are shown in Figure 3.5. The top row shows a Dextran case on one side of the parent branch. It can be seen that the CDL width varies along the channel wall. There are large cell-free regions and others where the RBCs are adjacent to the wall. A rouleaux can be observed in the centre of the image, made up of cells oriented in a range of directions. As the time passes from frame to frame the boundary of the cell-free region translates downstream and changes shape slightly. The rouleaux in the

middle of the image does not move significantly across the images. This shows how different cells move relative to each other and the way in which the CDL develops in time and space visually.

A PBS case for a low flow ratio in the daughter branch is shown in the bottom row of Figure 3.5. In this case, it can be seen that the cells are more evenly distributed. The CDL shape is smoother than in the presence of aggregation and the approximate pattern is convected downstream with subtle changes in the shape. It is worth noting that, particularly in the aggregating case in Figure 3.5 (this is because it is the parent branch as opposed to the low flow daughter branch, not because of the presence of aggregation), there are times when the CDL is measured within the diffraction region at the channel edge. This is possible as cells passing through this area still have the effect of changing the SD image, even though the image intensity is different from that away from the channel edge. There exists no better way of verifying a methodology for CDL estimation than comparing with a manual measurement, similarly to Kim et al. (2006). Therefore, to validate the method, manual measurements at 40 locations were compared to those calculated by the algorithm. The absolute residual differences had a mean and SD of ≈ 1 pixel which is equivalent to $0.65\mu m$.

Finally it should be mentioned that, as a result of the straight T configuration, the CDL at the outer wall was generally negligible, except at very low flow ratios in the Dextran case. Further specialisation of the processing algorithm would be required in order to reliably measure this region due to the very low velocities at the outer wall; therefore, only the CDL at the inner wall of the bifurcation was considered for this data. This is also a key feature of the mathematical model developed in §3.4.

The CDL characteristics can be considered more extensively by comparing them graphically in both time and space. The CDL width (δ) was normalised by the channel width, w, such that $\delta^* = \delta/w$. Figure 3.6a shows the instantaneous profile of δ^* along the inner wall of the daughter branch for the Dextran case for $Q^* = 0.25$ at three moments in time. It can be observed that the profile at t' changes very little for $t' + 16ms$ and is simply convected downstream. For $t' + 80ms$, the profile is similar but has altered slightly and advanced further downstream, although by different amounts at different locations. Figure 3.6b shows the temporal distribution of CDL width at three points in space for the same case. It can be seen that at each location, δ^* exhibits roughly the

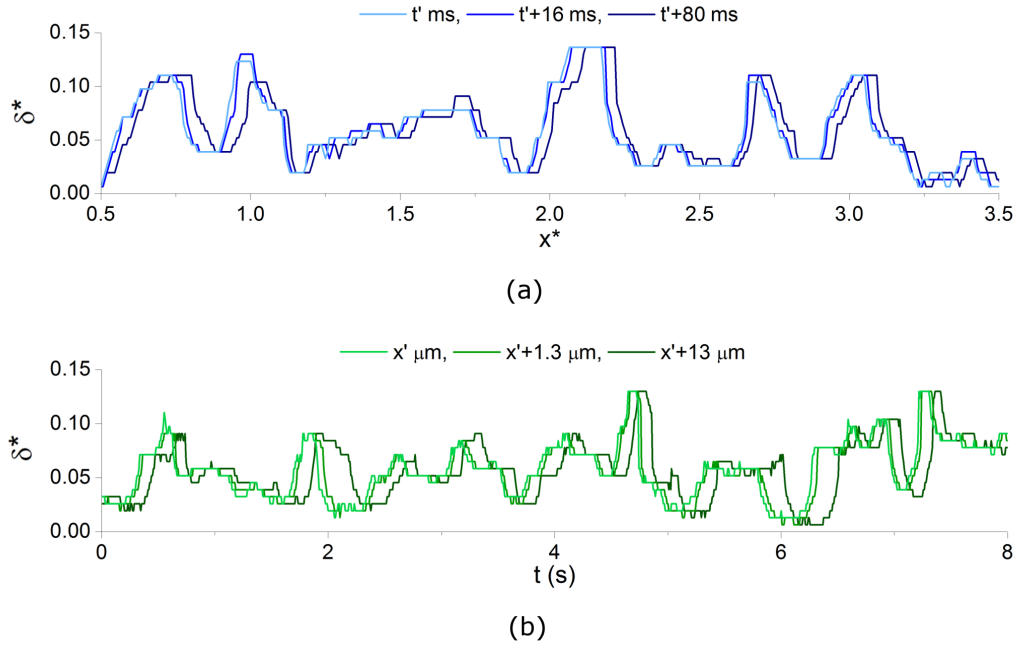

Figure 3.6: CDL width in space and time for the Dextran case with $Q^* = 0.25$. (a) Instantaneous CDL along the daughter branch at three points in time, relative to $t' = 2s$, (b) variation in CDL in time at three locations, relative to $x' = 3.5x^*$.

same fluctuations, with a phase shift dependent on the position in the channel. Hence, despite the fact that at a given moment in time there is a large variability in the CDL width, its overall distribution will be relatively consistent in time.

For each experimental data set acquired, there are 2000 images, with the CDL described at ≈ 2000 pixel locations, giving 4 million data points for each set. In the acquisition process, 35 Dextran and 35 PBS cases were acquired. Thus, to analyse the characteristics of the CDL, statistical averaging must be used. In the following section, this is carried out successively reducing the dimensions, through two- then one-dimensional probability distributions, to mean and standard deviations.

3.2.2 Statistical analysis

Probability distributions in time of δ^* at each location in space along a daughter branch are considered in Figure 3.7 for selected flow ratios. For the Dextran case (Figure 3.7a), δ^* is significantly increased in comparison to the PBS case (Figure 3.7b), and a wide distribution is observed. For $Q^* = 0.5$, the probability of δ^* is greatest along the channel wall and decreases towards the centre of the channel. At $Q^* = 0.25$, the

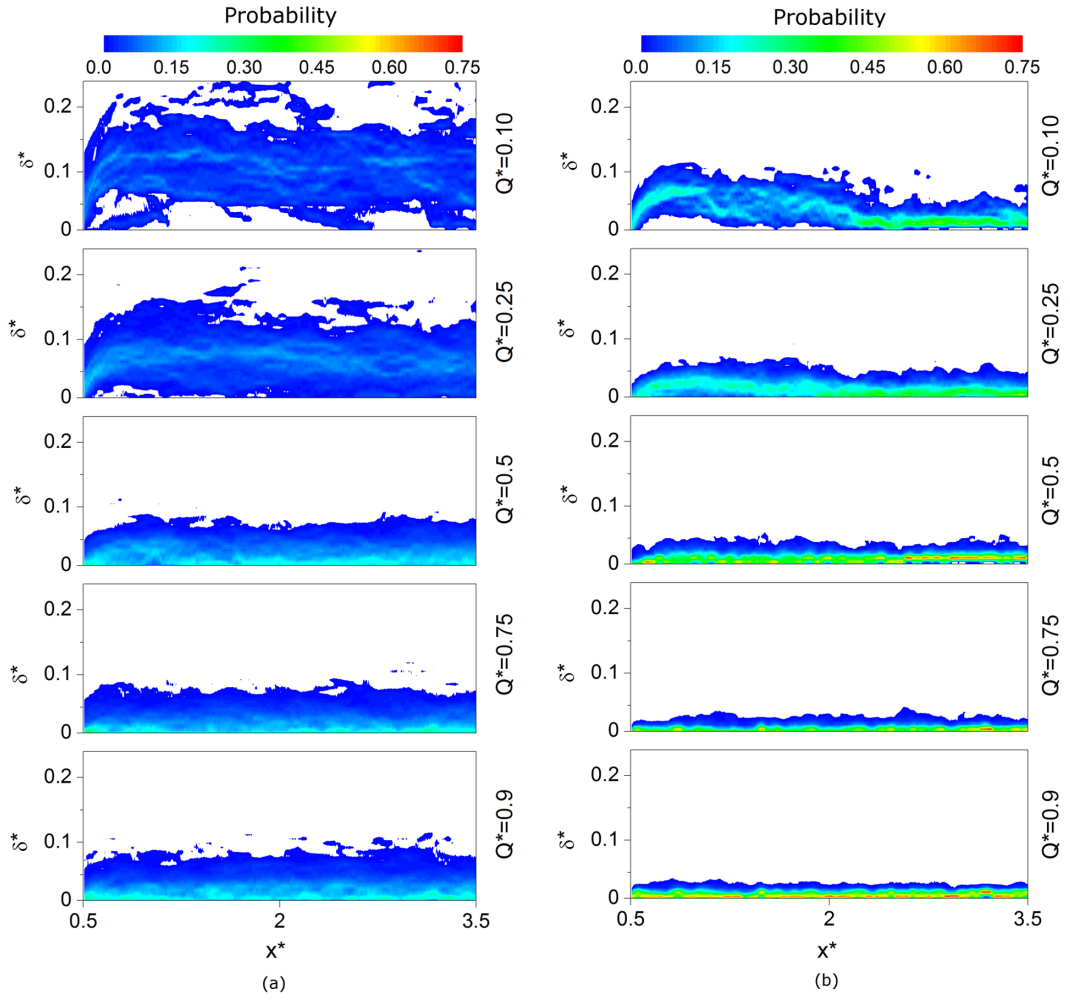

Figure 3.7: Probability distributions for normalised mean CDL width in the daughter branch at a selection of flow ratios for (a) Dextran case, (b) PBS case. The horizontal axis is normalised distance from the bifurcation and the vertical axis is the normalised CDL width. Contours indicate probability that the edge of the cell-depleted layer will be of a certain width for each axial location. White regions indicate no occurrences of CDL edge at that width and location.

modal width is observed at a position offset from the channel wall and the spread of the distribution is greatly increased. At $Q^* = 0.1$, these trends are exaggerated further, with maximum CDL widths as great as 25% of the channel width. Furthermore, regions of white (zero probability) can be observed between the wall and the CDL distribution. This region was truly a cell-free-layer.

For the PBS case (Figure 3.7b), the CDL distributions are significantly narrower. For $Q^* = 0.5$, the modal CDL width is at, or very close to, the wall. At $Q^* = 0.1$, the modal width moves away from the wall immediately after the bifurcation, then approaches the

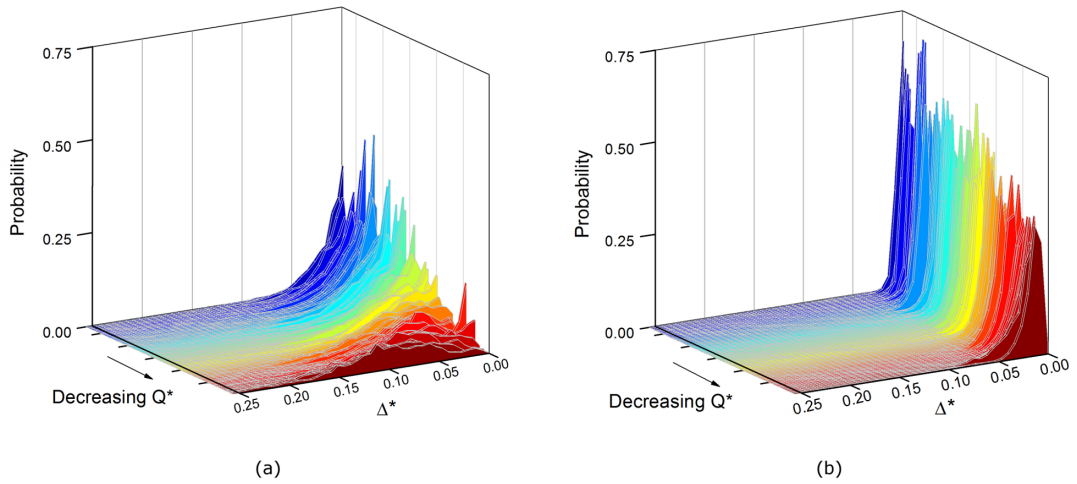

Figure 3.8: Probability distributions for spatially averaged (in the ROI), normalised mean CDL width, Δ^*. The stacks are ordered in terms of decreasing flow ratio, with blue representing high Q^* and red representing low Q^*. $0.1 < Q^* < 1$. (a) Dextran, (b) PBS case.

wall at around $x^* > 2.0$. For $Q^* = 0.25$, this movement away from the wall is also present, but is less pronounced, and the mode returns to the wall when $x^* = 2$. It is worth reiterating that the shape is not a result of inertial flow separation, and thus must be due to the interactions of the RBCs with local hydrodynamic forces or other cells.

The distribution of the CDL is considered further in Figure 3.8, which shows stacks of probability distribution functions of the normalised CDL width (δ^*) averaged along the ROI ($1.5 < x^* < 3.5$), Δ^*, for both the Dextran and PBS cases. At high flow ratios (blue), the modal CDL width is at, or close to zero for both Dextran and PBS cases. For the latter, the position of the modal CDL width does not move significantly away from the channel wall, but the distribution becomes slightly more spread out as Q^* decreases. For the Dextran case, the position of modal CDL width moves away from zero as Q^* decreases from 0.5, and the distribution becomes steadily flatter and broader as the flow ratio decreases, with a modal value of around 10% of the channel width for very low flow ratios.

This data is presented in an alternative manner in Figure 3.9, by considering cumulative frequency plots against the normalised radial location. These can be interpreted as the probability that a cell will pass between a given normalised radial channel location, y^*, and the wall (note $y^* = 0.5$ is coincident with the wall). As the CDL width is the position in the channel for which there are no cells closer to the wall, the cumulative

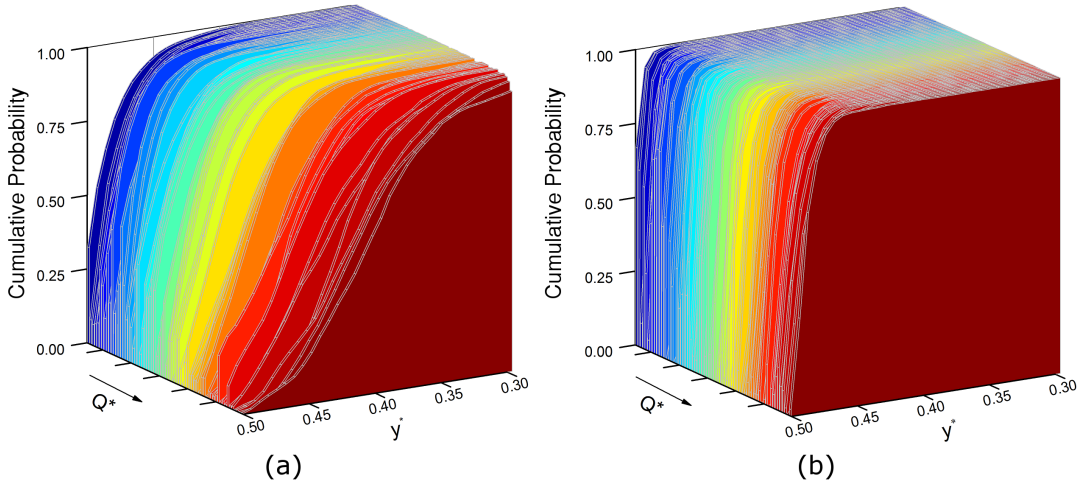

Figure 3.9: Cumulative frequency distributions corresponding to Figure 3.8.

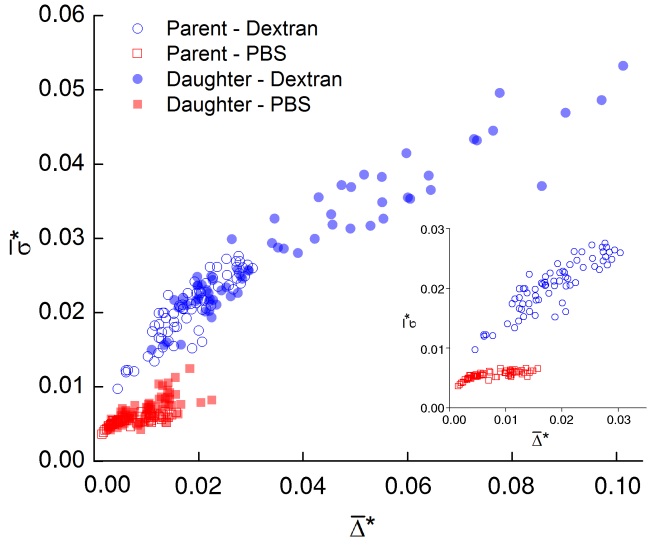

Figure 3.10: CDL roughness indicated by comparing normalised SD of CDL width against $\overline{\Delta^*}$. The inset shows parent branch only, for comparison with straight channel/vessel studies.

frequency plot is perhaps more intuitive. For example, at the lowest flow ratio for the Dextran case there is a probability of approximately 0.5 that a cell will be present between $y^* = 0.4$ and 0.5 ($\delta^* < 0.1$). However, for the highest flow ratio, there will always be cells in that region. The shape of the distribution for the Dextran case shows the influence aggregation has on the CDL compared to the PBS case in which aggregation is absent. In the latter case, there are always cells present for $y^* < 0.45$ (i.e. $\delta^* < 0.05$) and this does not change significantly as the flow ratio changes.

The roughness of the CDL is an important parameter as it will affect the temporal

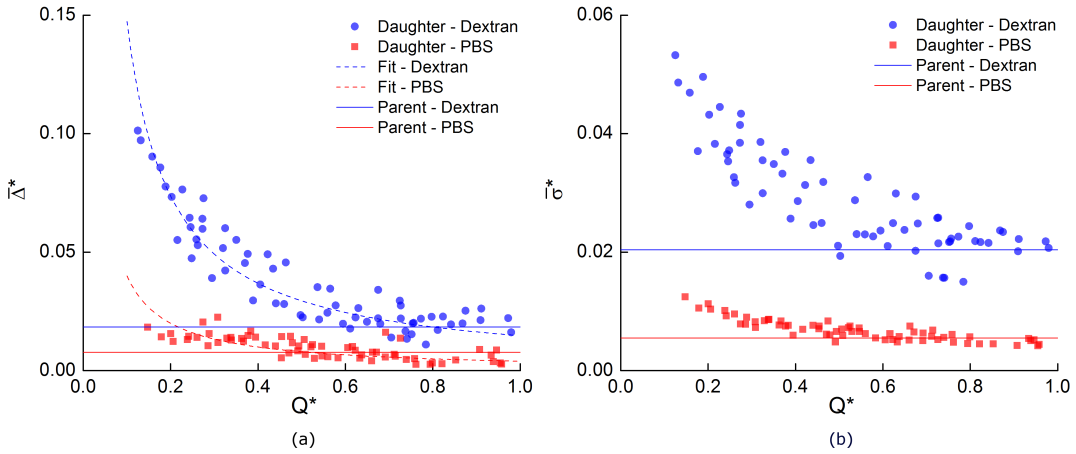

Figure 3.11: Effect of flow ratio on CDL characteristics. Solid lines represent mean values in parent branch. (a) $\overline{\Delta^*}$, dashed lines show fits to 3.1. Solid lines show average value in parent branch. (b) $\overline{\sigma^*}$, solid lines show average value in parent branch.

characteristics and magnitude of the shear stress developed at the wall, therefore it is prudent to consider how the width of the CDL affects its roughness; this was quantified using the axially (x) averaged (in the ROI) temporal SD of the CDL, normalised with respect to the channel width such that $\sigma^* = \sigma/w$ as shown in Figure 3.10 for the daughter and parent branches. The bar symbols on $\overline{\Delta^*}$ and $\overline{\sigma^*}$ are used to indicate values averaged in the lateral (y) direction to give a mean value for each Q^*. Although the distributions are strongly non-normal, the SD and mean CDL are commonly used to consider the characteristics of the CDL and so are utilised here. The inset in Figure 3.10 shows the values in the parent branch, considered to be the steady state results. As $\overline{\Delta^*}$ increases, the roughness, $\overline{\sigma^*}$, in the PBS case increases only slightly in contrast to the Dextran case, in which the roughness increases steadily with the mean width. This trend continues further in the daughter branches as can be seen in Figure 3.10. The spatial SD showed very similar trends (omitted here for brevity), since the temporal and spatial signals are strongly coupled, as can be seen in Figure 3.6.

The impact of the flow ratio on the average width of the CDL is considered in Figure 3.11a. The solid lines show the mean $\overline{\Delta^*}$ in the parent branch. In the Dextran case, $\overline{\Delta^*}$ was roughly doubled in the parent branch from 0.8% to 1.8% of the channel width, although as can be seen in the inset of Figure 3.10, $\overline{\Delta^*}$ was broadly distributed. In the PBS cases, the mean $\overline{\Delta^*}$ increased slightly as the proportion of flow entering the daughter branch decreased. However, for the Dextran case, the mean $\overline{\Delta^*}$ increased

significantly with decreasing Q^*, reaching approximately 10% for low flow ratios. It should be noted that the maximum instantaneous CDL width (or CFL width) was as large as 45% for $Q^* = 0.1$ in the Dextran case. For a given CDL width in the parent branch, $\overline{\Delta^*}_p$, if the cells exactly followed their streamlines, the CDL width in the daughter branch, $\overline{\Delta^*}_d$ would increase in proportion to $1/Q^*$ (assuming two dimensional flow). Deviations from this idealised situation, indicating movement of the cells away from their streamlines, can be accounted for by using a constant of proportionality α. Thus, the data are fit to the equation

$$\overline{\Delta^*}_d = \frac{\alpha \overline{\Delta^*}_p}{Q^*} \tag{3.1}$$

by minimising the mean square error. The coefficient α then indicates the extent of deviation from the idealised situation and was found to be 0.80 and 0.51 for the Dextran and PBS cases respectively. The fits are shown as dashed lines on Figure 3.11a.

Finally, Figure 3.11b shows how the roughness (SD) of the CDL was affected by aggregation and Q^*. It can be seen that the roughness increased as the flow ratio decreased, and that aggregation enhanced this effect significantly.

Having considered these trends in the distribution of the CDL, the corresponding velocity characteristics are analysed in the following section.

3.3 Velocity field

The time-averaged flow fields for 50:50 and 80:20 flow splits are shown in Figure 3.12 for the PBS case. At this scale, the Dextran cases were not qualitatively different and are hence not shown here for brevity. The velocity magnitude at each location is normalised relative to the maximum velocity for each case, to give U^*_{max}. Figures 3.12a and 3.12c show velocity magnitude contour plots for the whole domain. For both flow splits, a blunted parabolic shape can be observed in the parent branch, as would be expected in a high aspect ratio rectangular channel. As the flow enters the bifurcation region, the velocity rapidly decreases toward the stagnation point, which is centrally located for the 50:50 flow split, but offset towards the low flow branch for the 80:20 split. This can be seen more clearly in the vector plots in Figures 3.12b and 3.12d. No flow separation at the vertices of the bifurcation is observed, since the Reynolds number is low ($< 10^{-2}$) and the flow is dominated by viscous effects.

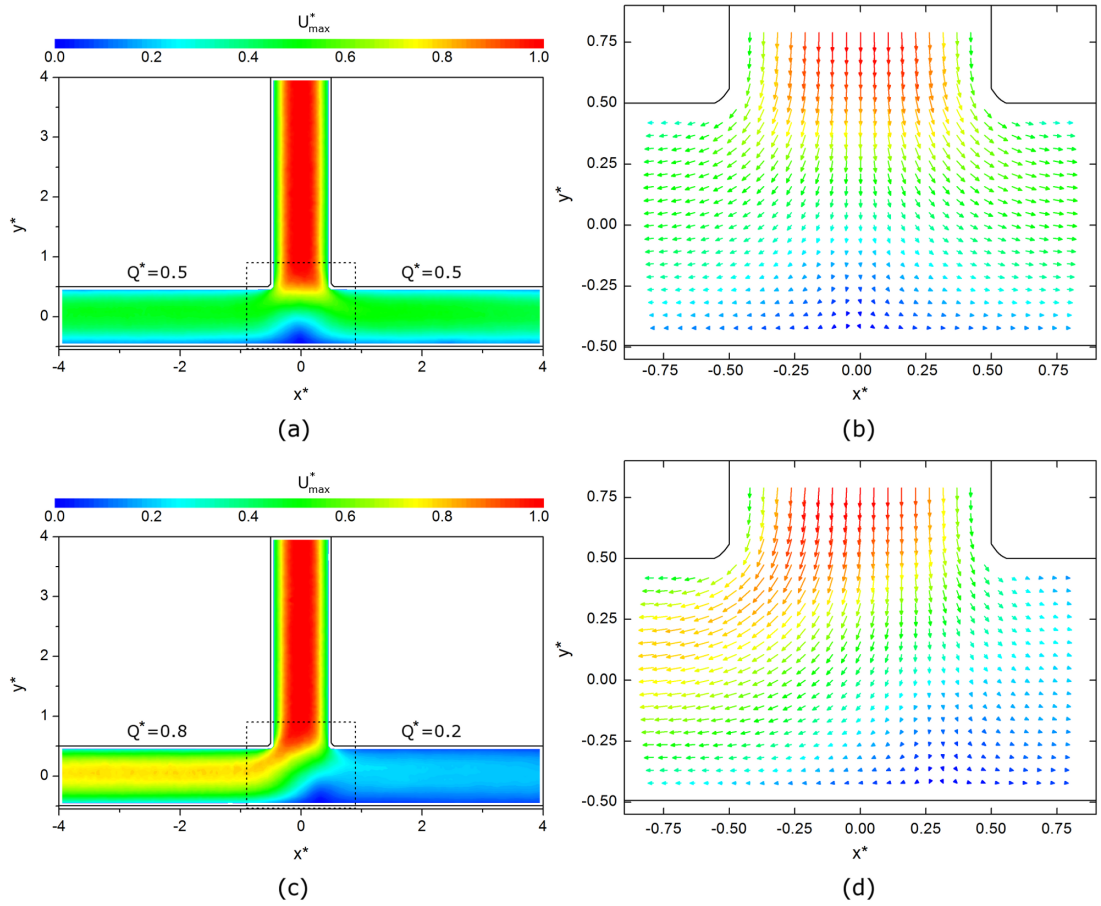

Figure 3.12: (a) and (c) RBC velocity magnitude contour plots obtained from PIV data for 50:50 and 80:20 flow splits, respectively. The dashed lines indicate region shown in (b) and (d): Vector fields in the region immediately around the bifurcation. Every other vector is omitted for clarity.

In the daughter branches, it can be seen that the lateral velocity component rapidly diminishes and a relatively constant velocity distribution is established by around $x^* \pm 1$. Finally, it should be noted that this profile can be observed to be slightly skewed towards the inner wall of the channel for all Q^*.

3.3.1 Velocity Profiles

To consider these distributions more closely, profiles in the parent branch and at low, medium and high flow ratios in the daughter branch are compared in Figure 3.13. Figure 3.13a shows velocity profiles in the parent branch for Dextran (blue) and PBS (red) cases, and compares these to the analytical solution for a Newtonian fluid (grey line, from Equation 1.10). The profiles are defined by averaging along the ROI and are normalised by their mean value ($\overline{U}$), which is calculated using trapezoidal integration

assuming zero velocity at the wall and a spline fit to interpolate the missing vectors near the wall. Hence, $U^* = U/\overline{U}$ (U^* is also used in the parent branch for simplicity, even though it is technically the v component of the velocity).

The circles in Figure 3.13 show the magnitude of the average velocity vectors and the error bars (which in this case are so small as to be covered by the circles in Figure 3.13a) represent one SD. The solid lines which coincide with the dots are fourth order polynomial fits to the data, added for clarity. It can be seen that the Dextran case is blunter than the PBS case. That is to say, U^* in the middle of the channel is reduced, while U^* close to the edges of the channel is increased. However, it should be noted that neither of the experimental profiles are as blunt as the analytical solution. The observation that aggregation blunts the velocity profile, is in line with those made by many other researchers (Bishop et al., 2001a; Reinke et al., 1987). However, it is expected that the profile would be more blunt than for the analytical solution, which is not the case. It should be noted that normalising by the average velocity requires assumptions about the RBC velocity at the walls, i.e. it is assumed that the no-slip condition exists. In reality this is not the case. Consider the argument made regarding the location of an RBC barycentre compared to the vessel wall. Except in the case where an RBC was adhered to the vessel wall (which was not observed in the present data), an RBC cannot have a zero velocity at the wall and a non-zero velocity elsewhere. As the RBCs are finite in size, and have a diameter comparable to the channel width (around one order of magnitude lower) one would not expect to observe a zero velocity at the wall. For a smaller channel, one would expect this effect to be enhanced. Unfortunately, due to the design of the system requiring pressure, rather than flow, control a direct measurement of the flow rate, which could be used to analyse the near wall velocity assumption, was not possible. This will be considered further in Chapter 5 (which uses a smaller diameter channel).

Figure 3.13b compares the velocity profiles for the daughter branch at a high flow ratio. It can be seen that both velocity profiles are skewed towards positive y^*, i.e. the inner wall of the daughter branch. In order to quantify the extent of skewing, a skewness parameter is defined. This is taken as the normalised distance from the channel centreline that the maximum velocity is located as a percentage. Mathematically,

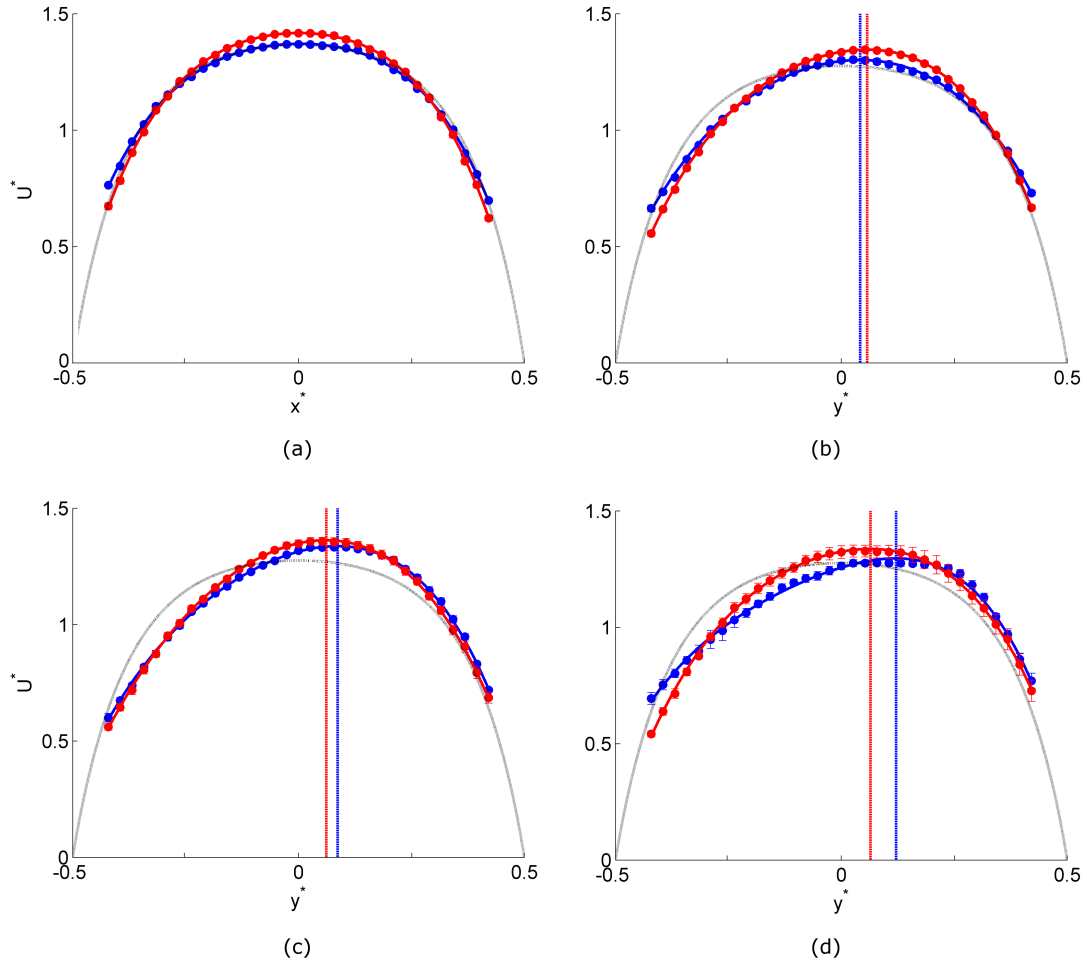

Figure 3.13: Sample normalised RBC velocity profiles. Grey line shows analytical solution for a Newtonian fluid according to Equation 1.10. Blue is Dextran case, Red is PBS case. (a) Parent branch (b) $Q^* = 0.80$, (c) $Q^* = 0.47$, (d) $Q^* = 0.22$.

$$S^* = y^*|_{u_{max}} \times 100\% \tag{3.2}$$

The velocity profile is first interpolated (using spline interpolation) to give 1000 points in the y coordinate across the channel, which increases the resolution of the skewness parameter. The value of $y^*|_{u_{max}}$ for each profile is indicated on the figures by the dashed vertical lines. In Figure 3.13b, the skewness for the Dextran and PBS cases are 4.2 and 5.7 % respectively. In this case, the PBS profile is slightly more skewed than the Dextran one. However, caution should be exercised in drawing conclusions from individual cases due to the inherent scatter in the data. It can also be seen that, as in the parent branch, the Dextran profile is significantly blunter than the PBS one. At an

almost equal flow ratio, as shown in Figure 3.13c, the profiles are skewed further. In this case, the Dextran case is more skewed at 8.7% than the PBS case at 6.2%. The profiles are also slightly less blunt, that is to say that their maximum U^* is slightly greater. Figure 3.13d shows profiles for low flow ratios. It can be seen that the velocity profile for the Dextran case is considerably more skewed than both the PBS case and for Dextran cases at higher flow ratios. Additionally, the profiles are blunter than they were for $Q^* = 0.47$.

In order to better understand the overall effect of aggregation and flow ratio parametrically, the bluntess and skewness of the profiles are considered in the next section.

3.3.2 Effects of flow ratio

Before discussing how the skewness changes as a function of the flow ratio, the presence of the skewness in itself should first be considered. For a Newtonian fluid, in a planar geometry there would be two velocity components in the immediate vicinity of a bifurcation which are non-zero, but one would expect the velocity profile to recover rapidly. For a non-Newtonian fluid the situation is less intuitive, but one could still expect a relatively rapid recovery of symmetry for the velocity profile. Indeed, some authors quote an expected distance of approximately one channel diameter for symmetry of the velocity profile to recover in blood flow (Cokelet, 1999). This value would be geometry dependent. In order to quantify this, some simple CFD simulations were carried out.

A model of the imaging area of the microchannel was created and meshed with elements of $4 \times 4 \times 4\mu m$. The branch lengths were extended to $10w$ in order to avoid boundary effects. The commercially available CFD package ANSYS CFX 13.0 (ANSYS, UK) was used to solve the Navier-Stokes equations for a laminar, continuous fluid in the geometry. Convergence was considered when all residuals were below 10^{-5}. Constant velocity input and a number of different constant pressure outputs were applied such that a range of flow ratios were considered for a single parent branch pressure. Both Newtonian ($\mu = 3.5mPa\ s$) and non-Newtonian fluid models were utilised. For the non-Newtonian model, a Carreau-Yasuda fluid was utilised, wherein the viscosity is defined according to

$$\frac{\mu - \mu_\infty}{\mu_z - \mu_\infty} = [1 + (\lambda\dot{\gamma})^a]^{(n-1)/a} \tag{3.3}$$

where μ_∞ is the infinity shear viscosity, μ_z is the zero shear viscosity, λ is a time constant, n is a power law index and a is the 'Yasuda exponent'. The values of the parameters used here are those applied by Gijsen et al. (1999).

In order to confirm that the mesh was sufficiently fine, the profile in the centre plane of the parent branch prior to the bifurcation was compared to the analytical solutions. The mean difference was found to be 0.88 %, implying that the mesh was suitable.

These simulations showed that for both fluids, symmetry and one-dimensional flow (i.e. $v = w = 0$) were recovered within around one to one and a half channel widths. While the velocity profile reached a relatively steady shape in a similar distance in the experimental data, the skewness persisted downstream. Thus, it is clear that the skewness observed in the velocity profiles of the RBCs in Figures 3.13b-d is predominantly a result of the two-phase nature of the flow and not the shear-dependent characteristics of blood. This will be considered further in Chapter 4.

Figure 3.14 shows how the skewness parameter varies with flow ratio for both the aggregating and non-aggregating cases. Note only the daughter branches are considered here as the parent branch velocity profiles were not skewed. Hypothetically, at $Q^* = 1$, wherein all of the flow enters a single daughter branch, the geometry acts as a simple corner, and the skewness should be small. This can be observed in both the Dextran and PBS cases in Figure 3.14. As the flow ratio decreases towards $Q^* = 0.5$, the skewness increases. The value $Q^* = 0.5$ is a significant point, as it separates the 'high flow' from the 'low flow' daughter branch. In the high flow branch, this trend of increasing skewness with flow ratio is highly significant ($P < 10^{-6}$). In the low flow daughter branch, the data is significantly more scattered, and there is no significant trend ($P > 0.5$), although the skewness is clearly greater for the Dextran than the PBS case. By observation, it could be proposed that the Dextran trend continues to increase while the PBS case decreases slightly as the flow ratio decreases below $Q^* = 0.5$, but more data points would be required to prove statistical significance in this relationship. This trend will be considered in further detail later in this chapter and in Chapter 4.

Also observed in Figure 3.13 is the fact that the bluntness varied as a result of both Dextran-induced RBC aggregation and flow ratio. A simple bluntness parameter can

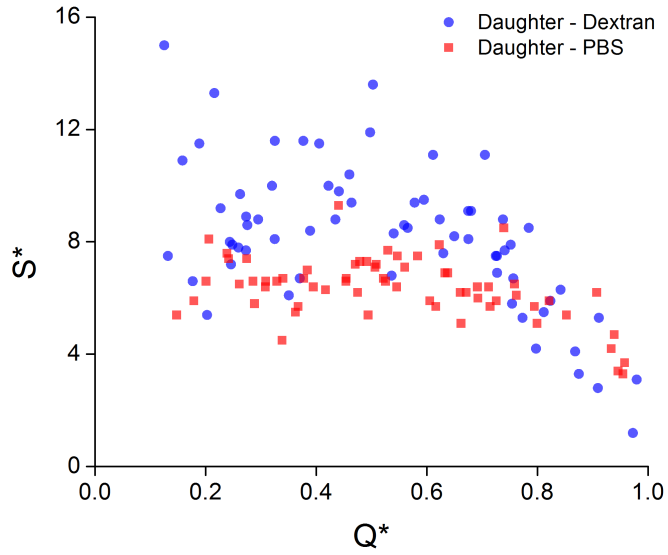

Figure 3.14: S^* against Q^* for Dextran and PBS cases.

be defined as the ratio of the mean to the maximum velocity:

$$B = \frac{\bar{U}}{U_{max}} \tag{3.4}$$

For Poiseuille flow, the bluntness would be $B = 0.5$, as the maximum velocity is twice the mean, while at $B = 1$, the maximum and mean velocities would be equal, indicating plug flow. As can be seen in Figure 3.13a, the maximum U^* (relative to the mean) is lower for the Dextran case than for the PBS case. Hence, the ratio of the mean to the maximum would be larger in this case. As mentioned previously, in order to calculate the mean velocity, the no-slip condition must be assumed at the walls. Such an assumption may introduce errors, but is necessary for this analysis to be applied. In order to provide a slightly more intuitive description of the bluntness, the values are normalised relative to the ratio of mean to maximum velocity in the centre plane for the analytical solution. Hence,

$$B^* = \frac{B}{B_N} \tag{3.5}$$

Where B_N is the bluntness for the analytical solution for a Newtonian fluid (and is hence geometry dependent). The bluntness, B^*, of the velocity profiles measured for different flow ratios is considered in Figure 3.15.

Data for $Q^* < 0.1$ are omitted, as the flux was not sufficient to obtain representative time averaged data. Additionally, outliers, considered as values more than two standard

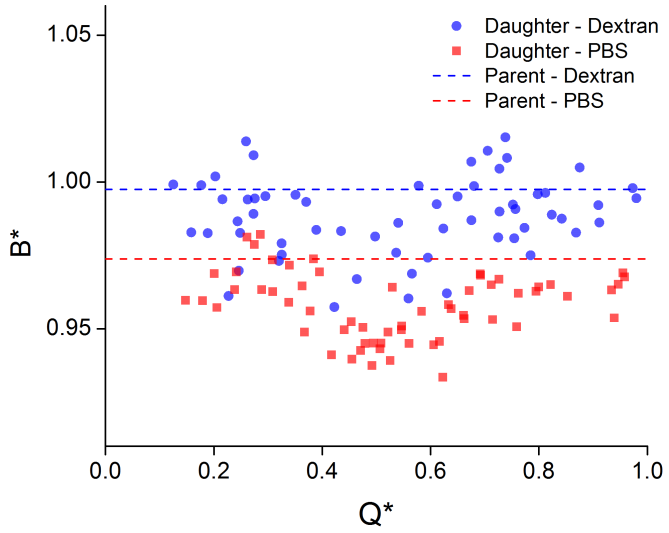

Figure 3.15: B^* against Q^* for Dextran and PBS cases. Dashed lines show mean values in parent branch.

deviations from the mean, were removed. The average bluntness in the parent branch for each case is indicated by a dashed line. For the Dextran case, the bluntness is not significantly different from the one for a Newtonian fluid (i.e. $B^* \approx 1$); however, for the PBS case the profiles are sharper (less blunt $B^* < 1$). Overall, it can be seen that the bluntness in the daughter branches is greater in the Dextran case.

Considering the bluntness in the daughter branch, at $Q^* = 1$, one would expect B^* to be equivalent to the parent branch, as the effective geometry becomes a simple $90°$ corner and, in the absence of inertia, the profile in the high flow daughter branch should therefore be close to that of the parent branch. This seems to be the case for both Dextran and PBS cases. Figure 3.15 illustrates that in the low flow branch ($Q^* < 0.5$), the bluntness decreased with increasing Q^*, while in the high flow branch ($Q^* > 0.5$) the bluntness increased with increasing Q^*, i.e. the opposite relationship was observed in the two branches. As $Q^* = 0.5$ indicates the transition from high to low flow branch, and due to the symmetry and clear trends observed in Figure 3.15, the data will be henceforth analysed in terms of whether they are greater or less than $Q^* = 0.5$. Using this approach, the significance of the observed trends can be considered using the probability that the correlation coefficient is insignificant, P, as summarised in table 3.1. For the PBS case, the trends are very significant. For the Dextran case, the P-value is just slightly above the often used significance value of 0.05, but is close enough to be considered significant.

Table 3.1: Probability that the correlation coefficient is insignificant, P, for bluntness, B^*, corresponding to Figure 3.15 and skewness, S^*, corresponding to Figure 3.14.

	$B^*, Q^* < 0.5$	$B^*, Q^* > 0.5$	$S^*, Q^* < 0.5$	$S^*, Q^* > 0.5$
Dextran case	0.0546	0.0524	0.7395	$< 10^{-6}$
PBS case	0.0003	0.0001	0.6533	$< 10^{-6}$

3.4 Mathematical Modelling

In this section a mathematical model is derived to investigate the hypothesis that the presence of the CDL on one side of the channel creates a region of low viscosity near the wall which is responsible for the skewed profiles discussed above. The model is also used to investigate the impact on wall shear stress (WSS) and resistance to flow. A simple two-fluid mathematical model is employed, assuming two dimensional flow of two immiscible fluids running parallel to one another between two fixed walls, as indicated in Figure 3.16. The fluid between $y = 0$ and δ^* represents the CDL, in which the viscosity will be that of the suspending medium, i.e. $\mu_\delta = \mu_0$. The second phase, the RBC core, lies in the region $\delta \leq y \leq w$. The viscosity of the RBC core can be defined in terms of the relative viscosity $\mu_c = \mu_r \mu_0 = \mu_r \mu_\delta$.

Full derivation of the model can be found in the appendix. After normalising and solving the Navier-Stokes equations, the non-dimensional velocities of the fluid in the CDL and RBC core are described by:

$$u_\delta{}^* = 6\left(My^* - y^{*2}\right) \tag{3.6}$$

$$u_c{}^* = \frac{6}{\mu_r}\left(My^* - y^{*2} + 1 - M\right) \tag{3.7}$$

where

$$M = \frac{\delta^{*2}\left(\mu_r - 1\right) + 1}{\delta^*\left(\mu_r - 1\right) + 1} \tag{3.8}$$

The skewness S^*, as defined in equation 3.2 for the experimental data is given by

$$S^* = \frac{1}{2}\left(1 - M\right) \tag{3.9}$$

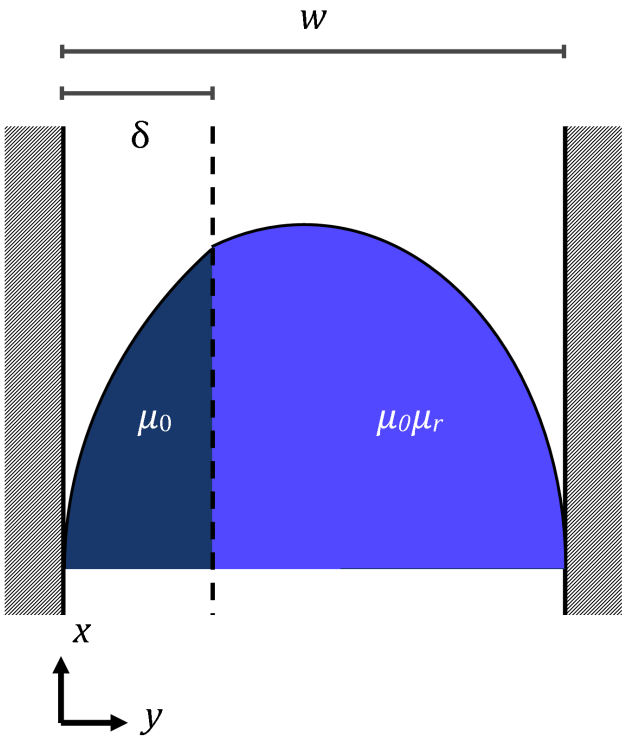

Figure 3.16: Schematic of the model to be solved analytically.

As the relative viscosity must always be greater than or equal to one, and the CDL width must be positive, M will be equal to one if $\delta = 0$, or $\mu_r = 1$, and less than one otherwise (see Equation 3.8). As a result, the velocity profile would always be skewed in the direction of the CDL. It should be noted that this analysis is based on the assumption of a one sided CDL. In the presence of a CDL on either side, the profile would be skewed towards the widest CDL. The skewness is plotted as a function of CDL width for three different core viscosities in Figure 3.17.

It can be seen that the skewness increases in response to the relative viscosity of the core increasing. As this would happen with increasing haematocrit, the figure implies that the effect of the CDL on the skewness of the velocity profile would be increased as the haematocrit increased. However, it has been noted that the CDL width tends to be decreased in the presence of high haematocrit (Kim et al., 2009). For all relative viscosities compared in Figure 3.17, the maximum skewness occurs for δ^* between 0.3 and 0.4, and the value of maximum skewness decreases as the relative viscosity increases.

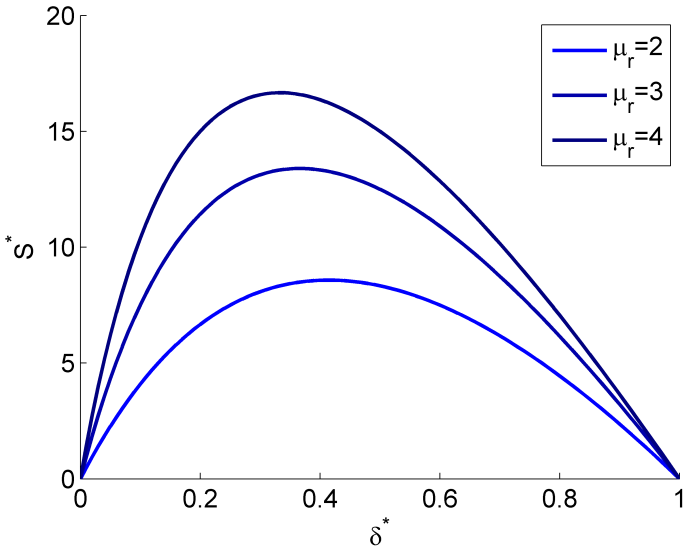

Figure 3.17: Skewness predicted by the mathematical model as a function of CDL width for three different core viscosities.

3.4.1 Wall shear stress

It is also interesting to consider how the skewing of the velocity profile would affect the WSS on each of the walls. The WSS is given by the product of the viscosity and the shear rate acting at the wall:

$$\tau = \mu \frac{du}{dy} \tag{3.10}$$

For the present model, the WSS acting on the wall coincident with the CDL is given by (see appendix)

$$\tau_\delta^* = M \tag{3.11}$$

where the WSS for the suspending medium only case is used for the purposes of normalisation. On the opposite wall, the normalised WSS is given by

$$\tau_c^* = 2 - M \tag{3.12}$$

As discussed earlier, $\delta^* < 1$, so $\delta^{*2} < \delta^*$, and hence $M \leq 1$. This means that the shear stress on the wall with highest viscosity will always be lower than for that of the suspending medium. However, the shear stress on the opposite wall will increase by the same proportion. This is a necessary condition given that the normalisation procedure

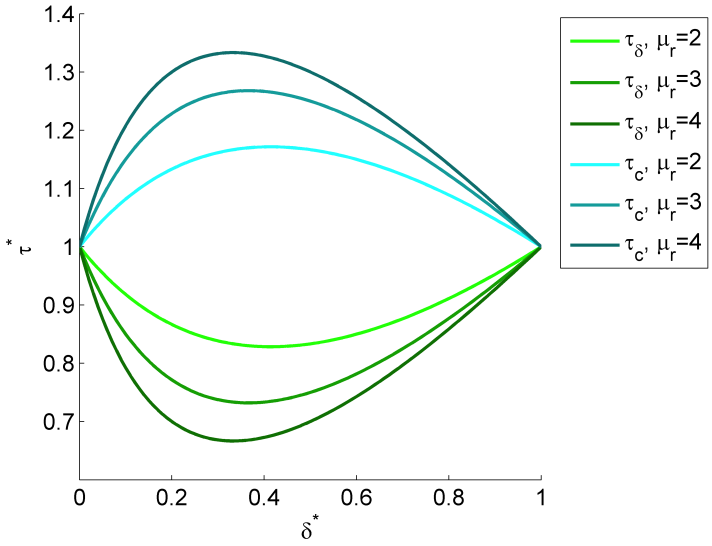

Figure 3.18: Normalised WSS predicted by the mathematical model as a function of CDL width for three different core viscosities.

defines a constant pressure drop. Thus, the net effect of the skewing on the WSS is zero, but certain regions are elevated while others are reduced.

Figure 3.18 shows how the WSS changes as a function of the CDL width for a range of different values of relative viscosity, which could be considered to scale with haematocrit. The WSS on the wall coincident with the CDL (τ_δ^*) is decreased in all cases, but is increased on the opposite wall (τ_c^*) for all core viscosities. The conclusion is that in the CDL, the increase in shear always has a smaller effect on the WSS than the reduction in viscosity (relative to the core). Conversely, on the opposite wall, the higher viscosity overrides the reduction in shear rate, resulting in an increased WSS, by as much as 30% for a relative core viscosity of 4. The shape of the curves is similar to that observed in Figure 3.17.

3.4.2 Apparent viscosity

The apparent viscosity of a fluid represents the viscosity of a Newtonian fluid that would give the same flow rate for a given pressure drop. Commonly in haemodynamics, the assumptions of fully developed, steady flow in a long straight tube of circular cross section are made, and hence the Hagen-Poiseuille equation can be used to calculate a viscosity which can be compared with an average for the more complex system. For the flow between two plates a width w apart, the apparent viscosity for a non-uniform viscosity fluid is given by

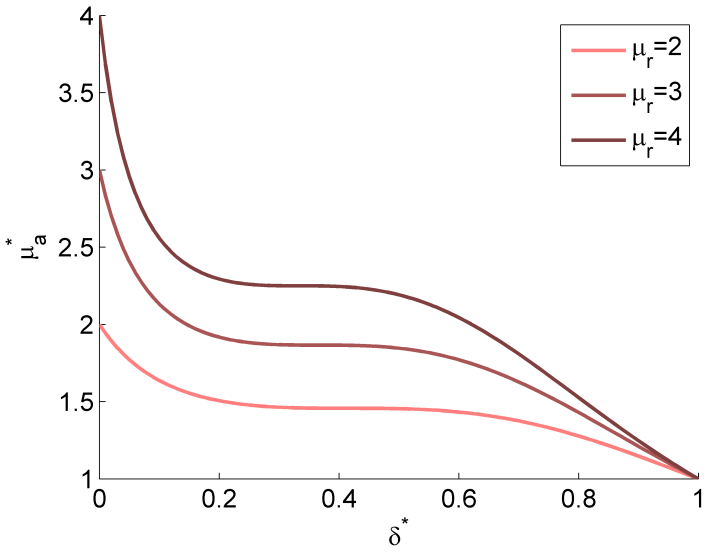

Figure 3.19: Apparent viscosity predicted by the mathematical model as a function of CDL width for three different core viscosities.

$$\mu_a = \frac{w^2}{12\overline{u}} \frac{\Delta p}{L} \tag{3.13}$$

For the present model, the non-dimensional relative apparent viscosity is given by

$$\mu_a^* = \mu_r \left(M^2 \left(\delta^* \left(\mu_r - 1 \right) + 1 \right) - 4M \left(1 - \delta^* \right) + 4 \left(1 - \delta^* \right) \right)^{-1} \tag{3.14}$$

If $\mu_r = 1$, $M = 1$, and thus $\mu_a^* = 1$. If there is no CDL, $\delta^* = 0$, so $M = 1$ and $\mu_a^* = \mu_r$. Figure 3.19 shows how the cell-depleted layer width affects the relative apparent viscosity for a range of relative core viscosities. It can be seen that the relative viscosity is rapidly reduced as the CDL width increases from 0 to 0.2, changes relatively little as the CDL width increases from 0.2 to 0.6, then reduces to 1 as the CDL approaches the entire channel width. The overall magnitude of the relative apparent viscosity increases with the relative viscosity of the core.

3.4.3 Link to experimental data

The preceding mathematical analysis has considered the effect of core viscosity and CDL width on various parameters describing the flow. However, in doing so, the relationships have assumed that μ_r and δ^* are independent parameters. However, for a given tube/channel haematocrit, as the CDL width increases, the haematocrit in the core, and hence the viscosity, must increase. Analytically, it is not possible to directly

convert the haematocrit into the viscosity, but a number of empirical relationships have been reported. Here, the model defined by Pries et al. (1992b) is utilised (see Equation 1.18). In their paper, values of E and F were tabulated for various haematocrit ranges and tube diameters. For the present study, data corresponding to the hydraulic diameter of the channel ($57\mu m$) was selected, which were acquired by Bayliss (1952). The data were acquired for haematocrits between 0.05 and 0.9 in a cylindrical tube of diameter $55\mu m$ and E and F were found to be 3.54 and -0.743 respectively. The R^2 for this particular set was 1.000 (Pries et al., 1992b). Thus

$$\mu_r = 1 + 3.54\left((1-H)^{-0.743} + 1\right) \tag{3.15}$$

Now, given that the channel haematocrit, H_C must be constant, it can be stated that

$$H_C = H\left(1 - \delta^*\right) \tag{3.16}$$

Hence, equation 3.15 can be written in terms of H_C and δ^* as

$$\mu_r = 1 + 3.54\left(\left(1 - \frac{H_C}{1-\delta^*}\right)^{-0.743} + 1\right) \tag{3.17}$$

One can consider the results in terms of the flow ratio using equation 3.17, with δ^* defined based on equation 3.1, noting that δ^* is considered to be constant in this model, hence $\delta^* = \overline{\Delta^*}$. Figure 3.20 shows sample velocity profiles calculated for flow ratios of 0.1 and 0.5, for Dextran and PBS cases (defined according to the parameters fit to equation 3.1 and 3.17). It should be noted that the effect of aggregation is considered here to only through the CDL width.

Note that the coordinate system is inverted in order to aid comparison with Figure 3.13. At both flow ratios considered, the profiles are skewed towards the CDL. The light vertical lines indicate the skewness, similarly to Figures 3.13b-d, while the vertical dashed lines show the CDL boundary. It can be seen that in the CDL region, the velocity is almost linear, and at the interface, there is a sudden increase in the velocity gradient in the CDL. The profiles are skewed towards the CDL in both cases. Comparing Figures 3.20a and b with Figures 3.13d and c respectively, it seems that the mathematical model predicts the skewness of the profiles qualitatively. It should be noted that since the

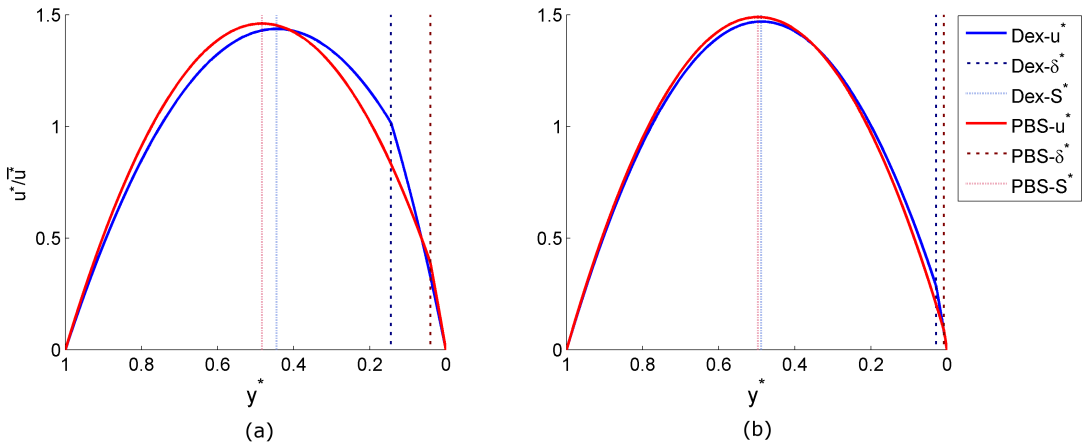

Figure 3.20: Velocity profiles calculated from the mathematical model. (a) $Q^* = 0.1$, (b) $Q^* = 0.5$.

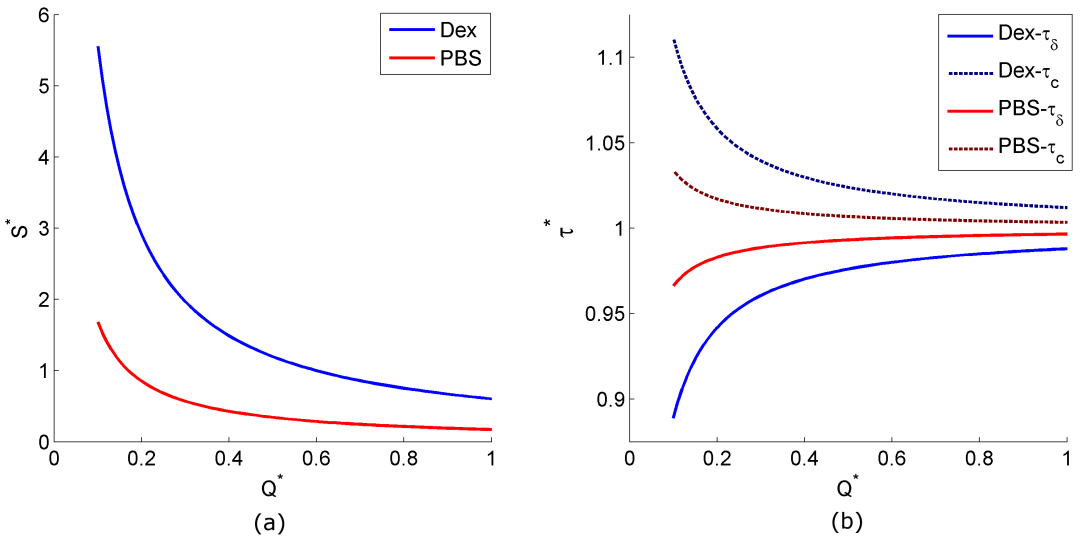

Figure 3.21: (a) Skewness and (b) normalised WSS, as a function of Q^* with δ defined from experimental data and core viscosity predicted from empirical data.

model assumed an infinite z distance, it was not capable of reproducing the bluntness which occurs in high-aspect ratio rectangular channels.

Figure 3.21 shows how the model predicts the skewness of the velocity profiles as a function of the flow ratio. It can be seen that for both the aggregating and non-aggregating cases the general observation that the skewness increases with decreasing flow ratio can be made. However, it is clear that the skewness is under-predicted compared with Figure 3.14. This suggests that the two-fluid model, while describing the general characteristics, is not sufficient to fully capture the observed trends.

Nonetheless, it is interesting to observe how the model predicts the changes in WSS

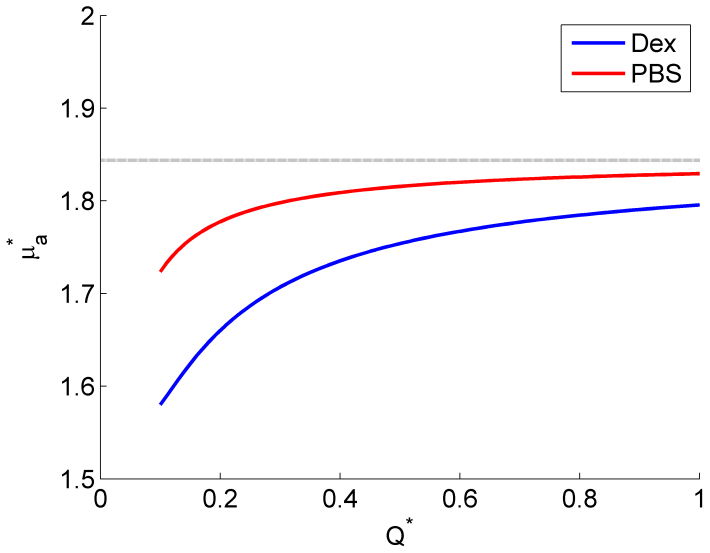

Figure 3.22: Apparent viscosity as a function of Q^* with δ defined from experimental data and core viscosity predicted from empirical data. Dashed black line indicates the case for which the CDL width is zero.

compared to the flow ratio. This is shown in Figure 3.21b. It can be seen that the WSS in the CDL decreases at lower flow ratio, and that the magnitude of the change in WSS is more than doubled in the presence of aggregation. The inverse is observed on the opposite wall.

Finally, the effect of the CDL on apparent viscosity is considered in Figure 3.22. The dashed black line shows the apparent viscosity for the case of no CDL. It can be seen that despite the zero net change in WSS, the apparent viscosity is significantly reduced by the presence of the CDL. Whereas this relationship may be intuitive for the standard consideration of axisymmetric flow, it was not previously clear how a single sided CDL would affect the apparent viscosity. It is worth noting that plasma skimming has not been considered in this analysis. If it were, the apparent viscosity would be decreased for $Q^* < 0.5$ and increased for $Q^* > 0.5$. This will be discussed further in Chapter 4.

3.5 Discussion

3.5.1 Velocity Profiles

Two key results reported above are the effect of flow ratio on the velocity profiles and CDL characteristics, and the amplifying effect of aggregation. From the images shown in Figure 3.2, it is clear that there is aggregation present in the Dextran case and that

the cells are not aggregated in the PBS case. Therefore the following discussion will treat the Dextran case and the presence of aggregation as synonymous. In the CFD simulations, for both Newtonian and Carreau-Yasuda viscosity models, the skewness was zero within one and a half channel widths of the bifurcation region for all flow ratios. While the velocity profile reached a steady shape in a similar distance in the experimental data, the skewness persisted downstream. Thus it is clear that the skewness observed in the velocity profiles of the RBCs in Figures 3.13b-d and summarised in Figure 3.14 is predominantly a result of the two-phase nature of the flow and not the shear-dependent characteristics of blood. The presence of the CDL results in reduced viscosity near the inner wall of the daughter branch, which skews the velocity profiles towards the CDL. The profiles shown in Figure 3.20 confirmed this assertion. This suggests that the existence of the CDL may be responsible for the observed skewness. This assertion was supported by the mathematical modelling, but the extent of skewing predicted by the model was not as extensive as those observed experimentally.

Das et al. (1998) showed that skewed viscosity profiles can result in skewed velocity profiles. Leble et al. (2011) recently reported a comparison of simulated Newtonian flow through a Y-bifurcation with particle tracking velocimetry (PTV) data from labelled RBCs. They observed similar profiles in both cases and the skewness appeared to diminish rapidly after the bifurcation. However, the flow rate was higher ($12\mu l/hr$) and the haematocrit was lower (0.14) in their study compared to the data reported here. It is also not clear whether the resolution in their velocity measurements was sufficient to pick up the subtle skewing observed here, which would likely be reduced in their Y-bifurcation geometry.

It is also apparent from the results in Figures 3.14 and 3.15 that aggregation had an influence on both the bluntness and skewness in the daughter branches. Aggregation increased the bluntness of the velocity profile by approximately 2.5% in the parent branch compared to the PBS case ($P < 0.0001$ from two-tailed *t*-test), and this trend continued for all flow ratios in the daughter branches. The skewness was also increased by a larger proportion in the Dextran samples for the lowest flow ratios (Figure 3.14). Nevertheless, the difference between PBS and Dextran samples appears not to be as large as might be expected, which can be attributed to specific characteristics of the flow studied here. All experiments were conducted at steady state and intermediate

flow rates, resulting at moderate pseudoshear rates, $\overline{\gamma}$, where aggregation dynamics are expected to be relatively suppressed. The pseudoshear rates in the parent branch for the present study were $\approx 6.25s^{-1}$ and decreased to $\approx 0.625s^{-1}$ in the daughter branch at the lowest Q^* studied. As the velocity fields in Figure 3.12 and the bluntness and skewness results in Figures 3.14 and 3.15 imply, the in-plane shear rate distribution in the flow would have been altered in the daughter branches. Effective shear distribution was not quantified in the present study as important information on the out of plane shearing field was not available; it is expected however, that the out of plane shear would be greater than the in-plane shear throughout the majority of the flow field. Additionally, the regions of highest in-plane shear would be at the channel walls, where the local haematocrit is generally low. Hence, the pseudoshear rates are probably sufficient to characterise the effective shear. These low pseudoshear rates would suggest that there would be significant aggregation occurring in the domain. However, the transit time of the RBCs/aggregates flowing from the parent to the daughter branches was relatively small. Aggregation is a time dependent phenomenon, with a half time of the order of 5 seconds for normal blood samples (Cokelet, 1980; Kaliviotis & Yianneskis, 2008). The distance travelled along the daughter branches was approximately $0.35mm$ and the average velocity in the parent branch was around $0.25mm/s$. Thus, as the flow ratio decreases, the transit time in the daughter branches increases from roughly 1.5 to 15 seconds. For low Q^*, and hence at the upper extreme of the transition times, it is expected that some aggregation may have occurred during data acquisition. However, from the present results it seems that, if present, this aggregation did not have sufficient time to significantly influence the velocity field.

3.5.2 Cell-Depleted Layer

The increase in mean CDL thickness observed in the parent branch in the presence of aggregation is in agreement with previous studies (Bishop et al., 2001a; Cokelet, 1980; Reinke et al., 1987; Alonso et al., 1995; Kim et al., 2007; Ong et al., 2010). Additionally, a number of studies have reported that at low flow rates there was a greater degree of CDL roughness in the presence of aggregation (Alonso et al., 1995; Ong et al., 2010; Namgung et al., 2011). The results shown in Figures 3.10 and 3.11b are in agreement with this result, in that the roughness was significantly greater for the

Dextran case. Considering Figure 3.2, it can be seen why this might be the case, as deviations in the edge of the CDL are much greater for aggregates than for individual cells. This significantly increased roughness would result in increased viscous dissipation, offsetting the reduction in flow resistance which the CDL might provide (Sharan & Popel, 2001). Furthermore, the increased CDL roughness may increase the WSS by intermittently increasing the velocity gradient at the wall (Namgung et al., 2011). Considering the skewed CDL distributions shown in Figures 3.8 and 3.9, the deviations from the mean value would be more frequent towards the wall and hence there would be a net increase in WSS. This effect may be somewhat attenuated, however, for the largest CDL widths observed for the Dextran case at low Q^*, as increased symmetry was observed in the distribution of Δ^* for these cases.

It was observed in Figure 3.7 that the probability distributions of δ^* were generally skewed towards the wall and the modal value only moved away from the wall in the presence of aggregation in the low flow branch. The positive skewness and the wider distributions caused by aggregation are in agreement with Ong et al. (2010) although in their study, the modal width was always away from the wall. This skewed distribution was also observed in the simulations of Fedosov et al. (2010b). Previous studies have only considered this distribution in straight vessel sections and the effect of flow ratio has not been investigated (with the exception of the recent paper by (Ong et al., 2012) who reported CFL distribution in a bifurcation*in vivo*.). The significant change in the shape of the distribution for low flow ratios when aggregation is present, shown in Figure 3.11, highlights the effect aggregation can have on the flow field. A simple fit based on the expected distribution of cells on either side of the separating streamline was applied to Figure 3.11a. The calculated values of the scaling parameter α were found to be 0.80 and 0.51 for aggregating and non-aggregating cases respectively. If α was equal to one, it would suggest that the CDL in the parent branch was uniformly stretched across the daughter branch, whilst values smaller than one would suggest that the cells deviate from their streamlines and impinge upon the layer. The α values reported above suggest that in the aggregating cases the cells followed their streamlines fairly well, whereas for non-aggregating cases interactions between the cells resulted in a CDL width of approximately half that which would exist in the absence of cell-cell collisions. The development of larger structures in the aggregating flow reduces their

freedom to move. This explanation is in agreement with Bishop et al. (2002), who found a slight decrease in the RMS deviation of cells in the presence of aggregation *in vivo*. The shape of the CDL probability distributions shown in Figure 3.7 for low flow ratios further supports this hypothesis. For $Q^* = 0.1$, as the flow exited the bifurcation, the CDL width rapidly increased, as it would if $\alpha = 1$. In the absence of aggregation, the distribution tends rapidly towards the vessel wall, as cell-cell interactions result in increasing impingement upon the CDL and thus depletion of its width. In the case of aggregation, the width remains relatively constant as the aggregates have less freedom of movement than individual cells. These data suggest that in the absence of aggregation, within complex geometries, CDL formation is attenuated by interactions between cells, but when the cells are aggregated, the restricted movement allows a large CDL of varying width to form. This phenomenon could potentially be used to enhance phase separation in microfluidic devices designed to extract plasma from whole blood.

3.5.3 Two-fluid analytical model

In order to investigate the skewed profiles and the effect of the CDL, a simple mathematical model was derived, based on two phases: the plasma and a RBC core of constant viscosity. Such an approach has been used for a range of different applications (Cokelet & Goldsmith, 1991; Doddi & Bagchi, 2009; Fenton et al., 1985; Sharan & Popel, 2001) but to the authors knowledge, there has been no published report of what happens when the distribution is not axisymmetric. The model provided analytical equations for the skewness, wall shear and apparent viscosity. Combining the model with experimental data for the CDL width and an empirical model for the viscosity of the core allowed for consideration of the skewness, wall shear and apparent viscosity with respect to the flow ratio or CDL width.

The skewness was under-predicted by the model by approximately 50%. However, the general trends of increasing skewness with decreasing flow ratio, and enhanced skewness as a result of aggregation (indirectly via the CDL width), were observed. The results suggested that the WSS could be described by the parameter M (Equation 3.8), which also defined the skewness. In simple terms, as the skewness increased, the WSS increased on the wall adjacent to the RBC core (i.e. opposite the CDL), as a result of the increased viscosity in that location.

For the present data, the CDL was only present (to a significant level) along the inner wall of the daughter branches. A similar asymmetry was observed by Ishikawa et al. (2011) in a Y-bifurcation. Alonso et al. (1995) found that the significant asymmetry in CDL width, which occurred in their study as a result of sedimentation, increased the effective viscosity. The results of the mathematical model, however, suggested that the presence of the CDL decreased the apparent viscosity of the fluid, despite the increased viscosity of the RBC core. As mentioned before, the distribution shown in Figure 3.19 would be more extreme if plasma skimming was considered. The effect of non-uniform haematocrit distribution on viscosity will be considered further in subsequent chapters.

Unsurprisingly, it seems that a two phase model is not suitable for capturing all of the characteristics of the flow. A similar conclusion was drawn for axisymmetric flow in previous studies (Das et al., 2007; Doddi & Bagchi, 2009). However, the analysis was useful in verifying how the spatial viscosity distribution could strongly influence velocity, shear stress and apparent viscosity.

3.5.4 Inferences to *in vivo* haemodynamics

Although the present study was carried out in a rectangular channel of relatively high aspect ratio, the results can be used to infer how aggregation would affect the velocities and CDL width *in vivo* in a qualitative sense. This study has shown that aggregation not only increases the CDL width in the steady state, but also further enhances it as the flow splits between two branches. In arterioles, such branching occurs regularly and thus aggregation will further accentuate the inherent heterogeneity of the distribution of RBCs throughout the microvasculature. The constant branching of vessels in the arterioles also leads to a non-uniform velocity distribution. It has been suggested that the velocity distribution returns to uniformity after a few diameters, but that haematocrit redistribution takes around 10 diameters (Cokelet, 1999; Pries et al., 1989). The present study has shown that the velocity profile can remain skewed further downstream than this. It is proposed that the CDL which forms along the inner wall of the bifurcation is responsible for the observed skewness. Due to the skewness, the velocity and hence volumetric flow of the CDL will be relatively increased and may enhance plasma skimming, should the subsequent branch happen to appear at the same location as the CDL. If a subsequent branch occurred on the opposing side to the original branch, the haema-

tocrit in the daughter branch would be increased. Furthermore, the flow in this branch would also be decreased due to the skewed velocity profile.

Across a whole microvascular bed, the specifics of the adjacent branch orientations could have a drastic impact upon the localised distributions, although regulatory mechanisms may act to maintain a relatively uniform pressure drop across the system. Current mathematical models are capable of predicting whole organ distributions of flow parameters, but are less successful on the scale of individual vessels (Cokelet, 1999). The current study supports the hypothesis that this may be a result of the haematocrit distribution, including the CDL, in adjacent bifurcations. The amplification of the CDL width in the presence of aggregation could therefore have a significant impact, which may be a factor in the contradictory results reported in the literature on the effect of aggregation *in vivo*.

3.6 Closure

In the present chapter, it has been shown that blood velocity profiles downstream of a microscale bifurcation tend to be skewed. The degree of skewing varies with flow ratio and RBC aggregation. The presence of a cell-depleted layer was observed to correlate with the skewing to some extent, and so a mathematical model was derived to investigate the relationship. Basic trends were reproduced by the model fairly accurately but the extent of skewing was less than that observed in the experimental data. The model considered that the fluid consisted of two parts, a CDL and a RBC core, each with a single viscosity. Given that viscosity is proportional to local haematocrit, this model overlooks the fact that there may be non-uniform haematocrit distribution within the RBC core, and that the CDL is in itself a distributed parameter.

In the next chapter, the haematocrit distribution is considered as a continuous parameter. A technique for inferring this distribution from images is developed and, with the use of computational fluid dynamics, the efficacy of the approach is analysed.

Chapter 4

Continuous viscosity and haematocrit profiles †

This chapter is concerned with establishing a new optical methodology for determining haematocrit concentration profiles within a straight-T bifurcating microchannel. This information is used to estimate a viscosity field within the channel that depends on haematocrit concentration. Experimentally determined velocity profiles are then subsequently compared those calculated from simulations that incorporate the spatial variation of viscosity.

4.1 Introduction

As discussed in the previous chapter, it is clear that the redistribution of haematocrit in bifurcating channels has a significant impact on local velocity and viscosity characteristics. The basic characteristics of the shapes of haematocrit distributions are commonly discussed, but there have not been to date, any parametric experimental quantitative descriptions of the shape of the profiles. Manjunatha & Singh (2002) measured haematocrit distributions *in vivo* using image processing methodologies, but only in a single vessel and with relatively low resolution, which precluded detailed analysis of the influence of the haematocrit and viscosity on the velocity. As such, it is not known how the

†The data presented in this Chapter has been published in 'Hematocrit, viscosity and velocity distributions of aggregating and non-aggregating blood in a bifurcating microchannel', *Biomechanics and Modelling in Mechanobiology* (Sherwood et al., 2012b). The work was also presented at the *14th International Congress of Biorheology and 7th International Conference on Clinical Hemorheology*, July $4^{th} - 7^{th}$ 2012, Istanbul, Turkey.

characteristics of haematocrit profiles downstream of a bifurcation will depend on the various parameters involved (e.g. parent branch haematocrit, flow rate, flow ratio and geometric factors) and importantly, how the shape will affect local and bulk properties, such as wall shear stress and apparent viscosity.

These factors were considered in Chapter 3, using a model wherein the haematocrit was either a given value, or 0:

$$\text{for } 0 < y^* < \delta^*,\ H = 0 \tag{4.1}$$

$$\text{for } \delta^* < y^* < 1,\ H = \frac{H_T}{1-\delta^*} \tag{4.2}$$

However, this approach is limited in two ways. Firstly, plasma skimming is not considered. In the presence of plasma skimming, the haematocrit would be reduced in the low flow branch and increased in the high flow branch, which would influence the relationships observed, by decreasing the viscosity for low flow ratios and increasing the viscosity for high flow ratios. Additionally, considering the fluid as two separate, but constant viscosity, phases is an over-simplification which is unlikely to be able to completely capture the behaviour of such a complex system.

In this chapter, the haematocrit distribution will be considered as a continuous one dimensional distribution, $H\left(y^*\right)$[†] for which

$$H_T = \int_{-0.5}^{0.5} H\left(y^*\right) dy^* \tag{4.3}$$

Firstly, a newly developed methodology for describing the haematocrit distribution will be described. The method is based on analysis of strobe illuminated images of RBCs flowing in a bifurcating microchannel. The results of this analysis will be briefly discussed, before moving on to conversion of the haematocrit distribution to viscosity distributions using an empirical model. The resulting viscosity distributions will be used in conjunction with CFD simulations in order to infer the effect of viscosity on velocity, wall shear and apparent viscosity.

In this chapter, the velocity data from the previous chapter will be combined with an additional data set, acquired under the same channel and fluid conditions, but using

[†]The coordinate y^* in the daughter branches would be replaced with x^* in the parent branch. However, for the sake of brevity and clarity, equations are stated in terms of y^*.

an additional imaging methodology. Alternate strobe and laser illumination were used in order to quasi-simultaneously acquire images of both the RBCs and fluorescent microparticles ($1\mu m$) suspended in the fluid at a concentration 0.1% by volume. Regions of interest are defined as in Chapter 3 (see Figure 3.1).

It should be noted that at the time of acquisition, it was not possible to acquire images of the RBCs using this technique which would allow for velocity measurement. Upon further development, this became possible and is used in Chapter 5. However, for this chapter, the RBC velocity data acquired with the halogen lamp are used for comparison purposes.

4.2 Haematocrit distribution technique

In this chapter, the relative viscosity of the fluid will be considered, i.e. the true viscosity normalised by that of the suspending medium. In order to further investigate the relationship between the velocity characteristics and the local gradients of RBC concentration, a methodology was developed for estimating time averaged relative viscosity profiles from the strobe illuminated images of RBCs.

Figures 4.1a and b show images of the RBCs in the microchannel, illuminated with the microstrobe for Dextran and PBS fluid samples, respectively. In the presence of Dextran, RBC aggregation can be observed, with linear rouleaux and other aggregates clearly visible, as highlighted in the inset. An irregular cell-free region adjacent to the inner wall can be seen in the $Q^* = 0.25$ branch, which in an instantaneous sense could be considered a cell-free layer. Spatially, as RBCs pass through this region, it could be considered to be a cell-depleted layer, as discussed in Chapter 3. However, for the present chapter this layer is considered to be part of the continuous haematocrit gradient. In the absence of Dextran (Figure 4.1b) the RBCs are dispersed and there are no visible aggregates, but a small cell free region can again be observed in the same location. Slight systematic intensity gradients can be observed in the instantaneous images of Figure 4.1a and b, but they are not distinct. However, when the images are time averaged, the intensity gradients become much clearer, as shown in Figure 4.1c and d. The normalised intensity of the time-averaged image is given by

$$I^*(x,y) = \frac{1}{NI_{max}} \sum_{i=1}^{N} I(x,y)_i \tag{4.4}$$

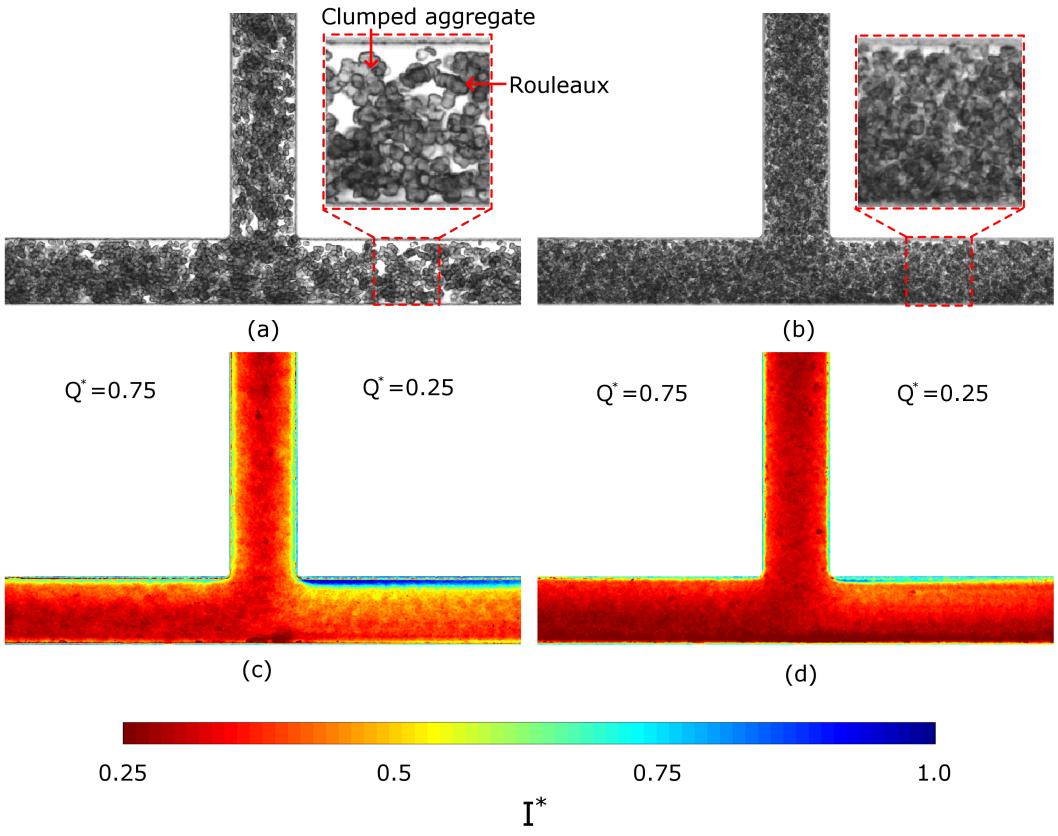

Figure 4.1: Top panels: sample instantaneous microstrobe illuminated images of the bifurcation. Bottom panels: time-averaged intensity images. (a, c). Dextran, (b, d) PBS.

where I_{max} is the maximum intensity of the image, corresponding to the regions of the channel where cells are absent (4096 for the present 12-bit images). N is the number of images in each data set and $I\,(x, y)$ is the image intensity at a given pixel location. In Figure 4.1, the colourbar is only shown from $I^* = 0.25$ as this was the minimum intensity observed in any of the data sets. In the parent branch, the intensity is lowest in the middle of the channel and regions of high intensity can be observed adjacent to the channel walls. In the Dextran case (Figure 4.1c) these high intensity regions near the wall are significantly larger than for the PBS case (Fig. 4.1d). Additionally, the region of low intensity in the centre of the parent branch is much broader for the PBS case. Assuming that intensity is inversely related to the local time-average haematocrit, these results are consistent with reports of increased radial migration (Bishop et al., 2001c; Reinke et al., 1987) and CDL width (Ong et al., 2010) in the presence of aggregation. In the daughter branches a gradient in intensity can be observed, decreasing from a maximum at the inner wall to a minimum at the outer wall. For the $Q^* = 0.25$ branch

in the Dextran case, a region of very high intensity can be observed at the inner wall corresponding to the cell-depleted region which is visible in Figure 4.1a. This is also present in the PBS case, but its width is significantly smaller. In the Dextran case, there is a small region of very low intensity around the stagnation point in the flow, which implies some degree of cell adhesion at this location. For the PBS case low intensity is observed all along the outer wall of the bifurcation.

This analysis requires the assumption that the intensity of the time averaged image at each location is proportional to the average haematocrit at that location. This assumption is based on the fact that due to the relatively small channel height used in the study ($40\mu m$), saturation and non-linear effects on the image intensity/cell concentration relationship are largely minimised. This is due to the relatively small number of overlaying cells in the direction of light transmission, which prevents high levels of light absorption and scattering when cell concentration increases. Figure 4.1 shows a minimum I^* of 0.25, which is 25% larger from the near-zero intensity expected at saturation and minimum light transmittance levels. Furthermore, it should be pointed out that for these measurements, although the centre of the focal plane is aligned with the middle of the channel, the depth of the channel and low numerical aperture are such that all cells within the channel will contribute to the intensity of the image, and hence the calculated haematocrit. This is a necessary condition to derive the total haematocrit in the channel.

Additionally, it is assumed that the RBC aggregation only affects the relative viscosity at a given location implicitly via its influence on the local haematocrit. That is to say that the extent of aggregation does not change significantly in the bifurcation. This assumption is reasonable since all measurements were taken at a steady state at which aggregate formation is expected to have reached equilibrium in the parent branch and transit times through the bifurcation region are too small to permit significant aggregation to occur. Furthermore, the flow rates and hence shear forces in the present data were sufficiently low that disaggregation would be unlikely to occur in the bifurcation within the acquisition period.

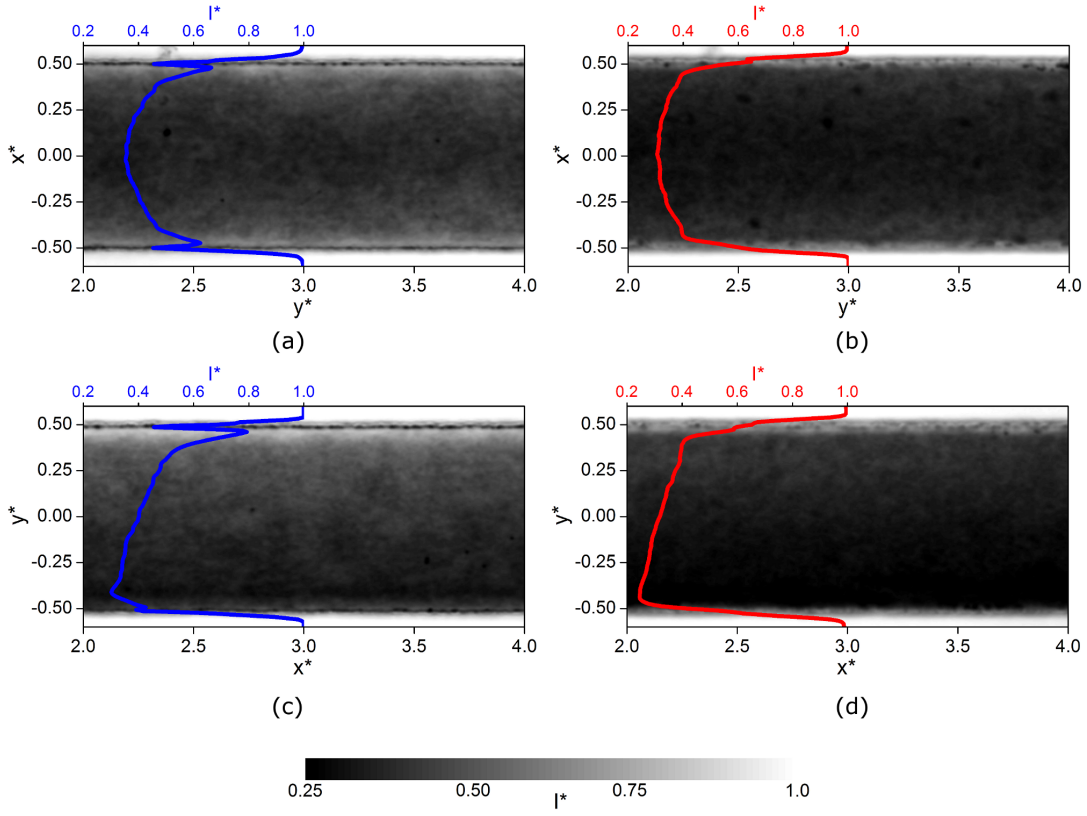

Figure 4.2: Time-averaged images in the regions of interest (ROI) with mean intensity profiles superimposed. (a) Parent branch, Dextran, (b) parent branch, PBS, (c) daughter branch , $Q^* = 0.50$, Dextran, (d) daughter branch, $Q^* = 0.50$, PBS.

4.2.1 Intensity Profiles

The intensity gradients are fairly uniform in the ROI in each branch. This can be seen more clearly in Figure 4.2, which shows the ROI in the parent branch and for $Q^* = 0.5$. The overlaid lines represent the average intensity value for each radial position within the region. It should be noted that the shape of the profile in proximity to the walls of the channel is different for the two suspending media; this was accounted for as described in the following paragraph. For the parent branch, in the presence of aggregation (Figure 4.2a), a parabolic distribution of intensity in the centre of the channel with linear gradients close to the wall is evident. The same distribution can be observed in the PBS case (Figure 4.2b), but the profile appears to be more blunted. In the daughter branches (Figures 4.2c and d), the linear gradients near the wall can still be observed, but the profile in the centre of the channel is skewed towards lower intensity values at the outer wall. In order to utilise these profiles for further analysis,

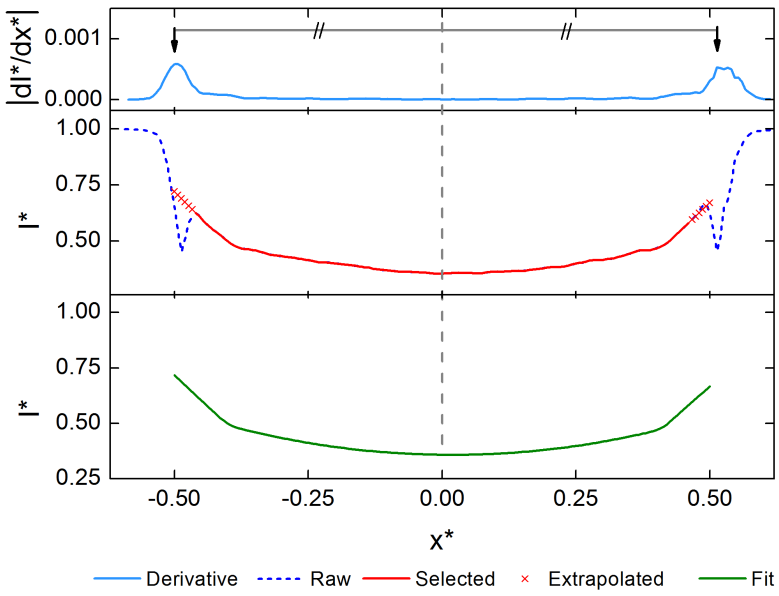

Figure 4.3: Depiction of the stages in locating, smoothing and fitting of the intensity profiles for Dextran case in the parent branch.

a certain amount of pre-processing is required, the methodology of which is shown in Figures 4.3 and 4.4.

Firstly, the relative location of the channel on the image should be accurately defined. To this end, the magnitude of the spatial intensity derivative, ($\left|\frac{dI^*}{dy^*}\right|$ or $\left|\frac{dI^*}{dx^*}\right|$), was calculated and smoothed using a moving average method (top panel in Figure 4.3), and the maxima were identified, as indicated by the arrows. These indicate the location of the outer edge of the channel wall, and hence this approach rectifies the artificial peaks observed in the Dextran cases in Figure 4.2. The centre of the channel is then assumed to be equidistant between the two maxima, indicated with a dashed grey line in Figure 4.3, from which the coordinate system is defined. By adjusting the focus of the microscope, it was observed that the true width of the channel was 152 pixels for the present data. However, this width would include the blurred regions of approximately $4-6$ pixels at the channel wall. Thus 70 pixels either side of the centre point were selected (solid red line) and the remaining 6 pixels closest to the wall were estimated using linear extrapolation, as indicated by the red crosses in the middle panels of Figures 4.3 and 4.4.

The experimentally determined intensity profiles exhibit some fluctuations which are considered to be experimental artefacts resulting from the finite number of images used in the averaging process. The curves should be smooth, both to provide a more general

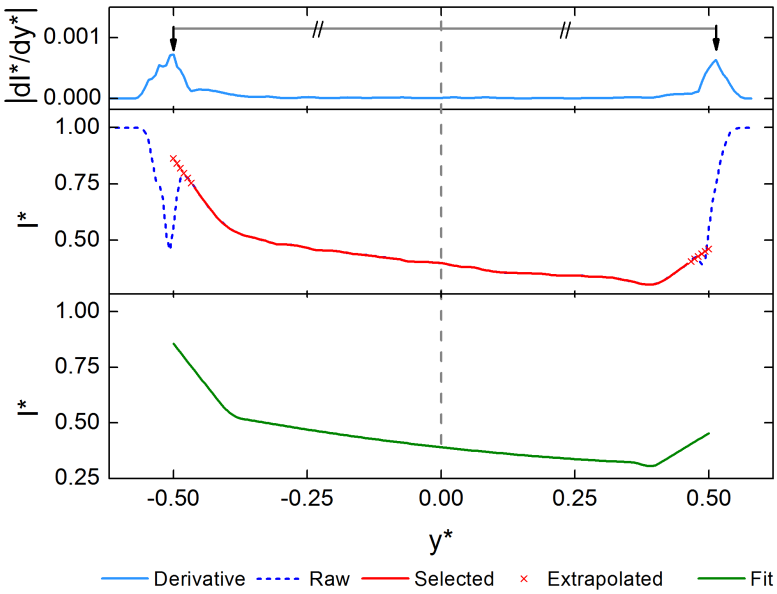

Figure 4.4: Depiction of the stages in locating, smoothing and fitting of the intensity profiles for Dextran case in the daughter branch for $Q^* = 0.5$.

description of the characteristics of the distribution and in order to reduce errors upon further analysis using the profiles. As described above, linear gradients in the intensity near the wall and a parabolic gradient in the channel centre can be observed. Therefore, a piece-wise linear-quadratic-linear polynomial was fitted to the data. The best fit to the data was calculated by testing each possible location of the intersection points between the separate pieces and minimising the maximum error between the fit and the experimental data. In order to avoid the inevitable discontinuities, spline interpolation was used to smooth the two points on either side of the intersection of the polynomial pieces. The resulting curves are indicated by the solid green line in Figure 4.3. Figure 4.4 shows the equivalent process for a daughter branch at a flow ratio of $Q^* = 0.5$.

It can be seen that for both the parent and daughter branches, the fitted curve accurately follows the experimentally determined intensity profiles. Many previous studies have considered the flow of blood on the microscale in terms of multiple separate phases (Das et al., 2007; Fenton et al., 1985; Sharan & Popel, 2001) (see also Chapter 3) representing the cell-free layer and the core flow. This analysis is inspired by this concept, but considers a continuous distribution of haematocrit to represent a time average state.

4.2.2 Haematocrit Profiles

If it is assumed that the haematocrit profile scales linearly with the image intensity, a conversion factor is required to relate the two. In order to derive such a conversion factor, the haematocrit in the parent branch in the PBS case was considered to be close to that of the reservoir haematocrit. Although a non-uniform haematocrit distribution is observed in the parent branch, at the flow rates studied, it is not expected that the Fåhraeus effect would have a significant impact. When aggregation is present, increased radial migration of RBCs is observed and so the Fåhraeus effect is liable to have a greater influence, making estimation of the haematocrit for calibration purposes unviable. Hence, the tube haematocrit, H_C is assumed to be equal to the feed haematocrit which was 0.25 for the PBS case. The average parent branch intensity distribution from the PBS cases is used to define a single calibration factor to convert from intensity to haematocrit. The calibration factor is then calculated according to the following relationship:

$$\beta = \frac{1}{H_C} \int_{0.5w}^{-0.5w} \left(1 - I^*\left(y\right)\right) dy \tag{4.5}$$

The correction $\left(1 - I^*\left(y\right)\right)$ is used so that high image intensity corresponds to increased transmission of light and hence lower haematocrit. The haematocrit profiles are thus described by

$$H\left(y\right) = \beta\left(1 - I^*\left(y\right)\right) \tag{4.6}$$

4.3 Viscosity modelling

Having established the haematocrit profiles, the viscosity profiles need to be determined. The second assumption on which the present analysis is based, i.e. that the viscosity at a given location is only a function of the local haematocrit, is ordinarily not considered applicable as it is well known that blood is a shear thinning fluid due to the deformation, alignment and tank treading characteristics of RBCs at high shear rates and their propensity to aggregate under low shear conditions. In the present study however, the pseudoshear rates range from $\approx 6.25s^{-1}$ in the parent branch to $\approx 0.625s^{-1}$ in the daughter branch at the lowest Q^* studied. As mentioned earlier, given that aggregate formation has reached equilibrium and that the highest shear rates occur in the

parent branch, it is expected that aggregation will not significantly affect the flow characteristics within the region of analysis. Aggregation is a time dependent phenomenon, with a time constant reported to be on the order of 5 seconds (Kaliviotis & Yianneskis, 2008; Cokelet, 1980). The daughter branches in the imaging region in this study are $0.35mm$ long and the average velocity in the parent branch was $\approx 0.25mm/s$. Thus, as the flow ratio decreases, the transit time in the daughter branches within the imaging region will increase from around 1.5 to 15 seconds. At this upper end it is expected that some aggregation may occur. However, no systematic variations in the intensity distributions in the images were observed in the ROI, implying that the change in aggregation state is minimal. This is not to say that aggregation will not affect the flow, but suggests that its impact is to modify the redistribution of cells in the bifurcation.

4.3.1 Empirical Viscosity Model

In order to relate the haematocrit to the viscosity, an empirical relationship can be utilised. The most relevant to this study is that described for tube flow by Pries et al. (1992b), as used in Chapter 3. To recapitulate Equation 3.15

$$\mu_r = 1 + 3.54\left((1-H)^{-0.743} + 1\right) \tag{4.7}$$

The addition of Dextran to the suspending medium increased the viscosity by 30%, but as the equation above is posed in terms of relative viscosity and the following analysis utilises normalised profiles, this difference should not influence the results.

A further assumption needs to be made here regarding the distribution of haematocrit and its effect on viscosity. It is assumed that minimal sedimentation occurs in the experiments, and that the flow can be considered to be parallel to the upper and lower walls of the channel. Hence equation 1.18 describes a local (intrinsic) haematocrit-viscosity relationship, but the values of E and F are specific to the channel dimensions (extrinsic), which takes into account the influence of the out-of-plane haematocrit gradients. To summarise, the viscosity is predicted from the acquired images according to

$$\mu_r = 1 + 3.54\left[(1-\beta+\beta I^*(y))^{-0.743} - 1\right] \tag{4.8}$$

4.3.2 Viscosity-Velocity Relationship

In order to investigate the influence of the estimated viscosity profiles on the velocity field, and thus confirm the original hypothesis or otherwise, a relationship between the velocity and viscosity must be derived. An analytical solution is provided for a constant viscosity fluid in a rectangular channel (Bruus, 2008); however, the inclusion of a spatially variant viscosity term $\mu(y)$ renders this solution inapplicable to the present data. Therefore, in order to calculate the effect of viscosity on velocity, a numerical approach was adopted, utilising the finite volume computational fluid dynamics (CFD) package ANSYS CFX 13.0 (ANSYS, UK). A rectangular channel of dimensions $100 \times 40 \times 2000\mu m$ was discretised with a structured grid of 1.6 million elements. Inflation layers were added near the wall in order to minimise errors in the estimation of wall shear stress (WSS).

Constant $0.25mm/s$ velocity input and zero pressure outlet boundary conditions were applied. Converting relative viscosity values to dimensional dynamic viscosity was achieved by multiplying by the suspending medium viscosity, μ_0. This was found to be $1mPa\ s$ and $1.3mPa\ s$ for the PBS and Dextran cases respectively using a cone and plate viscometer, but the former value was used for both cases in order to aid comparison. Convergence was considered when the root mean square residuals became less than 10^{-5}. It should be noted that, as normalised results will be considered, the absolute values of viscosity, velocity and pressure selected here are not important. From the results of each simulation, a velocity profile was extracted half way along the channel in the middle plane. A simulation with a constant viscosity distribution was calculated and the result matched the analytical solution with a mean difference of 0.88%, verifying the accuracy of the simulations.

Additional simulations were carried out to establish whether the skewed velocity profiles could occur as a result of non-Newtonian viscosity. For this purpose, a model of the whole bifurcation region was created with branch lengths extended to 10 channel widths, and was meshed approximately 2 million elements with inflation layers added at the walls. Simulations were carried out with an inlet velocity of $0.25mm/s$ and the flow ratio was defined by forcing a certain proportion of the inlet flow through each boundary. Both constant viscosity and Carreau-Yasuda fluids were considered (with parameters from Gijsen et al. (1999)).

4.4 Results and Discussion

The results presented in this section will be separated into six sections. Firstly, the characteristics of the bulk haematocrit distribution are discussed in order to verify the technique and draw comparisons with previous studies. Subsequently, the bifurcation CFD studies will be discussed in order to provide a frame of reference for the proceeding discussion. The viscosity and velocity distributions as predicted using the new methodology will be considered, followed by analysis of the wall shear and apparent viscosity.

4.4.1 Bulk Haematocrit Distribution

Having estimated the haematocrit profiles, the average haematocrit in each branch can be calculated by integrating across the channel. Based on the assumption that the tube haematocrit in the parent branch was $H_p = 0.25$ for the PBS case, the tube haematocrit for the parent branch in the Dextran case was calculated to be $H_p = 0.23$, as a result of the constant scaling factor β. This slight reduction is explicable, as the presence of aggregation would enhance the Fåhraeus effect. The effect of aggregation on the haematocrit in the daughter branches, H_d, is considered in Figure 4.5 in terms of the haematocrit ratio $H^* = \frac{H_d}{H_p}$.

Due to mass conservation, plasma skimming cannot occur when an equal proportion of the flow enters branches of equal diameter and this condition should be satisfied by the results presented in Figure 4.5. It can be seen that for both the Dextran and PBS blood samples, $H^* = 1$ for $Q^* = 0.5$. For $Q^* > 0.5$, H^* is slightly greater than one, but approaches unity for $Q^* = 1$, at which point all of the RBCs from the parent branch would enter the daughter branch. The distribution shown in Figure 4.5 is similar to those shown in a number of previous studies (Carr & Wickham, 1990; Dellimore et al., 1983; Fenton et al., 1985; Perkkiö et al., 1987; Pries et al., 1989) although the difference in geometry and flow rate between studies precludes direct comparison. Perkkiö et al. (1987) compared the haematocrit ratio for aggregating and non-aggregating blood and found that while the aggregating blood showed a trend similar to the one observed here, the non-aggregating blood haematocrit ratio remained constant. However, their study was carried out in much larger channels, at which one would not expect a significant redistribution of RBCs in the absence of aggregation. The relationship between

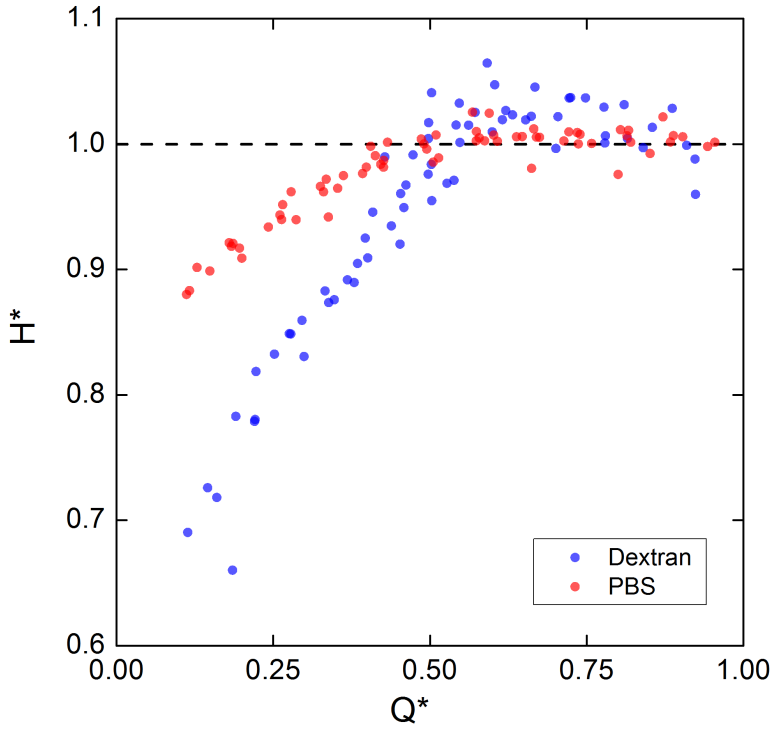

Figure 4.5: Haematocrit ratio against flow ratio for Dextran and PBS cases.

the RBC flux ratio, $F^* = \frac{F_d}{F_p}$, and the flow ratio, Q^*, provides a useful means to analyse plasma skimming. The $F^* = Q^*$ line would be followed by a continuous fluid and deviations from this line indicate the presence of plasma skimming. This analysis is carried out on bulk measurements of flow rate and discharge haematocrits. In the present study, the flux, F^*, is estimated using the average haematocrit and flow rate in each branch, $F^* = Q^* H^*$. The data is fit in the same manner as Pries et al. (1989) according to the equation

$$\text{logit}\,(F^*) = G + J\text{logit}\,(Q^*) \tag{4.9}$$

Where G is an asymmetry parameter which should equal zero for daughter branches of equal proportions. J is a parameter allowing for the deviation from the $F^* = Q^*$ line. Thus, as J becomes greater than 1, the extent of plasma skimming increases. It should be noted that Pries et al. (1989) also allowed for the critical flow ratio, beyond which cells only enter one branch, by modifying Q^* with an additional term. However, for the present data, upon fitting the curve, the critical flow ratio was found to be $Q^* = 0$, so the extra term is not included in the equation here for simplicity.

Figure 4.6 shows the flux-flow curve for the present data. It can be seen that for the

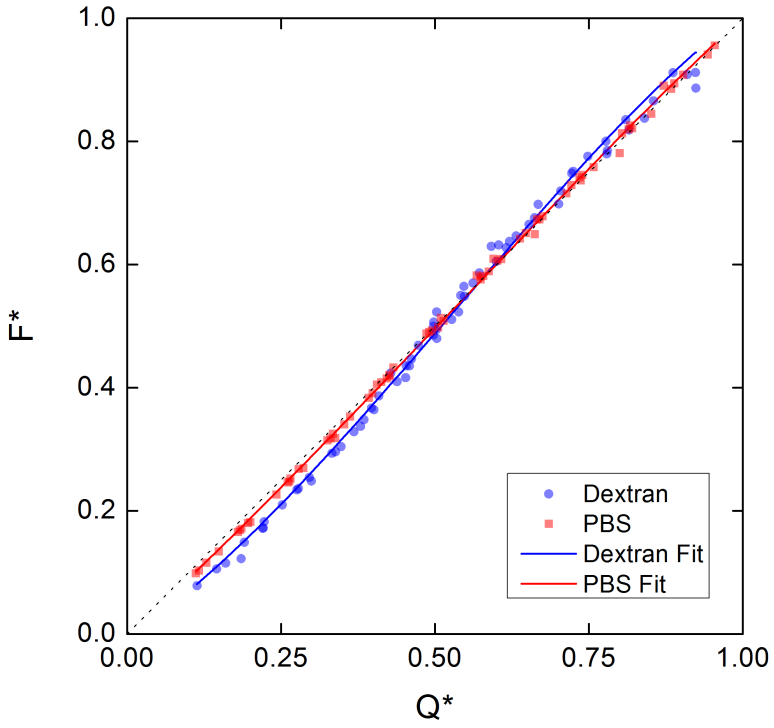

Figure 4.6: Flux flow curve with fits to Equation 4.9. Fitting parameters: Dextran: $G = 0.05, J = 1.16, R^2 = 0.9955$. PBS: $G = 0.02, J = 1.04, R^2 = 0.9993$.

PBS case, the curve is slightly displaced from the $F^* = Q^*$ line, indicating a very small amount of plasma skimming. For the Dextran case, the curve shows significant deviation from the $F^* = Q^*$ line, as expected. This implies that aggregation enhances plasma skimming which is in agreement with the literature (Gaehtgens et al., 1978; Gelin, 1963; Perkkiö et al., 1987). In order to test whether the fits are valid, the sum of the squared errors between the data and the lines described by 4.9 were compared to those for the $F^* = Q^*$ line. The sum of the square errors was reduced by 70% and 61% for the Dextran and PBS cases respectively, which suggests that the fits are appropriate.

4.4.2 Computational Fluid Dynamics in a Bifurcation

Before further discussing the characteristics of the experimental and computational profiles, some more detail will first be provided on the flow field in a bifurcating geometry for Newtonian and Carreau-Yasuda fluids[†]. In Chapter 3, it was discussed that the velocity profiles were observed to be skewed when averaged over a region 2-4 channel widths downstream of the bifurcation. To show that this is not the response one would

[†]A brief description of similar data was provided in Chapter 3, but is analysed in greater depth in this chapter.

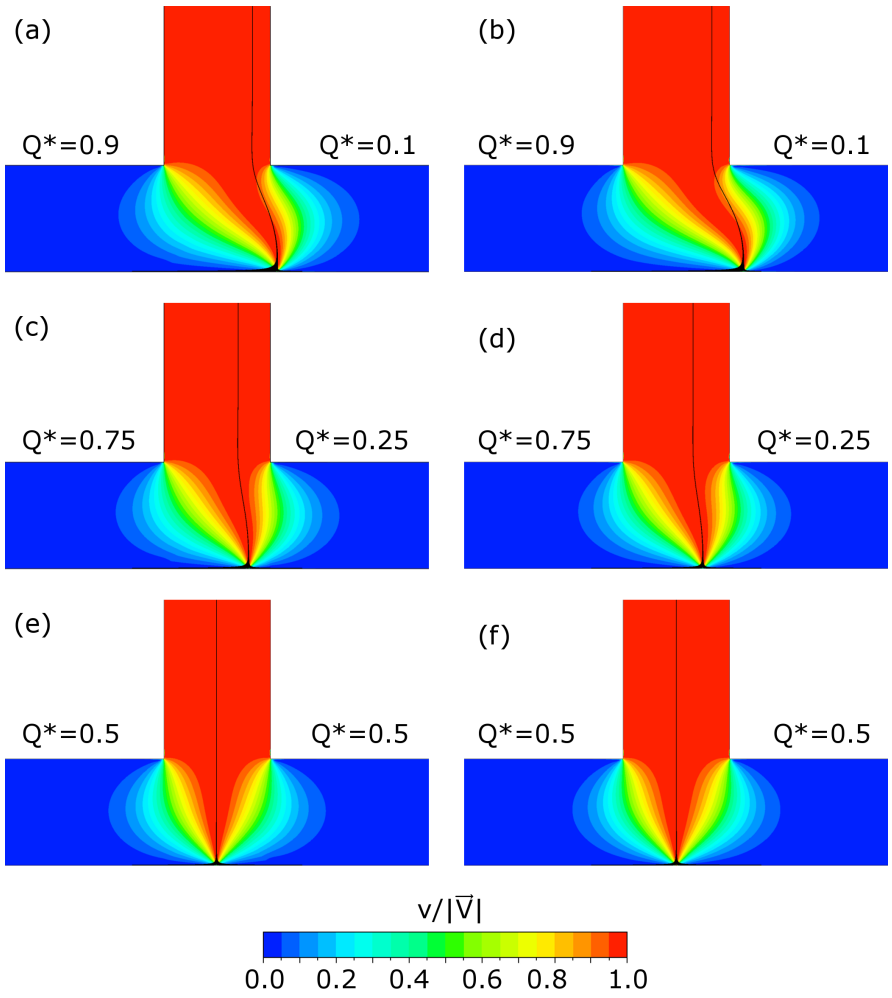

Figure 4.7: Proportion of velocity component acting in the y direction, $v/\left|\vec{V}\right|$ in the middle plane of the channel. Results from Newtonian and non-Newtonian bifurcation CFD. Left column: Newtonian fluid, flow split (a) 90:10, (c) 75:25, (e) 50:50 . Right column: Carreau-Yasuda fluid, flow split (b) 90:10, (d) 75:25, (f) 50:50. Black lines show separating streamlines.

expect from a Newtonian fluid, some CFD results are shown in Figure 4.7 for three different flow splits. In addition, the results for a non-Newtonian fluid are presented for the same flow splits. There is no consensus on which non-Newtonian model can most accurately represent blood, indeed whether any can (due to the heterogeneous haematocrit distribution). The model selected for this analysis is that used by one of the most cited non-Newtonian blood modelling studies (Gijsen et al., 1999).

Contours of the ratio of the y component of the velocity vector, v, to the total velocity magnitude, $v/\left|\vec{V}\right|$ at each location are shown in Figure 4.7. For the Newtonian fluid, given the very low Reynolds number, once v becomes very small, the profile will very rapidly attain symmetry due to the symmetric geometry (parallel walls). It can be seen

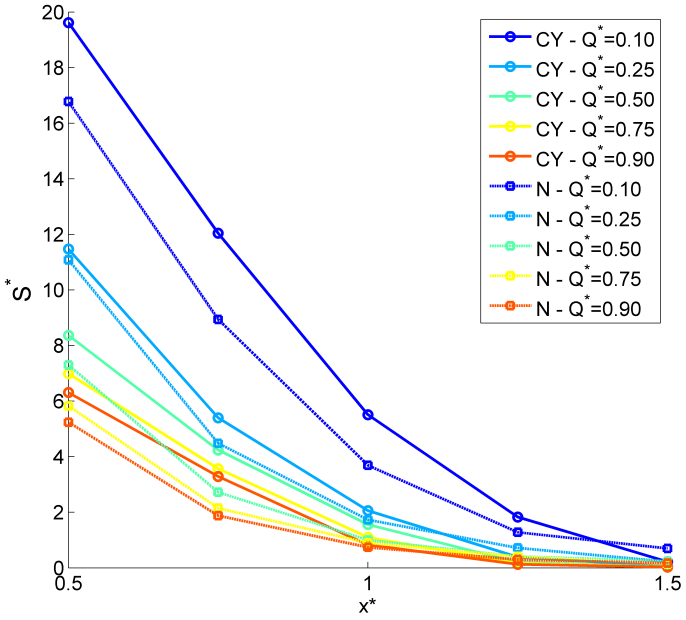

Figure 4.8: Velocity profile recovery for different flow ratios from CFD simulations. Dashed lines are Newtonian fluid (N), solid lines are Carreau-Yasuda fluid (CY).

that in all cases, the transverse velocity component reaches zero within less than one channel width from the bifurcation vertices. In general, the flow becomes parallel more quickly for higher flow ratios. The same is observed for the Carreau-Yasuda fluid.

If there was a transverse velocity component, a single component axial velocity profile would not provide all of the relevant information, hence this analysis provides confirmation that it is reasonable to use single velocity component profiles to consider the flow field for $x^* > 2$. The solid black lines on the figure show the separating streamlines, which separate the fluid entering each of the daughter branches. It can be seen that there is not a significant difference between the Newtonian and non-Newtonian cases, and that as the flow split increases, the separating streamline moves further from the centreline ($x^* = 0$) and becomes increasingly curved. To further consider how continuous Newtonian and non-Newtonian fluids behave, the recovery length is considered in Figure 4.8 for a range of flow ratios. Axial velocity profiles (u) were taken at 5 locations along the daughter branch from the bifurcation vertex along a length of one channel width, from which the skewness was calculated. It can be seen that for all cases, the skewness in the axial velocity profiles decreases exponentially, reaching a value which is negligibly small for $x^* > 1.5$. Although these profiles omit the trans-

verse velocity component shown in Figure 4.7, this was equal to zero for $x^* > 1.5$ for all cases. The use of a shear thinning Carreau-Yasuda fluid for the simulations acted to slightly increase the skewness for $0.5 \leq x^* \leq 1$, but the Newtonian fluid had a slightly longer recovery length.

These results show that the ROI used for averaging the velocity profiles is defined appropriately. Furthermore, it is clear that skewness would not be expected to be observed in velocity profiles further downstream than $x^* > 1.5$ for a Newtonian fluid. Furthermore, the non-Newtonian properties described by the Carreau-Yasuda model do not impose any significant difference in this region, i.e. the shear thinning properties cannot account for skewed velocity profiles. Hence, any skewness observed in velocity profiles must be a result of spatial viscosity gradients occurring as a result of the local haematocrit distribution. In the next section, the effect of flow ratio and aggregation on this viscosity distribution will be discussed.

4.4.3 Viscosity distribution

Figure 4.9 shows viscosity profiles in the parent branch (Figure 4.9a) and for a range of flow ratios in the daughter branch. The most striking feature is that the viscosity is higher for the PBS samples in all cases. However, it should be noted that as mentioned earlier, the tube haematocrit in the PBS case was greater than in the Dextran case, probably due to RBC aggregation inducing radial migration and hence increasing the Fåhraeus effect. Nonetheless, the differences in the shapes of the profiles are striking. Considering the parent branch (Figure 4.9a), it can be seen that in the PBS case, the distribution in viscosity is significantly more uniform than for the Dextran case. That is to say, in the Dextran case, the viscosity at the walls is relatively much lower than in the centre, and hence the gradients in viscosity are steeper. At $Q^* = 0.9$ (Figure 4.9b), the viscosity profile for the PBS case is almost flat at the outer wall of the daughter branch ($y^* = -0.5$), and the gradient at the inner wall is increased compared to the parent branch. For the Dextran case, a slight skewness in the profile is observed, but is less pronounced. However, conversely to the PBS case, there is still a steep viscosity gradient at the outer wall. As Q^* decreases through 0.7, 0.5 and 0.3, similar characteristics are observed, with increasingly linear distributions in the channel centre and increasing viscosity gradients at the walls. In all cases, the gradients are much greater

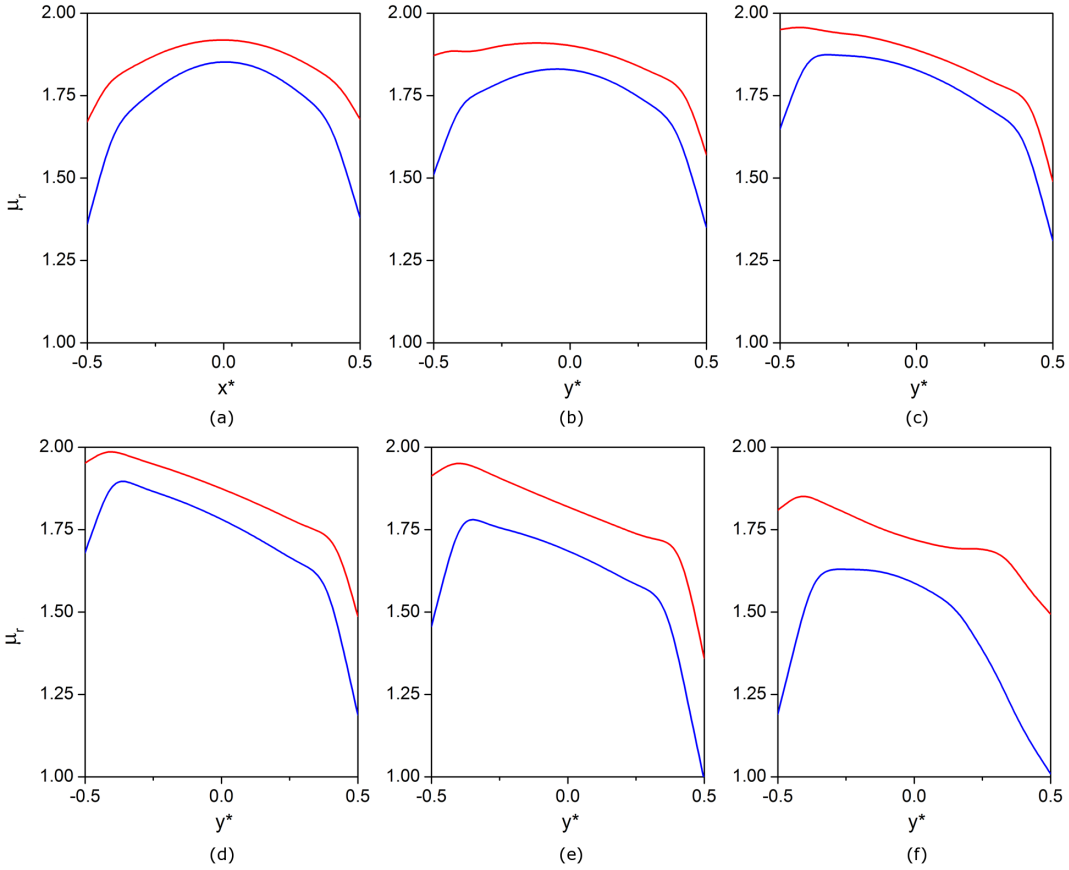

Figure 4.9: Viscosity profiles. Blue line - Dextran, red line - PBS. Parent branch (a) and daughter branch for, (b) $Q^* = 0.9$, (c) $Q^* = 0.7$, (d) $Q^* = 0.5$, (e) $Q^* = 0.3$, (f) $Q^* = 0.1$.

in the Dextran cases. At the lowest flow ratio for the Dextran case, $Q^* = 0.1$ shown in Figure 4.9f, the linear core region decreases to around half of the channel width, with wide regions of high viscosity gradient close to each wall.

Figure 4.10 shows the viscosity profiles for each of the flow ratios and fluids considered in the present study, as a continuous distribution in Q^*. The average parent branch distribution was appended to represent $Q^* = 1$, and the distributions were then smoothed in two dimensions using smoothing splines to give a continuous plot of the viscosity distribution across the daughter branches against Q^*. For both the Dextran and PBS cases, the profile is symmetric at $Q^* = 1$, corresponding to the parent branch. As the flow ratio decreases, the location of maximum viscosity moves towards the outer wall, reaching a maximum at a flow ratio slightly greater than $Q^* = 0.5$. This might be due to the complex interaction between the distributions of RBCs which collide with the static RBCs around the stagnation point. The maximum relative viscosities were $\mu_r = 1.91$

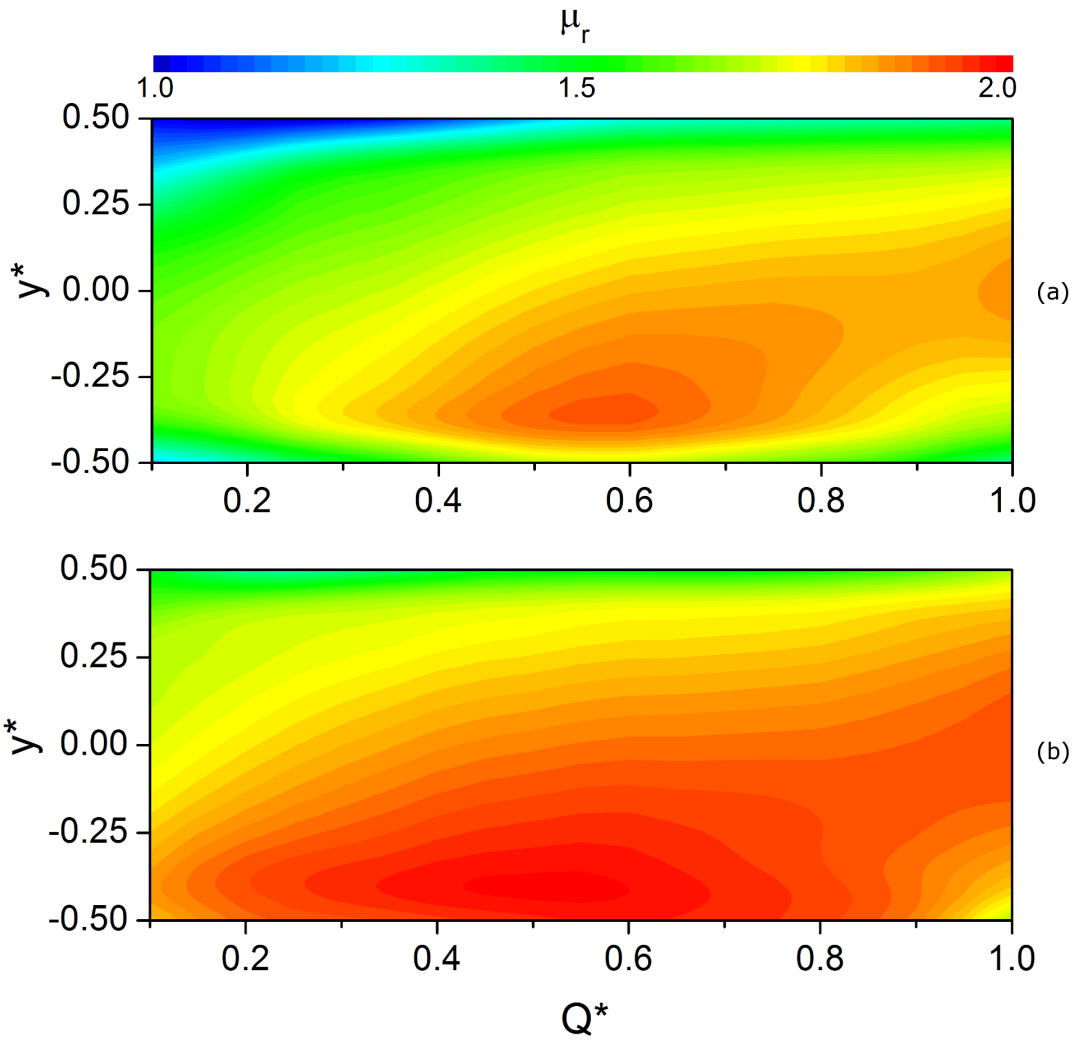

Figure 4.10: Continuous viscosity distribution as a function of Q^*.

for the Dextran case and $\mu_r = 1.99$ for the PBS case. As the flow ratio decreases from 0.5, a region of low viscosity near the inner wall becomes increasingly present, particularly for the Dextran case. This region corresponds with the 'cell-depleted layer', which RBCs pass through rarely.

4.4.4 Velocity profiles

Computational fluid dynamics was used to infer the effect of the previously discussed viscosity distributions on the velocity. Figure 4.11 shows two-dimensional cross sectional velocity contours from the CFD data for $Q^* = 0.1, 0.5$ and 0.9 for the Dextran and PBS cases. The out of plane coordinate is normalised relative to the channel height, $z^* = z/h$. It can be that all of the profiles are skewed towards the inner wall ($y^* = 0.5$), as was observed for the experimentally measured velocity profiles presented in Chapter

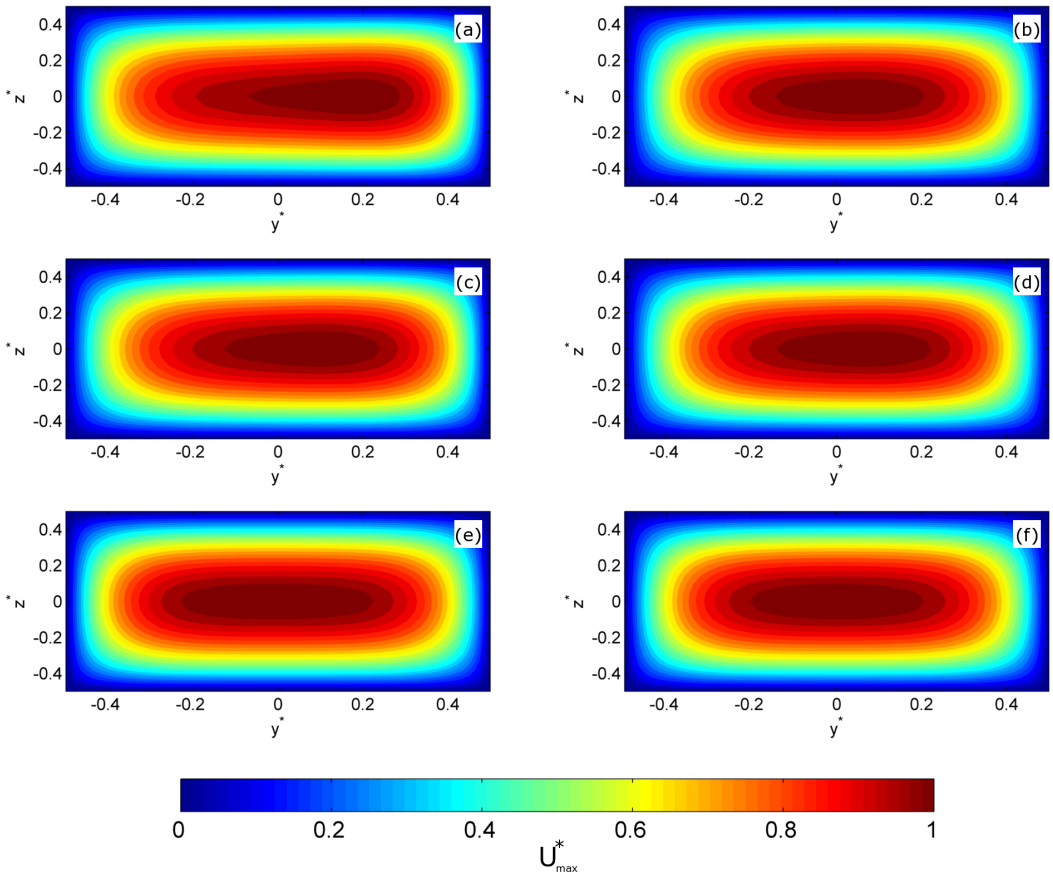

Figure 4.11: Cross-sectional (y, z plane) velocity contours for Dextran (left column) and PBS (right column) cases. (a,b) $Q^* = 0.1$, (c,d) $Q^* = 0.5$, (e,f) $Q^* = 0.9$.

3. In the out-of-plane direction (z^*), the velocity is not significantly different to that for a Newtonian fluid (as the viscosity was considered to be only a function of radial channel position). For the highest flow ratio, (Figures 4.11e and f) both Dextran and PBS cases are almost symmetric, but the central high velocity region is broader in the Dextran case, i.e. the velocity profile is more blunt. At $Q^* = 0.5$, the velocity profiles are skewed towards the inner wall with a marginally broader distribution again for the Detran case. At $Q^* = 0.1$, the PBS case is similar to that for $Q^* = 0.5$, but the Dextran case shows strong skewing towards the inner wall, with a significantly different, tear-drop shaped region of high velocity in the channel centre.

The PIV data is only available in the mid plane, so the velocity profiles for each experimental methodology are compared with those from the midplane of the CFD data and the viscosity profiles for three selected flow ratios. Figure 4.12 compares sample normalised velocity profiles, $U^*_{max} = U/U_{max}$ acquired from RBC μPIV, fluorescent

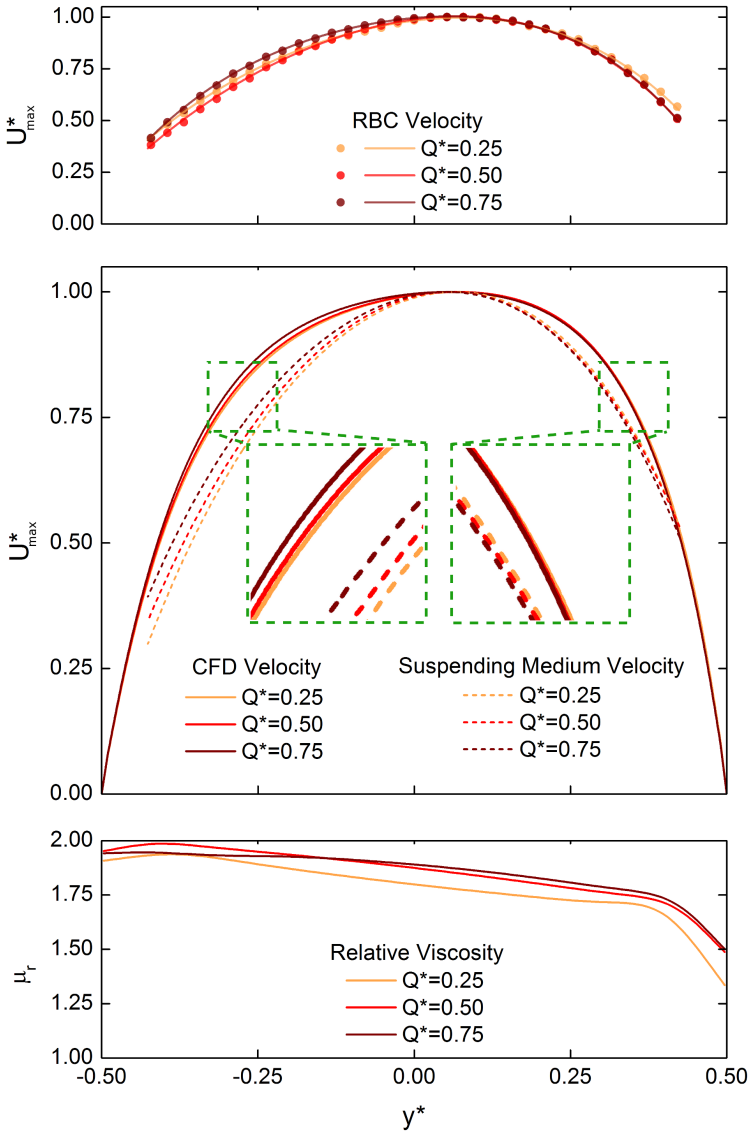

Figure 4.12: PBS case - Top panel: RBC μPIV velocity profiles and polynomial fits. Middle panel: Velocity profiles simulated using CFD, and fitted data from fluorescent μPIV for comparison. Insets highlight dependency of the shape of the profiles on Q^*. Bottom panel: Viscosity profiles.

μPIV and CFD along with the corresponding viscosity profiles for the PBS case. Figure 4.12a shows the RBC μPIV velocity profiles for flow ratios of $Q^* = 0.25, 0.5$ and 0.75 for the PBS case. These profiles are averaged along the ROI. The average coefficient of variation of the averaging process was less than 1% for all cases. The lines are fourth order polynomial approximates to the data, used to smooth out irregularities in the profiles and allow for a continuous description of the time-average velocity. Figure 4.12b shows the velocity profiles from the CFD analysis for the same flow ratios. On the same plot, the fitted values from the suspending medium data are shown as

dashed lines. It can be seen that the velocity profiles are skewed towards the inner wall ($y^* = 0.5$) for all cases, whereas the viscosity profiles (Figure 4.12c) are skewed in the opposite direction. This would be expected as increased friction between fluid layers in a region of higher viscosity would lead to reduced velocities in that region, skewing the profile towards the region of lowest viscosity. Although the bluntness of the CFD velocity profiles (solid lines) is notably greater than those of the suspending medium (dashed lines), the shape of the profiles is otherwise similar. The insets in Figure 4.12b highlight the order in which the curves appear for different flow ratios.

For positive y^*, the normalised velocity near the inner wall increases with decreasing flow ratio. For negative y^*, the opposite relationship is observed. This suggests a simple skewing of the profile, which would be expected as the viscosity profile is approximately linear for $y^* < 0.4$. The equivalent graphs for the Dextran case are shown in Figure 4.13.

Considering the insets in Figure 4.13b, the Dextran data follows the same trend as the PBS data at the inner wall, but the differences between cases are greater, particularly between the $Q^* = 0.25$ and $Q^* = 0.5$ cases. For negative y^*, the viscosity profiles for the Dextran case show a significant decrease near the outer wall, and this modifies the shape of the velocity profiles, with the $Q^* = 0.25$ and $Q^* = 0.5$ profiles exchanging relative positions. It is worth noting that the CFD data matches these trends in all cases considered here.

The full flow field CFD simulations for Newtonian and Carreau-Yasuda fluids showed that for all Q^*, the recovery length of the velocity profiles was less than $1.5x^*$. That is to say, the velocity profiles in the ROI were symmetric. Thus, it can be stated that the skewness observed in Figure 4.14 occurs as result of the non-uniform haematocrit distribution. To further test this hypothesis, the skewness parameter, S^*, defined as the normalised distance between the position of maximum velocity and the centre of the channel, was calculated. The skewness of the RBC μPIV and CFD profiles are compared in Figure 4.14. For each case, nineteen CFD simulations were run with viscosity profiles extracted from Figure 4.10 for $Q^* = 0.15$ to $Q^* = 0.95$. The flow ratio for these cases was defined based on the fluorescent-μPIV data. It can be seen that the skewness is greater for the Dextran case than the PBS case, particularly at low flow ratios, and that there is a good match between the experimental and simulated skewness

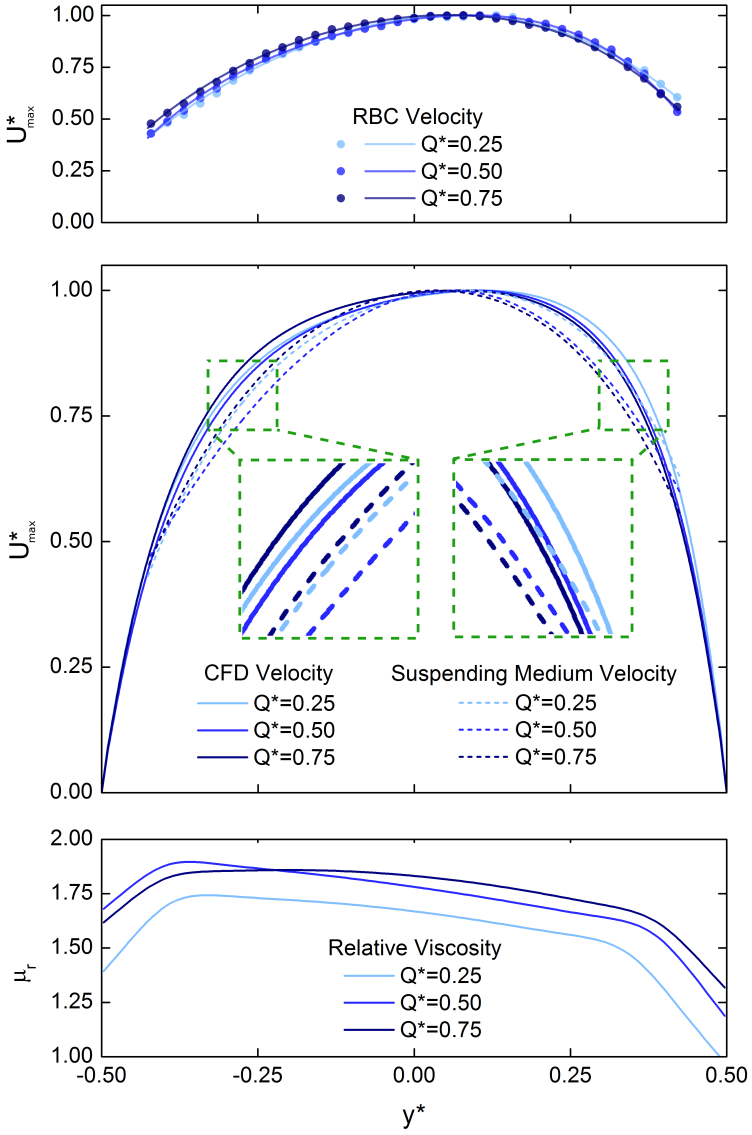

Figure 4.13: Dextran case - Top panel: RBC μPIV velocity profiles and polynomial fits. Middle panel: Velocity profiles simulated using CFD, and fitted data from fluorescent μPIV for comparison. Insets highlight dependency of the shape of the profiles on Q^*. Bottom panel: Viscosity profiles.

for both cases. Considering the experimental error in both the PIV processing and the subsequent analysis and smoothing procedures, the good agreement between the CFD profiles and velocity provides confidence that the viscosity modelling carried out in the present study is valid.

The bluntness of the velocity profiles is another important aspect of the flow that should be considered, as it is well established that blood velocity profiles tend to be blunted in the presence of aggregation (Bishop et al., 2001a; Reinke et al., 1987). Thus, given that the viscosity modelling approach has been shown to be valid for the particular cases

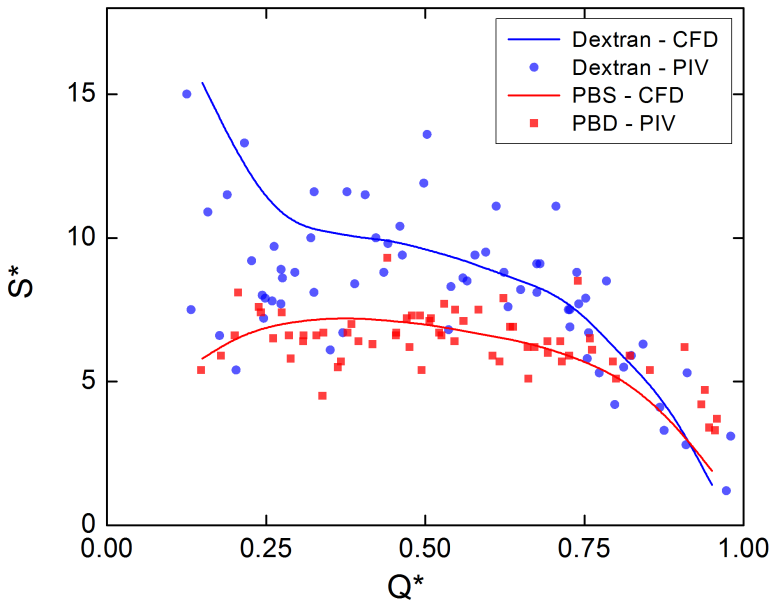

Figure 4.14: Comparison of skewness, S^*, calculated from RBC μPIV data (points) and CFD simulations (lines).

analysed in the present study, an increase in bluntness for the Dextran case should be visible in the results of the simulations. Figure 4.15a compares the velocity profiles generated using the average viscosity profiles in the parent branch for Dextran and PBS cases along with that generated using a constant viscosity (assuming a uniform haematocrit distribution).

The profile is slightly blunted in the PBS case, and more so in the Dextran case. This trend is also followed by the present experimental data as shown in Figure 4.15b. It should be noted that the experimentally derived velocity profiles are slightly less blunt than those obtained assuming constant viscosity, or equivalently, the analytical solution to the flow. This requires further investigation. Nonetheless, the current approach is capable of predicting the increased bluntness caused by RBC aggregation in the presence of Dextran.

4.4.5 WSS and apparent viscosity

It is interesting to consider the effect of the viscosity distribution on WSS and apparent viscosity, as was done in Chapter 3 for the mathematical model. Figure 4.16 shows how the WSS varies as a function of flow ratio. The solid circles indicate the inner wall (termed τ_δ for comparison with Chapter 3) and the hollow circles represent the outer wall (τ_c). There is a very clear correspondence between Figure 4.16 and Figure 4.5.

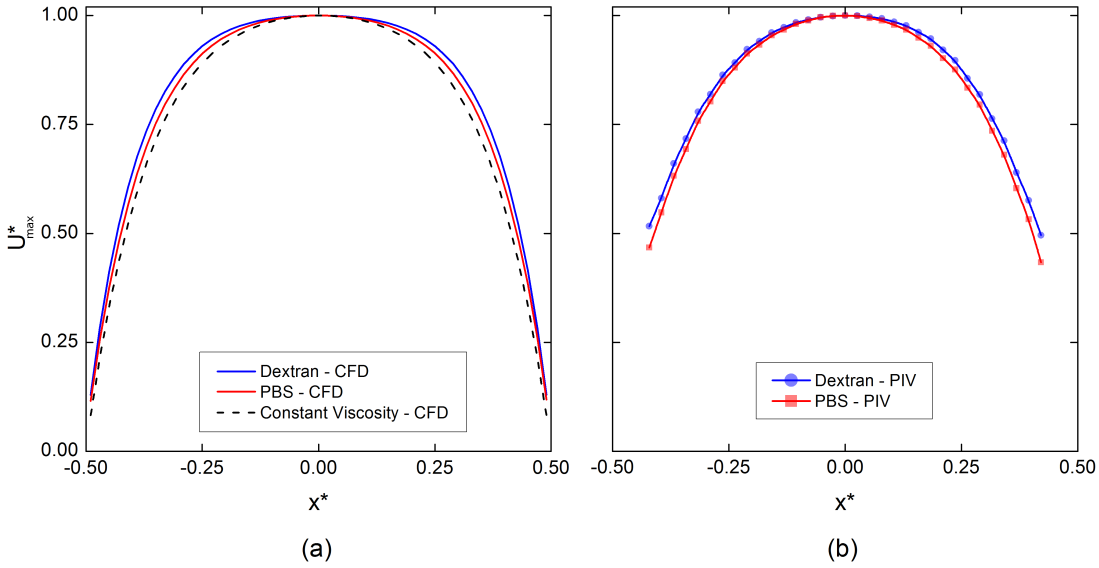

Figure 4.15: Velocity profiles in the parent branch. (a) CFD profiles from mean viscosity profiles in parent branch comparing Dextran, PBS and constant viscosity cases, (b) RBC μPIV data comparing Dextran and PBS cases.

This is a result of the dependence of WSS on viscosity, and the dependence of viscosity on haematocrit. Aside from the issue of the shape of the viscosity profile, it is clear from Equation 1.18 that the overall viscosity is highly dependent on overall haematocrit. Hence, the plasma skimming shown in Figure 4.5 is likely to reduce the overall WSS for a given flow rate. It should be noted that the average parent branch haematocrit was 8% lower for the aggregating case, hence the WSS and apparent viscosity would be expected to be lower.

It can be seen in Figure 4.16 that the WSS is lower at the inner wall than the outer wall for all cases, as was also predicted by the mathematical model in Chapter 3. For the PBS case and $Q^* > 0.5$ (high flow branch), the WSS at the inner wall decreases slightly, and the WSS at the outer wall increases slightly, as the flow ratio decreases. For the Dextran case, the shear stress at the inner wall remains almost constant while the WSS increases at the outer wall. In the low flow branch, for the Dextran case, the WSS decreases rapidly, probably as a result of the reduced overall channel haematocrit. The same trend is observed for the PBS case, but with a shallower slope. It is worth noting that the absolute magnitude of the WSS is not important in the present plot, as the velocity was constant. In practice, as the flow ratio decreases, the velocity in that branch will decrease proportionally, and so the shear rate and WSS will scale similarly;

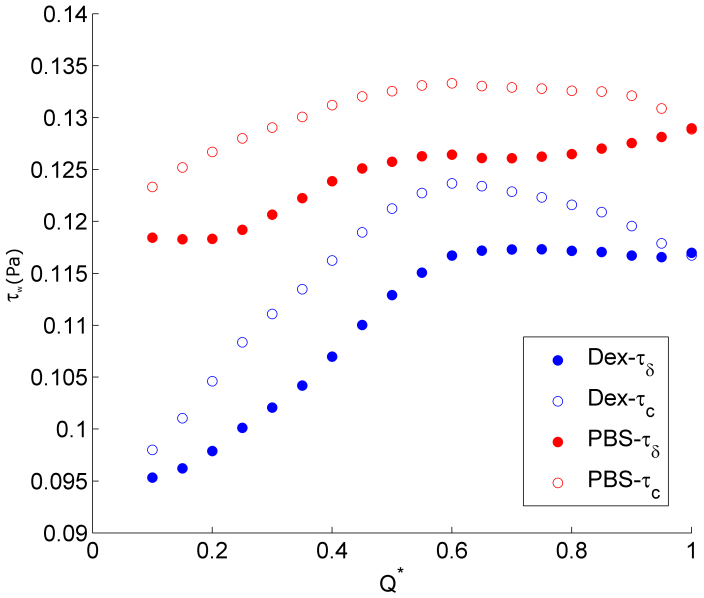

Figure 4.16: Average WSS on the channel walls from CFD as a function of flow ratio. Hollow circles $y^* = -0.5$ (subscript c) , filled circles $y^* = 0.5$ (subscript δ).

hence there would be a superimposed slope on the WSS data. Overall, it can be seen that aggregation decreases the WSS in the branches, as would be expected due the the enhanced radial migration observed in aggregating blood.

In Chapter 3 it was shown that based on the two-fluid approximation, the apparent viscosity decreased with increasing CDL width, and hence with decreasing flow ratio. The apparent viscosity for a rectangular channel can be derived from the equation for the flow rate

$$Q = \frac{h^3 w \Delta p}{12 \mu L}\left[1 - \sum_{n,odd}^{\infty} \frac{1}{n^5}\frac{192}{\pi^5}\frac{h}{w}\tanh\left(n\pi\frac{w}{2h}\right)\right] \tag{4.10}$$

Hence, for a given flow rate and pressure drop, the apparent viscosity is given by

$$\mu_a = \frac{h^3 w \Delta p}{12 Q L}\left[1 - \sum_{n,odd}^{\infty} \frac{1}{n^5}\frac{192}{\pi^5}\frac{h}{w}\tanh\left(n\pi\frac{w}{2h}\right)\right] \tag{4.11}$$

Which, for $h/w = 0.4$, and given $Q = \overline{U} h w$, can be simplified to

$$\mu_a = 0.2519\frac{h^2 \Delta p}{12 \overline{U} L} \tag{4.12}$$

Figure 4.17 shows how the apparent viscosity changed for the technique utilised in this chapter. Comparing Figure 4.17 with Figure 3.22, it can be seen that the same overall

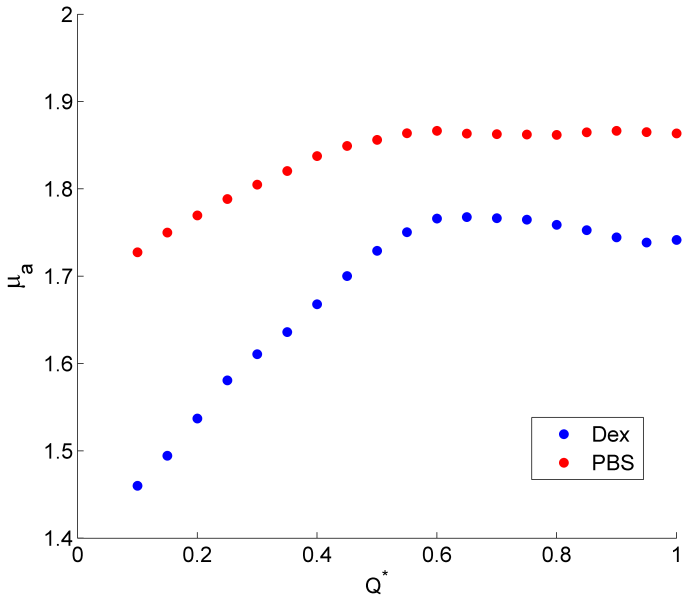

Figure 4.17: Apparent viscosity as predicted from the CFD data as a function of flow ratio.

trend is observed, with generally lower apparent viscosity in the daughter branch with a lower proportion of the overall flow. However, the shape of the curves based on the continuous model is less uniform, in that there is a clear difference between the high and low flow branches. It should be noted that the trends in Figure 4.17 are dependent on plasma skimming and the Fåhraeus effect, as well as the viscosity profiles. Separating these effects from one another shall be considered in greater depth in Chapter 5.

4.4.6 Limitations of the present approach

There is a certain degree of error inherent in μPIV analysis as a result of the finite volume, defined by the depth of focus of the imaging objective. For the fluorescent-μPIV data, the depth of field can be approximated using the method described by Olsen & Adrian (2000) (see Equation 2.3). For a $10\times$, $NA = 0.25$ objective, particle diameter of $1\mu m$ and an emission wavelength of $575nm$, it was found that particles across the entire depth of the channel contribute to the PIV measurement. For the RBC μPIV data, it is hard to predict z_{corr} as the aforementioned equation is defined assuming Gaussian particle distributions and coherent light. However, due to the significantly greater diameter of the RBC compared to the fluorescent tracer particles, z_{corr} could be expected to be larger for RBC μPIV than for the fluorescent μPIV, and hence also take the entire channel into account. It should be noted, however, that the influence of

particles on the correlation decreases with distance from the centre plane.

This finite depth of correlation would lead to an underestimation of the velocity magnitude. However, the normalised profile for the analytical solution for fully developed laminar flow in a rectangular channel does not change shape significantly at different depths. Hence, as normalised values are considered in the present study, this should not have a significant impact on the results. A commonly observed phenomenon in blood flow in horizontal channels is that, as the RBC density is greater than the plasma, RBCs tend to sediment. However, comparing the time scales (less than 1 minute) and flow rates used in the present study to the data of Alonso et al. (1995), it is expected that the effect of sedimentation will be minor in the present experiments. Moreover, no systematic change was observed in velocity or intensity results across the measurement period.

A further consideration in analysis of the present data is the relatively high aspect ratio of the channel. While this allowed for high resolution and ideal imaging properties, it is liable to influence the behaviour of the blood relative to round channels or ones with an aspect ratio closer to unity. This should be further investigated, but the fact that application of the model of Pries et al. (1992b), which was based on measurements in round channels, through use of the hydraulic diameter produced good agreement between methods is reassuring. The results of the present study showed that there is a strong qualitative agreement between velocity data obtained from RBC μPIV and CFD analyses of spatially variant viscosity fields. The CFD results were obtained based on the assumption that the viscosity of the fluid, for the particular system under consideration, is influenced predominantly by the haematocrit distribution. Nevertheless, a careful inspection of the graphs presented in Figures 4.12, 4.13 and 4.15 suggest that there are certain aspects of the flow that cannot be fully captured using the approach utilised in this study. This is to be expected to a certain degree as the fluid under study is complex in many aspects.

The technique used in this chapter is based on the assumption that the viscosity varies spatially such that it is dependent on a continuous, time-averaged haematocrit distribution. This quasi-continuum approach is unlikely to be valid for channels of diameters more comparable to the size of the cells. It seems reasonable to suggest that the assumption would break down for diameters less than $20\mu m$, as this is a critical dimension

observed in such phenomena as the Fåhraeus and Fåhraeus-Lindqvist effect (Cokelet, 1999). For significantly deeper channels, this analysis would become impractical experimentally as increased depth makes both PIV and haematocrit distribution difficult to analyse due to increased light absorption. For the present setup, such experiments become unfeasible for channels deeper than $60\mu m$. The assumption of the influence of haematocrit on viscosity has no rational upper limit; indeed Pries et al. (1992b) report their data for tube sizes up to $1mm$.

4.5 Closure

In the present chapter, a new technique has been described which provides a continuous one-dimensional viscosity profile. This approach was intended as a development of the two constant-viscosity phase analytical model considered in the previous chapter. The results indicated the presence of plasma skimming, which was enhanced by RBC aggregation. In the daughter branches, it was found that the haematocrit distribution displayed skewed profiles and the shape of the profile was dominated by flow ratio and the presence of aggregation. In order to examine the efficacy of the approach, the results were combined with CFD and an empirical viscosity model to predict velocity profiles. The simulations accurately predicted the observed skewness in the velocity profiles, supporting the importance of considering a continuous haematocrit distribution, rather than a CDL and RBC core. However, the velocity profile bluntness was overpredicted by the computational model and the high aspect ratio channel precluded further analysis due to lack of information in the out of plane direction.

In the next chapter, the present approach will be further developed using a channel with an aspect ratio of unity. This allows for certain assumptions to be made which lead to predicted three dimensional haematocrit distributions. Moreover, a calibration stage is carried out to improve the accuracy of the technique and the image acquisition technique is improved, allowing quasi-simultaneous measurements of both RBC and SM velocities. In addition to varying flow ratio, a range of parent branch flow rates are considered. The data comprises the first experimental parametric study of microscale blood flow analysed as a continuous multiphase fluid.

Chapter 5

Phase discrimination measurements [†]

This chapter describes a technique with which the velocities of both the RBCs and the suspending medium can be measured simultaneously. In combination with an extension of the haematocrit estimation technique developed in the previous chapter, this provides a full experimental description of blood as a multiphase fluid.

5.1 Introduction

In the previous chapter, a methodology for acquiring one-dimensional haematocrit profiles was developed and tested. In the present chapter, this approach will be further developed to provide three-dimensional haematocrit distributions throughout the entire bifurcation domain. Additionally, a technique which enables both phases of the blood to be measured quasi-simultaneously will be used, providing a measurement of the multiphase nature of blood. An additional parameter, the parent branch flow rate, is also investigated. The flow configuration utilised for this chapter is that of the 'side-T' bifurcation, wherein the 'daughter' branch is at 90 degrees to the 'parent' and 'outlet' branches (which are colinear). Figure 5.1 shows the geometry and relevant terminology to be used in this chapter. This geometry provides a better approximation of a blood vessel than the high aspect ratio channel used in Chapters 3 and 4. The width and height of all branches is $D = 50\mu m$ [‡]. The aspect ratio of unity allows for certain assumptions to be made about out of plane velocity and haematocrit distributions that would not be

[†]The data presented in this Chapter was presented at the *IMA Conference on Mathematics of Medical Devices and Surgical Procedures*, September $17^{th} - 19^{th}$ 2012, London, UK.

[‡]For simplicity D is used, as for an aspect ratio of unity, the hydraulic diameter is equal to the diameter of a cylindrical tube, more commonly associated with the geometry of a microvessel.

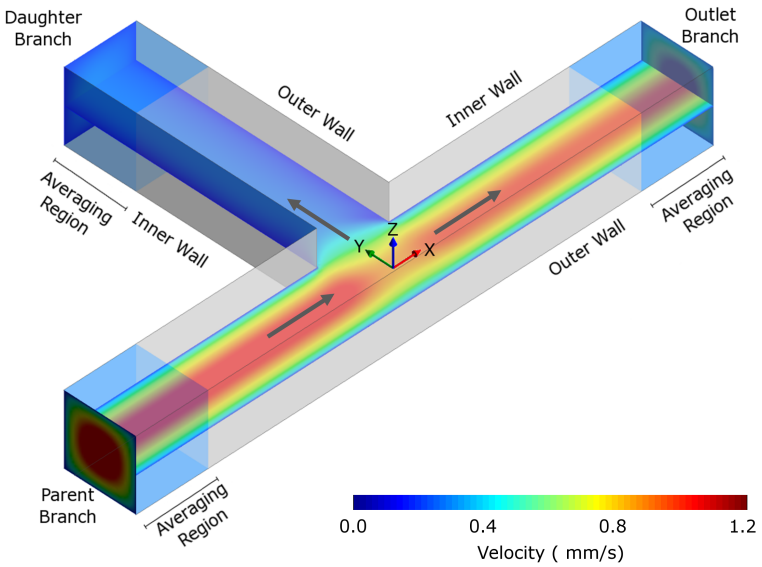

Figure 5.1: Terminology and coordinate system for the geometry used in the present chapter. Contours show sample velocity magnitude for $Q^* = 0.2$. Flow directions are indicated by the arrows. The region shown is the imaging region considered for the present data, but branches extend in all directions.

as viable for aspect ratios other than unity.

The system was modified so that double frame images could be acquired with strobe illumination, as described in Chapter 2. This allows quasi-simultaneous acquisition of images of the RBCs and fluorescent microparticles in the suspending medium (SM). The images are processed using ensemble average PIV algorithms to provide data on both phases of the fluid. Additionally, the RBC images are used to estimate the haematocrit distribution in a refinement of the technique used in the previous chapter.

The independent parameters analysed in the present chapter are the flow ratio and parent branch flow rate. The former ranges from $Q_d^* \approx 0.05 - 0.5$ in the daughter branch and $Q_o^* \approx 0.5 - 0.95$ in the outlet branch. The parent branch flow rate is presented as normalised average velocities (in channel 'diameters' per second), $V^* = \overline{U}/D \approx 12 - 160 s^{-1}$. As with previous chapters, samples suspended in PBS and Dextran solutions are utilised in order to consider the effects of RBC aggregation. A feed haematocrit of $H = 0.20$ was utilised and a total of 77 data sets were acquired.

In this chapter, a description of the haematocrit measurement technique is provided, followed by a discussion of the results for various flow rates and flow ratios. Subsequently, the experimental velocity measurements for each phase will be analysed and their relationship to the haematocrit distributions will be examined.

5.2 Development of the haematocrit distribution technique

In Chapter 4, a new technique was described which converted average image intensities into one-dimensional haematocrit distributions based on the assumption of a linear intensity - haematocrit curve. In the present chapter, a calibration is performed in order to obtain a more accurate relationship. Subsequently, instead of simply defining haematocrit profiles, full two-dimensional (x, y plane) distributions are acquired, made possible due to a larger number of acquired images and refinements to the technique. Further processing provides estimations of full three-dimensional haematocrit distributions. This section describes these stages in detail.

5.2.1 Calibration for image intensity vs. haematocrit curve

As in the previous chapter, the approach for estimating the haematocrit distribution is based on the averaging of a large number of instantaneous strobe-illuminated images, from which a time average intensity distribution can be calculated. As each cell absorbs a certain amount of the light provided by the strobe, the greater the number of cells that pass through a given pixel location, the less light will be transmitted and the intensity of the pixel $I(x, y)$ will decrease. To show the basis of the assumption and to familiarise the reader with the new geometry, Figure 5.2 shows sample images of the bifurcation region at low and high flow ratios for Dextran and PBS cases.

In Figure 5.2a and c, the proportion of flow entering the daughter branch is low and as a result there is a large cell-free region near the inner wall. This result should be considered in comparison with Figure 1.10, which shows a similar occurrence *in vivo*. For the Dextran case (Figure 5.2a), the cell-free region is greater than for the PBS case (Figure 5.2c), and persists downstream, whereas for the PBS case it can be seen that the RBCs rapidly impinge upon the layer, as was described in Chapter 3. At a higher flow ratio (Figure 5.2b and d), the cell-free region is smaller, but it can be seen that the local haematocrit is still reduced near the inner wall. However, the intensity distribution from a single image is not sufficient for the present purposes as it would have considerable scatter. Hence, as in the previous chapter, the average image from a stack of 120 images (2 for each of the 60 image pairs acquired for each data set) was calculated to give the intensity distribution of $I(x, y)$ in order to provide a smooth

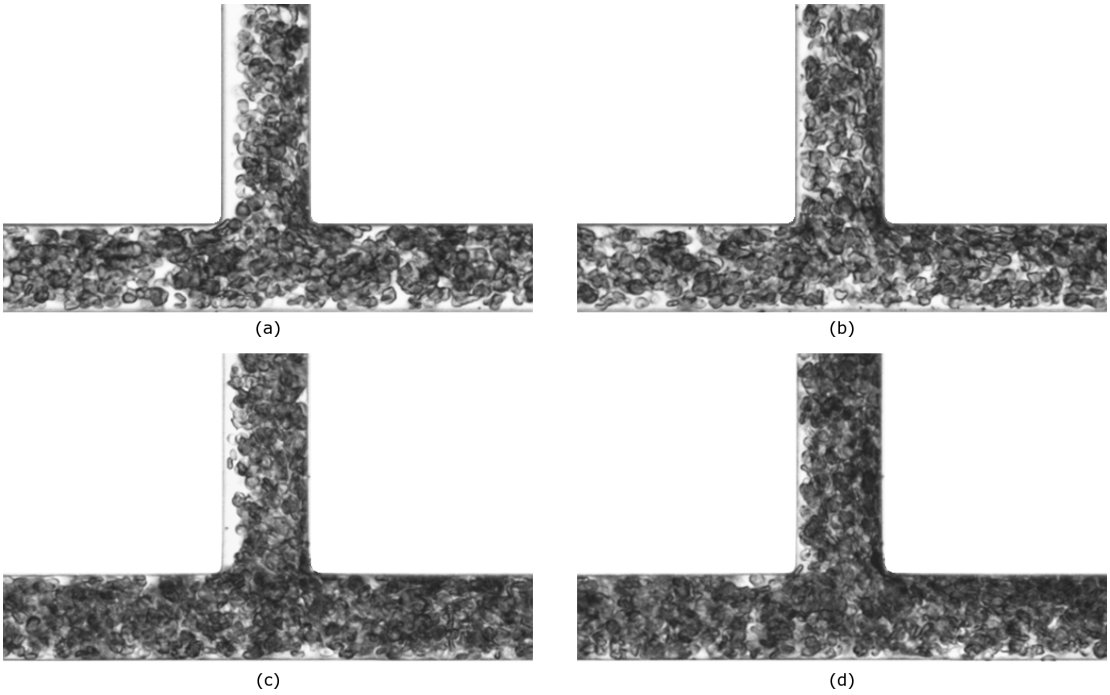

Figure 5.2: Sample images in bifurcation, enhanced for clarity. Flow enters from the left. (a) Dextran - $Q_d^* = 0.16$, (b) Dextran - $Q_d^* = 0.41$, (c) PBS - $Q_d^* = 0.14$, (d) PBS - $Q_d^* = 0.44$.

profile which would better represent the time averaged distribution of RBCs. This value was calculated as in Equation 4.4.

The relationship between the haematocrit and the normalised intensity then needs to be established. In order to do this, a number of images were acquired in a long straight section of the microchannel at a range of feed haematocrits from 0.05 to 0.3. Figure 5.3 shows sample images over $100\mu m$ long sections for the calibration data.

For each feed haematocrit, data at low, medium and high flow rates were acquired for both aggregating and non-aggregating cases. For each case, the average image was calculated and the intensity profile was averaged along the length of the channel. As can be seen in Figure 5.3, there are regions of around 4 pixels which are unusable at each channel wall due to diffraction at the channel edge (as discussed in Chapter 2). This region was cropped and a sixth order polynomial was fit through the remaining data points to extrapolate the data at the wall. The profile was then integrated to give an average intensity for each feed haematocrit, H_F. However, the feed haematocrit will not be equal to the haematocrit in the channel, H_C as a result of red cell screening at the entrance to the channel and the Fåhraeus effect. Gaehtgens et al. (1978) described cell screening relationships for aggregating (Equation 5.1) and non-aggregating (Equation

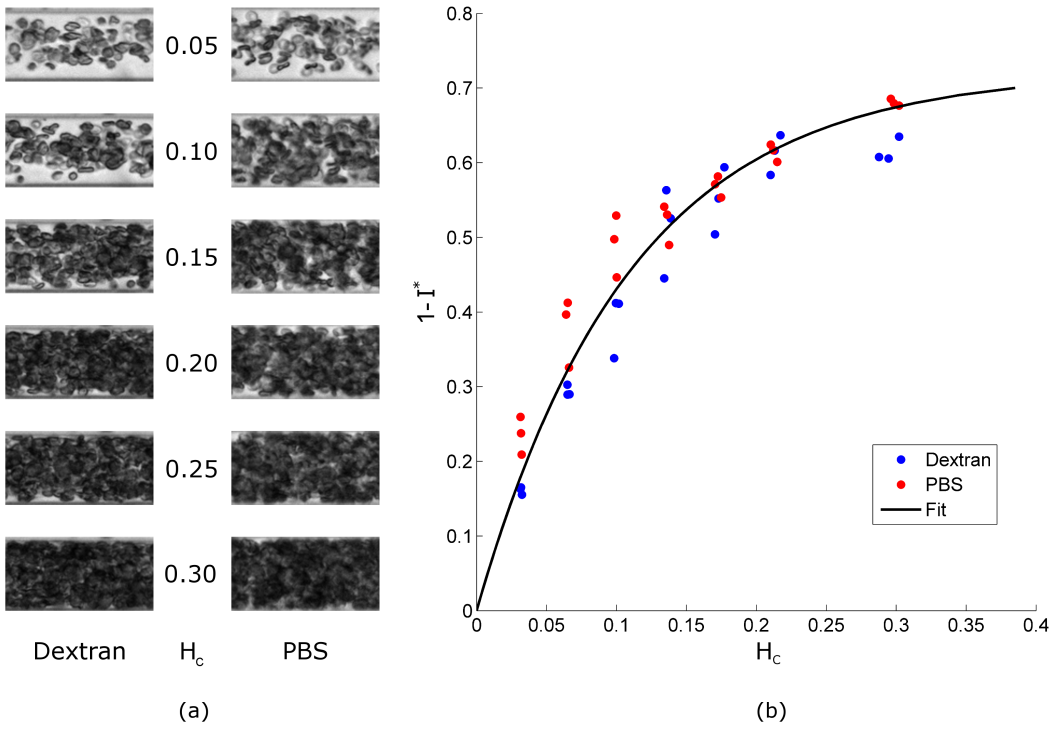

Figure 5.3: Calibration data. (a) Sample images at various haematocrits. Left column shows Dextran cases, Right column shows PBS cases. (b) Calibration curve comparing average intensity to channel haematocrit. Fit is of the form $1 - I^* = a\left(1 - e^{bH_c}\right)$.

5.2) samples in capillary tubes based on the normalised velocity:

$$H_D = H_F\left(0.901 + 0.029\log\left(\overline{U}/D\right)\right) \tag{5.1}$$

$$H_D = H_F\left(0.878 + 0.042\log\left(\overline{U}/D\right)\right) \tag{5.2}$$

where H_D is the discharge haematocrit. To account for the Fåhraeus effect, the empirical equation defined by Pries et al. (1990) was utilised

$$H_C = H_D\left(H_D + (1 - H_D)\left(1 + 1.7e^{-0.415D} - 0.6e^{-0.011D}\right)\right) \tag{5.3}$$

The estimated channel haematocrit can then be plotted against the average value of $1 - I^*$ (so that low values correspond to low haematocrit) for each of the cases acquired for the calibration (three flow rates, Dextran and PBS for each feed haematocrit) as shown in Figure 5.3. Non-linear regression, using an iterative least squares regression in Matlab, is then used to fit the data to an equation of the form

$$1 - I^* = a\left(1 - e^{bH_c}\right) \tag{5.4}$$

The parameter a represents the saturation point for $1 - I^*$ and b provides an indication of the non-linearity. Combining the data for Dextran and PBS cases at all flow rates the regression yields $a = 0.7219$ and $b = -9.079$ and the line is plotted in Figure 5.3. The R^2 value for this fit is 0.94.

5.2.2 Estimation of two-dimensional haematocrit distribution

Equation 5.4 was used to define the haematocrit distribution in the bifurcation as follows. As discussed with regards to the calibration images, the regions near the wall are not usable due to refraction at the wall/fluid interface, and the near wall data points were extrapolated as before.

This approach was carried out by sweeping along each branch: at each axial location, x (or y in the daughter branch) an average profile was calculated over a region of $x \pm 0.125D$ ($x \pm 6.25\mu m$) in order to reduce errors due to the finite number of images in the averaging process. The final distribution was then smoothed with a disk filter [†] with a radius of 3.

Figure 5.4 shows sample time average haematocrit distributions in the bifurcation for various flow rates and flow ratios. Considering Figure 5.4a, a Dextran case with a daughter branch flow ratio of $Q_d^* = 0.14$, it can be seen that in the parent branch, the haematocrit distribution is approximately symmetrical, with the highest values in the centre and very low values at the channel wall, due to the cell-depleted layer which occurs as a result of radial migration (and synaeresis in the presence of aggregation). At the far corner of the bifurcation, the haematocrit is greatly increased and along the outer wall (refer to Figure 5.1 for channel location terminology) of the daughter branch there is a region of elevated haematocrit. A corresponding enhanced cell-depleted layer can be observed at the inner wall. In the outlet branch, the haematocrit is significantly increased along the inner wall, and very slightly decreased on the outer wall compared to the parent branch. Figure 5.4c shows the haematocrit distribution at a higher flow ratio of 0.35 but with a lower parent branch velocity. In the parent branch, it can be seen

[†]Disk filters, also known as pillbox filters, are similar to Gaussian filters, but with a broader distribution.

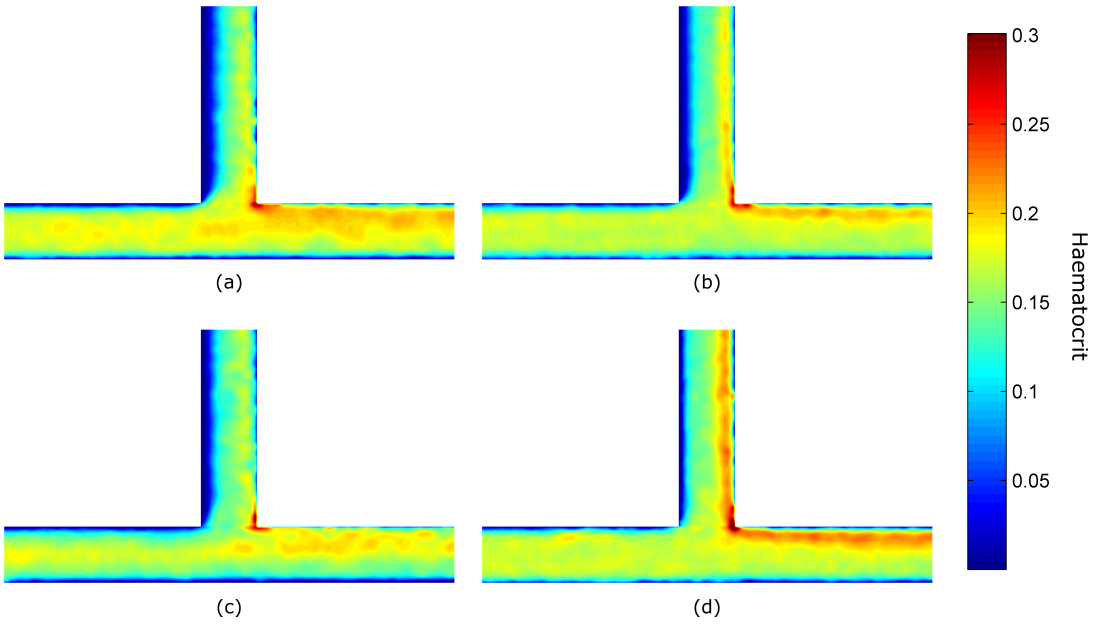

Figure 5.4: Selected average x, y haematocrit distributions. (a) Dextran - $V^* = 50.4s^{-1}$, $Q_d^* = 0.14$, (b) PBS $U_p = 32.4s^{-1}$, $Q_d^* = 0.14$, (c) Dextran - $U_p = 23.2s^{-1}$, $Q_d^* = 0.35$, (d) PBS - $U_p = 12.4s^{-1}$, $Q_d^* = 0.35$. Flow enters from the left.

that the haematocrit distribution is narrower, i.e. the RBCs are more concentrated in the centre of the channel, compared with the high velocity case shown in Figure 5.4a. The width of the cell-depleted region at the inner wall of the daughter branch is decreased compared to the lower flow ratio case (Figure 5.4a) and the high haematocrit region at the inner wall of the outlet branch is less intense. For the PBS cases, Figure 5.4b and d, the haematocrit distributions for the same flow ratios, show some similar characteristics to those in the Dextran cases, except that there are thin ($\approx 10\mu m$) bands of significantly increased haematocrit in both the daughter and outlet branches. Additionally, the cell-depleted region near the inner wall of the daughter branch is significantly smaller in the absence of aggregation.

5.2.3 Three-dimensional haematocrit distributions

In this chapter, three dimensional haematocrit distributions are derived in order to allow for phase discrimination and, in the subsequent chapter, to allow three dimensional simulations with haematocrit dependent viscosity. In order to derive a three-dimensional haematocrit distribution, the following assumption is made: given that the system is at a steady state and there is negligible sedimentation during the acquisition period, it is reasonable to assume that the (x, z) plane haematocrit distribution in the parent branch

is equivalent to that in the (x, y) plane. The parent branch haematocrit profile, H_p, is defined as the average profile in the averaging region indicated in Figure 5.1. Let the x location be termed x_p. As the data was acquired in the central plane, $z = 0$, hence $H_p = H_p(x_p, y, 0)$. The described assumption can be written as

$$H_p(x_p, 0, z) = H_p(x_p, y, 0) \tag{5.5}$$

In the case that $H_p(x_p, y, 0)$ is not perfectly symmetric, an asymmetry would be introduced in the (x, z) or (y, z) planes which would have no theoretical basis and would be an experimental artefact. Hence $H_p(x_p, y, 0)$ is forced to be symmetric by averaging the profile on each side of the centreline, creating a symmetric one dimensional profile, H_s, where the s indicates symmetry (note that the coordinate system shown in Figure 5.1 is such that in the centre of the parent branch is at $y = 0$).

$$H_s(x_p, y, 0) = H_s(x_p, -y, 0) = \frac{H_p(x_p, y, 0) + H_p(x_p, -y, 0)}{2} \tag{5.6}$$

The root mean square of the difference the raw (H_p) and symmetric (H_s) profiles was calculated for all cases and had a mean of 0.004 and a max of 0.009 (in units of haematocrit). Based on Equation 5.5, one can then write

$$H_z(x_p, 0, z) = H_s(x_p, \pm y, 0) \tag{5.7}$$

The technique assumes that all cells in the channel influence the absorption of light, and hence the estimated haematocrit a given (x, y) location represents the average haematocrit throughout the channel depth. Moreover, it is reasonable to assume that the relative distribution does not change throughout the channel in the out of plane direction, due to the planar geometry, unity aspect ratio and the absence of significant forces in the (x, z) or (y, z) planes. Hence, the symmetric profile $H_z(x_p, 0, z)$ is normalised with its mean, $\overline{H_z} = \frac{1}{D}\int H_z dz$, and used to define the haematocrit at a given location in the channel according to

$$H(x, y, z) = H(x, y)\frac{H_z(x_p, 0, z)}{\overline{H_z}} \tag{5.8}$$

Sample haematocrit distributions in the z-plane are shown in Figure 5.5 for a Dextran case at a low flow ratio. Figure 5.5a shows the parent branch haematocrit distribution. It

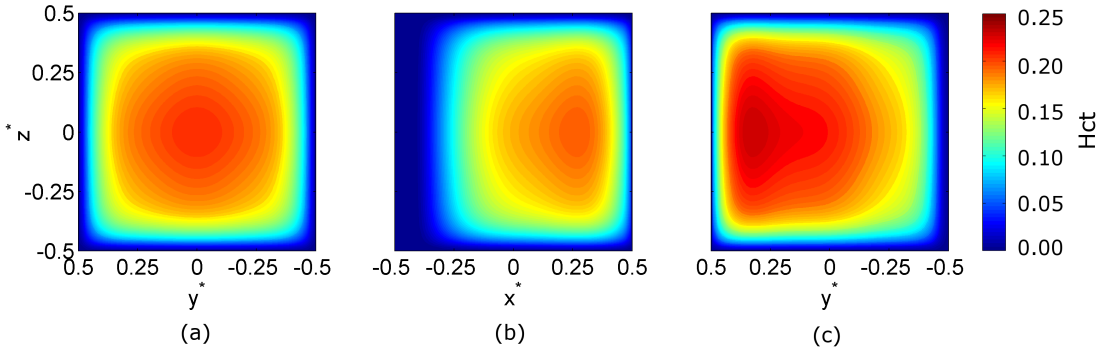

Figure 5.5: Sample z-plane haematocrit distributions for Dextran case - $U_p = 27.4s^{-1}$, $Q_d^* = 0.14$. (a) Parent branch (with enforced symmetry for clarity), (b) Daughter branch, (c) Outlet branch - note y^* axis is inverted to account for the flow direction.

can be seen that the haematocrit increases from zero at the channel edges to a maximum at the channel centre. In the daughter branch (Figure 5.5b), the distribution is strongly skewed towards the outer wall ($x^* = 0.5$), but the z plane distribution is equivalent to that in the parent branch, as a result of Equation 5.8. For the outlet branch (Figure 5.5c), there is a region of elevated haematocrit around $z^* = 0$, close to the inner wall ($y^* = 0.5$) and the distribution is significantly less skewed than for the daughter branch. It should be noted that even close to the high haematocrit region in the daughter branch, the haematocrit tends to zero at the walls, a necessary condition for the data to be realistic.

5.3 Multiphase flow analysis

In this chapter, the velocity of both phases of the blood (the RBCs and SM) were measured experimentally, in addition to the concentration of RBCs, from which the SM concentration can be derived. Using the velocities and concentrations of each phase, the total fluid flux can be calculated. In order to do this, the three dimensional velocity distribution needs to be defined. This is carried out by making the same assumption as for the haematocrit profiles, i.e. that due to the system being at a steady state and the planar geometry, in the absence of sedimentation, the (x, z) and (y, z) plane velocity should not be significantly different to that in the (x, y) plane in the parent branch. Hence a one dimensional profile $U_z\,(z)$ is defined from the parent branch velocity profile $U_p\,(x, y)$ at location x_p

$$U_z\left(x_p, 0, z\right) = U_p\left(x_p, y, 0\right) \tag{5.9}$$

This can be applied to the whole domain similarly to Equation 5.8 for the haematocrit distribution:

$$U\left(x, y, z\right) = U\left(x, y, 0\right) \frac{U_z\left(x_p, 0, z\right)}{U_{z,max}} \tag{5.10}$$

It should be noted that the normalisation of the velocity is carried out relative to the maximum velocity, $U_{z,max}$, as measurements in the midplane of the channel ($z = 0$) will provide maximum velocities. For the haematocrit, the technique assumes influence of all cells on the absorption of light, and hence the estimated value at a given (x, y) location represents the average haematocrit at that location.

The volumetric flow rate for the RBCs can be calculated according to

$$Q_{rbc} = \int\int H\left(y, z\right) U_{rbc}\left(y, z\right) dy\, dz \tag{5.11}$$

Where U_{rbc} is the RBC velocity data calculated from the PIV processing. Similarly, for the SM velocity data, U_{sm}, the volumetric flow rate is given by

$$Q_{sm} = \int\int \left(1 - H\left(y, z\right)\right) U_{sm}\left(y, z\right) dy\, dz \tag{5.12}$$

The total flux is then defined as the sum of the two phases

$$Q_{tot} = Q_{rbc} + Q_{sm} \tag{5.13}$$

As in previous chapters, the flow ratio is the proportion of flow entering a branch from the parent branch, defined as $Q_d^* = Q_d/Q_p$ and $Q_o^* = Q_o/Q_p$ for the daughter and outlet branches respectively, noting that ideally $Q_o^* = 1 - Q_d^*$. As increasing Q_d^* corresponds to decreasing Q_o^*, referring to 'low' or 'high' flow ratio could be ambiguous. Herein, such terms will refer to the daughter branch. In this chapter, the effect of the flow rate in the parent branch will be analysed relative to the normalised velocity, defined as $V^* = Q_{tot}/D^3$, giving units of channel 'diameters' per second (s^{-1}). In the daughter and outlet branches, both the normalised velocity and the flow ratio will be considered. The latter will also be defined based on the total flux, hence $Q_d^* = Q_{d,tot}/Q_{p,tot}$ and $Q_o^* = Q_{o,tot}/Q_{p,tot}$.

Table 5.1: Mean percentage errors in flux conservation for the total flow and the two phases.

	Dex (%)	PBS (%)
e_{tot}	2.49	6.12
e_{rbc}	1.67	4.21
e_{sm}	2.99	6.68

As discussed in §2.7.1, the bifurcation provides a means by which to test the accuracy of the assumptions made in this chapter via evaluating the conservation of mass. For the individual phases, the error in conservation of mass can be calculated for each phase according to Equation 2.6:

$$e = \frac{Q_p - Q_o - Q_d}{Q_p} \times 100\% \tag{5.14}$$

as the density is a constant and can thus be removed. For the total conservation of mass, the densities of the RBCs and SM (values provided in Chapter 1) are also taken into account. Each Q term is replaced by $\rho_{sm}Q_{sm} + \rho_{rbc}Q_{rbc}$.

Table 5.1 summarises these errors for each phase of the blood and the calculated total volumetric flux. It can be seen that in general, the Dextran cases were more accurate than the PBS cases for both phases. This may be due to the fact that the reduced freedom of motion of the cells results in more repeatable patterns between frames, improving the accuracy of the PIV algorithm. Aggregation has previously been reported to improve the accuracy of PIV processing algorithms (Dusting et al., 2009).

All values are relatively low, implying good accuracy in the results and providing some confidence that the extension of the two-dimensional data to three dimensions is valid. Any cases for which e_{tot}, e_{rbc} or e_{sm} were greater than 10% were omitted from the analysis (this was only the case for two PBS cases out of a total of 77 data sets).

5.4 Haematocrit distribution results

In this section the results of the haematocrit distribution measurements will be discussed, first in the form of bulk distribution (i.e. plasma skimming) then in terms of the individual profiles and their characteristics under different experimental conditions.

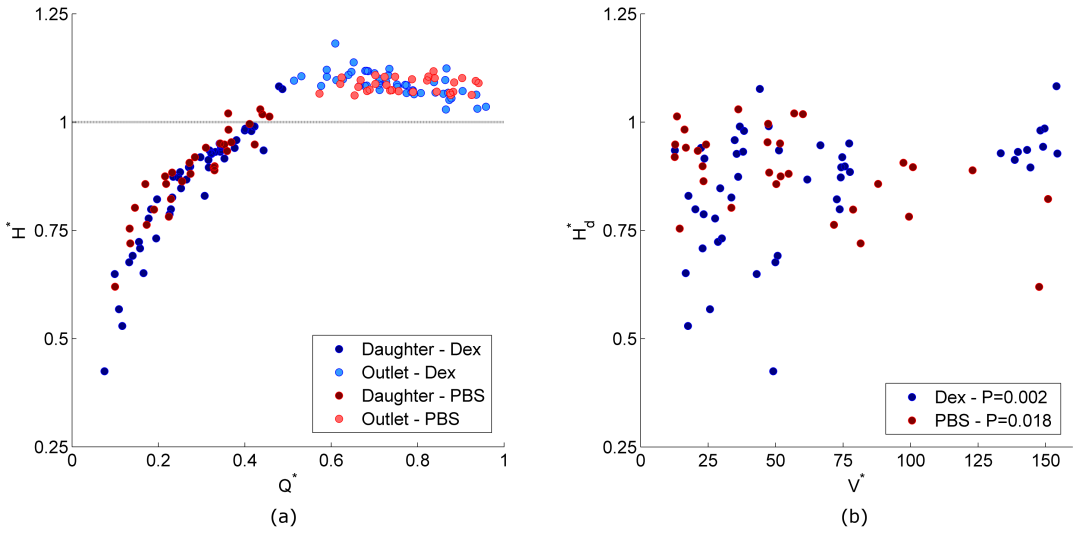

Figure 5.6: (a) Haematocrit ratio $H^* = H/H_p$ against flow ratio for the daughter and outlet branches, (b) Daughter branch haematocrit ratio $H_d^* = H_d/H_p$ against normalised parent branch velocity.

5.4.1 Bulk haematocrit distribution

Figure 5.6a shows the plot of the haematocrit ratio $H^* = H/H_p$ against Q^* (using Q_{tot}^* for the present data). It can be seen that in both the Dextran and PBS cases, the haematocrit ratio is increased in the outlet branch and decreased in the daughter branch. This is evidence of plasma skimming. The data shown in Figure 5.6 is comparable to Figure 4.5. However, in this case the plasma skimming effect is stronger (as can be seen from the relatively lower H^* values for $Q^* < 0.5$ and greater H^* for $Q^* > 0.5$), particularly for the PBS case, which contrary to the previous chapter shows almost as much plasma skimming as the Dextran case. The overall increase in plasma skimming relative to the previous chapter could be expected as the phenomenon has been reported to have a larger effect with decreasing channel dimensions (Fenton et al., 1985).

A further parameter which may affect plasma skimming is the parent branch flow rate, presented as a normalised velocity in Figure 5.6b. Although the data shows a certain amount of scatter, there are statistically significant trends in both the Dextran and PBS cases. For the PBS case, as the flow rate increases, the extent of plasma skimming also increases (decreasing H_d^*), whilst for the Dextran case the opposite trend is observed: the effect of plasma skimming decreases (increasing H_d^*) as the parent branch flow rate increases. These opposing trends will be discussed later in the chapter.

The flux/flow ratio curve is shown in Figure 5.7. The data is fit to the sigmoidal curve

defined by Pries et al. (1989), with $F^* = Q_{rbc}$ and $Q^* = Q^*_{tot}$:

$$F^* = \left[1 + e^{-(G + Jlogit(0.5 - T(0.5 - Q^*)))}\right]^{-1} \tag{5.15}$$

In this case, although the branches are of equal size, one would not expect a symmetric curve due to the geometric difference between the daughter and outlet branches (as opposed to the symmetrical 'straight-T' configuration considered in Chapters 3 and 4), hence G would not be expected to be 0. Furthermore, in this form of the equation, T is included, as the critical flow ratio (below which a haematocrit of zero is observed) was found to be non-zero. The parameters G, J and T are found to three decimal places using a brute force method [†] with the sum of the root mean square error for both branches as the fit quality criterion.

In both Dextran and PBS cases, it can be seen that plasma skimming is occurring, as the curves deviate from the $F^* = Q^*$ line, indicated in grey on the figure. Converting T into a critical flow ratio Q^*_0 according to $Q^*_0 = 0.5 - 0.5/T$ (Pries et al., 1989) gives $Q^*_d = 0.024$ and 0.014 for the Dextran and PBS cases respectively. The values found for the two cases are very similar and indicate the presence of a daughter branch flow ratio of around 2% at which no cells would enter the side branch. The J parameter, indicating the sigmoidal nature of the curve, is slightly greater for the PBS case while the asymmetry parameter G is greater for the Dextran case. Thus, for a flow ratio of 0.5, there would be more plasma skimming in the Dextran case.

5.4.2 Local haematocrit distribution

It was observed that the parent branch flow rate affected the degree of plasma skimming in the daughter branch. The reasons for this can be explained by considering the effect of parent branch flow rate on the parent branch haematocrit profiles. Figure 5.8 shows the haematocrit profile at low, medium and high normalised velocities for Dextran and PBS cases. The profiles shown are those which were used to define the out of plane distributions (H_s), and are therefore perfectly symmetrical.

For the Dextran case, at low V^* (Figure 5.8, light blue line) there is a very clear increase of RBC concentration in the channel centre. At higher velocities, wherein the extent

[†] A fit is calculated for each combination of parameters and the corresponding error is recorded. The parameter set which gives the minimum error is assumed to provide the best fit.

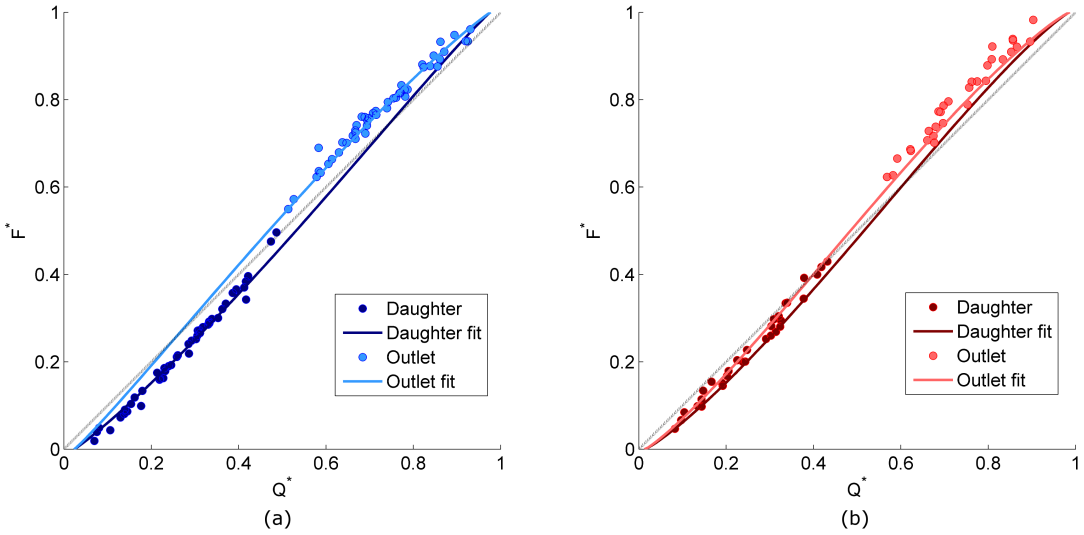

Figure 5.7: Flux-flow ratio curves for the daughter and outlet branches and fits according to Equation 5.15. (a) Dextran case: $G = \pm 0.140$, $J = 1.066$, $T = 1.050$, (b) PBS case: $G = \pm 0.073$, $J = 1.139$, $T = 1.029$.

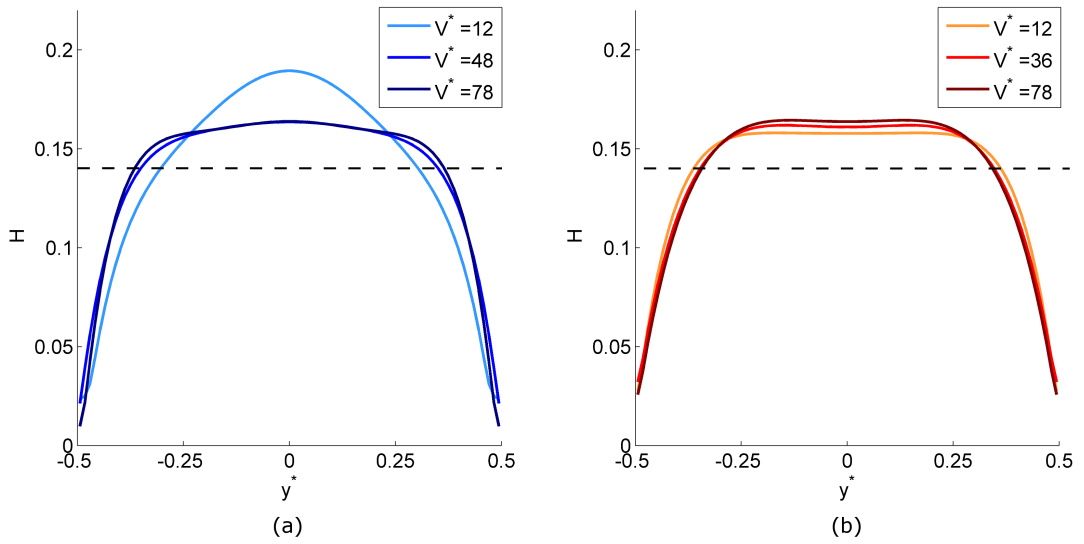

Figure 5.8: Sample haematocrit profiles in the parent branch (symmetric) for low medium and high normalised velocities. (a) Dextran case, (b) PBS case. Dashed line shows mean haematocrit (0.14).

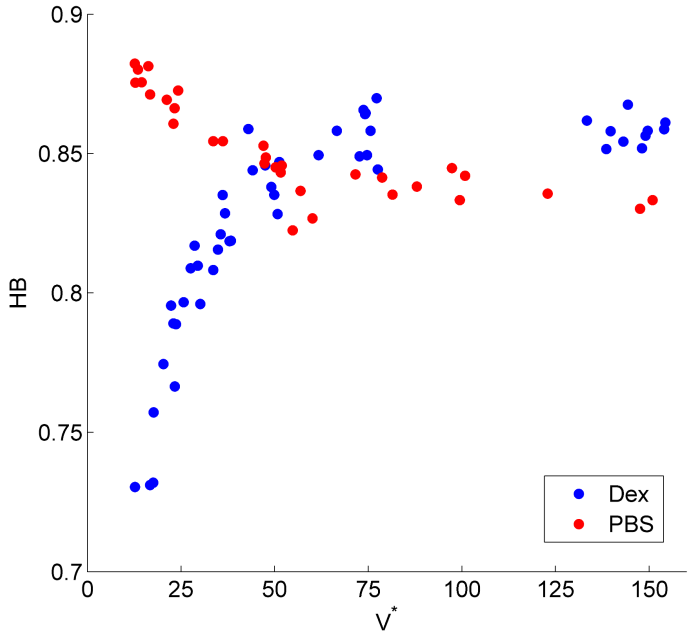

Figure 5.9: Haematocrit profile bluntness, *HB* against normalised velocity V^* in the parent branch.

of aggregation would be reduced, the profiles are much blunter. For the PBS case, the observed trend is opposite, in that the profiles are blunter at low flow ratios than at higher ones, although the differences between cases are less than for the Dextran case. In the absence of aggregation, this is likely a result of increased radial migration at higher flow rates (Caro et al., 2012).

In order to analyse these trends in more detail, a simple bluntness parameter, *HB*, is defined as the average haematocrit divided by the maximum haematocrit, similarly to that used by previous investigators for velocity profiles (Tangelder et al., 1986; Bishop et al., 2001a) and in Chapter 3 of the present study. This is plotted against normalised parent branch velocity in Figure 5.9. Note that $HB = 1$ would represent a uniform haematocrit distribution. It can be seen that at low velocities, the Dextran samples are significantly less blunt than the PBS cases, but at around $V^* = 50s^{-1}$ this relationship is inverted and the Dextran cases are marginally more blunt than the PBS ones. These trends arise from the interplay between radial migration, RBC deformation and RBC aggregation and will be discussed in more detail later in the chapter.

Comparisons of the haematocrit profiles are provided for the daughter and outlet branches in Figure 5.10. Figure 5.10a shows sample haematocrit profiles in the daughter branch at three flow ratios for the Dextran case. It can be seen that the profiles are

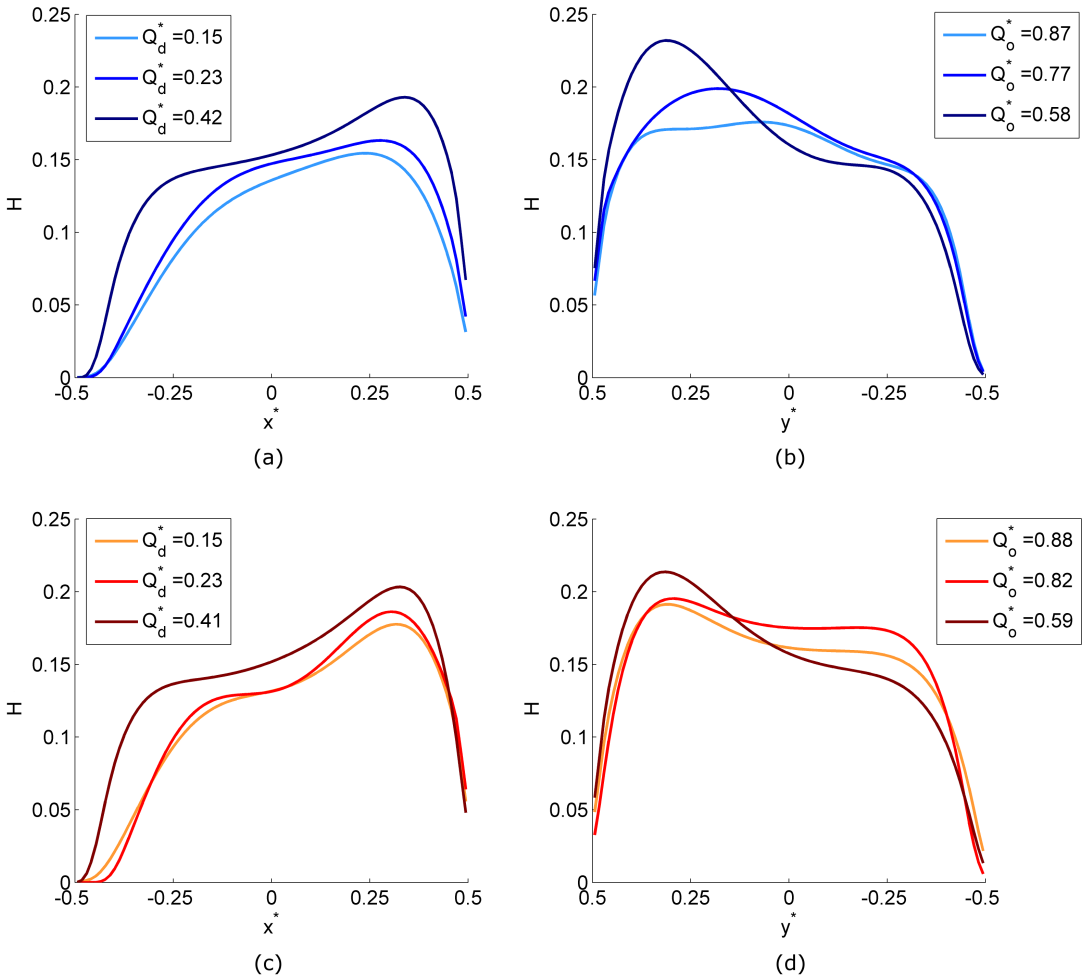

Figure 5.10: Sample haematocrit profiles for low medium and high flow ratios. (a) Dextran - Daughter, (b) Dextran - Outlet, (c) PBS - Daughter, (d) PBS - Outlet. Haematocrits are normalised such that the parent branch haematocrit for that case would be equal to 0.14.

all strongly skewed towards the outer wall ($x^* = 0.5$). In all cases, there is a peak in the region $x^* = 0.25 - 0.3$, which is closer to the wall and more pronounced, as Q_d^* increases.

There is a region of almost zero haematocrit at the inner wall ($x^* = -0.5$), and the haematocrit gradually increases with distance from the wall for all cases, although the region of low haematocrit is larger for the lower flow ratios. At the outer wall however, ($x^* = 0.5$), the minimum haematocrit is around 0.03 for the lowest flow ratio, increasing to more than 0.07 at the highest flow ratio, which is greater than it was for the parent branch in all cases. For the same flow ratio cases in the outlet branch (Figure 5.10b), the distributions are quite different. At the outer wall ($y^* = -0.5$) the gradient

of the haematocrit distribution is similar in all cases and comparable to those observed in Figure 5.8 for the parent branch. At the inner wall ($y^* = 0.5$), the haematocrit has a minimum of $0.06 - 0.08$, increasing as Q_o^* decreases. Notably, for the lowest Q_o^*, which is closest to an even distribution of flow between the two branches, there is a significant peak in haematocrit at around $y^* = 0.3$, which is not as pronounced in the cases where a greater proportion of flow enters the outlet branch ($Q_o^* = 0.77$ and 0.87). It should be noted that at $Q_d^* = 0$, $Q_o^* = 1$, the characteristics in the outlet branch should be very similar to the parent branch.

For the PBS case, at high Q_d^*, the profile in the daughter branch (Figure 5.10c) is similar to the Dextran case (Figure 5.10a), although the peak around $x^* = 0.3$ is more pronounced. At lower Q_d^*, the profiles are distinctly bimodal, which was not observed in the aggregating case.

In the outlet branch for the PBS cases (Figure 5.10d), the distributions are flatter than for the Dextran case. It can also be seen that for the PBS case, the outlet branch profiles are more similar to the profiles observed in the parent branch (Figure 5.8) than for the Dextran case.

In order to investigate the asymmetry of the profiles, a simple skewness parameter is considered, defined as the proportion of the total haematocrit which lies adjacent to the inner wall. This can be written for the daughter branch as

$$HS_d = \frac{\int_{-0.5}^{0} H\left(x^*\right) dx^*}{\int_{-0.5}^{0.5} H\left(x^*\right) dx^*} \tag{5.16}$$

and for the outlet branch as

$$HS_o = \frac{\int_{0}^{0.5} H\left(y^*\right) dy^*}{\int_{-0.5}^{0.5} H\left(y^*\right) dy^*} \tag{5.17}$$

where the change in coordinates is used in order to keep the inner wall on the same side of the profile. These equations are used for the haematocrit skewness, as opposed to the velocity skewness parameter used in the previous chapters, in order to capture more information about the shape of the profile as a whole. Determining the skewness based on the location of the maximum value (as carried out for the velocity skewness in Chapters 3-6) would not represent these profile shapes as effectively, as the peaks in the profiles shown in Figure 5.10 would dominate the results. The skewness defined by

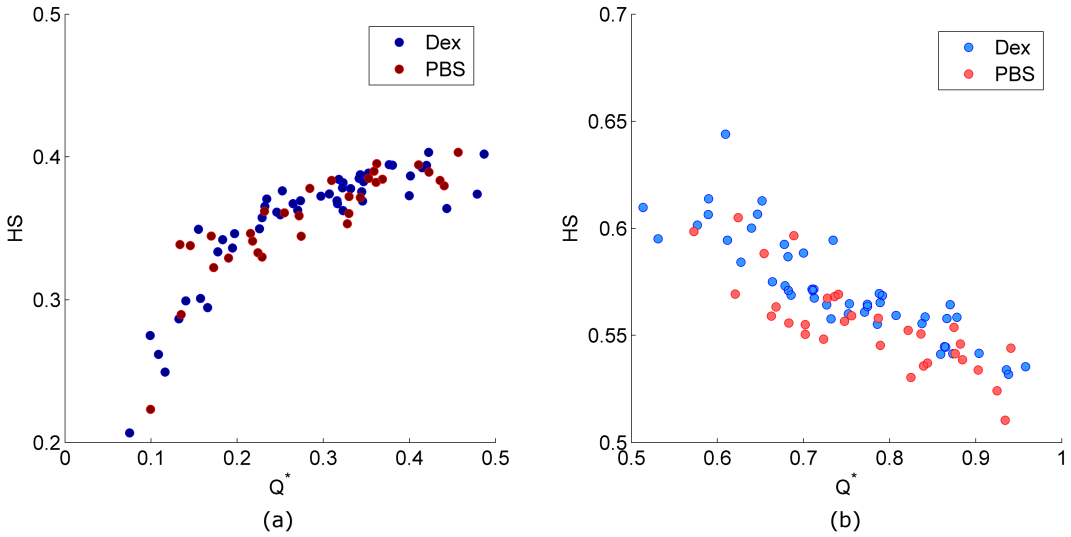

Figure 5.11: Haematocrit profile skewness, *HS* against flow ratio. (a) Daughter branch, (b) outlet branch.

Equations 5.16 and 5.17 is thus better for describing the haematocrit on each side of the channel.

HS is plotted against flow ratio in Figure 5.11. The trends for the PBS and Dextran cases are not significantly different. At low flow ratios in the daughter branch, the skewness is very high, with just 20% of the haematocrit in the channel lying on the side closest to the inner wall. As the flow ratio increases, this proportion rapidly increases and reaches a value of around 40% as Q_d^* approaches 0.5. In the outlet branch (Figure 5.11b), for an almost equal flow split ($Q_o^* \approx 0.5$), slightly more than 60% of the haematocrit lies close to the inner wall, and this reduces almost linearly, approaching 50 % (i.e. symmetry) at $Q_o^* = 1$. In the outlet branch, the skewness in the Dextran case is slightly greater than for the PBS case.

Analysis of these results shows that aggregation significantly affects the haematocrit distribution in the parent branch, particularly at low flow rates, but has less influence on the haematocrit profile asymmetry. The skewness in both the daughter and outlet branches is comparable for the PBS and Dextran cases; however the characteristics of the profiles differ slightly, with the Dextran cases generally being smoother, particularly in the daughter branch, wherein a bimodal shape was observed for the PBS case. The following section will consider the experimental velocity data and relate it to the haematocrit distribution.

5.5 Velocity results

The preceding discussion of the haematocrit distribution showed that the flow characteristics of the RBCs and the SM are quite different. The setup used for the present experiments allowed for quasi-simultaneous measurement of the two phases of the blood. In this section, the effects of flow rate and flow ratio on the velocities of the two phases will be discussed and related to the results of the haematocrit distribution. Figure 5.12 shows images, velocity magnitude and vector fields for an aggregating case with a flow ratio of 0.1 and a mean parent branch velocity of $2.2mm/s$.

Figure 5.12a and b show, preprocessed images are shown, acquired $166ms$ apart. The Velocity magnitude are superimposed as contours in Figure 5.12c and d. It can be seen that the velocity in the centre of the parent branch and outlet branch is greater for the RBCs than for the SM. Additionally, there is a visible difference in the shape of the velocity distribution at the entrance to the daughter branch. Figure 5.12e and f show velocity vectors in the bifurcation region. This figure serves to demonstrate the difference in the velocities of the two phases of the blood. Subsequent analysis of the velocity in this chapter will consider velocity profiles, averaged in the regions indicated in Figure 5.1.

5.5.1 Velocity profiles

Firstly, sample velocity profiles in the parent branch will be considered, wherein the independent parameter is the normalised velocity, V^*. Figure 5.13 shows parent branch velocity profiles normalised by the mean value, $(U^*(y))^\dagger$ for high and low flow rates. The profiles are normalised relative to the average total fluid velocity (Q_{tot}/D^2), giving U^*. The grey area indicates the analytical solution according to Equation 1.10. The dots on the figures show the relative velocity of the RBCs to the SM, that is:

$$U_{rel} = U_{rbc} - U_{sm} \tag{5.18}$$

For the Dextran case at low V^* (Figure 5.13a), the velocities of the SM and RBCs are very similar and hence the relative velocities are almost zero. Both phases show significant blunting in comparison to the analytical solution for a Newtonian fluid. There is

†Note that, as in previous chapters, U denotes axial velocity, not specifically the x-component of the velocity.

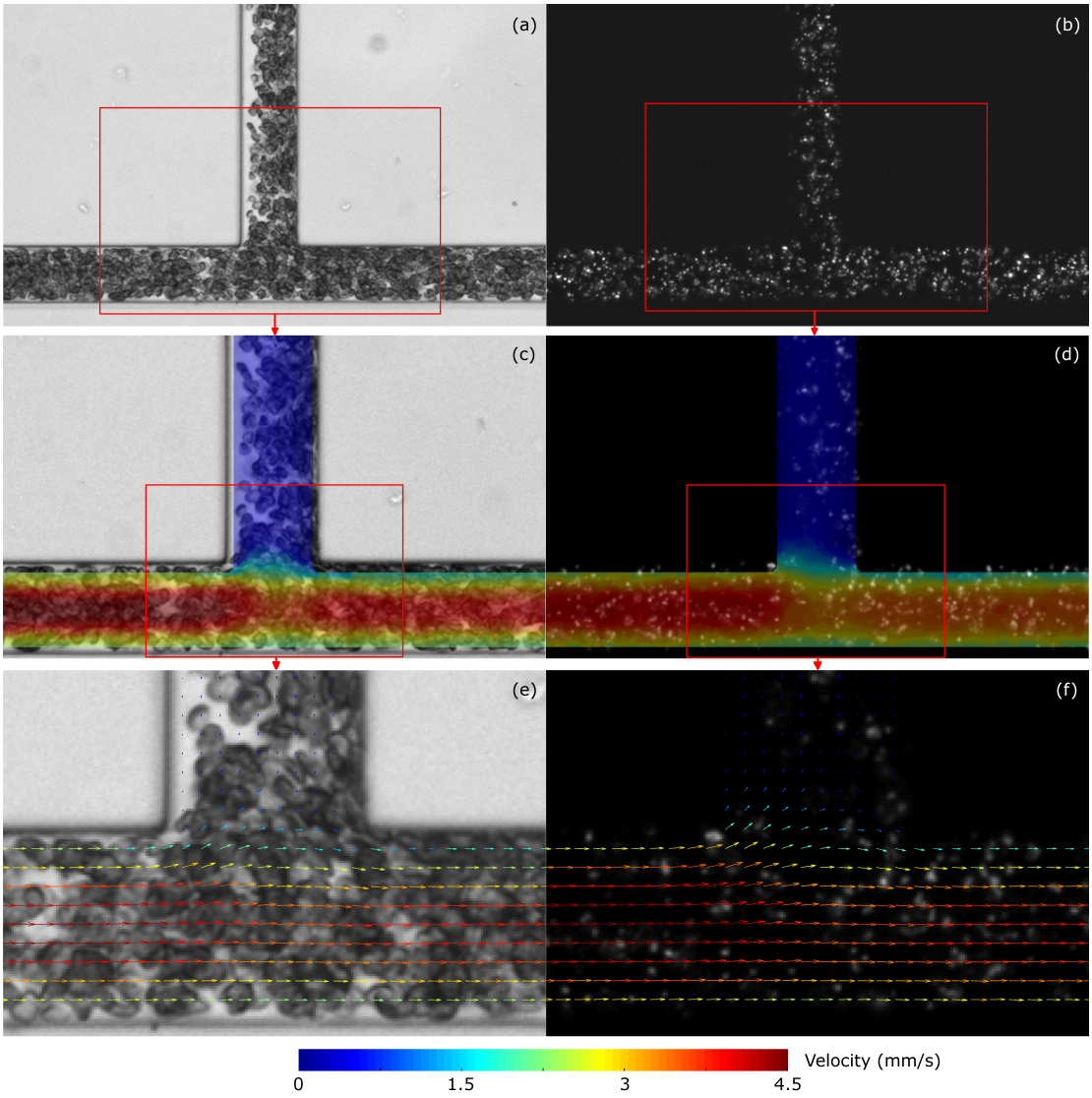

Figure 5.12: Extraction of velocity data from images. (a) Strobe-illuminated image, (b) Fluorescent particle image (c) Strobe illuminated image with RBC velocity superimposed as a contour, (d) Fluorescent particle image with SM velocity superimposed as a contour, (e) Strobe illuminated image with RBC velocity vectors superimposed, (f) Fluorescent particle image with SM velocity vectors superimposed. In (e) and (f), every other vector is omitted for clarity. Flow enters from the left, $Q^* = 0.13$, $V^* = 50$.

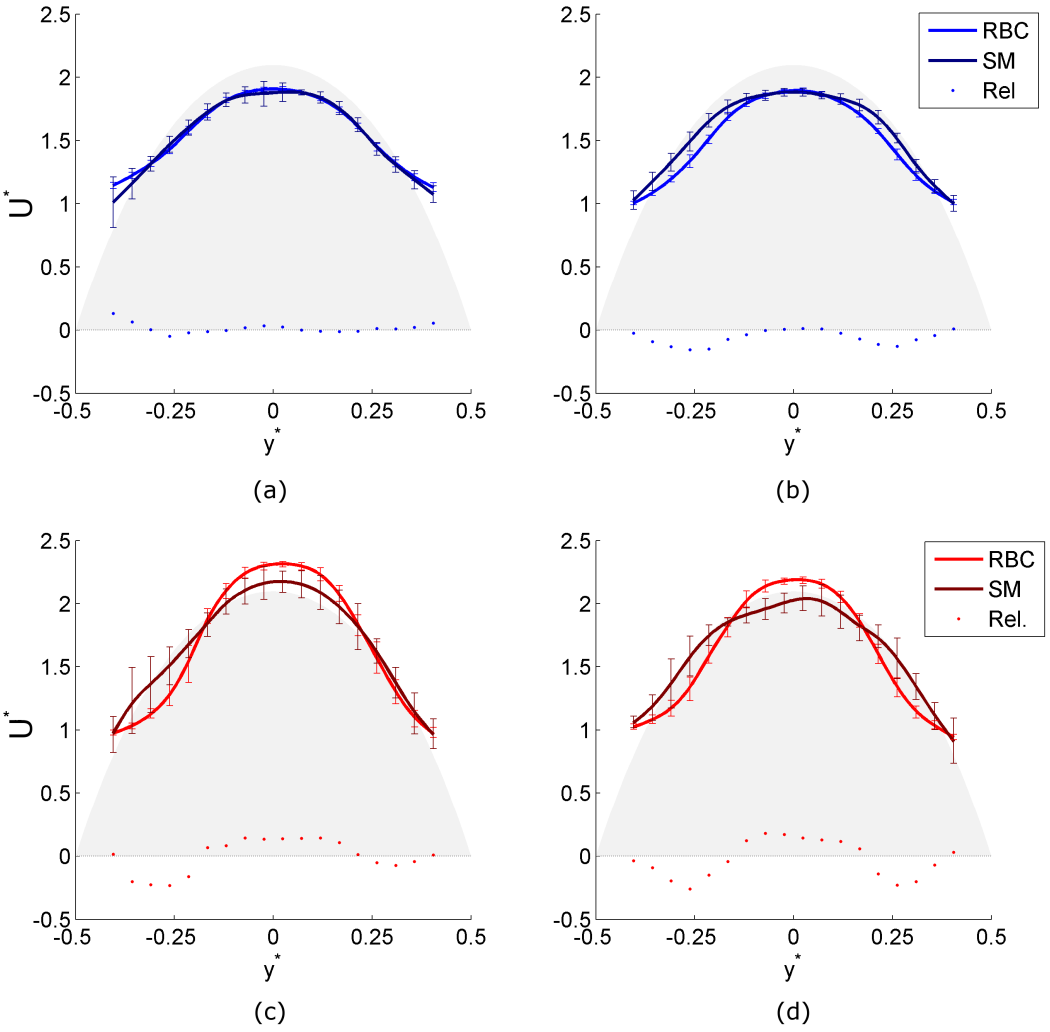

Figure 5.13: Experimental velocity profiles in the parent branch for the RBCs and the SM. Lines are spline fits and error bars show one standard deviation along averaging region of 1 channel width. (a) Dextran - $V^* = 17.7s^{-1}$, (b) Dextran - $V^* = 144.0s^{-1}$ (c) PBS - $V^* = 16.4s^{-1}$, (d) PBS - $V^* = 145.4s^{-1}$.

a notable bell shape to the profile. This shape is observable in experimental (Baker & Wayland, 1974; Choi et al., 2011; Moger et al., 2004; Zhong et al., 2011) and computational (Doddi & Bagchi, 2009) studies, but has not, to the author's knowledge, been discussed. At a higher flow rate (Figure 5.13b), the RBC velocity distribution retains its bell shape, but the SM velocity distribution is more parabolic, i.e. less 'bell-like'. Hence, there are regions at $y^* = \pm 0.25$ where the relative velocity is negative.

For the PBS case at low flow rate (Figure 5.13c), the bell shape distribution is more pronounced, and the velocity in the centre of the channel exceeds that of the analytical solution, particularly for the RBCs. At higher flow rate (Figure 5.13d), the profiles are

slightly blunter for both phases, but are still significantly less blunt than for the Dextran case. For the high flow rate PBS case, the SM velocity profile is similar to the analytical solution. The relative velocities are negative around $y^* = \pm 0.25$, but are positive for $-0.15 < y^* < 0.15$. It is worth noting that the errors in the SM velocity for the PBS case are larger than for the other data sets.

The velocity profiles in the daughter and outlet branches will be analysed first at low flow ratios ($Q_d^* \approx 0.15$), followed by high flow ratios ($Q_d^* \approx 0.42$). Figure 5.14a shows the velocities of the two phases for a Dextran case at $Q_d^* = 0.16$. As was observed in the previous chapters, the skewing of the velocity profiles is in the opposite direction to that of the haematocrit distribution. It can be seen that the velocity of the RBCs is relatively much lower than that of the SM, with a maximum relative velocity magnitude of more than $U^* > 0.5$ at around $x^* = -0.25$. Additionally, the bell shape is not visible in the profiles. In the outlet branch (Figure 5.14b), the profiles are skewed slightly in the opposite direction to the haematocrit profiles, but to a lesser extent than observed in the daughter branch. A slight bell shape, as observed in the parent branch, is visible in the RBC profile, and the relative velocity profile is comparable to that in the parent branch.

For the PBS case in the daughter branch (Figure 5.14c), the difference between the RBC and SM profiles is significant, but less pronounced than for the Dextran case (for which there was greater plasma skimming) and the bell shape is absent, as in the Dextran case (Figure 5.14a). The profiles are also notably less blunt than those of the Dextran case. In the outlet branch (Figure 5.14d), the bell shape is again visible in the RBC velocities, which are high close to the channel centre, but lower towards the outer wall ($y^* = -0.5$).

The corresponding velocity profiles for high flow ratios are provided in Figure 5.15. In the daughter branch, the profiles for both the Dextran and PBS cases (Figures 5.15a and c) are similar in character to those observed for low flow ratio (Figures 5.14a and c), but the relative velocities are significantly decreased. In the outlet branch for the Dextran case (Figures 5.15b), the relative velocity is almost zero and the profiles are similar to those at a lower flow ratio, if marginally more skewed and with less of a bell-shape (Figures 5.14b). For the PBS case, in the daughter branch (Figures 5.15c) the relative velocity between the two phases is significantly decreased and the profiles are more

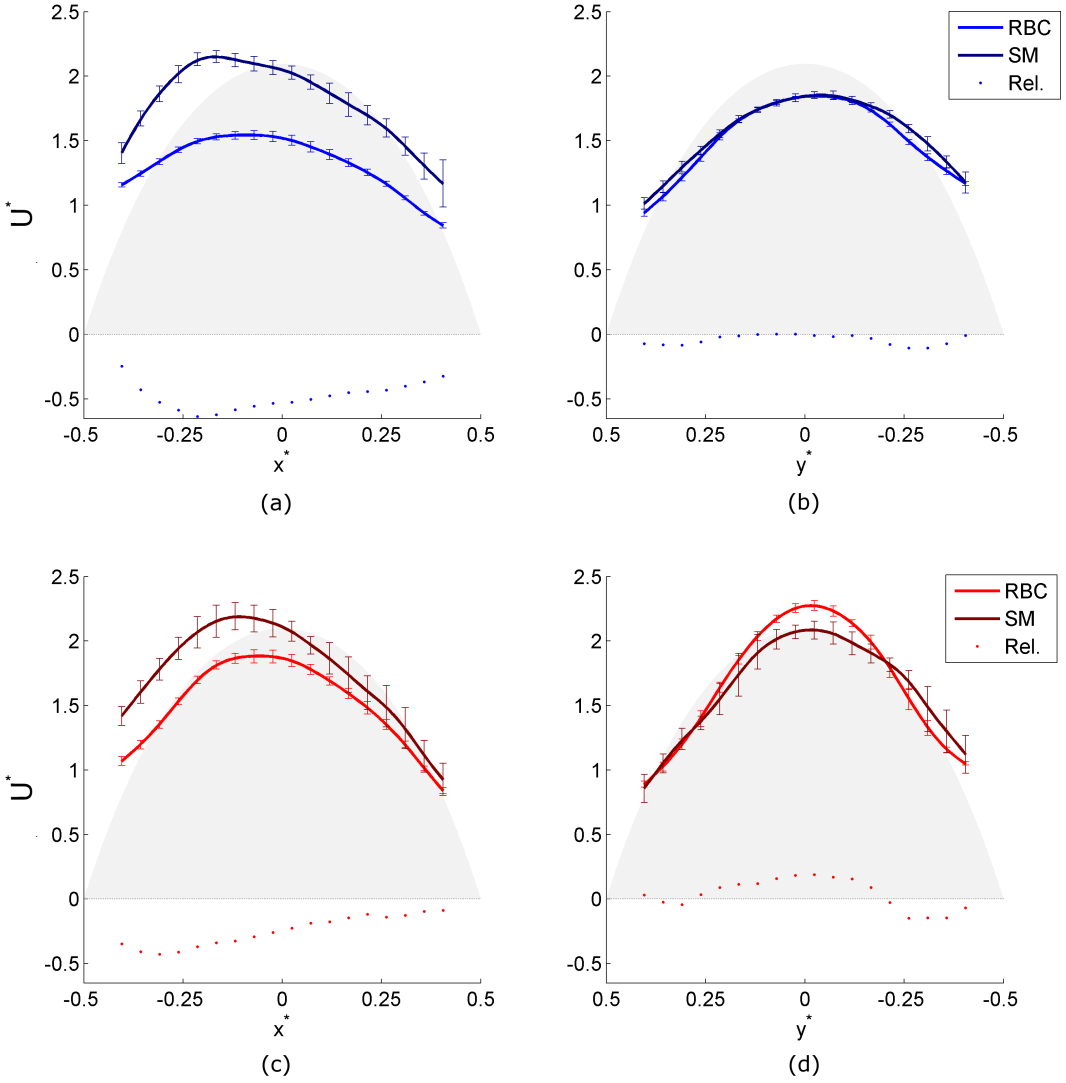

Figure 5.14: Experimental velocity profiles in the daughter branch for the RBCs and the SM at low flow ratio. Lines are spline fits and error bars show one standard deviation along averaging region of 1 channel width. (a) Dextran - Daughter, $Q_d^* = 0.16$, (b) Dextran- Outlet, $Q_o^* = 0.84$, (c) PBS - Daughter, $Q_d^* = 0.13$, (d) PBS - Outlet, $Q_o^* = 0.87$.

blunted when compared to the low flow ratio case (Figures 5.14c). In the outlet branch, the bell shape for the RBC velocity is slightly less strong for the high flow ratio case (compare Figures 5.15d and 5.14d), as a result of the fact that as Q_o^* decreases, the flow characteristics resemble less those in the parent branch.

5.5.2 Bluntness and skewness parameters

It is interesting to investigate how the characteristics of the velocity profiles change in relation to normalised velocity and flow ratio, as well as the haematocrit distributions. In these comparisons, statistical significance of observed trends will be expressed in

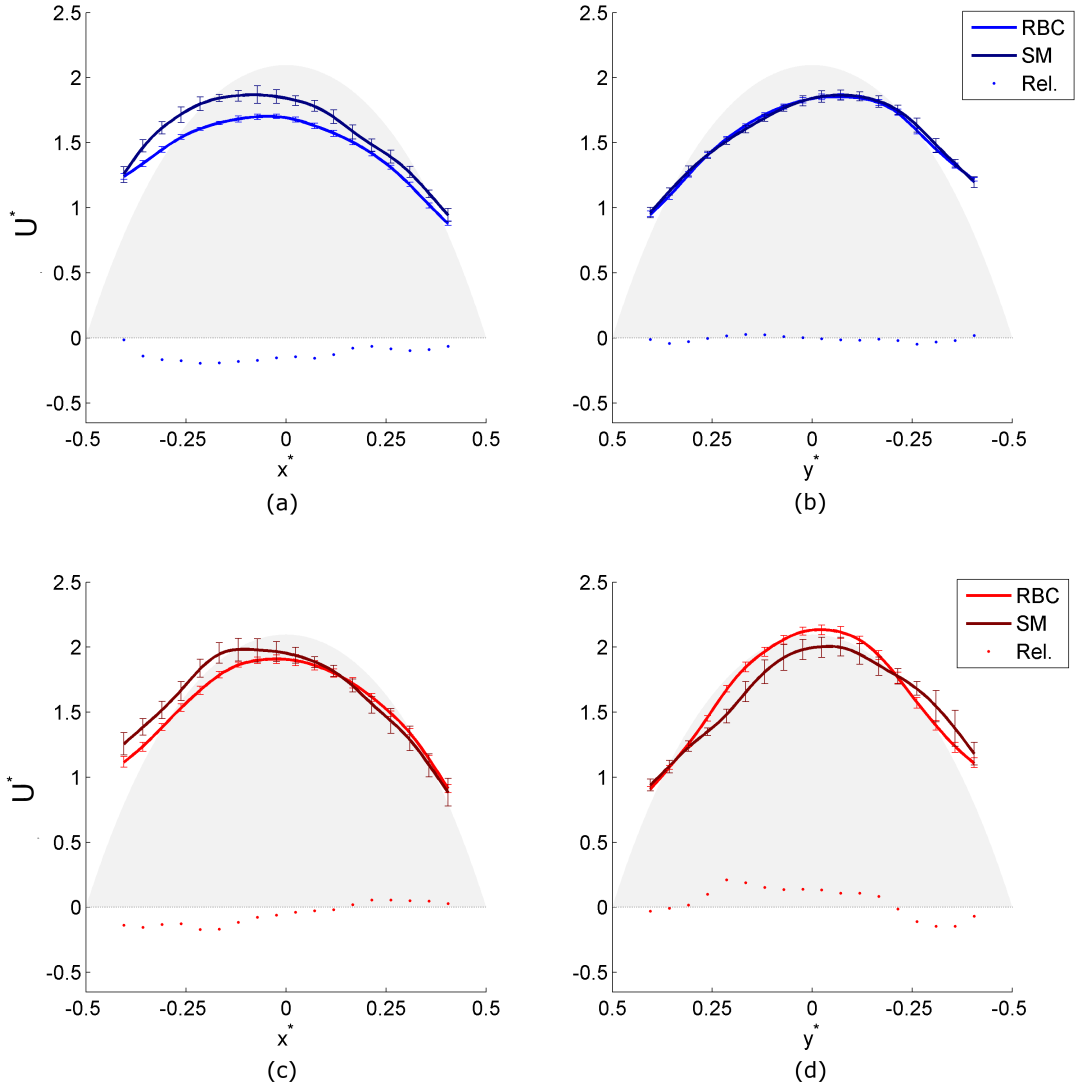

Figure 5.15: Experimental velocity profiles in the daughter branch for the RBCs and the SM at high flow ratio. Lines are spline fits and error bars show one standard deviation along averaging region of 1 channel width. (a) Dextran- Daughter, $Q_d^* = 0.41$, (b) Dextran- Outlet, $Q_o^* = 0.59$, (c) PBS - Daughter, $Q_d^* = 0.43$, (d) PBS - Outlet, $Q_o^* = 0.57$.

terms of the P-value of the Spearman's rank correlation coefficient ρ_c, unless stated otherwise. In calculation of ρ_c, the independent variable is ranked in ascending order and the Pearson's correlation coefficient, r_c, is calculated. This approach is more robust when the relationship between the variables is non-linear and is less sensitive to outliers, although as with r_c, the data must be monotonic. Significance values, are generally considered similarly to those of the Pearson's correlation coefficient, i.e. $P < 0.05$ indicates less than 5% chance that the observed trend is by random chance, and the strength of the relationship can be judged by the magnitude of the correlation coeffi-

cient. Guideline ranges of $0 - 0.35$, $0.36 - 0.67$ and $0.68 - 1.0$ are often quoted for weak, moderate and strong correlations respectively (Taylor, 1990), although the values depend on the number of samples. For 30 samples (the minimum used in this study), $P = 0.05$ corresponds to approximately $\rho_c < 0.30$.

The velocity bluntness, *VB*, will be defined as in Chapter 3[†], i.e. as the mean velocity normalised by the maximum velocity, and is calculated for the two dimensional profiles described by Equation 5.10 in the averaging regions shown in Figure 5.1. This parameter is shown as a function of normalised velocity in the parent branch in Figure 5.16. For the RBCs (Figure 5.16a), there is a reduction in the bluntness of the velocity profiles for the Dextran case as the flow rate increases. Conversely, for the PBS case, the bluntness increases with increasing flow rate. Although there is notable scatter for the PBS case, the trend is statistically significant. For the SM, the bluntness of the velocity profiles for the Dextran case increases for normalised velocities up to a peak in the region $V^* = 50s^{-1}$, and decreases thereafter (this normalised velocity will herein be used to define the border between the low and high flow regimes and is indicated by the vertical black line in the figure). This trend is non-monotonic and hence the P-value of the Spearman's rank correlation coefficient is very high ($P = 0.897$). However, if it is assumed that the data follows a linear trend on either side of this transition region, then $P = 0.006$ for $V^* < 50s^{-1}$ and $P = 0.028$ for $V^* > 50s^{-1}$ using the Pearson's correlation coefficient, which supports the observation of initially increasing then decreasing bluntness with increasing flow rate. For the PBS case there is a highly significant monotonic increase in bluntness as the flow rate increases.

The bluntness follows the same trend for both fluid phases for the PBS case, whereas for the Dextran case, opposite trends are observed for the RBCs and SM for $V^* < 50s^{-1}$. For the haematocrit profiles, it was observed that as V^* increased to around $50s^{-1}$, *HB* increased significantly for the Dextran case, while it decreased with about half the gradient or the PBS case. Above this normalised velocity, both cases levelled off, with the Dextran bluntness slightly higher than for the PBS.

One would expect a correlation between the bluntness of the velocity profile (*VB*) and the haematocrit profile (*HB*). The two parameters are compared directly in Figure 5.17. For the RBCs (circles), both the Dextran and PBS cases show a negative correla-

[†]The terminology *VB* is used as opposed to B in Chapter 3 in order to differentiate it from *HB*.

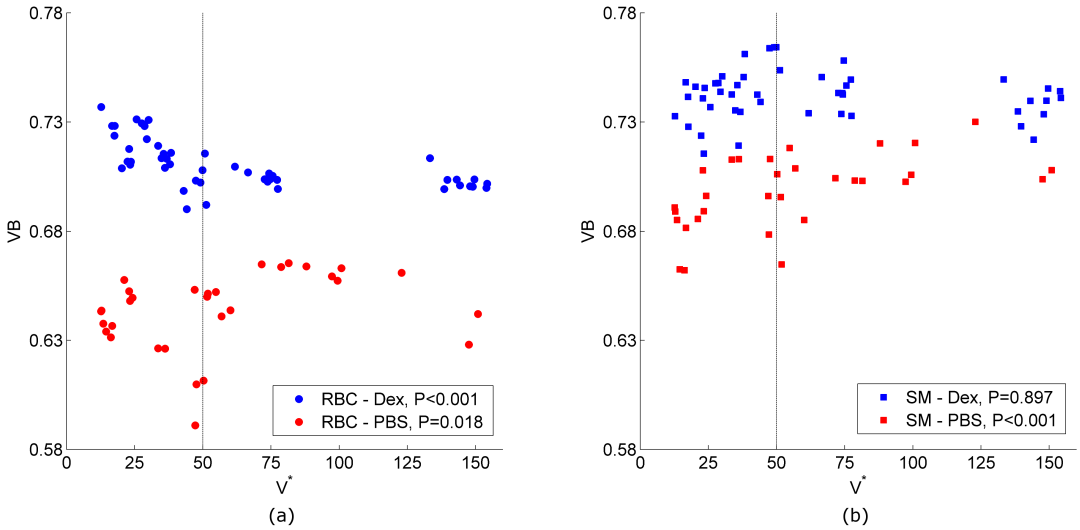

Figure 5.16: Experimental velocity bluntness, *VB* against normalised velocity in the parent branch. (a) RBC, (b) SM. Vertical lines show approximate division between high and low flow regimes.

tion between haematocrit bluntness and velocity profile bluntness which is statistically significant. For the PBS case (squares), the SM also shows a negative correlation. The non-monotonic trend of *HB* for the Dextran SM invalidates the Spearman's correlation coefficient. However, interrogating high and low velocity regions separately (again assuming linear trends) yields $\rho_c = 0.33, P = 0.095$ for $V^* < 50s^{-1}$ and $\rho_c = -0.54, P = 0.009$ for $V^* > 50s^{-1}$. While the value for $V^* < 50s^{-1}$ is above the normal value considered for statistical significance, it still implies a high likelihood that the observed trend is valid. This interesting trend will be discussed in more detail later in the chapter.

The skewness of the velocity profiles is also of interest. Figure 5.18 shows the skewness of the velocity profiles, *VS*, defined as in previous chapters [†], in the daughter and outlet branches against flow ratio. In the daughter branch, *VS* decreases with increasing flow ratio for all cases (RBC and SM, Dextran and PBS). In general, the skewness is greater for the SM, particularly at low flow ratios. In the outlet branch, for the Dextran case, *VS* is significantly related to the flow ratio ($P < 0.001$) for both the RBCs and SM. For the PBS case, there is a statistically significant but small decrease in skewness with increasing Q^* for the SM, but no significant trend is observed for the RBCs.

[†]As with the velocity bluntness, the terminology *VS* is used as opposed to S^* in Chapters 3 and 4 in order to differentiate it from *HS*. For this chapter, the fractional form is preferred to a percentage value.

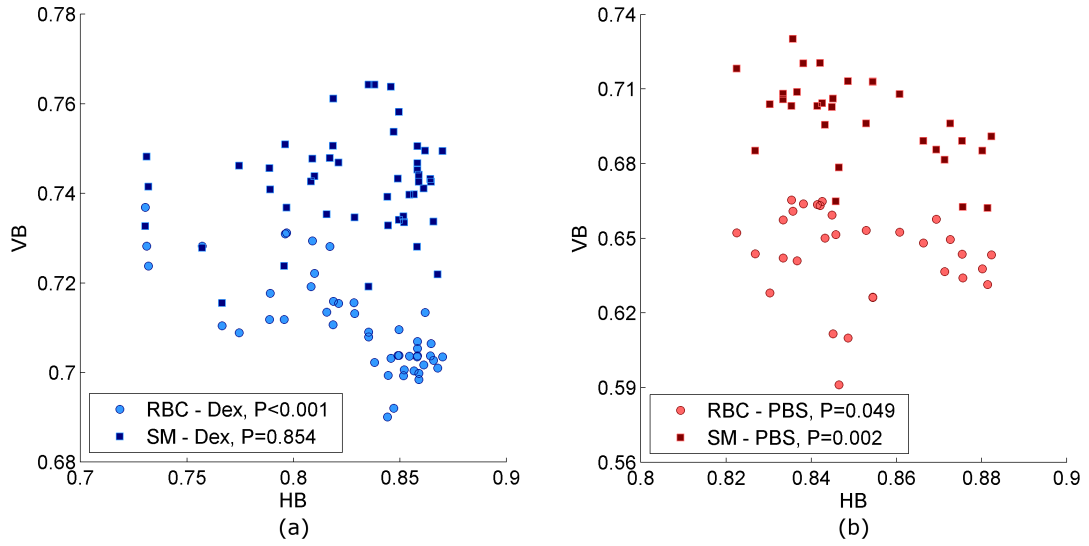

Figure 5.17: Experimental velocity bluntness against haematocrit bluntness. (a) RBC, (b) SM.

As has been demonstrated, the skewness in the velocity profiles arises due to the skewness of the haematocrit distribution. Figure 5.19 further supports this assertion, directly comparing *VS* to *HS*. With the exception of the RBCs for the PBS case in the outlet branch, all cases show statistically significant trends. In both branches, as *HS* becomes increasingly different from 0.5, *VS* increases.

From the preceding analysis, it is clear that there is a difference in the relationship between the two phases of the blood both in response to flow rate in the parent branch and flow ratio in the daughter and outlet branches. In this section, U_ϕ, defined as the mean relative velocity between the two phases normalised by the mean total velocity

$$U_\phi = \frac{D^2}{Q_{p,tot}} \frac{1}{D} \int U_{rel} dy \tag{5.19}$$

will be analysed with respect to flow rate, flow ratio, haematocrit bluntness and haematocrit skewness.

It was shown in Figure 5.13 that the relationship between the RBC and SM velocities is dependent on the normalised velocity, V^*. This is further considered in Figure 5.20a, which shows U_ϕ in the parent branch against normalised velocity. For the Dextran case at low V^*, U_ϕ is close to zero, meaning that the average velocities of each phase are equal. As mentioned earlier, there may be some systematic error in the absolute values of U_ϕ, due to the differences in the PIV analysis for the two phases. However, Poelma et al. (2012) reported that for a $10\times$ magnification, the two approaches should

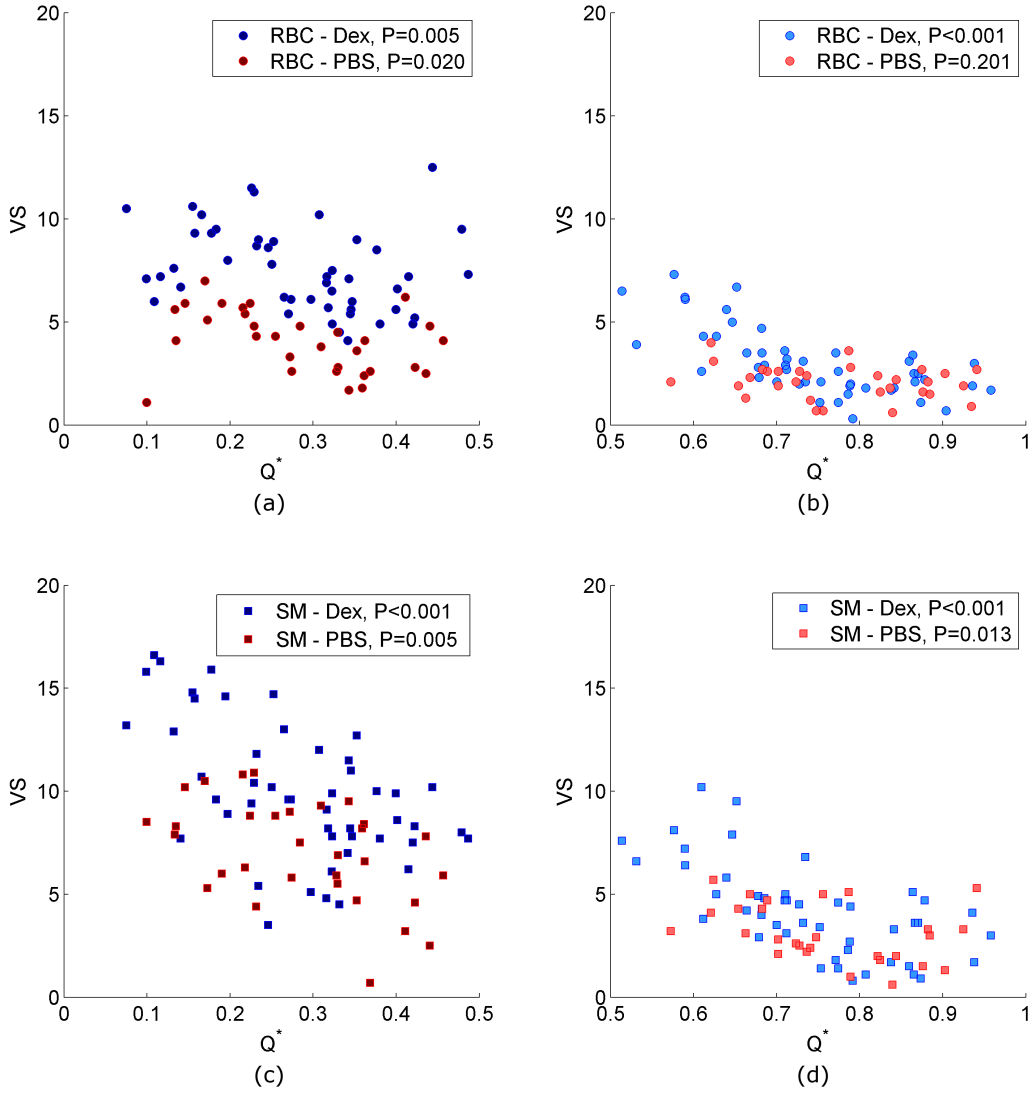

Figure 5.18: Experimental velocity skewness against flow ratio. (a) RBC - Daughter branch, (b) RBC - Outlet branch, (c) SM - Daughter branch, (d) SM - Outlet branch.

have similar characteristics. As V^* increases up to around $50s^{-1}$, U_ϕ decreases to approximately -0.1 and does not change significantly for further increases in the flow rate. The P-value for this trend indicates a high significance. Comparing Figure 5.20a with Figure 5.16, it can be seen that this trend is similar to that of the bluntness of the RBC velocity profiles. Furthermore, the trend also appears to be the inverse of the haematocrit bluntness shown in Figure 5.9. The data for the PBS are more scattered, but show a general decrease as the mean velocity increases. Conversely to the Dextran case, this is the same trend as observed for the haematocrit bluntness.

Figure 5.20b directly compares the haematocrit bluntness to U_ϕ. A significant negative

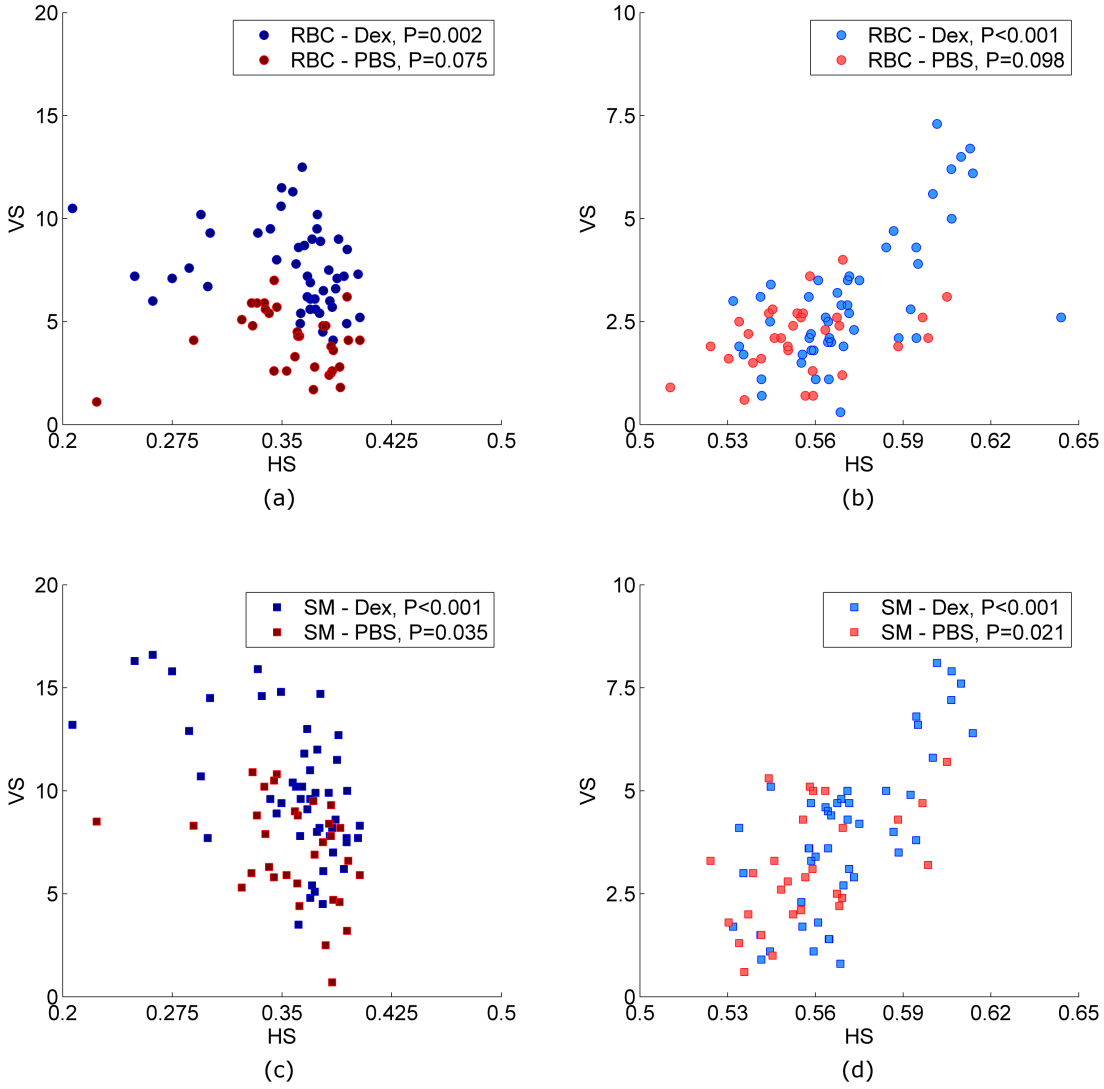

Figure 5.19: Experimental velocity skewness against haematocrit skewness. (a) RBC - Daughter branch, (b) RBC - Outlet branch, (c) SM - Daughter branch, (d) SM - Outlet branch.

correlation ($\rho_c = -0.519$) for the Dextran case and a highly significant positive correlation ($\rho_c = 0.517$) for the PBS case can be observed. For the latter, as the concentration of RBCs in the channel centre increases, the velocity of the RBCs relative to that of the SM decreases. This suggests that the increase in local haematocrit in the channel centre decreases the RBC velocity due to cell-cell interaction increasing the energy loss for the RBCs. The same trend might be expected of the Dextran case, but the opposite seems to be the case. This will be discussed in further detail in §5.6.2.

The relationship between U_ϕ and V^* is shown for the daughter and outlet branches in Figure 5.21. For both the Dextran and PBS cases, U_ϕ follows a similar trend and

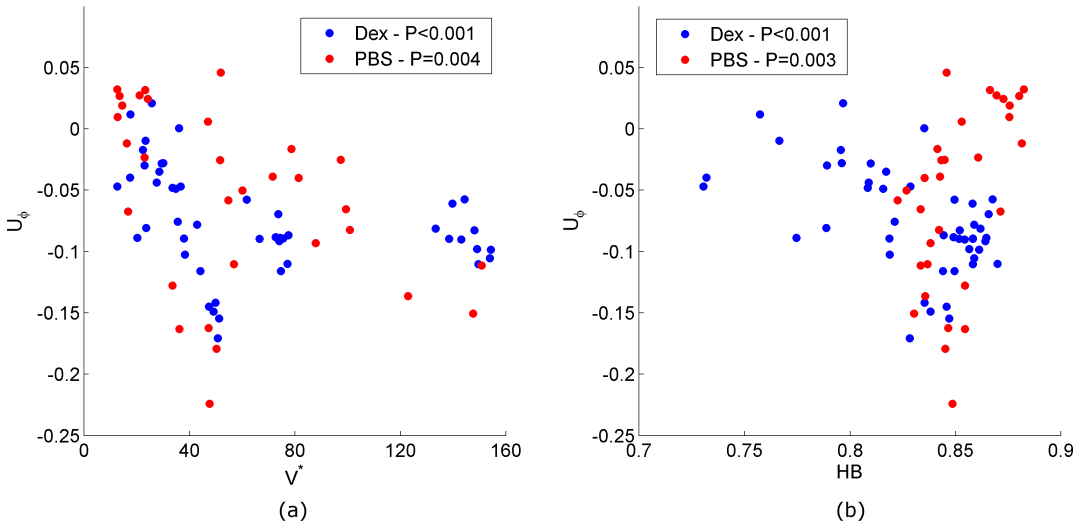

Figure 5.20: Relative velocity of RBCs in the parent branch as a function of (a) Normalised velocity and (b) Haematocrit bluntness *HB*.

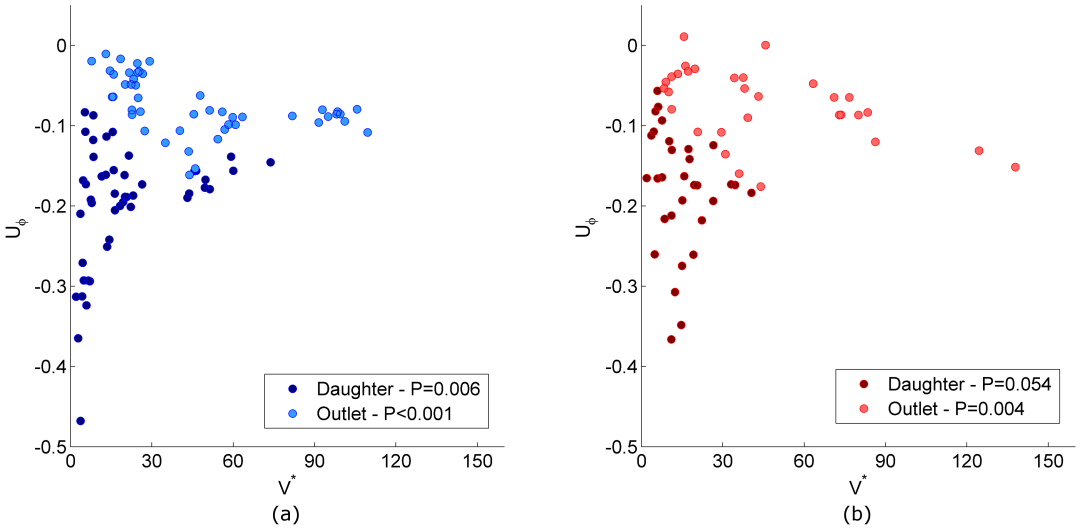

Figure 5.21: Relative velocity of RBCs in the daughter and outlet branches branch as a function of normalised velocity. (a) Dextran, (b) PBS.

magnitude in the outlet branch to that observed in the parent branch (Figure 5.20a). In the daughter branch for the Dextran case, there is a large range (-0.1 to -0.5) in U_ϕ at low V^*, which levels out at around -0.2 as V^* increases. Despite this scatter, the P-value for the data set is 0.006, indicating a significant positive correlation ($\rho_c = 0.40$), which is opposite to the parent and outlet branches. In the daughter branch for the PBS case, there is also a large range in U_ϕ at low V^* and here the trend is found to be just above the significance threshold $P = 0.054$ with a negative correlation, $\rho_c = -0.35$.

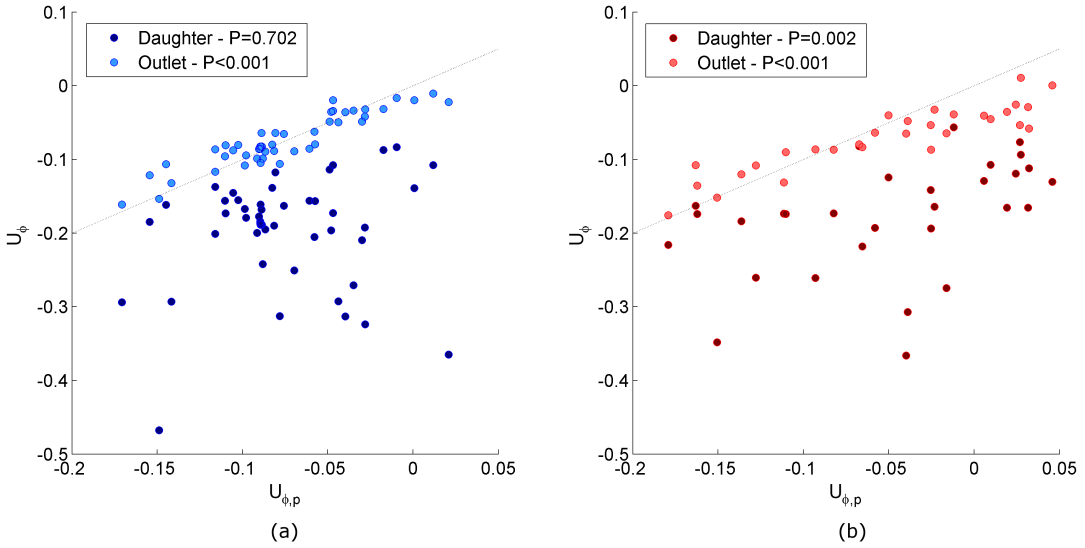

Figure 5.22: Relative velocity of RBCs in the daughter and outlet branches against relative velocity of RBCs in the parent branch. Lines show $U_\phi = U_{\phi,p}$. (a) Dextran, (b) PBS.

Hence, while the relative velocity is highly dependent on flow rate in the parent and outlet branches, there must be other factors which have a significant effect on U_ϕ in the daughter branch. This is further confirmed by comparing the relative velocity in the parent branch to those in the daughter and outlet branches as shown in Figure 5.22.

For both cases, the data for the outlet branch lie very close to the $U_{\phi,o} = U_{\phi,p}$ line, indicating that the relative velocity in the outlet branch is defined by that in the parent branch. However, in the daughter branch there is no significance in the relationship for the Dextran case. For the PBS case, the data lie below the $U_{\phi,d} = U_{\phi,p}$ line, but a significant trend is observed.

In Figure 5.23, U_ϕ is plotted against flow ratio, Q^*. In both the Dextran and PBS cases, the relative velocity in the daughter branch depends strongly on flow ratio, whilst in the outlet branch there is no dependence of U_ϕ on flow ratio.

Furthermore, the trends in Figure 5.23 are similar to those for the haematocrit skewness (Figure 5.11) and the haematocrit ratio (Figure 5.6). This shows the importance of the geometry on the velocity relationship between the two phases of the blood.

5.6 Discussion

Prior to drawing conclusions from the data presented above, the advantages and limitations of the techniques used in this chapter will be considered. Following this, the

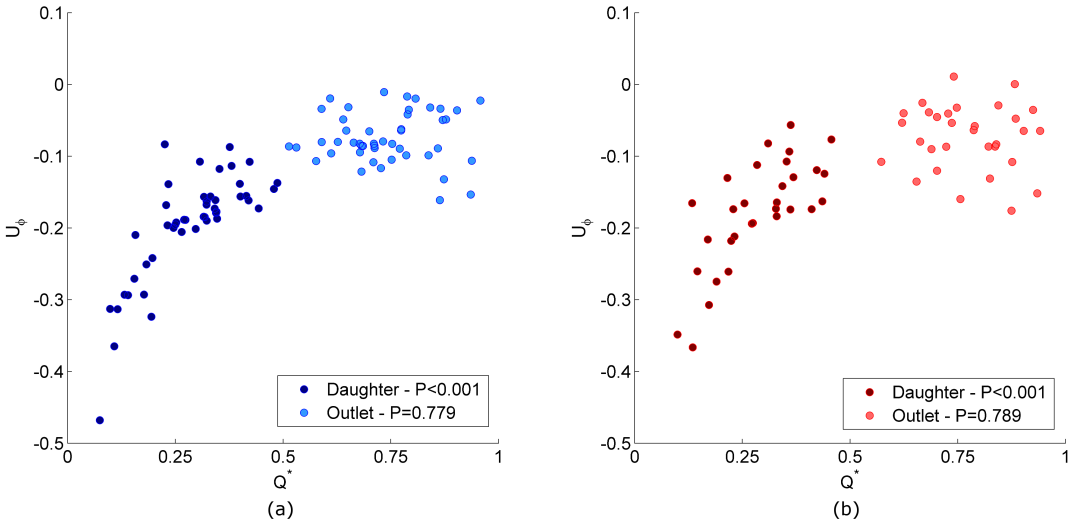

Figure 5.23: Ratio of average RBC to SM velocities in the daughter and outlet branches branch as a function of flow ratio. (a) Dextran, (b) PBS.

discussion will continue with analysis of the flow in the parent branch. This represents a fully developed condition at which RBC aggregation, deformation and migration have reached equilibrium conditions, as would be reached after a long straight section of vessel. Subsequently, the characteristics specific to a bifurcation will be considered, namely those in the daughter and outlet branches. Finally, the significance of the reported data to analysis of microhaemodynamics will be discussed.

5.6.1 Experimental approach

The experimental approaches used in the present chapter allowed for a high quantity of information to be extracted for each individual experiment. The novel aspects of this work are the simultaneous measurements of the velocity and concentration of both phases of the blood. Quantitative haematocrit profiles have been described by a few experimentalists prior to this research. Aarts et al. (1988) used a laser-Doppler approach to count cell and platelet concentrations in blood flow across a tube. However, in their study, they utilised high flow rates and a $3mm$ diameter tube. Nonetheless, they observed that the bluntness of the haematocrit profile decreased with increasing flow rate, as was observed in the present study. Manjunatha & Singh (2002) measured velocity and haematocrit distributions in a frog mesentery using image processing and tomographic approaches, respectively. Their results show skewed haematocrit distributions after each bifurcation, in a manner comparable to those reported in Figure 5.4.

Moger et al. (2004) used Dopper optical coherence tomography to measure RBC concentration and velocity profiles. They used a $150\mu m$ diameter capillary tube and also observed decreasing haematocrit profile bluntness at higher flow rates, and even the tubular pinch effect as the flow rates increased further. Pries & Secomb (2008) showed *in vivo* haematocrit profiles, but did not provide a significant discussion. Damiano et al. (2004) inferred viscosity profiles, which scaled with haematocrit, from velocity profiles. However, this approach precludes analysis of the interaction between velocity, haematocrit and viscosity, which is predefined by the assumptions in their model.

A calibration curve was calculated for the present data, rather than assuming a linear relationship between $1 - I^*$ and the channel haematocrit H_C, as was done in the previous chapter. The result was a relationship which was well represented by an exponential curve. The fitting identified an intensity saturation point as well as a non-linearity value. No significant difference in the fitted parameters was found at high or low flow rates, or between the Dextran and PBS cases for the curve and so a single set of parameters was used for the two data sets. From Figure 5.3, it can be seen that, if the highest feed haematocrit is omitted, a straight line would fit reasonably well through the data points, but would underestimate the haematocrit as the intensity approached the saturation point. For the previous chapter, the linear assumption was made, but as the channel was only $40\mu m$ in depth (a 20% reduction compared to this chapter) the linear intensity-haematocrit assumption would not be expected to adversely affect the results reported therein significantly. Nevertheless, the calibration stage refines the methodology developed in this study, which is necessary for the analysis presented in this chapter.

It should be noted that the values of H_C were estimated based on the feed haematocrit and empirical relationships for the Fåhraeus effect and cell screening, and hence this is a potential source of error. Ideally, the fitting would be carried out against direct measurements of the channel haematocrit. However, due to the requirement for a very short measurement time (due to sedimentation and aggregation in the outer flow system), the small channel size and the low flow rates used, the minute volumes of fluid which were perfused precluded such analysis for the present data. The values of a and

b which were found to fit Equation 5.4 are specific to the exact illumination method, channel depth, microscope objective, camera sensitivity and exposure time used for the present experiments. Hence, the calibration step would need to be carried out again if the present technique was to be repeated.

It can be seen in Figure 5.3 that at $H_F = 0.30$, the image is very dark. Around this haematocrit level, the sensitivity of the haematocrit technique starts to reach its limit. At higher haematocrit under the same illumination conditions, the saturation point was reached which indicates an upper haematocrit level for the technique. Furthermore, at this level, the RBC μPIV technique became less reliable due to reduced contrast and less repeatable patterns, and the standard μPIV also became less effective due to the cells absorbing and blocking the fluoresced light from the suspended microparticles. It was decided that due to these limitations, the present experiments would be carried out with a feed haematocrit of 0.20 (noting that local haematocrits reached as much as 0.3 in Figure 5.4). This feed haematocrit is in the physiological range for the length scales used here and optimised the efficiency of the measurement methodologies applied in the present experiments.

The application of alternating illumination methods with a single camera for the present data is a novel combination of two established experimental approaches which uniquely provided quasi-simultaneous Eulerian data on both phases of the blood flow. Sugii et al. (2005) used a method which combined PTV for the RBCs with PIV for the plasma. This approach has merit, but PTV requires very large amounts of data to be acquired in order to get a reliable Eulerian description of the flow field, and as mentioned previously, experimental time is very limited for the present experiments due to the presence of RBC aggregation. Furthermore, in the aforementioned study, only a single data set was reported and the authors found the velocities of both phases to be insignificantly different from the Poiseuillean profile. To the author's knowledge, there are no other studies reported in which the two phases have been measured simultaneously[†]. Poelma et al. (2012) used both methodologies, but alternated between them by physically mod-

[†]Although the data is technically only quasi-simultaneous, as the data are steady, it is not important to discriminate between the two.

ifying the setup. Ji & Lee (2008) applied both imaging methodologies, but only used the RBC images for qualitative analysis, as was the case in a number of other studies (Ishikawa et al., 2011; Lima et al., 2009a; Lima et al., 2008b).

Recently, Poelma et al. (2012) provided the first experimental paper directly comparing the effect of depth of correlation on RBC and fluorescent-particle based PIV approaches. They reported that for low magnifications, the depth of correlation for both techniques was similar, as the data are 'depth-saturated', meaning that the depth of correlation fills the majority of, or exceeds, the channel depth. Hence, both data techniques underestimate the velocity by a similar proportion, being 0.67 for a diameter of $50\mu m$ (note that the hydraulic diameter of a square channel is equal to its side length). However, it should be noted that this analysis makes the tacit assumption that the velocity of the RBCs and SM are equal, which is not observed to be the case for the present study.

A key assumption made in the present study was that the analysis time was sufficiently short that the effect of sedimentation was negligible. This enabled the use of the (x, y) plane distributions of velocity and haematocrit in the parent branch to be used to predict (x, z) plane (in the daughter branch) and (y, z) plane (in the parent and outlet branches) distributions. Alonso et al. (1995) studied the sedimentation effect at low shear rates in horizontal and vertical tubes in the presence of aggregation. They reported flow rates in terms of wall shear stress, which correspond to normalised velocities of $0.2 - 10s^{-1}$ for a $59\mu m$ diameter tube[†]. For that tube, the sedimentation effect was negligible for normalised velocities above $5s^{-1}$, even after 300 seconds. The lowest normalised velocity utilised in the present study in the parent branch was $12s^{-1}$. It was also observed that the effect of sedimentation was reduced for smaller tubes and at higher flow rates (Alonso et al., 1995). Given that in the present study all acquisition was carried out within 45 seconds of flow reduction (from the high disaggregating flow rate) in small

[†]Their calculation for wall shear stress is not explicitly stated, hence the wall shear for Poiseuille flow is used here. Alonso et al. (1995) did not mention what viscosity they used, however the above values are based on the plasma viscosity, which would give the highest estimated range of normalised velocities.

channels at high flow rates (relative to Alonso et al. (1995)), it seems reasonable to assume that sedimentation would not have had a significant effect on the present data.

5.6.2 Fully developed flow: Parent branch

This section will discuss the haemodynamic characteristics when the flow is fully developed (as explained above). The control parameters for this part of the data are limited to the presence or absence of aggregation and the normalised velocity. The resulting data comprise the bluntness of the haematocrit and velocity profiles and the phase velocity ratio.

In the preceding analysis, a normalised velocity, $V^* = \overline{U}/D$, (where $\overline{U} = Q_{tot}/D^2$) has been used rather than an absolute flow rate, in order to make the results more general. It should, however, be noted that scaling of microscale haemodynamic data is not strictly appropriate, due to the importance of the ratio of RBC size (not just the diameter) to the channel dimensions. Furthermore, the terminology normalised velocity has been used rather than the more common 'pseudoshear rate' (Bishop et al., 2001a; Ong et al., 2010; Reinke et al., 1987). As discussed in Chapter 1, if one considers Poiseuille flow, the average shear can be calculated by integrating the shear rate, which yields

$$\overline{\gamma}_p = \frac{16}{3}\frac{\overline{u}}{D} \tag{5.20}$$

As the hydraulic diameter of a rectangular channel is equal to that for an equivalent cylindrical pipe, the normalised velocity could be scaled by this value to give an estimate of the average shear rate in the channel. However, it should be noted that the shear rate can range from very high values at the channel walls to zero at the apex of the velocity profile.

It was observed that around normalised velocities of $50s^{-1}$, the characteristics of the flow changed significantly. According to Equation 5.20, this corresponds to an average shear rate of $260s^{-1}$. These values are far higher than those at which one would expect to see a significant influence of aggregation (Snabre et al., 1987). However, it should be noted that aggregation has been observed *in vivo* at pseudoshear rates (equivalent to normalised velocity) greater than $70s^{-1}$ (Bishop et al., 2004; Ong et al., 2010).

The normalised velocity of $50s^{-1}$ is observed to be a transition point in many of the results, so for simplicity, values above and below this value will be termed high and

low flow regimes, respectively.

In terms of absolute velocities, a normalised velocity of $50s^{-1}$ corresponds to an absolute velocity of $2.5mm/s$. Average velocities in the microvasculature tend to be in the range $0.5 - 10mm/s$ (Fung, 1997), which implies that even under normal physiological conditions, it is likely that aggregation will influence haemodynamics in the lower velocity vessels. Under certain pathological conditions in which aggregation is enhanced (Babu & Singh, 2004; Jain, 1988), aggregation could significantly alter the blood flow characteristics.

The haematocrit profile bluntness (*HB*) was a key parameter in defining the characteristics of the flow in the parent branch. RBCs migrate radially as a result of interactions with the flow field between the RBC and the channel wall, and in concentrated flows, the migration is counteracted by interactions between RBCs. At low flow rates, aggregation increases radial migration (Bishop et al., 2001c; Bishop et al., 2001a; Cabel et al., 1997), as well as inducing synaeresis (Goldsmith et al., 1989). For the Dextran case, at very low flow rates a sharp haematocrit profile was observed, which became blunter as the overall flow rate increased, as also observed by Palmer (1969). Furthermore, aggregating RBCs have been shown to have reduced dispersibility (Bishop et al., 2002; Bishop et al., 2001d), which would help in retaining a high RBC concentration in the channel centre in the presence of aggregation. At higher flow rates, the greater shear forces would cause disaggregation, increasing cell-cell interactions and counteracting the effects of synaeresis and radial migration. For the non-aggregating case, the haematocrit bluntness was high at low flow rates, but decreased as the flow rate increased, as has been observed experimentally (Aarts et al., 1988; Moger et al., 2004) and numerically (Freund & Orescanin, 2011), due to increased radial migration.

Reinke et al. (1987) observed that the width of the RBC core, which should correlate with haematocrit bluntness, increased for Dextran cases as the flow rate increased, and decreased slightly for RBCs suspended in saline (equivalent to PBS). Radial migration is expected to be enhanced at high flow rates (Caro et al., 2012), so this trend could also be expected. Interestingly, for $V^* > 50s^{-1}$, which seems to be a transition region, the haematocrit bluntness for the two cases settled at a steady value which was higher for the Dextran case than for the PBS case (Figure 5.9). This may be because,

even at high flow rates, although aggregation near the channel walls is expected to be negligible, there will be a region in the channel centre which will have some degree of aggregation. The relationships observed between the velocity and haematocrit profiles correspond to those described by Goldsmith (1968): there is an inverse relationship between haematocrit bluntness and velocity bluntness, as shown in Figure 5.17.

It was observed that as the haematocrit bluntness increased, the velocity profile became less blunt. This can be explained as a result of a number of complementary phenomena. As the haematocrit profile becomes less blunt (i.e. there is a greater concentration of RBCs away from the walls) the viscosity in the channel centre becomes relatively higher and the viscosity at the channel wall becomes relatively lower. As a result, the fluid velocity will decrease in the channel centre and increase close to the walls. This will blunt the velocity profile, resulting in increased shear rate near the walls, and decreased shear rate in the channel centre, further modifying the viscosity in the same manner as the haematocrit profile (as blood is a shear thinning fluid). Furthermore, the increased shear rate near the walls will enhance radial migration (Goldsmith, 1971). In the presence of an aggregating agent, such as Dextran, RBC aggregation would occur (or persist) in the regions of low shear rate, further blunting the velocity profiles by increasing the local viscosity in the channel centre. This effect would be very strong at low flow rates, but also visible at high flow rates, as the shear rate in the channel centre must be very small, irrespective of the absolute velocity. Therefore, velocity bluntness is expected to decrease for both Dextran and PBS cases as the haematocrit bluntness increases. Furthermore, the velocity profiles would be expected to be blunter in general in the presence of aggregation (Bishop et al., 2001a; Reinke et al., 1987; Nakano et al., 2003).

The aggregating and non-aggregating cases showed opposite trends in the RBC velocity bluntness (*VB*) in relation to the flow rate (Figure 5.16). *VB* decreased with increasing flow rate for the aggregating cases (Alonso et al., 1995; Bishop et al., 2001a; Gaehtgens et al., 1970; Reinke et al., 1986), whereas it increased slightly as the flow rate increased for non-aggregating blood. This later trend is not commonly reported, but Bishop et al. (2001a) found that non-aggregating blood velocity pro-

files decreased only very slightly in bluntness compared to the Dextran case as the flow rate increased *in vivo*. However, the data is consistent with that expected due to the influence of haematocrit bluntness on velocity bluntness (Goldsmith, 1968): comparing the velocity bluntness with the haematocrit bluntness (Figure 5.17) gives $\rho_c = -0.75, P < 0.001$ and $\rho_c = -0.36, P = 0.049$ for the RBCs in the Dextran and PBS cases respectively.

For the SM in the PBS case, the same trend was observed as for the RBCs. For the SM in the Dextran case, however, the velocity bluntness increased with increasing flow rate for $V^* < 50s^{-1}$ (Figure 5.16b), conversely to the trend observed for the RBCs (Figure 5.16a). Correspondingly, the expected inverse relationship between the two bluntness parameters (velocity and haematocrit) was observed in all cases with the exception of the SM in the Dextran case, which showed the opposite relationship to that expected on the basis of the preceding discussion (see Figure 5.17). For $V^* < 50s^{-1}$, i.e. in the low flow regime, the SM bluntness increased as the haematocrit bluntness increased.

The following mechanism is proposed to explain this observation, based on the concept that RBC aggregates influence the ability of the SM to flow separately to the RBCs. At the lowest flow rates, there is a high concentration of RBCs in the channel centre which are aggregated. Due to the additional energy cost in navigating the aggregates, the movement of the SM around these aggregates is retarded, and hence the two phases have very similar velocity profiles. As the SM velocity profile is expected to be blunter than that of the RBCs, the result is a reduction in the bluntness of the SM velocity profile. As the flow rate increases, the RBC concentration in the channel centre decreases due to the extent of aggregation decreasing as a result of disaggregating shear forces. This would allow the SM to flow more independently of the RBCs, and hence the SM velocity bluntness tends towards a higher value, as observed at higher flow rates (Figure 5.16). From Figure 5.20a, it can be seen that in the Dextran case, the relative velocity between the two phases, U_ϕ, is nearly zero at low flow rates and stabilises at around -10% for $V^* > 50s^{-1}$, which supports the idea that the interaction between the two phases decreases as the flow rate increases. For the non-aggregating case, the bluntness follows the expected trend for both phases of the fluid, indicating reduced influence of the RBCs on the SM in the absence of aggregation. For the PBS case, at low flow rates,

the relative velocities are around zero (Figure 5.20a), as was observed in the Dextran case, however, the bluntness of the SM is much greater than that of the RBCs (Figure 5.16). As the flow rate increases, the relationship between the velocity bluntness of the two phases stays approximately the same, conversely to the aggregating case.

The opposing trends observed between U_ϕ and *HB* for the Dextran and PBS cases (see Figure 5.20b) can also be explained by the same phenomenon. Although a statistically significant relationship was indicated by the Spearman's correlation coefficient for the entire data set, if the data is again split into high and low flow regimes, and Pearson's correlation coefficient is fit to the data, the results yield $r_c = -0.50, P = 0.012$ and $r_c = 0.56, P = 0.007$ for the low and high flow regimes respectively. This suggests strong correlations with opposite directions in the high and low flow regimes. *HB* and U_ϕ for the Dextran case at high flow rates are related in the same manner as those for the PBS case, i.e. the difference between the velocities of the two phases increases as the bluntness of the haematocrit profile decreases. It was proposed that this is because an increase in RBC concentration in the channel centre (in the absence of aggregation) increases cell-cell interactions which reduces the RBC velocities.

Conversely, this trend is inverted for the Dextran case in the low flow regime: the relative velocity is observed to decrease as the haematocrit in the channel centre increases. In accordance with the above discussion, the greater the extent of aggregation (which corresponds to lower haematocrit bluntness), the less possible it is for the SM to flow independently of the RBCs. As the extent of aggregation decreases (for V^* up to $50s^{-1}$), the SM flow is gradually less dependent on the RBC flow, and hence the relative velocity decreases towards levels expected in the absence of aggregation. The trend in U_ϕ against *HB* is inverted for $V^* > 50s^{-1}$, as the aggregates break up and the RBCs flow separately from one another, increasing the cell-cell interactions. Therefore, it could be said that the inversion of the U_ϕ against *HB* relationship for the Dextran case at low flow rates is a result of the dependence of *HB* on V^*, and hence the extent of aggregation, rather than as a direct influence of the haematocrit concentration profile.

Another interesting characteristic of the measured velocities was the 'bell-shaped' profile of the RBC velocities in the parent branch. This surprising result has not, to the author's knowledge, been discussed previously, although it is visible in a number of

experimental studies (Baker & Wayland, 1974; Choi et al., 2011; Moger et al., 2004; Zhong et al., 2011) and in a computational study by Doddi & Bagchi (2009). Furthermore, Bishop et al. (2001a) analysed velocity profiles *in vivo* and fit the data to Equation 1.14. The exponent K was found on average to be less than 2 (parabolic flow) for non-aggregating cases at medium to high flow rates. For a Newtonian fluid, an exponent of $K < 2$ is not possible (under the conditions of Poiseuille flow), and the presence of rigid particles in a Newtonian fluid blunts velocity profiles (Caro et al., 2012). Hence, for $K < 2$ the RBCs must be strongly influencing the velocity profile. Although the data was not clear enough to indicate whether there was a bell-shape present, it would explain the values of K below those of a parabolic velocity profile[†].

The bell-shape, which resulted in low velocity bluntness, was particularly pronounced for the PBS case, especially at low rates, and decreased as the haematocrit bluntness decreased. For the Dextran case, the bell shape was present but to a lesser extent. Both the RBC and SM profiles had this characteristic at low flow rates, while at higher flow rate the SM profiles lost their bell shape, as a result of the reduced interaction between the phases discussed above (see Figure 5.13). However, for the PBS data, the bell shape was not clear in the SM profiles. The following mechanism which leads to the bell-profile is proposed.

RBC velocities at the wall cannot be considered to be zero. The centre of mass of an RBC aligned so that its major diameter is perpendicular to the axial direction cannot get closer than $\approx 4\mu m$ to the wall. Even when it is in contact with the wall, part of the same cell will lie at least $8\mu m$ into the channel, which for the present geometry is 16% of the channel. Unless the RBC is adhered to the wall, it could be estimated that it would move with an average velocity equal to that for the SM at the location coincident with the centre of mass of the cell, i.e. $4\mu m$ from the channel wall. Hence for locations close to the vessel wall, the velocity would be much greater than would be expected for the continuous phase, while at the outer edge of the cell, the velocity would be reduced relative to the SM. This slow moving cell would interact with adjacent cells, reducing their velocity. However, as distance from the wall increased, there would be more

[†]It could be suspected that the bell shape is an artefact of the PIV approach and interference from the walls, however, it should be noted that all data (both Dextran and PBS, and SM and RBCs) were processed in exactly the same way.

interactions with neighbouring cells, hence closer to the channel centre, the influence of low velocity cells near the wall would decrease. This could explain the observed bell-shape in the experimental data.

In the Dextran case, the haematocrit near the wall was slightly lower than for the PBS case (see Figure 5.8), corresponding to an increased CDL width, as was noted for the Dextran case in Chapter 3. This would reduce the influence of the near-wall RBCs (as there would be less of them) and the aggregated RBCs in the channel centre would be more resistant to the effects of interaction, due to the decreased dispersibilty of RBC aggregates (Bishop et al., 2002) (see also Chapter 3). The combined effect would be a reduction in the extent of the bell-shape characteristics for the Dextran case, as observed in the present data.

5.6.3 Bifurcation: Daughter and outlet branches

In the vasculature, there will be some sections which are sufficiently long for the flow to fully develop, however, Carr & Xiao (1995) estimated that this is only the case in about 40% of vessels. The regular branching of vessels significantly changes the distributions of velocity and viscosity, which are dependent on flow rate, flow ratio and geometrical considerations such as the angle of the bifurcation and the branch widths.

The geometry used in the present data is such that the outlet branch is a continuation of the parent branch, while the daughter branch is perpendicular and hence characteristics from the parent branch are less likely to be continued in the daughter branch (see Figure 5.1). The present data was acquired such that the flow ratio (Q^*) should be independent of the parent branch normalised velocity (V^*), in order to enable separation of the two parameters. To test this condition, Pearson's correlation was applied to the two parameters. For the Dextran case, it was found that $P = 0.076$, implying no significant relationship. For the PBS case, the P-value was 0.024, indicating a significant correlation, with a corresponding correlation coefficient of $\rho_c = -0.4$. However, if the highest two velocity cases for the PBS data are omitted, then the P-value increases to 0.080. Hence, it is reasonable to assume that the two control parameters, V^* and Q^* are independent. Thus, for these data, the skewness of the velocity and haematocrit profiles was considered parametrically, as well as the relative velocity between the two phases of the fluid. Additionally, the bulk haematocrit ratio and RBC flux ratio were

analysed.

The lowest velocities analysed in the present study were $0.10mm/s$ for the daughter branch and $0.38mm/s$ for the outlet branch, corresponding to normalised velocities of 2 and 7.6 channel widths (D) per second. Given that the imaging region covered a length of $3.5D$ for each branch, the minimum transit times were 1.75 and 0.46 seconds for the daughter and outlet branches respectively. Given these short times and the time scale of the aggregation process (on the order of 5 seconds (Cokelet, 1980)), it is unlikely that significant aggregation takes place immediately after the bifurcation and hence in the region analysed here. Thus, as in Chapter 4, the observed effects of aggregation are a result of the aggregation that has occurred upstream of the bifurcation (i.e. in the parent branch), and the way in which it effects the distribution and dispersibility of the RBCs and the flow of the suspending medium.

Plasma skimming would be expected to occur under the conditions of the present investigation. This was shown in both the haematocrit ratio and RBC flux ratio plots to be a strong function of the flow ratio (Figures 5.6 and 5.7). The RBC flux ratio was fit to an empirical logit function (Pries et al., 1989) and while the PBS case parameters indicated slightly greater sigmoidal shape, the Dextran cases were more asymmetric, meaning that there was a greater difference between the daughter and outlet branches. In the previous chapter, for a symmetric 'straight-T' bifurcation, there was slightly more plasma skimming in the aggregating case than the non-aggregating case. For the present 'side-T' geometry, the Dextran and PBS cases had similar total plasma skimming. This indicates an importance of geometry on plasma skimming when RBC aggregation is present.

Fenton et al. (1985) found that parent branch flow rate was not an important factor in plasma skimming, however their data was acquired for relatively high flow rates. They grouped their results into three groups: $Re < 0.3$, $0.3 < Re < 3$ and $Re > 3$. The Reynolds number, $Re = \rho \overline{V} D/\mu$, can be estimated for the present data based on the apparent viscosity calculated using the CFD simulations, a blood density of $1039kg/m^3$ (see Chapter 6), and using $D = 50\mu m$ (as the hydraulic diameter of a square channel is equivalent to the cylindrical vessel diameter). This gives ranges $Re = 0.02 - 0.3$

for the present data, i.e. all data fit within the lower category considered by Fenton et al. (1985). Figure 5.6b showed that there was an effect of parent branch flow rate on the extent of plasma skimming. For the Dextran case, the extent of plasma skimming decreased with increasing flow rate, whilst the opposite was observed for the PBS case. This is the same trend as observed for the haematocrit profile bluntness. Directly comparing *HB* to H_d^* (an indication of plasma skimming) yields P-values of 0.02 and 0.05, respectively (not plotted for brevity). As *HB* decreases, the haematocrit in the channel centre is greater relative to the mean. Correspondingly, the haematocrit near the channel edges must decrease, which would enhance plasma skimming. Hence, the present data shows that, for low flow rates, plasma skimming is significantly affected by the parent branch flow rate, particularly in the presence of RBC aggregation, due to its effect on the haematocrit distribution in the parent branch.

The haematocrit profiles were observed to be skewed, with the haematocrit being increased near the outer wall of the daughter branch and the inner wall of the outlet branch (Figure 5.10), as would be expected if the RBCs, distributed as observed in the parent branch, were to directly follow streamlines. In general, the haematocrit profiles qualitatively matched those measured by Manjunatha & Singh (2002) and shown schematically by Cokelet (2011). At very low flow ratios, where only 10% of the total flow entered the daughter branch ($Q^* = 0.1$), almost 80% of the RBCs were located in the channel close to the outer wall ($HS = 0.2$, see Figure 5.11). This value tended towards around 60% for an equal flow split. Both Dextran and PBS cases showed similar trends (Figure 5.11a), although the shapes of the profiles were different (Figures 5.10a and c). In the outlet branch (Figure 5.11b), the skewness tended towards $HS = 0.5$ as more of the flow entered that branch (increasing Q^*). At approximately equal flow split, around 60% of the cells existed in the half of the channel closest to the inner wall $HS = 0.6$, with very slightly more for the Dextran case. Aside from the skewness, the haematocrit profiles in the outlet branch were similar to those of the parent branch, with less bluntness in the Dextran case, again indicating a continuation of the parent branch characteristics.

A greater degree of skewness in the velocity profiles was observed to occur in the daughter branch than the outlet branch, corresponding with the greater skewness of the

haematocrit profile (although in the opposite direction). In the daughter branch, the SM velocity skewness, was more affected by *HS* than the RBC velocity skewness (compare Figure 5.18c to a). Additionally, despite the similar *HS* (Figure 5.11), the Dextran case *VS* in the daughter branch was greater than that of the PBS case (Figures 5.18 a and c), and was more strongly correlated with flow ratio (Figure 5.18a and c). In the outlet branch, a similar trend was observed, but the PBS skewness only scaled with flow ratio for the SM (i.e. no correlation was observed between the RBC velocity skewness and the flow ratio, see Figure 5.18b and d). The velocity and haematocrit skewness were compared directly, and strong correlations were shown for RBC and SM for the Dextran cases, but only for the SM for the PBS case (Figure 5.19b and d).

The skewness in the velocity profiles arises as a result of the uneven haematocrit distribution. Where there are more RBCs, the local viscosity is increased due to the energy loss associated with flow in and around a large number of moving obstacles (RBCs). Additionally, SM velocity in regions of high haematocrit will be closer to that of the RBCs. This was observed for both aggregating and non-aggregating cases, although in the presence of aggregation, the energy loss would be increased and hence a greater degree of skewing would be expected. In the regions of high haematocrit, the velocities of the two phases of the blood were observed to be closer than in the low haematocrit region (compare Figure 5.10 to Figures 5.15 and 5.14), as the greater the local haematocrit, the more the RBCs will influence the SM velocity; this was particularly the case in the daughter branch. This explains the increase in *VS* with *HS* for the SM for all cases. The RBC velocities seem to be less influenced by their local concentration than the SM velocities, as would be expected due to the finite size of the RBCs compared to the continuum SM. RBC aggregation further enhanced this effect, as the phenomenon reduces RBC dispersibility, meaning the RBCs travel together and the SM flow is greatly retarded. Therefore, the effect of the haematocrit is greater on the SM than the RBC velocity. This is supported by increased bluntness in the parent branch for the SM compared to the RBC (Figure 5.16).

The present experimental setup allowed for simultaneous measurement of both phases of the blood and hence calculation of the relative velocity between the two phases. In the parent branch, it was shown that the relative velocity was mainly influenced by the

parent branch haematocrit profile bluntness, except in the presence of significant RBC aggregation. The results in the daughter and outlet branches, however, were different.

In the outlet branch, the relative velocity was strongly influenced by the flow rate in that branch, following the same trend as in the parent branch (Figures 5.21 and 5.22), but not by the flow ratio (Figure 5.23). In the daughter branch, the relative velocity was strongly influenced by flow ratio (Figures 5.23), and hence the haematocrit ratio. However, U_ϕ was less affected by the absolute flow rate (Figure 5.21) in the daughter branch than the outlet branch. For the PBS case, the significance of the trend in U_ϕ against V^* was just less than the commonly considered level ($P = 0.054$), but showed a decrease in U_ϕ for higher velocities, as observed in the parent branch (Figure 5.20). For the Dextran case, a trend of increasing relative velocity with increasing flow rate was observed. However, the data for the daughter branch in Figure 5.21 are highly scattered for low V^* making it hard to further investigate the trend, and indicating that V^* is not the dominant parameter in the daughter branch.

Comparing the daughter and outlet branch mean relative velocities directly to those in the parent branch (Figure 5.22), showed that the outlet and parent branch relative velocities are almost identical in all cases (using Pearson's correlation coefficient $r_c = 0.92$ and 0.90, with $P < 0.001$ for both Dextran and PBS cases). For the daughter branch in the Dextran case, there was no correlation ($P = 0.702$), while there was a positive correlation for the PBS case ($P = 0.002$), albeit a less strong one than for the outlet branch.

Hence, it seems that the ratio of the velocity of the two phases in the outlet branch is almost entirely dependent on the relative velocity (and hence the haematocrit bluntness) and the state of aggregation in the parent branch. This is due to the geometry resulting in the outlet branch being a continuation of the parent branch.

In the daughter branch, the relative velocity is predominantly dependent on the flow ratio (Figure 5.23), which in turn scales directly with the haematocrit ratio (Figure 5.6): as the ratio of RBC to SM by volume (haematocrit) decreased, the relative velocity of the RBCs also decreased significantly. Additionally, the haematocrit ratio correlates very strongly with the skewness of the haematocrit profile ($\rho_c = 0.87$ and $\rho_c = 0.85$ for Dextran and PBS cases, both with $P < 0.001$, not shown). Both the Dextran and PBS cases displayed similar relationships in terms of both haematocrit ratio and skewness.

5.7 Significance of the reported data

Measurements of blood velocity using PIV approaches have recently become quite common. Using either the RBCs as tracers (Hove et al., 2003; Nakano et al., 2003) or suspending fluorescent particles in the fluid (Damiano et al., 2004; Vennemann et al., 2006) are two commonly used approaches. Poelma et al. (2012) reported that the two measurement methods diverge as the depth of field decreases relative to the channel depth (Poelma et al., 2012), but assume that the measurements would be otherwise equivalent. However, the results of the present study showed quite different results in terms of the two phases of the blood velocity. The relative velocity between the two phases differed by around 10% at high flow rates in the parent branch, and by up to 50% in the daughter branch. Furthermore, a strong bell-shape was observed in the RBC velocity profile, which is postulated to be a result of RBC-RBC and RBC-wall interactions. Finally, aggregation was observed to significantly modify the characteristics of the relative velocity even at very high flow rates (wherein aggregation is often assumed to be negligible). The combination of these phenomena highlight how important it is to account for both phases of the blood.

While haematocrit distributions have previously been described qualitatively (Cokelet, 2011) and quantitatively (Manjunatha & Singh, 2002), the present study represents the first parametric analysis of haematocrit distributions in a bifurcation. The observed trends qualitatively matched those described elsewhere; the parametric analysis has provided information from which inferences about the interplay between various microhaemodynamic phenomena, such as RBC aggregation and radial migration, are possible.

Combining the data on both haematocrit and velocity distribution throughout the channel provides an opportunity to validate future computational simulations with a higher degree of accuracy than has been hitherto possible. Computational approaches in which RBCs are treated individually as a collection of springs (Fedosov et al., 2010a; Imai et al., 2010) can provide a large amount of data on the velocities of both phases of the blood. If such models are capable of reproducing the experimental data observed in the present work, then they could help to further clarify the mechanics behind the observed trends and either support the proposed mechanisms or provide alternative explanations. Furthermore, the data could be used directly in a hybrid approach to modelling blood

flow as a continuum, by combining the haematocrit distribution with empirical viscosity models. This approach is investigated in Chapter 6.

The conversion of two-dimensional to three-dimensional data used in the present study required that the microchannel cross section was square (i.e. there was a unity aspect ratio). However, it may be possible to extend the technique to a circular cross-section, by accounting for the difference in channel depth by weighting the values across the channel. If a sufficiently two-dimensional microvascular network could be found *in vivo*, then the approach could be extended to animal work. Although the resolution of the data would inevitably be decreased, and the degree of scatter would be greater, such information could be invaluable in developing better understanding of microvascular blood flow.

5.8 Closure

The aim of the present chapter was to provide a more complete description of the haemodynamics in a bifurcating geometry. Newly developed experimental techniques provided quantitative data on haematocrit distributions in a bifurcation for different flow rates and flow ratios. Furthermore, by acquiring data on the velocities of both the RBCs and SM, analysis of the relative velocity between the phases was possible. The results showed a number of interesting trends, and RBC aggregation was observed to greatly alter the characteristics compared to samples in which aggregation was absent. Due to experimental limitations, it was not possible to directly infer information on the effect of RBC aggregation on apparent viscosity. Additionally, for the reasons discussed in §1.4.6, accurate wall shear stress data was not available. In the next chapter, apparent viscosity and wall shear stress values for the present data are calculated by using the experimental data as an input to CFD simulations. The estimated three-dimensional haematocrit distributions are combined with a haematocrit and shear dependent empirical viscosity model in order to produce a hybrid computational model of the blood flow in the present bifurcating geometry.

Chapter 6

A hybrid approach to modelling microhaemodynamics

In this chapter a continuum computational approach model is developed that utilises experimentally measured haematocrit profiles. A viscosity model which is dependent on both the local haematocrit concentration and shear rate is utilised. The model is then numerically solved for the appropriate boundary conditions and the computed velocity profiles compared with experimentally determined values.

6.1 Introduction

It is widely accepted that blood viscosity has shear-thinning properties which are also dependent on haematocrit. Such relationships have been described in detail for bulk haematocrits (Chien, 1970; Pries et al., 1992b), but descriptions of localised effects are scarce (Das et al., 1998; Hokkanen, 1989) and have hitherto only been provided based on simulations. In Chapter 5, experimental data on haematocrit and velocity distributions of both the RBCs and the SM was collected and analysed. In the present chapter, these data are used to provide input to a hybrid computational approach for the simulation of microhaemodynamics.

Macroscale (arterial size) blood flow simulations commonly assume that the blood is a Newtonian fluid, although shear-thinning models, such as the Carreau-Yasuda model (Gijsen et al., 1999) can be utilised in order to make the simulations more realistic. However, there is no consensus on which model best represents true blood flow, as a result of a lack of sufficiently detailed experimental data for validation, and hence some degree of subjectivity is involved in the selection of the most appropriate model (Soulis

et al., 2008).

A number of groups (Fedosov et al., 2010b; Imai et al., 2010) have recently developed sophisticated computational models based on modelling individual RBCs as a collection of interconnected springs, which allow highly detailed simulations of microvascular blood flow. These methods have proved able to predict well known microvascular phenomena, such as radial migration and the Fåhraeus and Fåhraeus-Lindqvist effects, but further rigorous comparison with detailed experimental data is still required. Furthermore, the approach is associated with great computational requirements, and this limits its use. Two-dimensional models of individual RBCs using, for example, the immersed boundary (Bagchi, 2007; Eggleton & Popel, 1998) or lattice-Boltzman (Hyakutake et al., 2006; Zhang et al., 2008) approaches are less computationally expensive, but by assuming planar RBCs, they have their own limitations.

The approach used in this chapter considers blood as a continuum, which is reasonable for vessel scales down to approximately $20\mu m$ (Cokelet, 1999), but defines the viscosity as a function of shear rate and haematocrit in aggregating and non-aggregating blood samples. The Quemada model (Cokelet, 1987; Quemada, 1977; 1978a; 1978b), is used for this purpose, employing empirically defined parameters. This approach allows for simulations with a very low computational expense, but with a strong haemodynamic basis, which is validated via direct comparison with experimental results.

The haematocrit distributions derived in the previous chapter are used in conjunction with experimental velocity measurements to provide boundary conditions, and the shear dependent terms in the Quemada model are calculated intrinsically within the simulation. For each of the cases acquired in Chapter 5, a simulation of the flow is carried out in the domain indicated in Figure 5.1. Additional simulations are also carried out, assuming uniform haematocrit distributions, in order to allow analysis of the effect of the haematocrit distribution separately from the mean haematocrit and flow rate.

In addition to providing an alternative approach to blood flow simulations, the results allow for consideration of the wall shear stress and apparent viscosity under different circumstances, which was not possible from the experimental data.

The chapter will proceed with a description of the Quemada model and empirically defined fits to its parameters, followed by the details of the computational fluid dynamics simulations. The velocity results will be analysed and compared to the total fluid flux

calculated from the experiments in order to validate the model. Finally, the dependence of wall shear stress and apparent viscosity in each of the branches will be considered in relation to the normalised velocity, flow ratio and the skewness and bluntness parameters.

6.2 Definition of viscosity

In the present chapter, both the shear rate and haematocrit dependent aspects of blood viscosity will be accounted for. One model which captures both phenomena is that of Quemada (1977; 1978a; 1978b). This model is derived from first principles and is described by

$$\mu = \frac{\mu_0}{(1 - 0.5kH)^2} \tag{6.1}$$

where μ_0 is the suspending medium viscosity, H is the haematocrit and the parameter k is described by

$$k = \frac{k_0 + k_\infty \sqrt{\gamma_r}}{1 + \sqrt{\gamma_r}} \tag{6.2}$$

k_0 is the intrinsic viscosity of the fluid at zero shear, i.e. the parameter defines the contribution of the RBCs to the viscosity of the fluid under static conditions. k_∞ is the intrinsic viscosity at infinite shear (hence negating aggregation effects). The term γ_r is defined according to $\gamma_r = \gamma/\gamma_c$: the shear rate at a given location, $\gamma^\dagger$, divided by the critical shear rate γ_c. The latter can be considered to be the inverse of the relaxation time for the mechanism which causes the fluid to be non-Newtonian (namely a combination of RBC aggregation and deformation). The values of k_0, k_∞ and γ_c have been empirically defined by Dufaux et al. (1980) and Cokelet (1987) using a Couette viscometer. They recorded viscosity under a number of shear and haematocrit conditions and calculated the parameters for each data set. The parameters were plotted against haematocrit and fits of the natural log of each parameter were calculated:

$$\ln\left(k_{0,A}\right) = 3.874 - 10.41H + 13.80H^2 - 6.738H^3 \tag{6.3}$$

†Note that γ is used as opposed to $\dot{\gamma}$ in order to be consistent with other papers referring to the Quemada model.

$$\ln(k_{0,N}) = 0.6534 + 2.350H - 3.451H^2 - 1.120H^3 \tag{6.4}$$

$$\ln(k_{\infty}) = 1.3435 - 2.803H + 2.711H^2 - 0.6479H^3 \tag{6.5}$$

$$\ln(\gamma_{c,A}) = -6.7597 + 25.626H - 18.988H^2 \tag{6.6}$$

$$\ln(\gamma_{c,N}) = 7.7381 - 7.5411H \tag{6.7}$$

The subscripts A and N indicate aggregating and non-aggregating samples. Note that k_{∞} is defined for both aggregating and non-aggregating cases, as under infinite shear no aggregation would be present.

Figure 6.1 shows graphically the dependence of the parameters on haematocrit. It can be seen that k_{∞} decreases as the haematocrit increases. This is a result of increased RBC deformation at high RBC concentration, which allows the RBCs to align with the flow and undergo 'tank-treading' which reduces their contribution to the flow resistance. The dotted line section on the figure indicates extrapolation of the fitted curve beyond the experimental data sets of Cokelet (1987). The viscosity at zero shear rate (Figure 6.1b) increases slightly for the non-aggregating case as the haematocrit increases. This is due to the increased interactions between RBCs at higher concentrations. Conversely, the intrinsic viscosity at zero shear rate for aggregating blood decreases at higher haematocrit, as when there are more cells, they are inevitably more closely packed and hence the effect aggregation has on the viscosity is relatively decreased.

The critical shear rate, γ_c, is shown in Figure 6.1c. Recall that this parameter can be considered to relate to the inverse of the timescale of the phenomenon which causes non-Newtonian behaviour, t_c. For the non-aggregating case, $t_c \approx 0$ as RBC deformation is almost instantaneous (with a time constant of $0.06s$ (Cokelet, 1980)). For the aggregating case, the critical shear rate starts with a very low value and increases with increasing haematocrit. However, aggregation time is very dependent on the geometry: in tube flow, RBCs preferentially tend towards the tube centre (radial migration) which would increase the chance of cell-cell collisions and consequently aggregation rate.

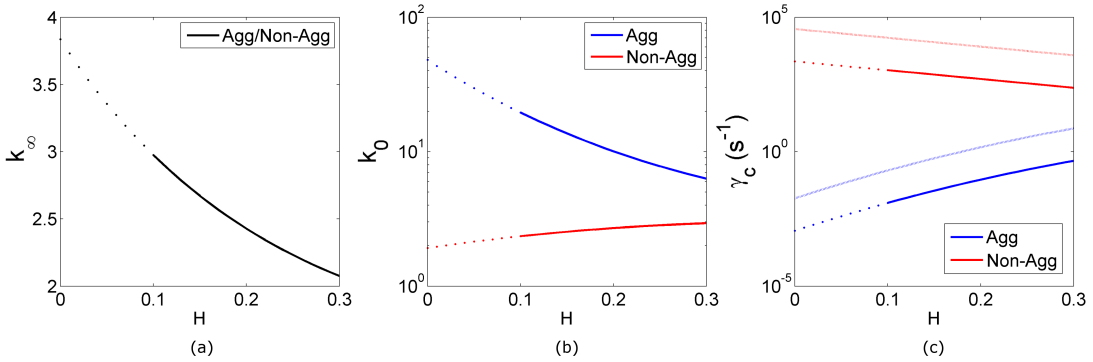

Figure 6.1: Quemada parameters as defined in Equations 6.3-6.7. (a) k_∞, (b) k_0, (c) γ_c. Dashed line sections indicate extrapolations of the fitted lines beyond the minimum haematocrit considered in the definition of the empirical values (Cokelet, 1987).

Hence, the data for this parameter defined in a Couette viscometer may overestimate aggregation time, and thus underestimate γ_c. In order to counter this in the present experiments, the term γ_c was multiplied by 16, as indicated by the dashed lines in Figure 6.1c, which is the equivalent of dividing the $\sqrt{(\gamma/\gamma_c)}$ term in Equation 6.2 by a factor of four. As this term appears on both the numerator and the denominator, the effect is to relatively increase the effect of the zero shear intrinsic viscosity term compared to the infinite shear viscosity term.

Figure 6.2a compares the relative viscosity, $\mu_r = \mu/\mu_0$ as a function of haematocrit at shear rates of 1, 10, 100 and 1000 s^{-1} calculated from the Quemada model with the empirical parameters. Figure 6.2b shows the same data but with the modification of the γ_c term, denoted μ_r'. It can be seen that the non-aggregating data is not significantly affected, but for the aggregating case, the relative viscosity is greatly increased at low shear rate as the haematocrit increases. The effect of the applied modification to the model is further considered in Figure 6.2c, which shows the ratio of the normal to the modified relative viscosity. For very low shear rates on the order of unity, the modified relative viscosity increased almost ten-fold at a haematocrit of 0.2. The relative difference is reduced for lower haematocrits and higher shear rates. Given that in a channel, the haematocrit at the wall is decreased and the shear rate correspondingly increased, the effect of the proposed modification will be to increase the viscosity in the channel centre and hence enhance bluntness of the velocity profile. Initial simulations without the modification predicted velocity profiles that were not blunt enough (compared to

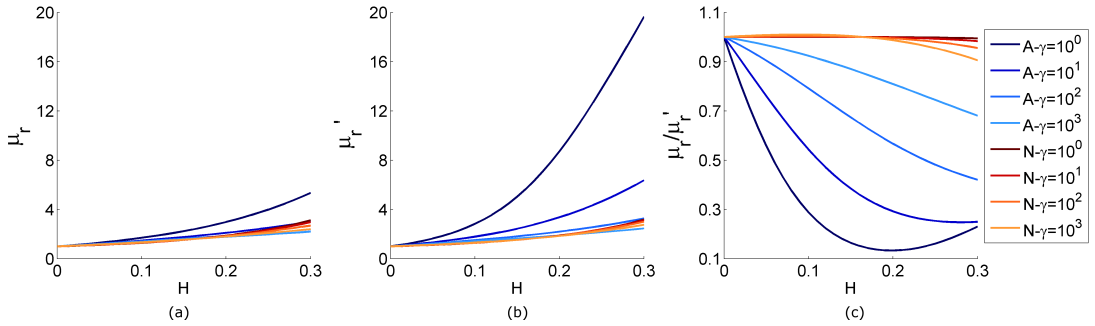

Figure 6.2: Quemada viscosity as a function of haematocrit at different shear rates. (a) with empirical parameters (Cokelet, 1987; Dufaux et al., 1980), (b) with $0.25\gamma_c$, (c) Ratio of normal to modified Quemada viscosity.

the experimental measurements), and so a small number of values of the modification parameter were tried. The selected value of sixteen was chosen as it gave results which most closely matched the experimental data.

A final comment should be made regarding aggregation: the variability of RBC 'aggregability' in the general population is very large (up to 100% (Meiselman, 2009)) and the choice of suspending medium also changes the characteristics of the effect. The present study does not seek to investigate these parameters, as could be done with relative ease in a Couette system, but instead aims to elucidate the effect that aggregation has on flow characteristics in idealised geometries that represent segments of the microvasculature.

6.3 Computational approach

ANSYS CFX 14.0 (ANSYS, UK) was used to simulate the flow in the bifurcation. A model domain was generated with branches of $7.5D$ in length. The domain was meshed with $819,200$ structured cubic elements with a side length of $1.5625\mu m$, giving 32 elements across the diameter of the channel.

ANSYS CFX uses a finite volume method with an implicit pressure based algorithm. Advection terms were calculated using the high resolution method in which the blend factor is adjusted non-linearly in order to be as close to one as possible without the introduction of new extrema in the solution. Diffusion terms are calculated using parametric shape functions. Interpolation of velocity terms is carried out using tri-linear interpolation and linear-linear interpolation is used for pressure interpolation. Pressure-velocity

coupling is carried out using 4^{th} order Rhie-Chow approach.

In order to validate the chosen mesh size, results were compared to a coarse mesh with a total of $200,000$ cubic elements with side length $2.5\mu m$. A fine mesh was also analysed, in which the cubic elements had $1\mu m$ sides, giving $3,125,000$ elements in total. The aggregating case with the lowest flow ratio of $Q^{=}0.085$ was selected and the parent branch velocity was set to $7.5mm/s$. The pressure drop between the parent branch and both branches varied by 1.4% between the medium and coarse and less than 0.7% between the medium and fine meshes. The velocity bluntness in the parent branch varied by less than 0.5% between the results of the three meshes. After interpolating the coarse and medium velocities onto the fine mesh, the maximum velocities were found at the same location for all three meshes. After further interpolation to give the skewness parameter, the skewness changed by 3% between the medium and coarse meshes and 1.5% between the medium and fine meshes.

Hence, the changes made by each refinement decreased as the mesh became finer, but the differences were small. Thus the medium mesh was selected as a trade-off between speed and resolution (as interpolation can be used in the post processing stage).

The fluid was considered to be continuous with viscosity defined according to Equations 6.3-6.7, where the haematocrit at each location was defined using the experimental data. The calculated channel haematocrit in the parent branch for the experimental data were 0.13 ± 0.01 and 0.15 ± 0.01[†] for Dextran and PBS cases respectively. This difference is very small; however, applying this in the model would make it difficult to directly compare results. Therefore, all haematocrit distributions were normalised such that the average parent branch haematocrit was 0.14. Given that the simulations were designed to replicate the experimental measurements, in addition to the estimated haematocrit distribution, the boundary conditions were defined based on the experimental measurements. The inlet was defined according to the analytical equation (Equation 1.11), normalised so as to have the same mean as the experimental data, $\overline{U_p}$. This approach is used rather than directly applying the measured profiles, so as to allow the profiles to naturally develop. This is because analysis of the ability of the model to predict velocity profiles is the most suitable way of validating the data, and predefining profiles would preclude such a comparison.

[†]As a result of the Fåhraeus effect and RBC screening.

For the daughter branch, a constant velocity boundary condition was applied based on the flow ratio from the experimental data. As the ideal situation of $Q_d^* = 1 - Q_o^*$ was not met exactly by the experimental data, a corrected value of Q_d^*, was used. The daughter branch outlet velocity was thus set to be $\overline{U_d} = \overline{U_p}\left(Q_d^* + 1 - Q_o^*\right)/2$. The boundary of the outlet branch was set to $0Pa$. The flow was considered to be laminar and the fluid density was $1039kg/m^3$ (based on mean haematocrit of 0.14, and RBC and plasma densities of 1025 and $1125kg/m^3$ respectively). For the PBS solution, μ_0 was measured with a viscometer and found to be $1.0mPa\ s$. The addition of Dextran increased this value to $1.3mPa\ s$. However, to allow for better comparison between cases, μ_0 was set to $1.0mPa\ s$ for both cases. Convergence was defined when the root mean square residuals were less than 10^{-5}.

In order to decouple the effects of bulk haematocrit due to plasma skimming from the shape of the haematocrit distribution, an additional set of simulations was carried out, wherein, a long straight channel of length $16D$ was used for the parent, daughter and outlet branches. The geometry was meshed with the same element size as the bifurcation. In the parent branch, haematocrits were set to 0.14. In the daughter and outlet branches, haematocrits were defined according to the values measured in the experimental data, scaled as before. For all cases, the inlet velocity was defined similarly to the bifurcation simulations, i.e. the analytical solution was scaled according to $\overline{U_p}$, $\overline{U_d}$ or $\overline{U_o}$ (where $\overline{U_o} = \overline{U_p}\left(Q_o^* + 1 - Q_d^*\right)/2$). A total of 45 aggregating and 32 non-aggregating cases were examined at a range of parent branch flow rates and flow ratios.

6.4 Results and discussion

In this chapter, the results and discussion are combined. A comparison between the experimental and computational velocity data will first be given, followed by analysis of the wall shear stress and apparent viscosity. Subsequently, the efficacy of the proposed methodology will be discussed.

6.4.1 Velocity characteristics

In order to analyse whether the model is capable of predicting the key characteristics of the blood velocity, the velocity profiles will be considered. Firstly, the parent branch will be analysed in isolation, comparing the uniform and distributed haematocrit

models in order to highlight the differences between the two. The computational and experimental profiles will then be compared for all branches under different flow conditions. In order to simplify the discussion, the terms Dextran and PBS will be taken to be synonymous with aggregating and non-aggregating respectively, as was done for the previous chapters.

Figure 6.3 shows velocity profiles in the parent branch, comparing the profiles calculated using the experimental haematocrit distribution, termed CFDH herein, to those acquired with a uniform distribution, termed CFDU[†]. For the CFDU data, the results for the PBS case at low and high flow rates (Figure 6.3c and d) are almost identical to those of the analytical solution (Bruus, 2008) (indicated by the shaded grey area on the figure). For the Dextran case, the CFDU profile is slightly blunted at high flow rate (Figure 6.3b) and more so at the low flow rate (Figure 6.3a), although the degree of blunting is small.

For the non-uniform haematocrit cases (CFDH) however, the velocity profile for the Dextran case at low flow rate is very blunt (Figure 6.3a), but becomes less so at a higher flow rate (Figure 6.3b). For the PBS case at low flow rate (Figure 6.3c), the velocity profile for the CFDH data is blunter than that for the CFDU data. At high flow rate (Figure 6.3d), the CFDH velocity profile is more blunt than for at low flow rate, and closely matches that of the Dextran case at high flow rate (Figure 6.3b).

This trend was also observed for the experimental data (Figure 5.13). The slight asymmetry of the CFDH cases is a result of asymmetry in the applied haematocrit distributions (the symmetry condition was only applied in the (x, z) and (y, z) planes). These results show that the CFDH model is more capable of replicating the flow field than the CFDU approach and confirms the importance of accounting for the local haematocrit distribution.

Given that the computational model considers the blood as a single continuous fluid with spatially variant viscosity, comparison with the experimental data should be carried out relative to the total fluid velocity (the sum of the RBC and plasma components), for which the total fluid velocity profile must be defined. The total flux was defined in Equation 5.13 as $Q_{tot} = Q_{rbc} + Q_{sm}$, with Q_{rbc} and Q_{sm} defined according to Equa-

[†]In the terminology CFDH and CFDU, the CFD stands for computational fluid dynamics. H indicates the experimental haematocrit distribution and U represents a uniform haematocrit.

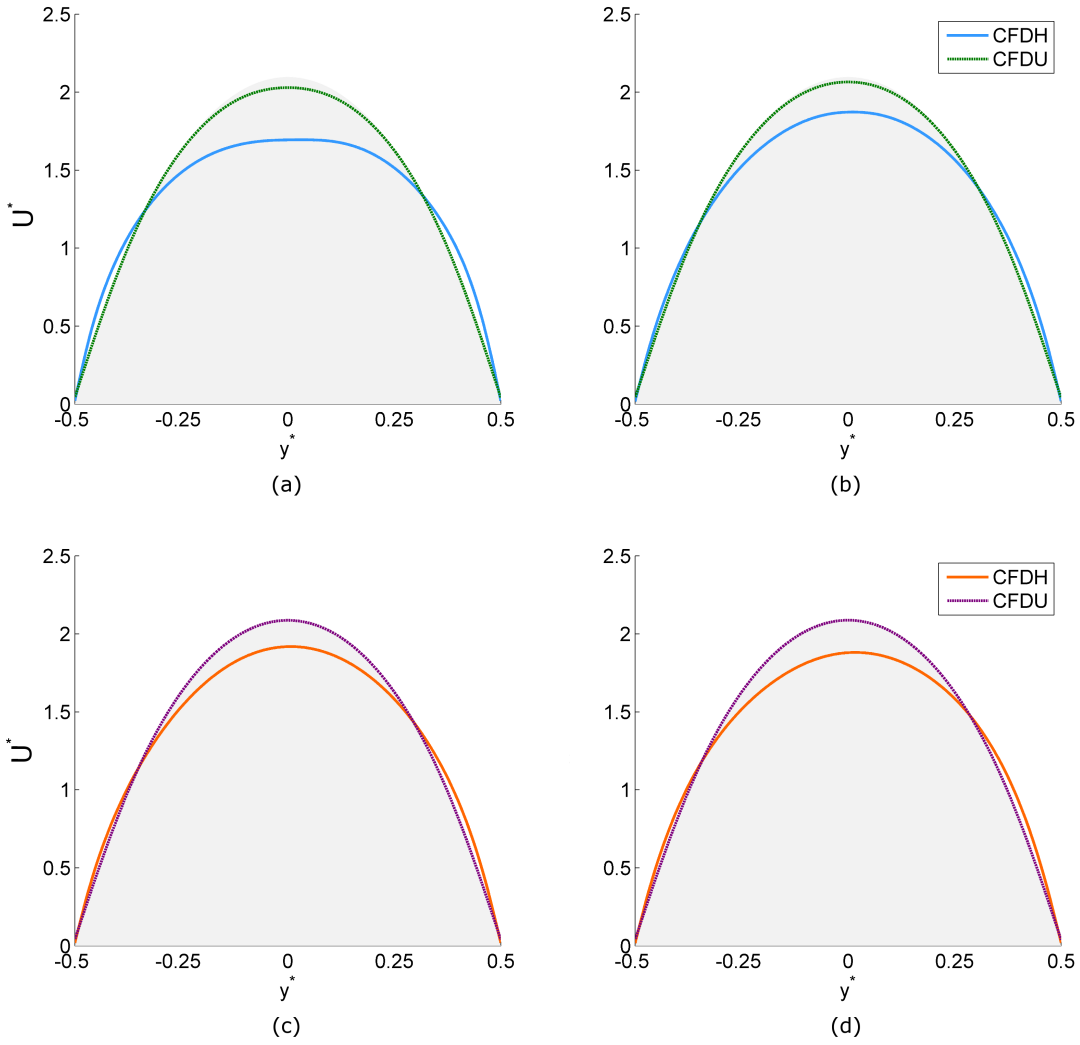

Figure 6.3: Comparison between CFD velocity profiles in the parent branch for haematocrit distribution and uniform haematocrit. Shaded grey shows analytical solution. (a) Dex - $V^* = 17.7s^{-1}$, (b) Dex - $V^* = 144.0s^{-1}$, (c) PBS - $V^* = 16.4s^{-1}$, (d) PBS - $V^* = 145.4s^{-1}$.

tions 5.11 and 5.12 respectively. Given that the flow in the averaging regions can be assumed to be one dimensional (i.e. there is only one non-zero velocity component), for an infinitesimal area dA

$$dQ_{tot}\left(y,z\right) = \int\int_{dA} U_{rbc}\left(y,z\right) H\left(y,z\right) dydz + \int\int_{dA} U_{sm}\left(y,z\right)\left(1 - H\left(y,z\right)\right) dydz \tag{6.8}$$

At this infinitesimal area, the velocity and haematocrit can be assumed to be constant, hence

$$dQ_{tot}\left(y,z\right) = U_{rbc}\left(y,z\right) H\left(y,z\right) dA + U_{sm}\left(y,z\right)\left(1 - H\left(y,z\right)\right) dA \tag{6.9}$$

The average velocity in the area dA, is then given by

$$U_{tot}\left(y,z\right) = \frac{dQ_{tot}}{dA} = U_{rbc}\left(y,z\right) H\left(y,z\right) + U_{sm}\left(y,z\right)\left(1 - H\left(y,z\right)\right) \tag{6.10}$$

The total fluid velocity profiles can thus be calculated according to Equation 6.10. To do this, the experimental velocity profiles are first interpolated to the resolution of the haematocrit profiles using spline interpolation. For clarity, these will simply be referred to as experimental velocity profiles herein.

The computational velocity profiles are compared to the experimental profiles in the parent branch in Figure 6.4, which shows the same cases as Figure 5.13. It is worth noting that, as the simulation makes the assumption of a continuous single phase fluid of varying viscosity, it will not be capable of predicting the bell-shaped curve observed in the experimental data, as this was a result of the discrete nature of the RBCs.

For the aggregating case at high flow rate (Figure 6.4b), the difference between the computational and experimental data is almost zero. At low flow rate, the CFDH velocity profile for the aggregating case is more blunt in the channel centre than for the experimental data, but accurately predicts the velocities closer to the channel walls. The bell shape in the experimental data is reflected in the difference between the velocity profiles in the figure, as it is not predicted by the model.

For the non-aggregating case at low flow rate, the data are similar to the aggregating case, in that the CFD and experimental data are very similar near the walls, but the model fails to reproduce the bell-shape in the channel centre. For the high flow rate case, there is an asymmetry visible in the experimental velocity profile, but otherwise the profiles are fairly similar except in the channel centre, which is a limitation of the present approach.

Figure 6.5 compares the experimental and computational velocity profiles in the daughter and outlet branches at low flow ratio (the same cases as Figure 5.14). Considering first the daughter branch for the Dextran case in Figure 6.5a, it can be seen that the CFD profile has a very similar shape to that of the experimental data. In the outlet branch, the computational and experimental velocity profiles also match very well. In both cases,

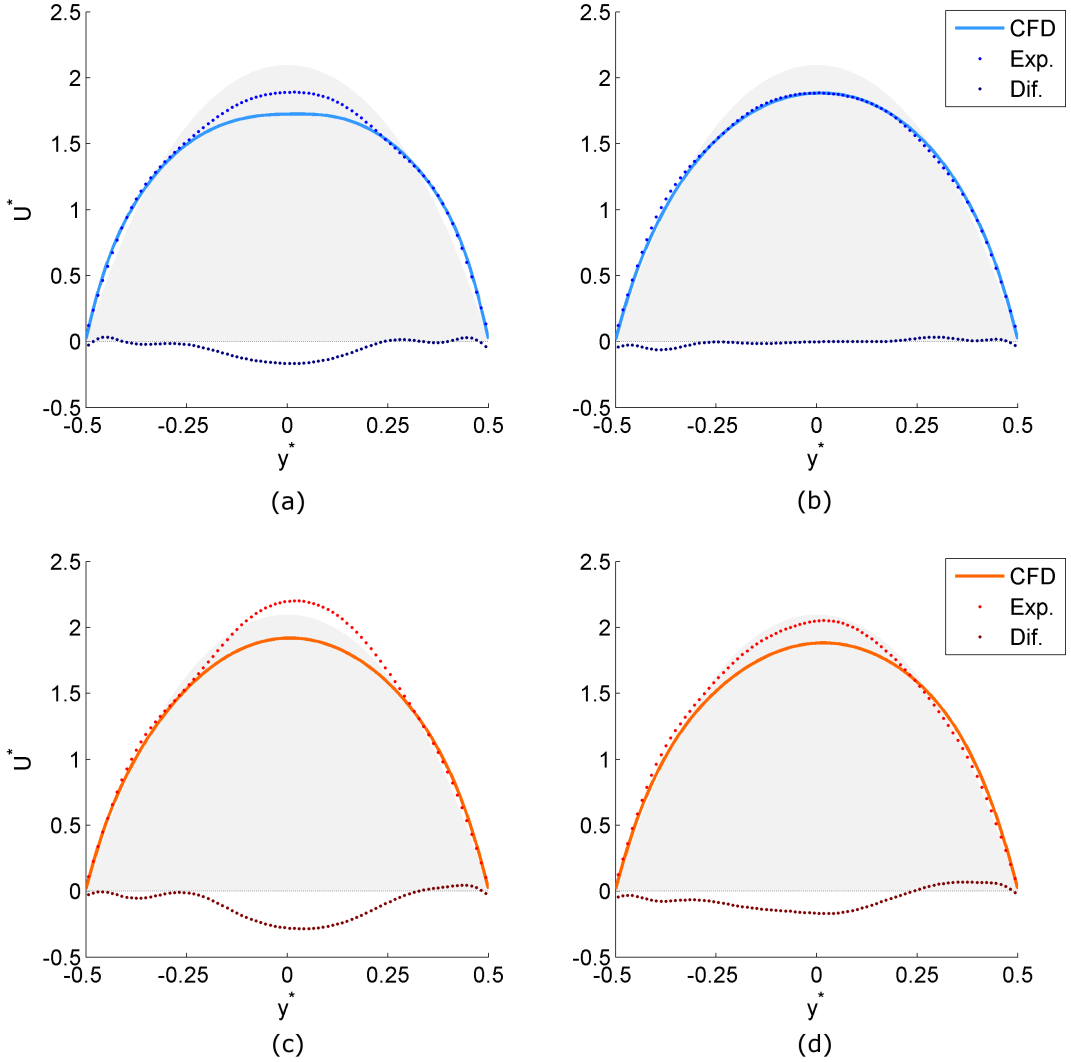

Figure 6.4: Comparison between computational (CFD) and experimental (Exp.) profiles, and the difference between the two (Dif.) in the parent branch. Shaded grey shows analytical solution. Dark lines show the difference between the CFD profile and the experimental . (a) Dextran - $V^* = 17.7s^{-1}$, (b) Dextran - $V^* = 144.0s^{-1}$, (c) PBS - $V^* = 16.4s^{-1}$, (d) PBS - $V^* = 145.4s^{-1}$.

there is a systematic difference, with the CFD velocity being slightly lower towards the channel edges and slightly higher in the channel centre, however, the difference is negligible. The match between the experimental and computational profiles is not quite as good for the PBS cases, as was observed for the parent branch. The skewing in the profiles is slightly under predicted in both daughter and outlet branches, and the latter also shows a large difference in the channel centre, wherein the bell-shape of the profile was carried over from the parent branch.

Figure 6.6 shows a similar comparison for a high flow ratio (the same cases as Figure

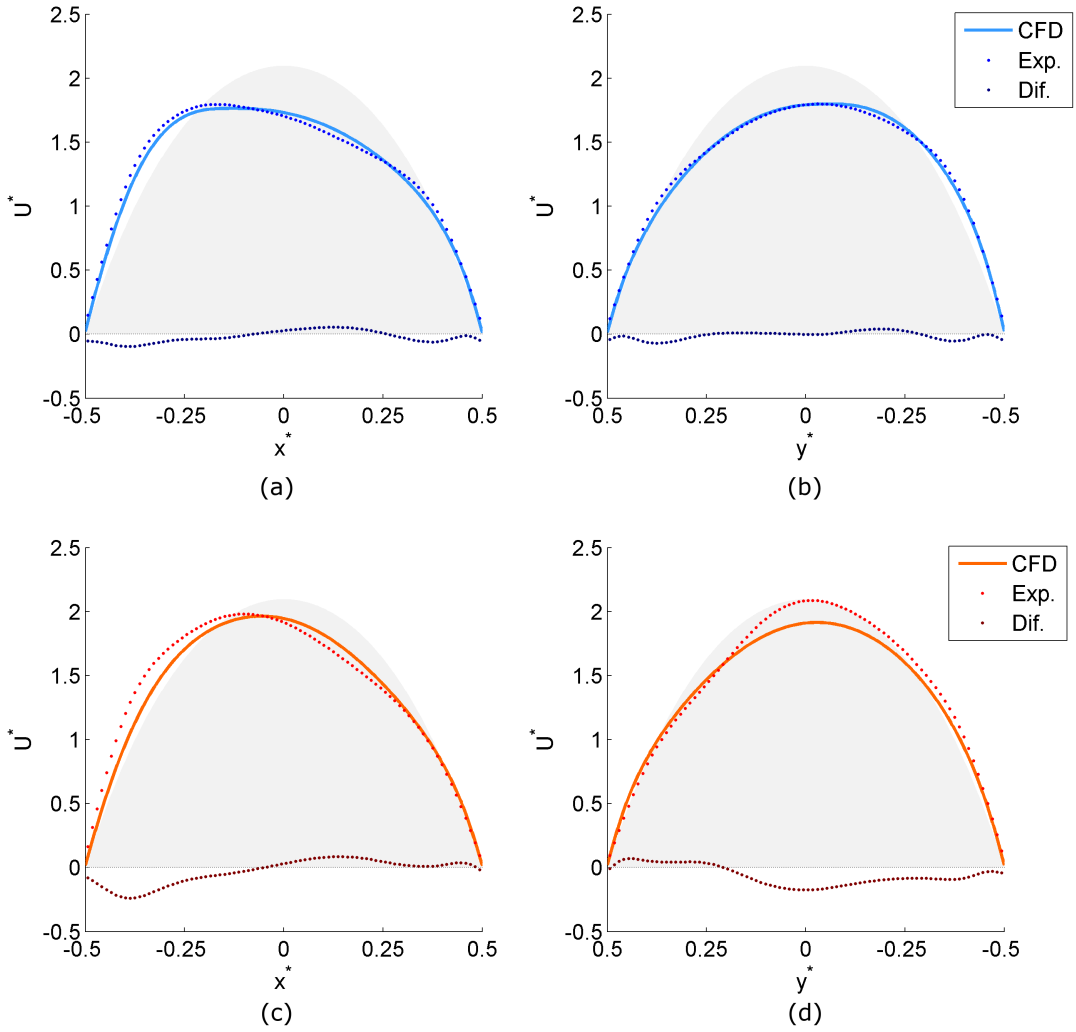

Figure 6.5: Comparison between computational (CFD) and experimental (Exp.) profiles, and the difference between the two (Dif.) in the daughter and outlet branches at low flow ratio. (a) Dextran - Daughter, $Q_d^* = 0.16$, (b) Dextran - Outlet, $Q_o^* = 0.84$, (c) PBS - Daughter, $Q_d^* = 0.13$, (d) PBS - Outlet, $Q_o^* = 0.87$.

5.15). For the Dextran case (Figures 6.6a and b), the experimental and computational velocity profiles are very similar, and the same systematic difference observed for the low flow ratio can be seen in both branches, but the differences are again very small. For the PBS case (Figure 6.6c), the daughter branch profile is better estimated at the high flow ratio than at the low flow ratio (Figure 6.5c). In the outlet branch (Figure 6.6d), similar characteristics are observed at both high and low flow ratios.

To summarise, the computational model succeeded in reproducing the experimental velocities with remarkable accuracy for the Dextran case, as well as reasonably reproducing the correct shapes in the PBS case, aside from the bell-shape characteristics,

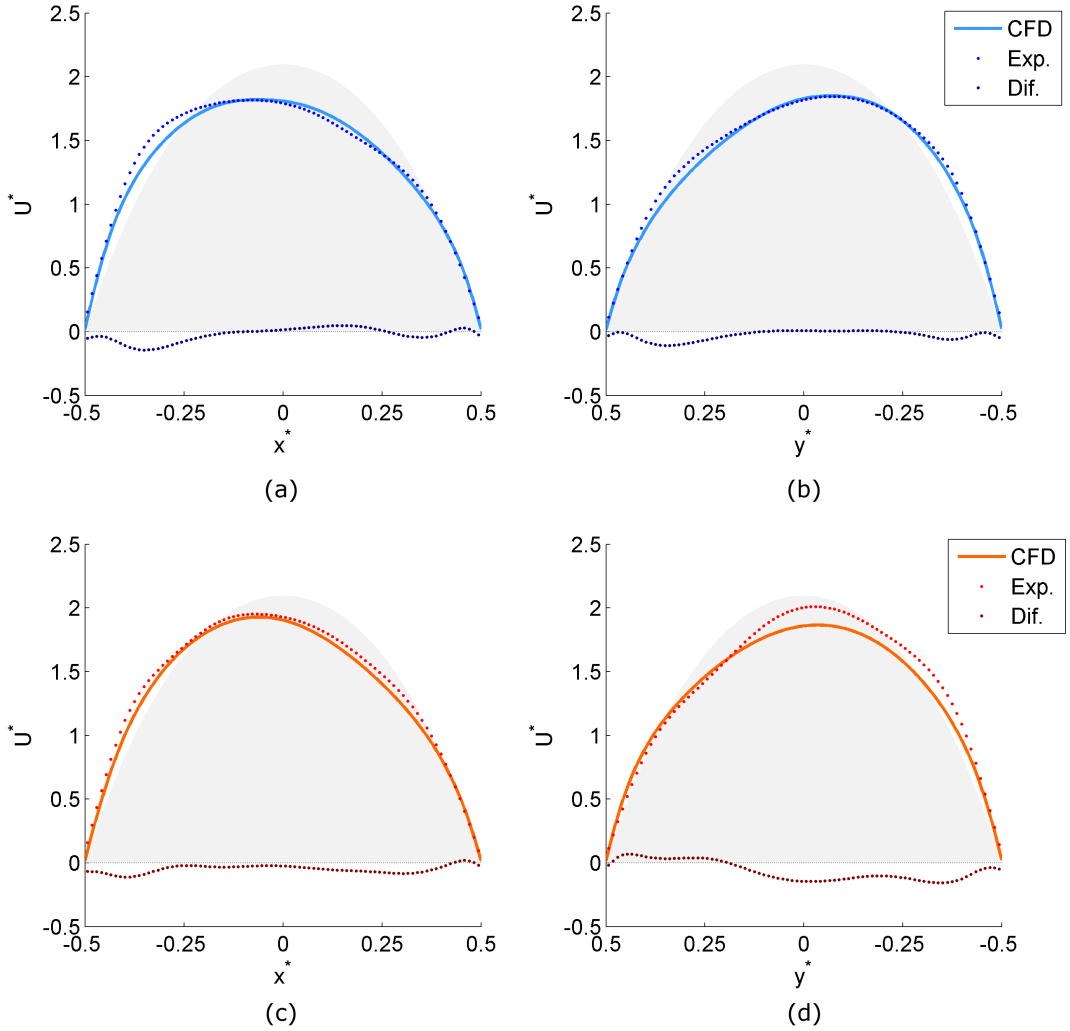

Figure 6.6: Comparison between computational (CFD) and experimental (Exp.) profiles, and the difference between the two (Dif.) in the daughter and outlet branches at high flow ratio. (a) Dextran - Daughter, $Q_d^* = 0.41$, (b) Dextran - Outlet, $Q_o^* = 0.59$, (c) PBS - Daughter, $Q_d^* = 0.43$, (d) PBS - Outlet, $Q_o^* = 0.57$.

which are beyond the purview of the present computational approach. For all cases the predicted velocities close to the wall are very similar to the experimental data, which is necessary for the analysis of wall shear and apparent viscosity.

The bluntness and skewness characteristics of the predicted velocity profiles will now be investigated. Figure 6.7 shows the predicted velocity bluntness, *VB*, plotted against the normalised velocity for the CFDH (circles) and CFDU (squares) cases in the parent branch. For the latter, *VB* changes relatively little as the flow rate increases. For the PBS case, there is a negligible change in *VB* for all shear rates, and for the Dextran case, there is a gradual decrease in *VB* as the shear rates increase. This is due to the

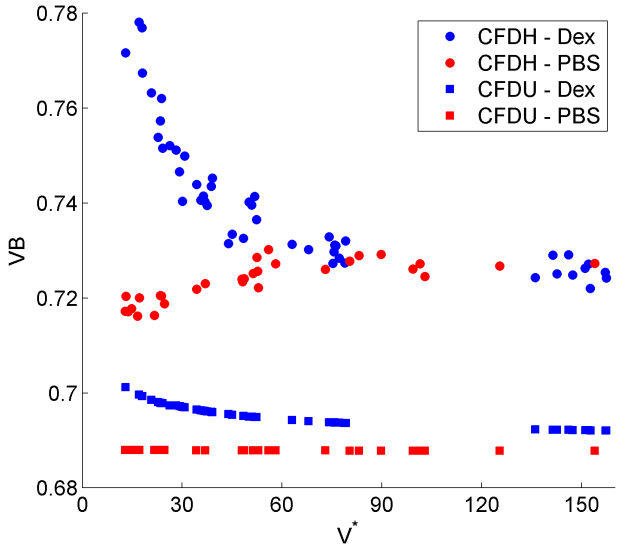

Figure 6.7: Comparison of velocity bluntness against normalised velocity in the parent branch for the haematocrit distribution and uniform haematocrit computational models.

relationship defined by Equation 6.7 (as shown in Figure 6.1). At all flow rates, *VB* for the PBS cases is higher for the CFDH data than for the CFDU data, as the haematocrit profile decreases the Quemada viscosity near the wall, blunting the velocity profile. As V^* increases, *VB* increases as the haematocrit profile bluntness decreases.

For the Dextran case, there is a significant decrease in *VB* with increasing V^*. The magnitude of the blunting is greater than for the experimental data at low V^* (due to the absence of the bell shape), but the trend follows that of the RBCs closely (see Figure 5.16) and has a similar magnitude at high V^*. For the PBS case, there is an increase in *VB* as V^* increases, as was observed for both the SM and RBCs in the experimental data. Above $V^* = 50s^{-1}$, the PBS and Dextran cases both have a relatively constant velocity bluntness with approximately the same value.

The velocity skewness, *VS* is plotted as a function of Q^* in Figure 6.8. It can be seen that, for all cases, there is a statistically significant trend. For the Dextran case, the skewness decreases rapidly as the flow ratio increases to around 0.25 and then decreases relatively little for high flow ratios. The velocity skewness for the PBS case, however, decreases only very slightly in response to the flow ratio changing, despite the haematocrit skewness (*HS*) being similar to that of the Dextran case (Figure 5.11). This implies that the skewness in the velocity profiles is influenced by the shear thinning nature of the fluid in combination with the haematocrit distribution. The difference in

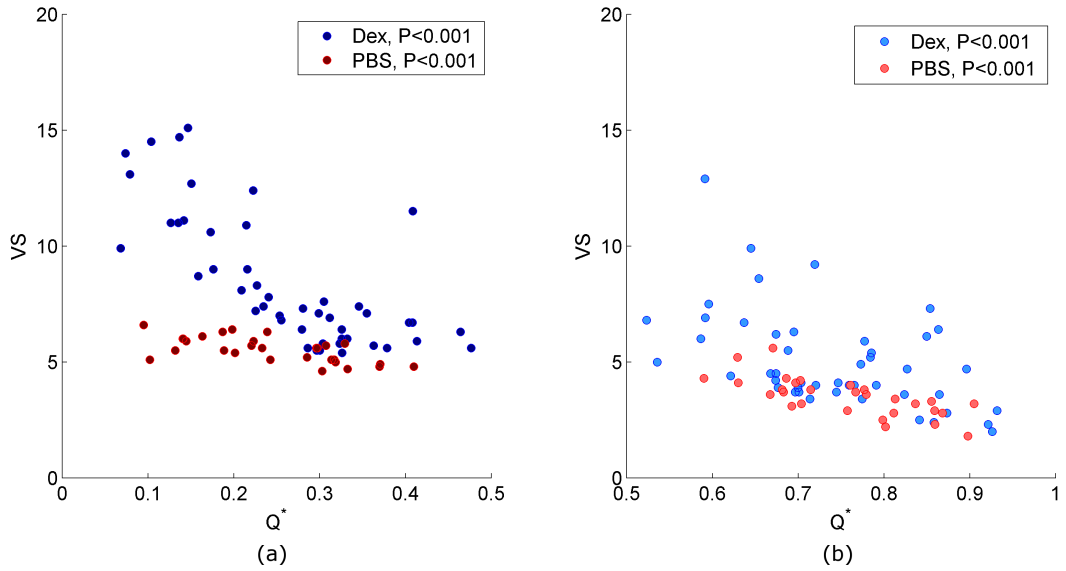

Figure 6.8: Comparison of velocity skewness against flow ratio for the haematocrit distribution computational model. (a) Daughter branch, (b) Outlet branch.

shape of the haematocrit profiles between the Dextran and PBS cases shown in Figure 5.10, which is not captured by the *HS* parameter, may also have an effect. In the outlet branch (Figure 6.8b), clear trends in decreasing skewness with increasing Q_o^* are also observed. In this branch, the Dextran data exhibit generally higher *VS* values and are more scattered.

The velocity skewness predicted by the simulations is compared directly to that of the experimental total velocity profiles in Figure 6.9. It can be seen that for the Dextran case in both branches, there is a very strong and significant trend between the experimental and simulated data. For the daughter branch, the slope is slightly less than one, meaning that the simulations marginally underestimate the skewness. In the outlet branch, the minimum skewness is slightly overpredicted but the slope is close to unity. For the PBS case, the skewness in the outlet branch is well predicted by the computational approach. However, in the daughter branch, there is not a significant relationship observed for the PBS case (although the P-value of 0.084 is just over the significance value of 0.05).

From the comparison of the predicted flow characteristics as a function of key parameters using experimental haematocrit distributions (CFDH), it is clear that the CFDH model is effective at predicting the data derived experimentally. Thus the simulated flow parameters can now be used to consider the wall shear stress and apparent viscosity.

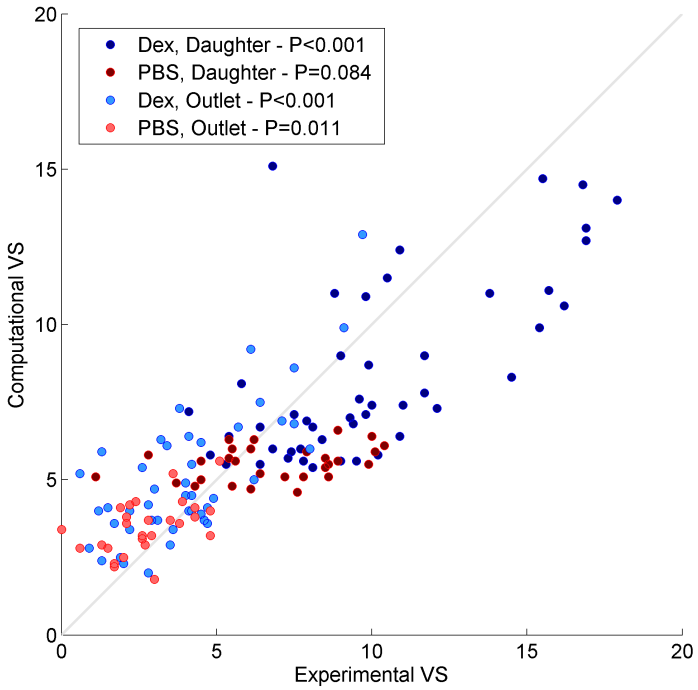

Figure 6.9: Comparison of velocity skewness from the simulations against that for total experimental velocity profiles. Grey line indicates perfect match. P values are from Pearson's correlation coefficient.

6.4.2 Wall shear stress

As mentioned previously, the wall shear stress (WSS) acting on vessel walls is a very important mechanical force, as it is a key component in the control of a large proportion of physiological processes via mechanotransduction. In the preceding chapters, the effect of WSS was analysed in response to changing flow ratio. This analysis will also be carried out with the present data, but additionally the effect of parent branch flow rate will also be considered. It is worth recalling that the shear stress is given by $\tau = \mu\gamma$, and that for the present model $\mu = f\,(H, \gamma)$.

Figure 6.10a shows how the WSS predicted by the CFDH and CFDU models (denoted by τ_h and τ_u respectively) varies as a function of normalised velocity in the parent branch. The values of τ shown in this figure are the average of those acting on all walls of the channel in the averaging region (Figure 5.1). It is clear that in all cases, the WSS increases as the flow rate increases, as would be expected. It can also be seen that for all cases, $\tau_u > \tau_h$. This is a result of the haematocrit being reduced at the wall for τ_h, which lowers the local viscosity and hence shear stress. However, it has been shown

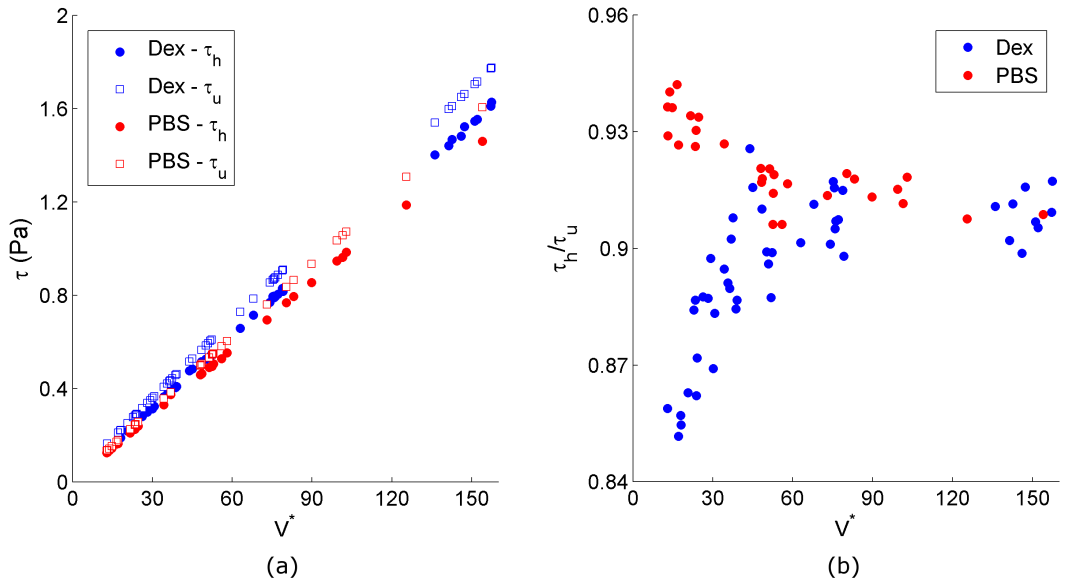

Figure 6.10: Wall shear stress against normalised velocity in the parent branch from the simulations. (a) absolute values, (b) ratio of the WSS value calculated from haematocrit distribution model (CFDH) to those from the uniform haematocrit model (CFDU).

that this additionally blunts the velocity profile, which would increase the local shear rate.

Figure 6.10b compares the ratio of τ_h/τ_u: the wall shear stress ratio (WSSR). This normalisation removes the effect of the overall flow rate. Furthermore, both models (CFDH and CFDU) have the same shear thinning characteristics, so this normalisation serves to reduce the effect of shear thinning and hence allow for better analysis of the influence of the haematocrit distribution. The figure shows a trend which is very similar to that of the haematocrit bluntness (Figure 5.9), although for $V^* > 50s^{-1}$ the WSS in the Dextran and PBS cases have approximately the same value of 90% of that predicted if the haematocrit distribution is not accounted for, whereas the haematocrit bluntness was slightly higher for the Dextran case for $V^* > 50s^{-1}$. This implies that, in long straight channel sections the reduced haematocrit at the wall in the Dextran case compared to the PBS case is counteracted equally by the relative increase in shear rate at the wall.

The WSSR in the daughter and outlet branches in presented in Figure 6.11. For this section, the inner and outer walls are considered separately. The normalisation (τ_h/τ_u) removes the effects of both absolute velocity and plasma skimming, i.e. bulk haemat-

ocrit (see Figure 5.6) from the analysis. If the CFDH data was analysed without normalisation, the wall shear stress would be greatly decreased in the daughter branch and increased in the outlet branch, as the viscosity is highly haematocrit dependent (see Figure 6.2). The WSSR thus shows the influence of haematocrit distribution on the WSS.

It should be recalled that for the daughter branch, at the inner wall the shear rate is increased (due to the skewed velocity profile) and the viscosity is decreased due to the lower local haematocrit and increasing shear rate. With these two contrary effects, it is not immediately clear how the WSS will be affected. The opposite occurs at the outer wall with decreasing shear rate and increasing haematocrit. The outlet branch shows the same response, but with the effects on the inner and outer walls inverted.

For the Dextran case in the daughter branch, at low flow ratios (Figure 6.11a) the WSS at the outer wall (squares) is approximately the same as it would be if the haematocrit were uniformly distributed across the channel (WSSR$= \tau_h/\tau_u \approx 1$). As the flow ratio increases, the WSSR decreases, despite the haematocrit at the wall becoming closer to the uniform haematocrit value (the haematocrit near the inner wall increases with increasing flow ratio: see Figure 5.10). At the inner wall (circles), the WSSR is 0.8 at low flow ratios and increases slightly as the flow ratio increases.

In the outlet branch for the Dextran case (Figure 6.11b), the WSSR is greater than unity at the inner wall, despite the lower haematocrit for the CFDH case. As the flow ratio increases, the WSSR decreases to below one. At the outer wall, there is no significant trend, but the WSSR remains below 0.9, meaning a 10% reduction in WSS due to the non-uniform haematocrit distribution.

For the PBS case the changes in WSSR as a function of flow ratio are less pronounced than for the Dextran case. At the inner wall of the daughter branch (Figure 6.11c, circles) and the outer wall of the outlet branch (Figure 6.11d, squares), both regions where the haematocrit is reduced and the shear rate (dv/dx and du/dy respectively) is increased, there is no significant change of WSSR in response to varying Q^*. At the opposite walls, the data follow the same trends as for the Dextran case.

In Figure 6.11, the average WSSR values are indicated by crosses. For all cases in both branches, the non-uniform haematocrit distribution reduces the overall wall shear stress. The effect is most significant in the daughter branch for the Dextran case (Figure

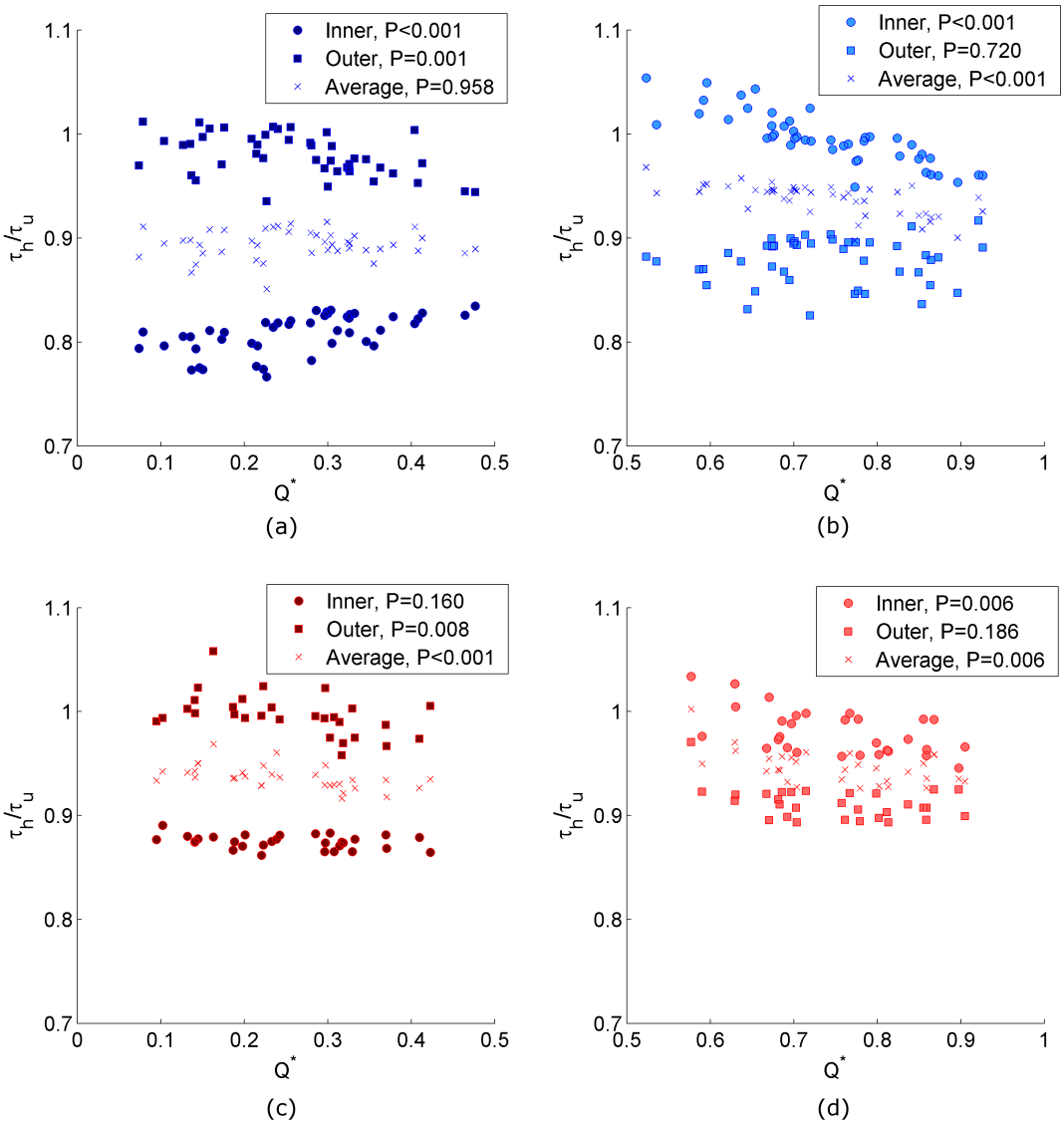

Figure 6.11: Ratio of WSS calculated from haematocrit distribution model (CFDH) to uniform haematocrit model (CFDU) against flow ratio. (a) Dextran- Daughter, (b) Dextran- Outlet, (c) PBS - Daughter, (d) PBS - Outlet.

6.11a), where a 10% reduction is observed, but the value is independent of flow ratio. In all other cases (Figures 6.11b, c and d), the average WSS is reduced by around 5% due to the non-uniform haematocrit distribution and decreases further with increasing flow ratio.

6.4.3 Apparent viscosity

Although wall shear and apparent viscosity are intrinsically linked, it is valuable to consider the two separately. While the WSS plays a key role in vascular regulation via mechanotransduction, the apparent viscosity affects the way that the blood flows

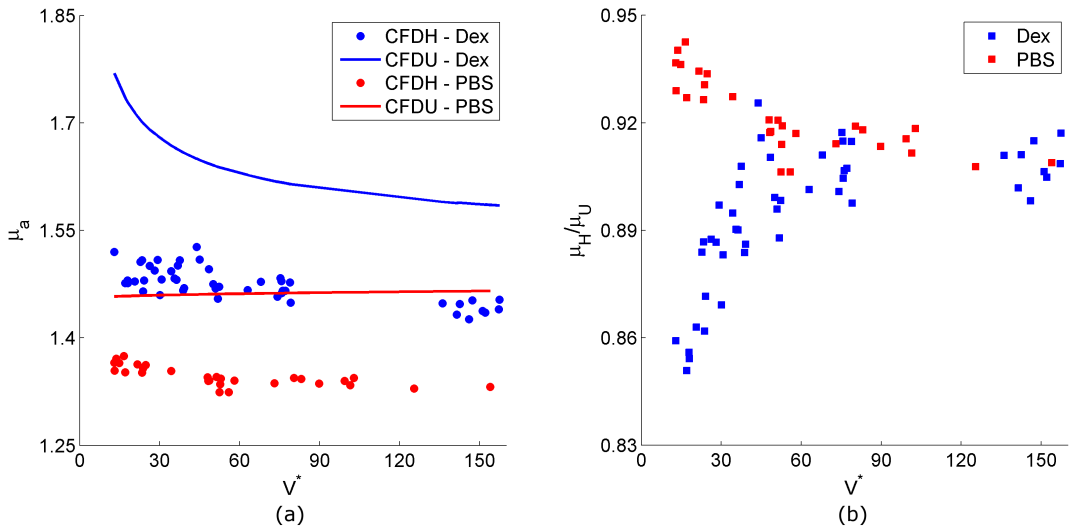

Figure 6.12: Apparent viscosity against normalised velocity in the parent branch from the simulations. (a) absolute values, (b) ratio of the apparent viscosity calculated from haematocrit distribution model (CFDH) to uniform haematocrit model (CFDU).

through a vascular network. On a local scale, an individual vessel with reduced apparent viscosity will have increased flow for a given pressure gradient. Equivalently, increased apparent viscosity will result in a greater pressure drop in order to maintain flow rates. Modelling the combined interactions between the sequential, and often parallel, vessels in a microvascular network is beyond the scope of the present study, but these results could be beneficial in the refinement of such models. Furthermore, a greater understanding of the effect of aggregation on viscosity is still required, as reports in the literature often have contradictory results (see Chapter 1).

In the parent branch, the apparent viscosity decreases with increasing flow rate, as would be expected for a shear thinning fluid. However, the trends shown in Figure 6.12a are quite different for the CFDH and CFDU cases. Considering the latter, the Dextran case has a high apparent viscosity at low flow rate which decreases rapidly as the flow rate increases. The apparent viscosity in the PBS case remains almost constant, with only a very slight increase at higher flow rates. This is due the relationship defined by Equation 6.7 (and see Figure 6.1), defined empirically using a Couette viscometer (Cokelet, 1987). For the CFDH data, which also takes into account the influence of the haematocrit distribution, the apparent viscosity is reduced in both Dextran and PBS cases, due to the reduction of haematocrit, and thus local viscosity, at the vessel walls.

For the Dextran case, the slope of the CFDH data is greatly decreased compared to the CFDU data. For the PBS case, the CFDH data shows a slight decrease in apparent viscosity with increasing flow rate, contrary to that observed for the CFDU data. This is a result of the decreasing haematocrit bluntness with increasing flow rate.

Figure 6.12b shows the ratio of the apparent viscosities for the CFDH and CFDU cases, μ_h/μ_u. This will be termed the apparent viscosity ratio, and the normalisation is carried out for the same reasons as described above for the WSSR, τ_h/τ_u. The figure shows a very similar trend to that of the WSSR (Figure 6.10), and the haematocrit bluntness *HB* vs. V^* curve (Figure 5.9). This indicates that in the parent branch, apparent viscosity is mainly dependent on the haematocrit bluntness.

In order to further analyse the relationship between *HB* and μ_h/μ_u, the two are compared directly in Figure 6.13. It can be seen that there is a very strong correlation and that the relationship is approximately the same for both the Dextran and PBS cases, although the apparent viscosity ratio is higher for the PBS cases. For the Dextran case, the potential increase in apparent viscosity at low shear rates due to increased aggregation (as predicted by the CFDU model) is partly offset by the enhanced radial migration (resulting in sharper haematocrit profiles). In the PBS case, a 'shear-thinning' relationship is observed for the CFDH data, but is due to the haematocrit distribution becoming less blunt, rather than the direct influence of shear rate on RBC deformation (as this relationship is not visible in the CFDU data).

The observed trends in apparent viscosity against normalised velocity can be compared with the results of Reinke et al. (1987). Although they found greater apparent viscosities in general as a result of their much higher haematocrit (0.45), they also observed that the non-aggregating viscosity was much greater than that of aggregating cases. The present data showed that the Dextran case viscosity was higher than for the PBS case, but the specific magnitudes are defined by the Quemada model, and so this discrepancy is not of concern. Reinke et al. (1987) found a similar trend for non-aggregating cases (serum or saline as a suspending medium) to that observed for the PBS case in the present data, but found increasing apparent viscosity for aggregating cases with Dextran solution as a suspending medium. However, their study only investigated normalised velocities up to approximately $25s^{-1}$, and so the overlap between the two studies is not large, which precludes further comparison. Cokelet & Goldsmith (1991) observed

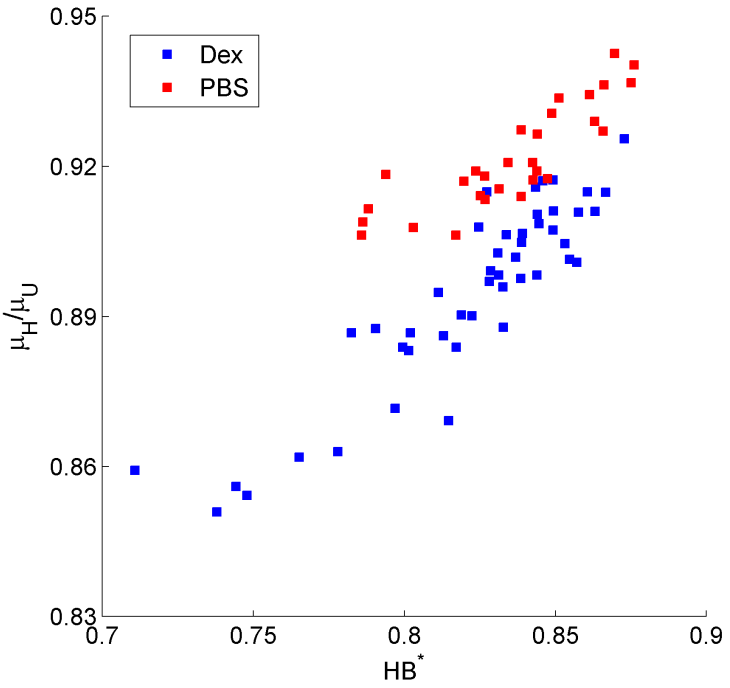

Figure 6.13: Apparent viscosity ratio against haematocrit bluntness in the parent branch.

decreasing flow resistance for normalised velocities above $5s^{-1}$ in a vertical tube with flow going up or down. Fedosov et al. (2011) modelled blood flow in a tube using the dissipative particle dynamics approach, and observed similar trends to those reported here: as the shear rate increased, the apparent viscosity decreased. In the presence of RBC aggregation, the low shear viscosity was greater, and the viscosity decreased more rapidly as the shear rate decreased due to the break up of RBC aggregates.

In the daughter and outlet branches, both the flow rate and the flow ratio are expected to influence the apparent viscosity. The effect of flow ratio on the apparent viscosity is shown in Figures 6.14a and b. In the daughter branch, there is a very strong correlation between Q^* and μ_a. However, in the outlet branch, there is no significant relationship for the Dextran case, and a slight, but significant, reduction in apparent viscosity as the flow ratio increases for the PBS case. These trends however, are likely to be dominated by the phenomenon of plasma skimming, which reduces the overall viscosity by reducing bulk haematocrit in the daughter branch and vice versa in the outlet branch. In order to consider the effect of the non-uniform haematocrit distribution, Figures 6.14c and d compare the apparent viscosity ratio μ_h/μ_u to the flow ratio. In the daughter branch (Figure 6.14c), for both cases, the apparent viscosity decreases as the flow ra-

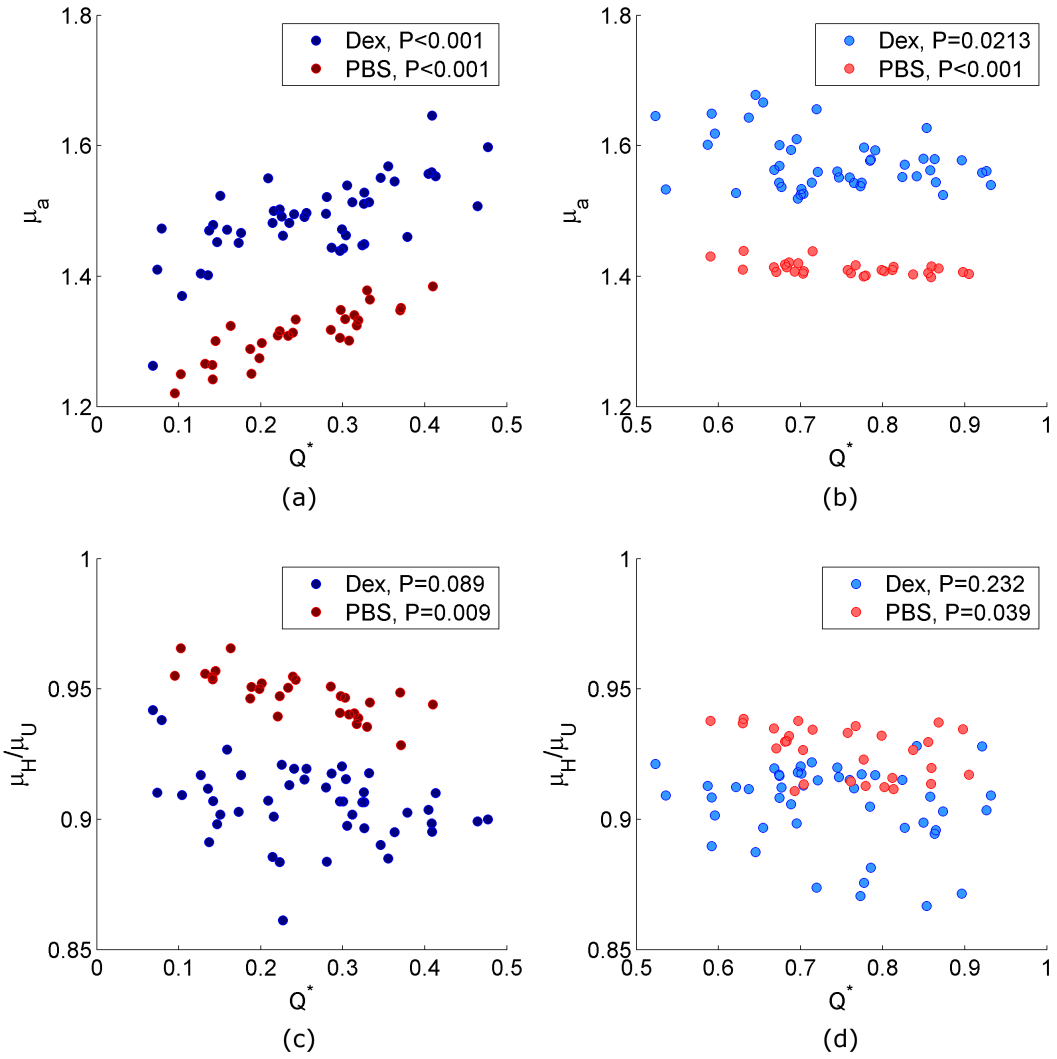

Figure 6.14: Apparent viscosity against flow ratio in the (a) daughter and (b) outlet branches. Apparent viscosity ratio against flow ratio in the (c) daughter and (d) outlet branches.

tio increases. This relationship is significant for the PBS case, and just beyond the commonly used significance level of $P = 0.05$ for the Dextran case.

In the outlet branch (Figure 6.14d), the PBS case apparent viscosity ratio reduces slightly with increasing flow ratio, but there is no significant trend for the Dextran case. In order to investigate the cause for these trends, the viscosity is plotted against haematocrit skewness in Figure 6.15.

In the daughter branch (Figure 6.15a), both cases show a strong trend of decreasing apparent viscosity as *HS* increases towards 0.5. This indicates that overall, the skewing of the haematocrit profiles results in an increase in the apparent viscosity (as $HS = 0.5$ indicates equal proportion of flow on each side of the centreline). In the outlet

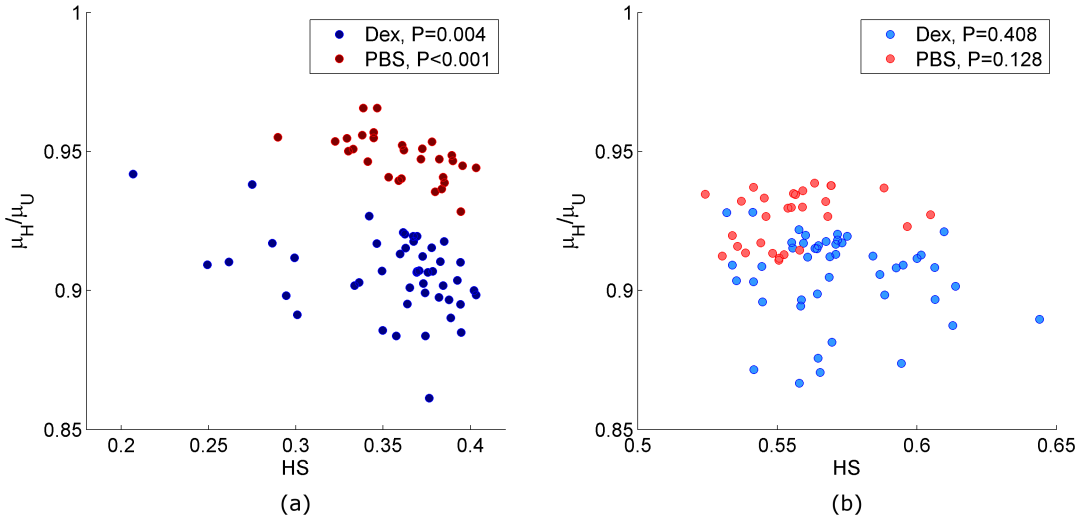

Figure 6.15: Apparent viscosity ratio against haematocrit skewness in the (a) daughter and (b) outlet branches.

branch (Figure 6.15b), neither the PBS nor Dextran cases show any dependence on the haematocrit skewness.

The effect of flow rate on the apparent viscosity ratio in the daughter and outlet branches is shown in Figure 6.16. In the daughter branch, no significant correlation is observed for the Dextran case, with $P = 0.109$. For the PBS case, there is a decrease in apparent viscosity with increasing flow rate ($P = 0.039$). It is interesting to note however, that for the apparent viscosity, μ_a (not shown here for brevity), there is no significant trend with flow rate for Dextran or PBS cases ($P = 0.656$ and $P = 0.811$ respectively).

This implies that, although the flow rate effect on the haematocrit profile in the daughter branch is to reduce the apparent viscosity compared to a uniform haematocrit distribution (for the PBS case), this effect is not significant compared to the effect of flow ratio modifying the haematocrit skewness.

In the outlet branch (Figure 6.16b), the trends are very similar to those observed in Figure 6.12b for the parent branch. This confirms that the flow in the outlet branch is strongly defined by the parent branch flow characteristics, as opposed the that in the daughter branch which is more dependent on flow ratio.

Comparing the apparent viscosity ratio in the daughter and outlet branches (Figure 6.16) to that in the parent branch (Figure 6.12) it can be seen that the values are similar, with the exception of the PBS case in the parent branch wherein the apparent viscosity

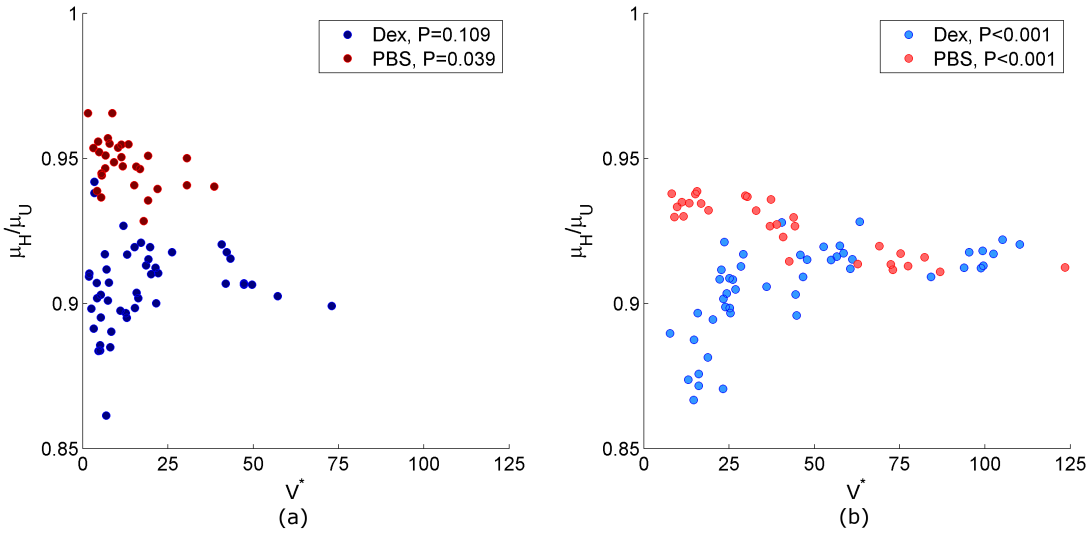

Figure 6.16: Apparent viscosity ratio against normalised velocity in the (a) daughter and (b) outlet branches.

ratio is greater. However, for all cases, the apparent viscosity ratio is less than one, meaning that the viscosity is decreased by the presence of the non-uniform haematocrit distribution. Considering the analysis of apparent viscosity in Chapter 3 (3.22), it can be seen that, despite the simplicity of the model, the predicted reduction in apparent viscosity due to the one-sided CDL is similar in magnitude to the present data.

The question of whether RBC aggregation increases or decreases apparent viscosity is one which many researchers have investigated and which still requires clarification (Meiselman, 2009; Meiselman & Baskurt, 2006). However, no consensus has been reached, with some studies indicating an increase (Bishop et al., 2001a; Cabel et al., 1997; Soutani et al., 1995), others finding no change (Gustafsson et al., 1981), and a number of studies showing a decrease of apparent viscosity due to RBC aggregation (Baskurt et al., 1999; Charansonney et al., 1993). Although the Quemada model defined the viscosity to be higher for the aggregating cases than for the non-aggregating cases, the apparent viscosity ratio was lower for the Dextran case than the PBS case. In the parent branch, this could be expected, as after a long straight segment, aggregation and radial migration have a sufficiently long time to have an effect. The data showed that in the outlet branch, characteristics from the parent branch tend to persist, and hence the same analysis could be made. However, in the daughter branch, RBC aggregation decreased the apparent viscosity ratio. In the next section, the advantages

and limitations of the present approach will be discussed.

6.4.4 Critical evaluation of the computational approach

In this chapter, a hybrid experimental-computational approach was proposed, in order to provide a computationally efficient methodology to blood flow modelling and to estimate the WSS and apparent viscosity for the data acquired in Chapter 5. The effects of both the flow ratio and parent branch flow rate were investigated, and hence it was necessary to use a constitutive model which included both shear rate and haematocrit dependent properties. The Quemada model was chosen for this reason, although the shear rate dependence was modified to better fit the experimental data. This could be explained by the fact that in defining the empirical values for k_0, k_∞ and γ_c, a Couette viscometer was utilised (Dufaux et al., 1980; Cokelet, 1987). The shear environment in such a system is uniform, and thus quite different to the localised elevated shear rates observed in a round or square conduit. Given that the data are empirical, it thus seems entirely reasonable to modify existing parameters as was done for the present simulations. The Quemada model has previously been utilised by Das et al. (1998) to estimate the effect of haematocrit distribution on velocities. However, they used artificial haematocrit distributions, and so it was not possible to tell whether their data would match experimental measurements. Furthermore, the present approach simulated the whole bifurcation region, rather than just a straight channel section.

Although the Quemada model has been utilised previously using generated haematocrit distributions, the methodology used here is relatively novel, in that it takes into account experimental measurements of the haematocrit distribution and flow at the boundaries. However, the approach is limited as it still does not fully account for the multiphase nature of the blood; the RBCs are not explicitly considered, only implicitly as a continuous haematocrit distribution. As a result, the 'bell-shape' character of some of the measured velocity profiles was not predicted by the model. Such a shape would theoretically be reproducible only if there was an inverse viscosity profile. This would occur only if the haematocrit was lower in the channel centre and higher at each wall. A possible solution to this is addition of an additional viscosity term, relating to the influence of near-wall cells. The proposed additional viscosity term would need to be dependent on the location in the channel (in order to account for the level of influence)

as well as the shear rate, haematocrit and the presence or otherwise of an aggregating agent in the suspending medium.

Although simple continuum models generally do not accurately capture velocity profiles of blood, the use of directly measured haematocrit profiles resulted in greatly increased accuracy for the simulations. For future applications, the approach could be made more general by developing a method to predict general haematocrit distributions based on streamlines and RBC dispersibility, which could potentially allow for network scale simulations with improved accuracy but low computational expense. Mansour et al. (2010) attempted this, but their results do not bear much resemblance to the present data. Hence it is proposed that an empirical approach would be better suited for the definition of such a relationship. If this was achieved, the approach could be used to improve *in silico* models of cardiovascular networks, which still struggle to accurately capture characteristics on the scale of individual vessels (Cokelet, 1999).

Despite the discussed limitations, the predicted velocities near to the wall were well replicated in most cases, which provides support for the model's use in the analysis of WSS and apparent viscosity. Moreover, the computational time was minimal (an average of 12.5 minutes for each bifurcation simulation on a desktop machine: Intel i7, 16GB RAM).

6.5 Closure

In this chapter, the experimental data described in Chapter 5 were utilised in a hybrid approach to continuum modelling of microvascular blood flow. The estimated haematocrit distribution was combined with the Quemada viscosity model with empirically defined parameters and experimentally defined boundary conditions. The model showed great promise as an efficient method for simulating blood flow on the microscale. The simulations also allowed for estimation of wall shear stress and apparent viscosity, and revealed the importance of the geometry as well as the presence or absence of aggregation on these parameters. Further development of the model could involve direct prediction of the haematocrit distribution for a given flow ratio and geometry. With such data, accurate modelling of microvascular networks could be achieved.

In the final section of this thesis, conclusions will be drawn based on all four results chapters and recommendations for future work will be provided.

Chapter 7

Conclusions and future work

7.1 Introduction

The main aim of the present study was to improve understanding of microscale blood flow using advanced measurement techniques *in vitro*. The phenomenon of RBC aggregation was given particular attention and all studies were carried out at physiologically relevant haematocrits for the length scales considered. The presence of RBC aggregation made the experimental requirements complex and so a custom pressure controlled perfusion system was developed. In order to acquire high resolution data, μPIV was combined with new image processing methodologies. Microvascular bifurcations were represented by idealised microchannels in which the parameter space could be accurately controlled. The acquired data was processed in order to extract data on velocity distributions, cell-depleted layer characteristics and RBC distributions. The data was further analysed in order to deduce further information on key flow parameters such as WSS and apparent viscosity. A novel modelling approach to microhaemodynamics was also proposed.

7.2 Main Contributions

The following is a list of the main contributions of the present study:

- The present study has provided high resolution Eulerian blood flow field descriptions in microscale bifurcating geometries for physiologically relevant haematocrit using μPIV, where previous studies have predominantly provided only bulk characteristics. Furthermore, details of the cell-depleted layer have been provided with high spatial and temporal resolution.

- The first experimental description of blood as a multiphase fluid has been provided. This was achieved using a custom built system to quasi-simultaneously acquire data on the velocity and concentration of both the RBCs and suspending medium.

- Novel hybrid numerical simulations have been carried out using experimental data on local RBC distribution and empirical models to predict viscosity distribution. Results yielded quantitative data on the relationship between viscosity and velocity.

- The role of RBC aggregation in idealised geometries has been elucidated in detail. By comparing all results for aggregating and non-aggregating cases, details of the effect of aggregation on flow characteristics and vice versa have been described.

7.3 Summary of main findings

In this section, a summary of the main findings of the present work will be given.
In order to study microscale blood flow *in vitro*, capillary tubes have been widely used. However, this precludes analysis of branching geometries such as those observed in the microvasculature. The relatively new field of microfluidics has provided a new platform in which to study microscale biological phenomena. However, the control of flow in microfluidic systems is still predominantly carried out with the use of syringe pumps, despite the poor accuracy and temporal response of such systems. Pressure control systems provide much better stability and response times. In microfluidic systems, the microchannel itself is generally the region with the smallest geometric regions; hence the fluid shear stress is greatest in the microchannel. When analysing RBC aggregation, a shear-dependent phenomenon, aggregation in the system outside the microchannel limits the acquisition time for individual experiments, with high flow rates imposed between data sets. The pressure system was thus required to have a very rapid and accurate time response. In the present study, an experimental setup and protocol for microfluidic experiments using aggregating blood samples was developed and described in detail. This information may be very useful for future studies as it provides a reliable methodology to acquire repeatable data in a complex mechanical

environment.

The cell-depleted layer (CDL) is a region near the channel or vessel wall that has a very low concentration of RBCs. The layer is formed as a result of the interaction between the RBCs and the fluid around them, which generates a force towards the channel centre. However, cell-cell interactions oppose this motion, resulting in a rough layer which changes in space and time. A new methodology for measuring the CDL was developed based on motion detection instead of image intensity analysis, as has been previously reported. This allowed the CDL distribution throughout the whole bifurcation region to be acquired simultaneously, whereas previous methods considered only individual analysis lines. This technique was used to provide highly detailed information on the CDL distribution in a bifurcating microchannel with the 'straight-T' configuration. It was observed that the CDL distribution was highly dependent on flow ratio, and the width increased proportionally to the inverse of the fraction of flow entering the daughter branch. However, the width was reduced as a result of cell-cell interactions. RBC aggregation reduced the cell-cell interactions and hence the CDL was larger in the presence of aggregation and persisted further downstream.

Velocity profiles in the daughter branch were observed to be significantly skewed, contrary to what would be expected for Newtonian and non-Newtonian fluids (as verified by CFD simulations) and the expected response of blood. The skewness of the velocity profile was found to increase with decreasing flow ratio and in the presence of RBC aggregation. It was posited that this may be due to the CDL, which followed the same trends. In order to investigate this hypothesis, a simple analytical model was derived, in which a CDL was considered on one side of the channel only. Using experimental data on the CDL width and an empirical model to estimate viscosity, the model was able to predict the observed trends in skewness of the velocity profiles, although the amount of skewing was under-predicted. Furthermore, the model suggested that the apparent viscosity would be decreased as a result of the CDL, particularly at low flow ratios (without assuming plasma skimming). RBC aggregation enhanced the effect by altering the CDL distribution, reducing the viscosity further. Wall shear stress was observed to decrease on the wall adjacent to the CDL, but increase by the same magnitude

on the opposite wall and scaled directly with the velocity skewness.

In order to better analyse these trends, the same microchannel was used to acquire quasi-simultaneous fluorescent μPIV images and brightfield images using strobe illumination. The green microstrobe provided high-contrast images which allowed for the development of a new technique to quantify the haematocrit distribution from acquired images. The technique was capable of identifying plasma skimming and it was observed that the phenomenon was enhanced by RBC aggregation. With the same empirical viscosity model that was used for the analytical model, the haematocrit distributions were converted into viscosity distributions and 'maps' were generated for the viscosity profile as a function of flow ratio for both aggregating and non-aggregating samples. As the viscosity was considered to be a function of the channel width, a numerical approach was used to infer the influence of the haematocrit profiles on the velocity profiles, and to investigate wall shear tress and apparent viscosity. Each branch of the bifurcation was considered separately and the viscosity profile along the channel was utilised in a commercial CFD package. Analysis of the results showed that the skewness of the predicted profiles matched very well the experimental skewness data. However, the bluntness of the profiles was over-predicted. The wall shear stress was again observed to decrease for low flow ratios and with RBC aggregation, but the average value also changed, with a net reduction for low flow ratios. The apparent viscosity in the high flow branch was almost constant, but reduced significantly in the low flow branch.

The technique for analysing the haematocrit distribution as one dimensional profiles was then adapted to provide three-dimensional distributions. This was done by utilising microchannels with unity aspect ratio and through assuming planar flow (i.e. gravitational forces were negligible in the time frames considered). Additionally, a calibration was carried out showing an exponential relationship between haematocrit and image intensity. The image acquisition method was improved such that it was possible to acquire quasi-simultaneous PIV images of both the RBC (using microstrobe illumination) and the suspending medium (using laser illumination of suspended microparticles). In combination with the haematocrit distribution, it was then possible

to discriminate between the two-phases of the blood under a range of flow conditions in a bifurcation. An interesting 'bell-shape' was observed in the velocity profiles of the RBCs, particularly in the absence of aggregation. This was attributed to RBCs rolling along the wall and their influence on adjacent cells. Aggregation was observed to reduce the RBC concentration near the wall and the effect was thus lessened.

Analysis was carried out on the relative velocity between the two phases of the blood, and a number of interesting relationships were observed. In general, the suspending medium displayed more blunt velocity profiles than the RBCs, and the bluntness of the velocity profiles decreased as the haematocrit profile bluntness increased in the absence of aggregation. For the Dextran case, at high flow rates the same was observed, but at low flow rates, the suspending medium velocity bluntness was decreased to the level of the RBCs. At very low flow rates, the relative velocity between the two phases was almost zero, but as the flow rate increased and the RBCs became increasingly disaggregated, the relative velocities of the two phases diverged. For velocities above 50 channel widths per second, the relative velocity plateaued, with the mean suspending medium velocity around 10% lower than that of the RBCs, in agreement with the Fåhraeus-Lindqvist effect. This provided insight into how RBC aggregation affects the flow of not only RBCs, but also the suspending medium. In viscous-dominated flow, geometry is often not considered to be important, however, the geometry was also shown to be of importance, as characteristics were convected from the parent branch to the outlet branch, but much less to the daughter branches. Plasma skimming was observed in the present data to be not only a function of flow ratio, but also the parent branch flow rate, as a result of the haematocrit distribution and was enhanced by RBC aggregation.

Using the three-dimensional haematocrit distributions, the Quemada viscosity model was utilised in conjunction with CFD simulations of the experimental data acquired for the phase-discrimination analysis. The Quemada model uses empirically defined haematocrit dependent parameters and displays shear dependence. This model was applied with experimentally derived boundary conditions in a model of the microchannel. For validation of the model, simulated velocity profiles were compared to experimental

total velocity profiles (combined, RBC and SM velocities weighted with their concentrations). Very good agreement was observed between the simulations and experiments, particularly for the aggregating case. Equivalent simulations with uniform haematocrit distributions were carried out for purposes of normalisation and comparison and highlighted the importance of considering the distribution of RBCs in such simulations. By normalising with the uniform haematocrit simulations, it was possible to infer information on wall shear stress and apparent viscosity that was only dependent on the haematocrit distribution. A feed haematocrit of 0.2 was used, which after RBC screening and the Fåhraeus effect yielded a channel haematocrit of approximately 0.14. At this level of haematocrit, shear-thinning characteristics of blood (as measured in viscometers) are reported to be negligible. However, it was observed that, particularly in the presence of aggregation, radial migration in the parent branch reduced the near wall viscosity. As a result, both the wall shear stress and apparent viscosity were observed to scale very closely with the bluntness of the haematocrit profile in the parent branch: both parameters were reduced by around 10% at high flow rates due to the non-uniform RBC distribution. At low flow rates, aggregation further reduced these parameters whilst in the absence of aggregation they were increased with increasing flow rate, due to the blunter RBC distribution. In the daughter branch, the apparent viscosity was observed to decrease with decreasing flow ratio as a result of plasma skimming, but the effect of the increased non-uniformity of the RBC distribution was to relatively increase the flow resistance.

7.4 Significance of the data

A large number of medical conditions are greatly effected by, or significantly alter, microvascular blood flow characteristics such as RBC aggregation and viscosity. Furthermore, large numbers of biomedical microdevices for rapid healthcare analysis are being developed. Better understanding of the flow characteristics of blood is essential, not only in understanding medical conditions, but also in developing more efficient ways to treat and monitor them. The present study has provided a number of new approaches for use in such studies, as well as a large amount of new data on microhaemodynamic phenomena.

The use of idealised geometries and accurate control and acquisition systems has al-

lowed for parametric analysis of selected key parameters with a degree of accuracy which was hitherto not possible. The effect of RBC aggregation on the velocity and distribution of the RBCs and the velocity of the suspending medium have been investigated and quantitative data has been provided. Microvascular blood flow is highly complicated, and further understanding is required. Computational models of blood flow in microvascular networks are generally ineffective on a vessel to vessel scale. The very complex relationships between haematocrit and velocity considered in the present study, which are not usually accounted for, indicate a possible cause for this deficiency. The hybrid computational method proposed in the present study could potentially be developed to predict haematocrit distributions based on fluid streamlines and could provide a more accurate, but computationally inexpensive, advancement on present approaches. There are an increasing number of computational methods in which each RBC is modelled individually, but these methods require further validation. The present data, particularly using the phase discrimination approach, is ideal for this application. Although the *in vitro* environment used in the present study lacks the realism of the *in vivo* environment, the results highlight the importance of further considering the two-phases of the blood separately and the influence of RBC aggregation, and developing new tools for that purpose. Achieving sufficiently uniform illumination to apply the haematocrit distribution technique *in vivo* would be very difficult, but would provide very important data if it was achieved. The CDL technique, however, could be easily applied to *in vivo* data, and could provide more information than present approaches which are carried out only on analysis line, rather than the whole domain. Finally, the approach used for measurement of both velocity phases could be applied *in vivo*.

7.5 Future work

Direct continuation of the present work should focus on the application of the phase discrimination approach to cover the parameter space in greater detail. Firstly, as the present work has highlighted the importance of geometry, a range of Y- and T- bifurcations should be analysed, as well as converging geometries and sequential bifurcations. The diameter of the channels, and the angle between them should be modified to provide more information which could potentially be compiled and used in computational studies. Fluid parameters, such as haematocrit, suspending medium (using

plasma or other Dextrans), a wider range of flow rates and altered RBC deformability could be analysed in greater depth with the newly developed technique. The effects of pulsatile flow on RBC aggregation have not been analysed in depth, and could be considered using the custom system developed in the present work. Additionally, seeding of endothelial cells within the microchannel would complicate imaging approaches, but would bring the research closer to the *in vivo* environment, thus improving the scope of the acquired data.

The present data, in combination with additional data sets could be used to verify computational approaches, which would in turn be able to help confirm or deny the posited mechanical relationships which led to the results observed in this study and ultimately lead to greater understanding of the parameters effecting microvascular blood flow.

Appendix

A model for blood flow with an asymmetric CDL

In this appendix, the derivation of the mathematical model utilised in Chapter 3 is provided in full.

Navier-Stokes equations

Assuming steady, laminar, parallel flow of a Newtonian fluid with negligible gravity effects, the Navier-Stokes equations reduce to

$$\frac{d^2u}{dy^2} = \frac{1}{\mu}\frac{dp}{dx} \tag{1}$$

Which, assuming a constant pressure drop, $\frac{dp}{dx} = \frac{-\Delta p}{L}$ becomes

$$\frac{d^2u}{dy^2} = \frac{-1}{\mu}\frac{\Delta p}{L} \tag{2}$$

Integrating this equation twice yields

$$\frac{du}{dy} = \frac{-1}{\mu}\frac{\Delta p}{L}y + c_a \tag{3}$$

$$u = \frac{-1}{2\mu}\frac{\Delta p}{L}y^2 + c_a y + c_b \tag{4}$$

For which the constant must be found for each of the two fluids. Firstly, as is common practice in such analyses, this equation can be normalised using a standard non-dimensionalisation approach.

Non-dimensionalisation

A suitable value needs to be chosen for normalising the velocity. If one assumes that the haematocrit is zero, hence $\delta = w$, then we have a single fluid (plasma) for which the boundary conditions are

$$y = 0, u = 0 \tag{5}$$

$$y = w, u = 0 \tag{6}$$

Hence, $c_b = 0$ and

$$c_a = \frac{1}{2\mu_0}\frac{\Delta p}{L}w \tag{7}$$

Therefore,

$$u_0 = \frac{1}{2\mu_0}\frac{\Delta p}{L}y\left(w - y\right) \tag{8}$$

Noting that the viscosity is μ_0. The mean velocity is found by integrating across the channel width

$$\overline{u}_0 = \frac{1}{2\mu_0}\frac{1}{w}\frac{\Delta p}{L}\int_0^w \left(yw - y^2\right) dy \tag{9}$$

$$\overline{u}_0 = \frac{w^2}{12\mu_0}\frac{\Delta p}{L} \tag{10}$$

This can then be used to normalise the velocity according to

$$u = u^*\overline{u}_0 \tag{11}$$

Hence, u^* gives the ratio of the velocity to the average for a continuous plasma flow. Non-dimensionalising δ and y with respect to the channel width w,

$$y = y^*w \tag{12}$$

$$\delta = \delta^*w \tag{13}$$

and substituting into equation 4 yields

$$u^*\overline{u}_0 = \frac{-w^2}{2\mu}\frac{\Delta p}{L}y^{*2} + c_a w y^* + c_b \tag{14}$$

Noting that

$$\frac{-w^2}{2\mu_0}\frac{\Delta p}{L} = -6\overline{u}_0 \tag{15}$$

and so

$$u^*\overline{u}_0 = -6\overline{u}_0\frac{\mu_0}{\mu}y^{*2} + c_a w y^* + c_b \tag{16}$$

Dividing through by $\overline{u}$ and redefining the constants ($c_c = c_a w/\overline{u}_0$, $c_d = c_b/\overline{u}_0$) yields

$$u^* = -6\frac{\mu_0}{\mu}y^{*2} + c_c y^* + c_d \tag{17}$$

This equation will be solved assuming a CDL on one side of the channel, as observed in the daughter branches of the bifurcation in the experiments repoted above. The velocity of the fluid in the CDL will be termed u_δ and the velocity in the core will be u_c. The boundary conditions governing this system are:

The no-slip condition at each wall

$$y^* = 0, {u_\delta}^* = 0 \tag{18}$$

$$y^* = 1, {u_c}^* = 0 \tag{19}$$

At the interface, both fluids must have the same velocity

$$y^* = \delta^*, {u_\delta}^* = {u_c}^* \tag{20}$$

At the interface, the shear stresses on each fluid must be equal,

$$y = \delta^*, \tau_\delta = \tau_c \tag{21}$$

Hence,

$$y = \delta^*, \mu_\delta\frac{du_\delta}{dy} = \mu_c\frac{du_c}{dy} \tag{22}$$

Recalling that $\mu_\delta = \mu_0$ and $\mu_c = \mu_r\mu_0$, equation 22 becomes (considering non-dimensionalisation)

$$y = \delta^*, \frac{d{u_\delta}^*}{dy^*} = \mu_r\frac{d{u_c}^*}{dy^*} \tag{23}$$

Starting with the BC described by equation 18, it can be seen that equation 17 yields $c_d = 0$ for the first fluid. The equations governing the system are thus

$$u_\delta{}^* = -6y^{*2} + c_1 y^* \tag{24}$$

$$u_c{}^* = \frac{-6}{\mu_r} y^{*2} + c_2 y^* + c_3 \tag{25}$$

The boundary conditions can now be used to solve for the constants c_1, c_2 and c_3.

Solving for constants

The no-slip condition on the right hand wall ($y^* = 1, u_c{}^* = 0$) yields

$$\frac{-6}{\mu_r} + c_2 + c_3 = 0 \tag{26}$$

The equal velocity BC ($y^* = \delta^*, u_\delta{}^* = u_c{}^*$) yields

$$-6\delta^{*2} + c_1\delta^* = \frac{-6}{\mu_r}\delta^{*2} + c_2\delta^* + c_3 \tag{27}$$

Now,

$$\frac{du_\delta{}^*}{dy^*} = -12y^* + c_1 \tag{28}$$

and

$$\frac{du_c{}^*}{dy^*} = \frac{-12}{\mu_r} y^* + c_2 \tag{29}$$

Hence, equation 23 gives

$$c_1 = \mu_r c_2 \tag{30}$$

Equations 26, 27 and 30 are three equations in the unknowns c_1, c_2 and c_3. Rearranging equation 27 and substituting c_1 from equation 30 gives

$$-6\delta^{*2}\left(\frac{\mu_r - 1}{\mu_r}\right) + c_2\delta^*\left(\mu_r - 1\right) - c_3 = 0 \tag{31}$$

Adding equation 26 and rearranging yields

$$c_2 = \frac{6}{\mu_r} M \tag{32}$$

Where

$$M = \frac{\delta^{*2}(\mu_r - 1) + 1}{\delta^{*}(\mu_r - 1) + 1} \tag{33}$$

Hence,

$$c_1 = 6M \tag{34}$$

and

$$c_3 = \frac{6}{\mu_r}(1 - M) \tag{35}$$

So finally, the equations for the normalised velocity in each fluid are

$${u_\delta}^* = 6\left(My^* - {y^*}^2\right) \tag{36}$$

$${u_c}^* = \frac{6}{\mu_r}\left(My^* - {y^*}^2 + 1 - M\right) \tag{37}$$

with the non-dimensional parameter, M defined as in equation 33.

Skewness

In order to consider the skewness of the velocity profiles from the derived equations, one can differentiate equations 36 and 37 to give

$$\frac{du_\delta^*}{dy^*} = 6(M - 2y^*) \tag{38}$$

$$\frac{du_c^*}{dy^*} = \frac{6}{\mu_r}(M - 2y^*) \tag{39}$$

the maximum velocity occurs when either equation (and therefore clearly both equations) are equal to zero, hence when

$$y^* = \frac{1}{2}M \tag{40}$$

To convert this y^* to S^*, this must be subtracted from 0.5 (as the y co-ordinate system is defined as 0 to 1 as opposed to -0.5 to 0.5)

$$S^* = \frac{1}{2}(1 - M) \tag{41}$$

Wall shear stress

The wall shear stress is given by the product of the viscosity and the shear rate acting at the wall:

$$\tau = \mu \frac{du}{dy} \tag{42}$$

The wall shear stress for the suspending medium only case will be used for the purposes of normalisation. Considering equation 38 for $\delta^* = 1$, hence $M = 1$, τ_0 is given by

$$\tau_0 = 6\mu_0 \left(1 - 2y^*\right) \tag{43}$$

Hence, for the CDL, at $y^* = 0$,

$$\tau_0 = 6\mu_0 \tag{44}$$

and at $y^* = 1$ the wall shear stress would be

$$\tau_0 = -6\mu_0 \tag{45}$$

These values can be used to normalise the wall shear stress. Considering that the shear at the wall coincident with CDL is defined by equation 38 evaluated at $y^* = 0$, the wall shear stress acting on that wall can be given as

$$\tau_\delta = 6\ \mu_0 \left(M - 2y^*\right)\big|_{y^*=0} = 6\mu_0 M \tag{46}$$

And hence, normalising with equation 44,

$$\tau_\delta^* = \frac{6\mu_0 M}{6\mu_0} = M \tag{47}$$

At the wall opposite the CDL ($y^* = 1$), the wall shear stress, τ_c, can be defined using equation 38 as

$$\tau_c = 6\ \mu_0 \mu_r \frac{1}{\mu_r} \left(M - 2y^*\right)\Big|_{y^*=1} = 6\mu_0 \left(M - 2\right) \tag{48}$$

And hence, normalising with equation 45,

$$\tau_c^* = \frac{6\mu_0 \left(M - 2\right)}{-6\mu_0} = 2 - M \tag{49}$$

Apparent viscosity

The apparent viscosity for a non-uniform viscosity fluid is thus given by

$$\mu_a = \frac{w^2}{12\overline{u}} \frac{\Delta p}{L} \tag{50}$$

However, given that $u = u^* u_0$, substituting the definition of u_0 from equation 10 gives

$$\mu_a = \frac{w^2}{12\overline{u^* u_0}} \frac{\Delta p}{L} = \frac{\frac{w^2}{12\overline{u^*}} \frac{\Delta p}{L}}{\frac{w^2}{12\mu_0} \frac{\Delta p}{L}} = \frac{\mu_0}{\overline{u^*}} \tag{51}$$

Hence, normalising the apparent viscosity with that of the suspending medium, μ_0, gives a relative apparent viscosity

$$\mu_a^* = \frac{1}{\overline{u^*}} \tag{52}$$

Now, a general equation for $\overline{u^*}$ must be derived by integrating the velocity profiles across the two fluids:

$$\overline{u^*} = \int_0^{\delta^*} u_\delta dy^* + \int_{\delta^*}^1 u_c dy^* \tag{53}$$

Substituting in the definitions of u_c and u_δ from equations 36 and 37

$$\overline{u^*} = 6 \left(\int_0^{\delta^*} \left(M y^* - y^{*2} \right) dy^* + \frac{1}{\mu_r} \int_{\delta^*}^1 \left(M y^* - y^{*2} + 1 - M \right) dy^* \right) \tag{54}$$

and integrating yields

$$\overline{u^*} = 6 \left(\left[\frac{M y^{*2}}{2} - \frac{y^{*3}}{3} \right]_0^{\delta^*} + \frac{1}{\mu_r} \left[\frac{M y^{*2}}{2} - \frac{y^{*3}}{3} + y^* (1 - M) \right]_{\delta^*}^1 \right) \tag{55}$$

$$\overline{u^*} = \left[3M y^{*2} - 2y^{*3} \right]_0^{\delta^*} + \frac{1}{\mu_r} \left[3M y^{*2} - 2y^{*3} + 6y^* (1 - M) \right]_{\delta^*}^1 \tag{56}$$

$$\overline{u^*} = 3M\delta^{*2} - 2\delta^{*3} + \frac{1}{\mu_r} (3M - 2 + 6(1 - M)) - \frac{1}{\mu_r} \left(3M\delta^{*2} - 2\delta^{*3} + 6\delta^* (1 - M) \right) \tag{57}$$

This equation can be rearranged (details to be found in appendix A), to yield

$$\overline{u^*} = \frac{1}{\mu_r} \left(M^2 (\delta^* (\mu_r - 1) + 1) - 4M (1 - \delta^*) + 4 (1 - \delta^*) \right) \tag{58}$$

the relative apparent viscosity is thus given by

$$\mu_a^* = \mu_r \left(M^2 \left(\delta^* \left(\mu_r - 1 \right) + 1 \right) - 4M \left(1 - \delta^* \right) + 4 \left(1 - \delta^* \right) \right)^{-1} \tag{59}$$

Analysis of these results can be found in Chapter 3, §3.4.

References

Aarts, P., van den Broek, S., Prins, G., Kuiken, G., Sixma, J. & Heethaar, R. (1988), "Blood Platelets Are Concentrated near the Wall and Red Blood Cells, in the Center in Flowing Blood", *Arteriosclerosis* **8**, 819–824.

Abkarian, M., Faivre, M. & Viallat, A. (2007), "Swinging of Red Blood Cells under Shear Flow", *Physical Review Letters* **98**, 188–302.

Adrian, R. & Westerweel, J. (2011), *Particle Image Velocimetry*, Cambridge University Press.

Alonso, C., Pries, A., Lerche, D. & Gaehtgens, P. (1995), "Transient rheological behavior of blood in low-shear tube flow: velocity profiles and effective viscosity", *American Journal of Physiology: Heart and Circulatory Physiology* **268**, H25–H32.

Armstrong, J., Meiselman, H. & Fisher, T. (1999), "Evidence against macromolecular bridging as the mechanism of red blood cell aggregation induced by nonionic polymers", *Biorheology* **36**, 433–437.

Audet, D. & Olbricht, W. (1987), "The Motion of Model Cells at Capillary Bifurcations", *Microvascular Research* **33**, 377–396.

Babu, N. & Singh, M. (2004), "Influence of hyperglycemia on aggregation, deformability and shape parameters of erythrocytes", *Clinical Hemorheology and Microcirculation* **31**, 273–280.

Bagchi, P. (2007), "Mesoscale Simulation of Blood Flow in Small Vessels", *Biophysical Journal* **92**, 1858–1877.

Bagchi, P., Johnson, P. & Popel, A. (2005), "Computational Fluid Dynamic Simulation of Aggregation of Deformable Cells in a Shear Flow", *Journal of Biomechanical Engineering* **127(7)**, 1070–1080.

Baker, M. & Wayland, H. (1974), "On-Line Volume Flow Rate and Velocity Profile Measurement for Blood in Microvessels", *Microvascular Research* **7**, 131–143.

Barabino, G., Platt, M. O. & Kaul, D. (2010), "Sickle Cell Biomechanics", *Annual Review of Biomedical Engineering* **12**, 345–367.

Barbee, J. & Cokelet, G. (1971), "The Fåhraeus Effect", *Microvascular Research* **3**, 6–16.

Barber, J., Alberding, J., Restrepo, J. & Secomb, T. (2008), "Simulated Two-dimensional Red Blood Cell Motion, Deformation, and Partitioning in Microvessel Bifurcations", *Annals of Biomedical Engineering* **36(10)**, 1690–1698.

Baskurt, O. & Meiselman, H. (2008), "RBC Aggregation: More Important than RBC Adhesion to Endothelial Cells as a Determinant of *in vivo* Blood Flow in Health and Disease", *Microcirculation* **15**, 585–590.

Baskurt, O., Bonyard, M., Cokelet, G., P., C., Cooke, B., Forconi, S., Liao, F., Hardeman, M., Jung, F., Meiselman, H., Nash, G., Nemeth, N., Neu, B., Sandhagen, B., Shin, S., Thurston, G. & Wautier, J. (2009a), "New guidelines for hemorheological laboratory techniques", *Clinical Hemorheology and Microcirculation* **42**, 75–97.

Baskurt, O., Bor-Küçükatay, M. & Yalçin, O. (1999), "The effect of red blood cell aggregation on blood flow resistance", *Biorheology* **36**, 447–452.

Baskurt, O., Neu, B. & Meiselman, H. (2012), *Red blood cell aggregation*, CRC press.

Baskurt, O., Uyuklu, M., Ulker, P., Cengiz, M., Nemeth, N., Alexy, T., Shin, S., Hardeman, M. & Meiselman, H. (2009b), "Comparison of three instruments for measuring red blood cell aggregation", *Clinical Hemorheology and Microcirculation* **43**, 283–298.

Bayliss, L. (1952), Rheology of blood and lymph, *in Deformation and Flow in Biological Systems*, North-Holland.

Bishop, J., Nance, P., Popel, A., Intaglietta, M. & Johnson, P. (2001a), "Effect of erythrocyte aggregation on velocity profiles in venules", *American Journal of Physiology : Heart and Circulatory Physiology* **280**, H222–H236.

Bishop, J., Nance, P., Popel, A., Intaglietta, M. & Johnson, P. (2001b), "Erythrocyte margination and sedimentation in skeletal muscle venules", *American Journal of Physiology: Heart and Circulatory Physiology* **281**, H951–H958.

Bishop, J., Nance, P., Popel, A., Intaglietta, M. & Johnson, P. (2004), "Relationship between erythrocyte aggregate size and flow rate in skeletal muscle venules", *American Journal of Physiology: Heart and Circulatory Physiology* **286**, H113–H120.

Bishop, J., Popel, A., Intaglietta, M. & Johnson, P. (2001c), "Effects of erythrocyte aggregation and venous network geometry on red blood cell axial migration", *American Journal of Physiology : Heart and Circulatory Physiology* **281**, H939–H950.

Bishop, J., Popel, A., Intaglietta, M. & Johnson, P. (2001d), "Rheological effects of red blood cell aggregation in the venous network: A review of recent studies", *Biorheology* **38**, 263–274.

Bishop, J., Popel, A., Intaglietta, M. & Johnson, P. (2002), "Effect of aggregation and shear rate on the dispersion of red blood cells flowing in venules", *American Journal of Physiology: Heart and Circulatory Physiology* **283**, H1985–H1996.

Bronkhorst, P., Grimbergen, J., Brakenhoff, G., Heethaar, R. & Sixma, J. (1997), "The mechanism of red cell (dis)aggregation investigated by means of direct cell manipulation using multiple optical trapping", *British Journal of Haematology* **96**, 256–258.

Bruus, H. (2008), *Theoretical Microfluidics*, Oxford University Press.

Cabel, M., Meiselman, H., Popel, A. & Johnson, P. (1997), "Contribution of red blood cell aggregation to venous vascular resistance in skeletal muscle", *American Journal of Physiology: Heart and Circulatory Physiology* **41**, H1020–H1032.

Caro, C., Pedley, T., Schroter, R. & Seed, W. (2012), *The mechanics of the circulation, 2nd edition*, Cambridge University Press.

Carr, R. & Wickham, L. (1990), "Plasma skimming in serial microvascular bifurcations", *Microvascular Research* **40**, 179–190.

Carr, R. & Wickham, L. (1991), "Influence of vessel diameter on red cell distribution at microvascular bifurcations", *Microvascular Research* **41**, 184–196.

Carr, R. & Xiao, J. (1995), "Plasma Skimming in Vascular Trees- Numerical Estimates of Symmetry Recovery Lengths", *Microcirculation* **2(4)**, 345–353.

Cebral, J., Castro, M., Burgess, J., Pergolizzi, R., Sheridan, M. & Putman, C. (2005), "Characterization of Cerebral Aneurysms for Assessing Risk of Rupture By Using Patient- Specific Computational Hemodynamics Models", *AJNR American Journal of Neuroradiology* **26**, 2550–2559.

Charansonney, O., Mouren, S., Dufaux, J., Duvelleroy, M. & Vicaut, E. (1993), "Red blood cell aggregation and blood viscosity in an isolated heart preparation", *Biorheology* **30**, 75–84.

Chesnutt, J. & Marshall, J. (2009), "Effect of particle collisions and aggregation on red blood cell passage through a bifurcation", *Microvascular Research* **78**, 301–313.

Chesnutt, J. & Marshall, J. (2010), "Structural Analysis of Red Blood Cell Aggregates Under Shear Flow", *Annals of Biomedical Engineering* **38**, 714–728.

Chien, S. (1970), "Shear Dependence of Effective Cell Volume as a Determinant of Blood Viscosity", *Science* **168(934)**, 977–979.

Chien, S. & Jan, K. (1973), "Ultrastructural Basis of the Mechanism of Rouleaux Formation", *Microvascular Research* **5**, 155–166.

Chien, S., Sung, L., Kim, S. a. B. A. & Usami, S. (1977), "Determination of Aggregation Force in Rouleaux by Fluid Mechanical Technique", *Microvascular Research* **13**, 327–333.

Chien, S., Tvetenstrand, C., Farrell Epstein, M. & Schmid-Schönbein, G. (1985), "Model studies on distributions of blood cells at microvascular bifurcations", *American Journal of Physiology: Heart and Circulatory Physiology* **17(4)**, H568–H576.

Choi, S., Kim, W., D., C., Park, C. & Lee, H. (2011), "Blood cell assisted in vivo Particle Image Velocimetry using the confocal laser scanning microscope.", *Optics Express* **19(5)**, 4357–4368.

Cicha, I., Suzuki, Y., Tateishi, N. & Maeda, N. (2003), "Changes of RBC aggregation in oxygenation-deoxygenation: pH dependency and cell morphology", *American Journal of Physiology: Heart and Circulatory Physiology* **284**, H2335–H2342.

Cokelet, G. (1980), "Rheology and hemodynamics", *Annual Review of Physiology* **42**, 311–324.

Cokelet, G. (1987), The Rheology and tube flow of blood, *in Handbook of Bioengineering*, McGraw-Hill.

Cokelet, G. (1999), "Viscometric, *in vitro* and *in vivo* blood viscosity relationships: how are they related?", *Biorheology* **36**, 343–358.

Cokelet, G. (2011), Hemorheology and Hemodynamics, *in Colloquium Series in Integrated Systems Physiology: From Molecule to Function*, Morgan & Claypool.

Cokelet, G. & Goldsmith, H. (1991), "Decreased Hydrodynamic Resistance in the Two-Phase Flow of Blood Through Small Vertical Tubes at Low Flow Rates", *Circulation Research* **68**, 1–17.

Damiano, E., Long, D. & Smith, M. (2004), "Estimation of viscosity profiles using velocimetry data from parallel flows of linearly viscous fluids: application to microvascular haemodynamics", *Journal of Fluid Mechanics* **512**, 1–19.

Das, B., Bishop, J., Kim, S., Meiselman, H., Johnson, P. & Popel, A. (2007), "Red blood cell velocity profiles in skeletal muscle venules at low flow rates are described by the Casson model", *Clinical Hemorheology and Microcirculation* **36**, 217–233.

Das, B., Johnson, P. & Popel, A. (1998), "Effect of nonaxisymmetric hematocrit distribution on non-Newtonian blood flow in small tubes", *Biorheology* **35(1)**, 69–87.

Dellimore, J., Dunlop, M. J. & Canham, P. B. (1983), "Ratio of cells and plasma in blood flowing past branches in small plastic channels", *American Journal of Physiology : Heart and Circulatory Physiology* **244**, H635–H643.

Dintenfass, L. (1985), "Red Cell Aggregation in Cardiovascular Diseases and Crucial Role of Inversion Phenomenon", *Angiology* **36**, 315–326.

Dodd, L. & Johnson, P. (1991), "Diameter changes in arteriolar networks of contracting skeletal muscle", *American Journal of Physiology: Heart and Circulatory Physiology* **260(3-2)**, H662–H670.

Doddi, S. & Bagchi, P. (2009), "Three-dimensional computational modeling of multiple deformable cells flowing in microvessels", *Phys. Rev. E* **79**, 046318.

Doyeux, V., Podgorski, T., Peponas, S., Ismailand, M. & Coupier, G. (2011), "Spheres in the vicinity of a bifurcation: elucidating the Zweifach-Fung effect", *Journal of Fluid Mechanics* **674**, 359–388.

Dufaux, J., Quemada, D. & Mills, P. (1980), "Determination of rheological properties of red blood cells by Couette viscometry", *Revue de Physique Appliquêe* **15**, 1367–1374.

Dusting, J., Kaliviotis, E., Balabani, S. & Yianneskis, M. (2009), "Coupled human erythrocyte velocity field and aggregation measurements at physiological haematocrit levels", *Journal of Biomechanics* **42**, 1438–1443.

Eggleton, C. & Popel, A. (1998), "Large deformation of red blood cell ghosts in a simple shear flow", *Physics of Fluids* **10(8)**, 1834–1845.

El-Kareh, A. & Secomb, T. (2000), "A model for red blood cell motion in bifurcating microvessels", *International Journal of Multiphase Flow* **26**, 1545–1564.

Eppiheimer, M. & Lipowsky, H. (1996), "Effects of Leukocyte-Capillary Plugging on the Resistance to Flow in the Microvasculature of Cremaster Muscle for Normal and Activated Leukocytes", *Microvascular Research* **51**, 187–201.

Evans, E. (1983), "Bending elastic modulus of red blood cell membrane dervied from buckling instability in micropipet aspiration tests", *Biophysical Journal* **43**, 27–30.

Evans, E. & Fung, Y. (1972), "Improved Measurements of the Erythrocyte Geometry", *Microvascular Research* **4**, 335–347.

Fåhraeus, R. (1929), "The suspension stability of the blood", *Physiological Reviews* **9(2)**, 241–274.

Faivre, M., Abkarian, M., Bickraj, K. & Stone, H. (2006), "Geometrical focusing of cells in a microfluidic device: An approach to separate blood plasma", *Biorheology* **43**, 147–159.

Falcó, C., Vayá, A., Simó, M., Conreras, T., Santaolaria, M. & Aznar, J. (2005), "Influence of fibrinogen levels on erythrocyte aggregation determined with the Myrenne aggregometer and the Sefam erythro-aggregometer", *Clinical Hemorheology and Microcirculation* **33**, 145–151.

Fedosov, D., Caswell, B. & Karniadarkis, G. (2010a), "A Multiscale Red Blood Cell Model with Accurate Mechanics, Rheology, and Dynamics", *Biophysical Journal* **98**, 2215–2225.

Fedosov, D., Caswell, B., Popel, A. & Karniadakis, G. (2010b), "Blood Flow and Cell-Free Layer in Microvessels", *Microcirculation* **17**, 615–628.

Fedosov, D., Pan, W., Caswell, B., Gompper, G. & Karniadakis, G. (2011), "Predicting human blood viscosity in silico", *Proceedings of the National Academy of Sciences* **108 (29)**, 11772–11777.

Fenton, B., Carr, R. & Cokelet, G. (1985), "Nonuniform red cell distribution in 20 to 100 μm bifurcations", *Microvascular Research* **29**, 103–126.

Fiddes, L., Raz, N., Srigunapalan, S., Tumarkan, E., Simmons, C., Wheeler, A. & Kumacheva, E. (2010), "A circular cross-section PDMS microfluidics system for replication of cardiovascular flow conditions", *Biomaterials* **31**, 34593464.

Forconi, S. & Gori, T. (2009), "The evolution of the meaning of blood hyperviscosity in cardiovascular physiopathology: Should we reinterpret Poiseuille?", *Clinical Hemorheology and Microcirculation* **42**, 1–6.

Freund, J. & Orescanin, M. (2011), "Cellular flow in a small blood vessel", *Journal of Fluid Mechanics* **671**, 466–490.

Fronek, K. & Zweifach, B. (1975), "Microvascular pressure distribution in skeletal muscle and the effect of vasodilation", *American Journal of Physiology* **228(3)**, 791–796.

Fujiwara, H., Ishikawa, T., Lima, R., Matsuki, N. Imai, Y., Kaji, H., Nishizawa, M. & Yamaguchi, T. (2009), "Red blood cell motions in high-hematocrit blood flowing through a stenosed microchannel", *Journal of Biomechanics* **42**, 838–843.

Fung, Y. (1973), "Stochastic Flow in Capillary Blood Vessels", *Microvascular Research* **5**, 34–48.

Fung, Y. (1990), *Biomechanics: Motion, Flow, Stress and Growth*, Springer.

Fung, Y. (1993), *Biomechanics: Mechanical Properties of Living Tissues.* 2^{nd} *edition*, Springer.

Fung, Y. (1997), *Biomechanics: Circulation.* 2^{nd} *edition*, Springer.

Gaehtgens, P., Kreutz, F. & Albrecht, K. (1978), "Fåhraeus effect and cell screening during tube flow of human blood. II. Effect of Dextran-induced cell aggregation", *Biorheology* **15**, 155–161.

Gaehtgens, P., Meiselman, H. & Wayland, H. (1970), "Velocity Profiles of Human Blood at Normal and Reduced Hematocrit in Glass Tubes up to 130 μ Diameter", *Microvascular Research* **2**, 13–23.

Gelin, L. (1963), "A method for studies of aggregation of blood cells, erythrostasia and plasma skimming in blood branching capillary tubes", *Biorheology* **1**, 119–127.

Gijsen, F., van de Vosse, F. & Janssen, J. (1999), "The influence of the non-Newtonian properties of blood on the flow in large arteries: steady flow in a carotid bifurcation model", *Journal of Biomechanics* **32**, 601–608.

Goldsmith, H. (1968), "The microrheology of red blood cell suspensions", *The Journal of General Physiology* **52(1)**, 5–28.

Goldsmith, H. (1971), "Red cell motions and wall interactions in tube flow", *Federation proceedings* **30**, 1578–1588.

Goldsmith, H., Bell, D., Spain, S. & McIntosh, F. (1999), "Effect of red blood cells and their aggregates on platelets and white cells in flowing blood", *Biorheology* **36**, 461–468.

Goldsmith, H., Cokelet, G. & Gaehtgens, P. (1989), "Robin Fåhraeus: evolution of his concepts in cardiovascular physiology", *American Journal of Physiology: Heart and Circulatory Physiology* **3(2)**, H1005–H1015.

Gustafsson, L., Appelgren, L. & Myrvold, H. (1981), "Effects of increased plasma viscosity and red blood cell aggregation on blood viscosity *in vivo*", *American Journal of Physiology: Heart and Circulatory Physiology* **10**, H513–H518.

Hahn, C. & Schwartz, M. (2009), "Mechanotransduction in vascular physiology and atherogenesis", *Nature Reviews* **10**, 53–62.

Halpern, D. & Secomb, T. (1992), "The squeezing of red blood cells through parallel-sided channels with near-minimal widths", *Journal of Fluid Mechanics* **244**, 307–322.

Hokkanen, J. (1989), "A two-fluid model for hematocrit distribution in microvascular networks", *Medical Physics* **16(3)**, 319–325.

House, S. & Johnson, P. (1986), "Diameter and blood flow of skeletal muscle venules during local flow regulation", *American Journal of Physiology* **250**, H828–H837q.

Hove, J., Köster, R., Forouhar, A., Acevedo-Bolton, G., Fraser, S. & Gharib, M. (2003), "Intracardiac fluid forces are an essential epigenetic factor for embryonic cardiogenesis", *Nature* **421**, 172–177.

Hyakutake, T., Matsumoto, T. & Yanasea, S. (2006), "Lattice Boltzmann simulation of blood cell behavior at microvascular bifurcations", *Mathematics and Computers in Simulation* **72**, 134–140.

Imai, Y., Kondo, H., Ishikawa, T., Lim, C. & Yamaguchi, T. (2010), "Modeling of hemodynamics arising from malaria infection", *Journal of Biomechanics* **43**, 1386–1393.

Imai, Y., Nakaaki, K., Kondo, H., Ishikawa, T., Lim, C. T. & Yamaguchi, T. (2011), "Margination of red blood cells infected by Plasmodium falciparum in a microvessel", *Journal of Biomechanics* **44**(8), 1553 – 1558.

Intaglietta, M. (2009), "Increased blood viscosity: Disease, adaptation or treatment?", *Clinical Hemorheology and Microcirculation* **42**, 305–306.

Ishikawa, T., Fujiwara, H., Matsuki, N., Yoshimoto, T., Imai, Y., Ueno, H. & Yamaguchi, T. (2011), "Asymmetry of blood flow and cancer cell adhesion in a microchannel with symmetric bifurcation and confluence", *Biomedical Microdevices* **13**, 159–167.

Jäggi, R., Sandoz, R. & Effenhauser, C. (2007), "Microfluidic depletion of red blood cells from whole blood in high-aspect-ratio microchannels", *Microfluid Nanofluid* **3**, 47–53.

Jain, R. (1988), "Determinants of Tumor Blood Flow: A Review", *Cancer Research* **48**, 2641–2658.

Ji, H. & Lee, S. (2008), "*In vitro* hemorheological study on the effect of human blood flow in a microtube", *Clinical Hemorheology and Microcirculation* **40**, 19–30.

Johnson, P. (2008), Overview of the Microcirculation, *in Handbook of Physiology: Microcirculation,* 2^{nd} *edition*, Elsevier, pp.xi–xxiv.

Jovtchev, S., Djenev, I., Stoeff, S. & Stoylov, S. (2000), "Role of electrical and mechanical properties of red blood cells for their aggregation", *Colloids and Surfaces. A: Physicochemical and Engineering Aspects* **164**, 95–104.

Jung, F. (2010), "From hemorheology to microcirculation and regenerative medicine: Fåhraeus Lecture 2009", *Clinical Hemorheology and Microcirculation* **45**, 79–99.

Kaliviotis, E. & Yianneskis, M. (2008), "Fast response characteristics of RBC aggregation", *Biorheology* **45**, 639–649.

Kaliviotis, E. & Yianneskis, M. (2009), "An energy-rate based blood viscosity model incorporating aggregate network dynamics", *Biorheology* **46**, 487–508.

Kaliviotis, E., Dusting, J. & Balabani, S. (2011), "Spatial variation of blood viscosity: Modelling using shear fields measured by a μ PIV based technique", *Medical Engineering and Physics* **33(7)**, 824–831.

Kamoun, W., Chae, S.-S., Lacorre, D., Tyrell, J., Mitre, M., Gillisen, M., Fukumura, D., Jain, R. & Munn, L. (2010), "Simultaneous measurement of RBC velocity, flux, hematocrit and shear rate in vascular networks", *Nature Methods* **7(8)**, 655–662.

Karnis, A., Goldsmith, H. & Mason, S. (1963), "Axial migration of particles in Poiseuille flow", *Nature* **200**, 159–160.

Katritsis, D., Kaiktsis, L., Chaniotis, A., Pantos, J., Efstathopoulos, E. P. & Marmarelis, V. (2007), "Wall Shear Stress: Theoretical Considerations and Methods of Measurement", *Progress in Cardiovascular Diseases* **49**(5), 307 – 329. ¡ce:title¿Special Articles¡/ce:title¿.

Kenner, T. (1989), "The measurement of blood density and its meaning", *Basic Research in Cardiology* **84**, 111–124.

Kersaudy-Kerhoas, M., Dhariwal, R., Desmulliez, M. & Jouvet, L. (2010), "Hydrodynamic blood plasma separation in microfluidic channels", *Microfluid Nanofluid* **8**, 105–114.

Kim, S., Kong, R., Popel, A., Intaglietta, M. & Johnson, P. (2006), "A Computer-Based Method for Determination of the Cell-Free Layer Width in Microcirculation", *Microcirculation* **13**, 199–207.

Kim, S., Kong, R., Popel, A., Intaglietta, M. & Johnson, P. (2007), "Temporal and spatial variations of cell-free layer width in arterioles", *American Journal of Physiology: Heart and Circulatory Physiology* **293**, H1526–H1535.

Kim, S., Ong, P., Yalcin, O., Intaglietta, M. & Johnson, P. (2009), "The cell-free layer in microvascular blood flow", *Biorheology* **46**, 181–189.

Kim, S., Popel, A., Intaglietta, M. & Johnson, P. (2005), "Aggregate formation of erythrocytes in postcapillary venules", *American Journal of Physiology: Heart and Circulatory Physiology* **288**, H584–H590.

Klitzman, B., Popel, A. & Duling, B. (1983), "Oxygen Transport in Resting and Contracting Hamster Cremaster Muscles: Experimental and Theoretical Microvascular Studies", *Microvascular Research* **25**, 108–131.

Leble, V., Lima, R., Dias, R., Fernandes, C., Ishikawa, T., Imai, Y. & Yamaguchi, T. (2011), "Asymmetry of red blood cell motions in a microchannel with a diverging and converging bifurcation", *Biomicrofluidics* **5**, 044120.

Lee, J. & Smith, N. (2008), "Theoretical Modeling in Hemodynamics of Microcirculation", *Microcirculation* **15**, 699–714.

Lee, J., Ji, H. & Lee, S. (2007), "Micro-PIV measurements of blood flow in extraembryonic blood vessels of chicken embryos", *Physiological Measurement* **28**, 1149–1162.

Lee, S., Kim, B. & Lee, J. (2009), "Experimental study on the fluid mechanics of blood sucking in the proboscis of a female mosquito", *Journal of Biomechanics* **42**, 857–864.

Levick, J. (2009), *An indtroduction to cardiovascular physiology, 5th edition*, Hodder Arnold.

Lima, R., Ishikawa, T., Imai, Y., Takeda, M., Wada, S. & Yamaguchi, T. (2008a), "Radial dispersion of red blood cells in blood flowing through glass capillaries: the role of hematocrit and geometry", *Journal of Biomechanics* **41**, 2188–2196.

Lima, R., Ishikawa, T., Imai, Y., Takeda, M., Wada, S. & Yamaguchi, T. (2009a), "Measurement of Individual Red Blood Cell Motions Under High Hematocrit Conditions Using a Confocal Micro-PTV System", *Annals of Biomedical Engineering* **37(8)**, 1549–1559.

Lima, R., Oliveira, M., Ishikawa, T., Kaji, H., Tanaka, S., Nishiizawa, M. & Yamaguchi, T. (2009b), "Axisymmetric polydimethysiloxane microchannels for *in vitro* hemodynamic studies", *Biofabrication* **1**, 1–7.

Lima, R., Wada, S., Takeda, M., Tsubota, K. & Yamaguchi, T. (2007), "*In vitro* confocal micro-PIV measurements of blood flow in a square microchannel: The effect of the haematocrit on instantaneous velocity profiles", *Journal of Biomechanics* **40**, 2752–2757.

Lima, R., Wada, S., Tanaka, S., Takeda, M., Ishikawa, T., Tsubota, K., Imai, Y. & Yamaguchi, T. (2008b), "*In vitro* blood flow in a rectangular PDMS microchannel: experimental observations using a confocal micro-PIV system", *Biomedical Microdevices* **10**, 153–167.

Lima, R., Wada, S., Tsubota, K. & Yamaguchi, T. (2006), "Confocal micro-PIV measurements of three-dimensional profiles of cell suspension flow in a square microchannel", *Measurement Science and Technology* **17**, 797–808.

Lipowsky, H. (2005), "Microvascular Rheology and Hemodynamics", *Microcirculation* **12**, 5–15.

Lipowsky, H. & Zweifach, B. (1974), "Network Analysis of Microcirculation of Cat Mesentery", *Microvascular Research* **7**, 73–83.

Lipowsky, H., Usami, S. & Chien, S. (1980), "*In vivo* Measurements of 'Apparent Viscosity' and Microvessel Hematocrit in the Mesentery of the Cat", *Microvascular Research* **19**, 297–319.

Liu, A., Nickerson, A., Troyer, A., Yin, X., Cary, R., Thornburg, K., Wang, R. & Rugonyi, S. (2011), "Quantifying blood flow and wall shear stresses in the outflow tract of chick embryonic hearts", *Computers & Structures* **89**(11??12), 855 – 867.

Liu, Y., Lai, Y., Nagaraj, A., Kane, B., Hamilton, A., Greene, R., McPherson, D. & Chandran, K. (2001), "Pulsatile flow simulation in arterial vascular segments with intravascular ultrasound images", *Medical Engineering and Physics* **23**, 583–595.

Long, D., Smith, M., Pries, A., Ley, K. & Damiano, E. (2004), "Microviscometry reveals reduced blood viscosity and altered shear rate and shear stress profiles in microvessels after hemodilution", *Proceedings of the National Academy of Sciences* **101(27)**, 10060–10065.

Lowe, G. (1988), *Clinical Blood Rheology*, CRC Press.

Maeda, N. & Shiga, T. (1985), "Inhibition and acceleration of erythrocyte aggregation induced by small macromolecules", *Biochimica et Biophysica Acta* **843(1-2)**, 128–136.

Maeda, N., Kon, K., Imaizumi, K., Sekiya, M. & Shiga, T. (1983), "Alteration of rheological parameters of human erythrocytes by crosslinking of membrane proteins", *Biochimica et Bioplophsica Acta* **735**, 104–112.

Makita, S., Jaillon, F., Yamanari, M., Miura, M. & Yasuno, Y. (2011), "Comprehensive *in vivo* micro-vascular imaging of the human eye by dual-beam-scan Doppler optical coherence angiography", *Optics Express* **19(2)**, 1271–1283.

Manjunatha, M. & Singh, M. (2002), "Digital blood flow analysis from microscopic images of mesenteric microvessel with multiple branching", *Clinical Hemorheology and Microcirculation* **27**, 91–106.

Mansour, M., Bressloff, N. & Shearman, C. (2010), "REd blood cell migration in microvessels", *Biorheology* **47**, 73–93.

Martini, F. H. (2004), *Fundamentals of Anatomy and Physiology, 6th edition*, Prentice Hall.

Meinhart, C., Wereley, S. & Santiago, J. (1999), "PIV measurements of a microchannel flow", *Experiments in Fluids* **27**, 414–419.

Meiselman, H. (2009), "Red blood cell aggregation: 45 years of being curious", *Biorheology* **46**, 1–19.

Meiselman, H. & Baskurt, O. (2006), "Hemorheology and hemodynamics: Dove andare?", *Clinical Hemorheology and Microcirculation* **35(1-2)**, 37–43.

Migliavacca, F. & Dubini, G. (2005), "Computational modeling of vascular anastomoses", *Biomechanics and Modeling in Mechanobiology* **3**, 235–250.

Moger, J., Matcher, S., Winlove, C. & Shore, A. (2004), "Measuring red blood cell flow dynamics in a glass capillary using Doppler optical coherence tomography and Doppler amplitude optical coherence tomography", *Journal of Biomedical Optics* **9(5)**, 982–994.

Mohandas, N. & Gallagher, P. (2008), "Red cell membrane: past, present, and future", *Blood* **112**, 3939–3948.

Nakano, A., Sugii, Y., Minamiyama, M. & Niimi, H. (2003), "Measurement of red cell velocity in microvessels using particle image velocimetry (PIV)", *Clinical Hemorheology and Microcirculation* **29**, 445–455.

Namgung, B., Ong, P., Johnson, P. & Kim, S. (2011), "Effect of Cell-Free Layer Variation on Arteriolar Wall Shear Stress", *Ann* **39(1)**, 359–366.

Namgung, B., Ong, P., Wong, Y., Lim, D., Chun, K. & Kim, S. (2010), "A comparative study of histogram-based thresholding methods for the determination of cell-free layer width in small blood vessels", *Physiological Measurement* **31**, N61–N70.

Neu, B. & Meiselman, H. (2002), "Depletion-Mediated Red Blood Cell Aggregation in Polymer Solutions", *Biophysical Journal* **83**, 2482–2490.

Ohashi, K., Tung, D.-L., Wilson, J., Zweifach, B. & Schmid-Schönbein, G. (1996), "Transvascular and Interstitial Migration of Neutrophils in Rat Mesentery", *Microcirculation* **3(2)**, 199–210.

Olsen, M. & Adrian, R. (2000), "Out-of-focus effects on particle image visibility and correlation in microscopic particle image velocimetry", *Experiments in fluids* **Suppl.**, S166–S174.

Ong, P., Jain, S. & Kim, S. (2012), "Spatio-temporal variations in cell-free layer formation near bifurcations of small arterioles", *Microvascular Research* **83**, 118–125.

Ong, P., Jain, S., Namgung, B., Woo, Y. & Kim, S. (2011a), "Cell-Free Layer Formation in Small Arterioles at Pathological Levels of Erythrocyte Aggregation", *Microcirculation* **18**, 541–551.

Ong, P., Jain, S., Namgung, B., Woo, Y., Sakai, H., Lim, D., Chun, K. & Kim, S. (2011b), "An automated method for cell-free layer width determination in small arterioles", *Physiological Measurement* **32**, N1–N12.

Ong, P., Namgung, B., Johnson, P. & Kim, S. (2010), "Effect of erythrocyte aggregation and flow rate on cell-free layer formation in arterioles", *American Journal of Physiology: Heart and Circulatory Physiology* **298**, H1870–H1878.

Ong, P.Ng, P., Jain, S. & Kim, S. (2011c), "Temporal variations of the cell-free layer width may enhance NO bioavailability in small arterioles: Effects of erythrocyte aggregation", *Microvascular Research* **81**, 303–312.

Otsu, N. (1979), "A threshold selection method from gray-level histograms.", *IEEE Transactions on Systems, Man and Cybernetics* **9**, 62–66.

Ott, C., Lardi, E., Schulzki, T. & Reinhart, W. (2010), "The influence of erythrocyte aggregation on induced platelet aggregation", *Clinical Hemorheology and Microcirculation* **45**, 375–382.

Palmer, A. (1969), "Influence of absolute flow rate and rouleau formation on plasma skimming in vitro", *American Journal of Physiology* **217(5)**, 1339–1345.

Pearson, M. & Lipowsky, H. (2000), "Influence of erythrocyte aggregation on leukocyte margination in postcapillary venules of rat mesentery", *American Journal of Physiology: Heart and Circulatory Physiology* **279**, H1460–H1471.

Pearson, M. & Lipowsky, H. (2004), "Effect of Fibrinogen on Leukocyte Margination and Adhesion in Postcapillary Venules", *Microcirculation* **11**, 295–306.

Perkkiö, J., Wurzinger, L. & Schmid-Schönbein, G. (1987), "Plasma and platelet skimming at T-junctions", *Thrombosis Research* **45**, 517–526.

Poelma, C., Kloosterman, A., Hierck, B. & Westerweel, J. (2012), "Accurate blood flow measurement: are artifical tracers necessary?", *PLoS One* **7(9)**, e45247.

Poelma, C., Van der Heiden, K., Hierck, B., Poelmann, R. & Westerweel, J. (2009), "Measurements of the wall shear stress distribution in the outflow tract of an embryonic chicken heart", *Journal of the Royal Society Interface* **7 (42)**, 91–103.

Popel, A. & Johnson, P. (2005), "Microcirculation and Hemorheology", *Annual Review of Fluid Mechanics* **37**, 43–69.

Potter, D. & Damiano, E. (2008), "The Hydrodynamically Relevant Endothelial Cell Glycocalyx Observed *in vivo* Is Absent *in vitro*", *Circulation Research* **102**, 770–776.

Potter, D., Jiang, J. & Damiano, E. (2009), "The Recovery Time Course of the Endothelial Cell Glycocalyx *in vivo* and Its Implications *in vitro*", *Circulation Research* **104**, 1318–1325.

Pozridikis, C. (2005), "Numerical Simulation of Cell Motion in Tube Flow", *Annals of Biomedical Engineering* **33(2)**, 165–178.

Prabhakarpandian, B., Pant, K., Scott, R., Patillo, C., Irimia, D., Kiani, M. & Sundaram, S. (2008), "Synthetic microvascular networks for quantitative analysis of particle adhesion", *Biomedical Microdevices* **10**, 585–595.

Pries, A. & Secomb, T. (2005), "Microvascular blood viscosity *in vivo* and the endothelial surface layer", *American Journal of Physiology: Heart and Circulatory Physiology* **289**, H2657–H2664.

Pries, A. & Secomb, T. (2008), Principles of Microvascular Structure and Function, *in Handbook of Physiology: Microcirculation,* 2^{nd} *edition*, Elsevier, chapter 1, pp.1–158.

Pries, A., Fritzsche, A., Ley, K. & Gaehtgens, P. (1992a), "Redistribution of Red Blood Cell Flow in Microcirculatory Networks by Hemodilution", *Circulation Research* **70**, 1113–1121.

Pries, A., Habazettl, H., Ambrosio, G., Hansen, P., Kaski, J., Schächinger, V., Tillmans, H., Vassalli, G., Tritto, I., Weis, M., de Wit, C. & Bugiardini, R. (2008), "A review of methods for assessment of coronary microvascular disease in both clinical and experimental settings", *Cardiovascular Research* **80**, 165–174.

Pries, A., Ley, K., Claassen, M. & Gaehtgens, P. (1989), "Red Cell Distribution at Microvascular Bifurcations", *Microvascular Research* **38**, 81–101.

Pries, A., Neuhaus, D. & Gaehtgens, P. (1992b), "Blood viscosity in tube flow: dependence on diameter and hematocrit", *American Journal of Physiology* **263(6 pt 2)**, H1770–1778.

Pries, A., Secomb, T. & Gaehtgens, P. (1996), "Biophysical aspects of blood flow in the microvasculature", *Cardiovascular Research* **32**, 654–667.

Pries, A., Secomb, T. & Gaehtgens, P. (2000), "The endothelial surface layer", *Pflügers Archive - European Journal of Physiology* **440**, 653–666.

Pries, A., Secomb, T., Gaehtgens, P. & Gross, J. (1990), "Blood flow in microvascular networks - experiments and simulation", *Circulation Research* **67**, 826–834.

Pries, A., Secomb, T., Gessner, T., Sperandio, M., Gross, J. & Gaehtgens, P. (1994), "Resistance to Blood Flow in Microvessels *in vivo*", *Circulation Research* **75(5)**, 904–915.

Pries, A., Secomb, T., Jacobs, H., Sperandio, M., Osterloh, K. & Gaehtgens, P. (1997), "Microvascular blood flow resistance: role of endothelial surface layer", *American Journal of Physiology: Heart and Circulatory Physiology* **273**, H2272–H2279.

Quemada, D. (1977), "Rheology of concentrated disperse systems and minimum energy dissipation principle I. Viscosity-concentration relationship", *Rheologica Acta* **16**, 82–94.

Quemada, D. (1978a), "Rheology of concentrated disperse systems II. A model for non-newtonian shear viscosity in steady flows", *Rheologica Acta* **17**, 632–642.

Quemada, D. (1978b), "Rheology of concentrated disperse systems III. General features of the proposed non-newtonian model. Comparison with experimental data", *Rheologica Acta* **17**, 643–653.

Quinn, D., Pivkin, I., Wong, S., Chiam, K.-H., Dao, M., Karniadarkis, G. & Suresh, S. (2010), "Combined Simulation and Experimental Study of Large Deformation of Red Blood Cells in Microfluidic Systems", *Annals of Biomedical Engineering* **39(3)**, 1041–1050.

Raffel, M., Willert, C., Wereley, S. & Kompenhams, J. (1998), *Particle Image Velocimetry : A Practical guide,* 2^{nd} *edition*, Spring.

Rampling, M., Meiselman, H. & Baskurt, O. (2004), "Influence of cell-specific factors on red blood cell aggregation", *Biorheology* **41**, 91–112.

Reinke, W., Gaehtgens, P. & Johnson, P. (1987), "Blood viscosity in small tubes: effect of shear rate, aggregation, and sedimentation", *American Journal of Physiology : Heart and Circulatory Physiology* **253(3)**, H540 –H547.

Reinke, W., Johnson, P. & Gaehtgens, P. (1986), "Effect of Shear Rate Variation on Apparent Viscosity of Human Blood in Tubes of 29 to 94 μm Diameter", *Circulation Research* **59(2)**, 124–132.

Reneman, R., Arts, T. & Hoeks, A. P. (2006), "Wall shear stress–an important determinant of endothelial cell function and structure–in the arterial system in vivo. Discrepancies with theory.", *Journal of Vascular Research* **43(3)**, 251–269'.

Roberts, B. & Olbricht, W. (2006), "The distribution of freely suspended particles at microfluidic bifurcations", *AIChE Journal* **52**, 199–206.

Rogerson, S., Grau, G. & Hunt, N. (2004), "The Microcirculation in Severe Malaria", *Microcirculation* **11**, 559–576.

Rosano, J., Tousi, N. amd Scott, R., Krynska, B., Rizzo, V., Prabhakarpandian, B., Pant, K., Sundaram, S. & Kiani, M. (2009), "A physiologically realistic *in vitro* model of microvascular networks", *Biomedical Microdevices* **11**, 10511057.

Saadatmand, M., Ishikawa, T., Matsuki, N., Abdekhodaie, M., Imai, Y., Ueno, H. & Yamaguchi, T. (2011), "Fluid particle diffusion through high-hematocrit blood flow within a capillary tube", *Journal of Biomechanics* **44**, 170–175.

Santiago, J., Wereley, S., Meinhart, C., Beebe, D. & Adrian, R. (1998), "A particle image velocimetry system for microfluidics", *Experiments in Fluids* **25**, 316–319.

Savery, M. & Damiano, E. (2008), "The Endothelial Glycocalyx is Hydrodynamically Relevant in Arterioles throughout the Cardiac Cycle", *Biophysical Journal* **95**, 1439–1447.

Schmid-Schönbein, G. (1999), "Biomechanics of microcirculatory blood perfusion", *Annual Review of Biomedical Engineering* **1**, 73–102.

Schmid-Schönbein, G., Gaehtgens, P. & Hirsch, H. (1968), "On the Shear Rate Dependence of Red Cell Aggregation *in vitro*", *The Journal of Clinical Investigation* **47**, 1447–1454.

Schmid-Schönbein, H., Volger, E. & Klose, H. (1972), "Microrheology and Light Transmission of Blood. II. The Photometric Quantification of Red Cell Aggregate Formation and Dispersion in Flow", *Pflügers Archive* **333**, 140–1555.

Secomb, T., Styp-Rekowska, B. & Pries, A. (2007), "Two-Dimensional Simulation of Red Blood Cell Deformation and Lateral Migration in Microvessels", *Annals of Biomedical Engineering* **35(5)**, 755–765.

Seo, T., Schachter, L. & Barakat, A. (2005), "Computational Study of Fluid Mechanical Disturbance Induced by Endovascular Stents", *Annals of Biomedical Engineering* **33(4)**, 444–456.

Shahidi, M., Wanek, J., Gaynes, B. & Wu, T. (2010), "Quantitative assessment of conjunctival microvascular circulation of the human eye", *Microvascular Research* **79**, 109–113.

Sharan, M. & Popel, A. (2001), "A two-phase model for flow of blood in narrow tubes with increased effective viscosity near the wall", *Biorheology* **38**, 415–428.

Sherwood, J., Dusting, J., Kaliviotis, E. & Balabani, S. (2012a), "The effect of red blood cell aggregation on velocity and cell-depleted layer characteristics of blood in a bifurcating microchannel", *Biomicrofluidics* **6**, 024119.

Sherwood, J., Dusting, J., Kaliviotis, E. & Balabani, S. (2012b), "Hematocrit, Viscosity and Velocity Distributions of Aggregating and Non-Aggregating Blood in a Bifurcating Microchannel", *Biomechanics and Modeling in Mechanobiology* **Epub:**, ahead of print.

Shevkoplyas, S., Gifford, S., Yoshida, T. & Bitensky, M. (2003), "Prototype of an *in vitro* model of the microcirculation", *Microvascular Research* **65**, 132–136.

Shin, S., Park, M., Ku, Y. & Suh, J. (2006), "Shear-dependent aggregation characteristics of red blood cells in a pressure-driven microfluidic channel", *Clinical Hemorheology and Microcirculation* **34**, 353–361.

Sia, S. & Whitesides, G. (2003), "Microfluidic devices fabricated in poly(dimethylsiloxane) for biological studies", *Electrophoresis* **24**, 3563–3576.

Skalak, T. & Schmid-Schönbein, G. (1986), "The Microvasculature in Skeletal Muscle - IV. A Model of the Capillary Network", *Microvascular Research* **32,**, 333–347.

Smith, M., Long, D., Damiano, E. & Ley, K. (2003), "Near-Wall μ-PIV Reveals a Hydrodynamically Relevant Endothelial Surface Layer in Venules *in vivo*", *Biophysical Journal* **85**, 637–645.

Snabre, P., Bitbol, M. & Mills, P. (1987), "Cell disaggregation behavior in shear flow", *Biophysical Journal* **51**, 795–807.

Sollier, E., Rostaing, H., Pouteau, P., Fouillet, Y. & Achard, J. (2009), "Passive microfluidic devices for plasma extraction from whole human blood", *Sensors and Actuators B* **141**, 617–624.

Soulis, J. V., Giannoglou, G. D., Chatzizisis, Y. S., Seralidou, K. V., Parcharidis, G. E. & Louridas, G. E. (2008), "Non-Newtonian models for molecular viscosity and

wall shear stress in a 3D reconstructed human left coronary artery", *Medical Engineering & Physics* **30**(1), 9 – 19.

Soutani, M., Suzuki, Y., Tateishi, N. & Maeda, N. (1995), "Quantitative evaluation of flow dynamics of erythrocytes in microvessels: influence of erythrocyte aggregation", *American Journal of Physiology: Heart and Circulatory Physiology* **268**, H1959–H1965.

Steinman, D. (2002), "Image-Based Computational Fluid Dynamics Modeling in Realistic Arterial Geometries", *Annals of Biomedical Engineering* **30**, 483–497.

Sugii, Y., Nishio, S. & Okamoto, K. (2002), "*In vivo* PIV measurement of red blood cell velocity field in microvessels considering mesentery motion", *Physiological Measurement* **23**, 403–416.

Sugii, Y., Okuda, R., Okamato, K. & Madarame, H. (2005), "Velocity measurement of both red blood cells and plasma of *in vitro* blood flow using high-speed micro PIV technique", *Measurement Science and Technology* **16**, 1126–1130.

Tangelder, G., Slaaf, D., Muijtjens, A., Arts, T., oude Egbrink, M. & Reneman, R. (1986), "Velocity Profiles of Blood Platelets and Red Blood Cells Flowing in Arterioles of the Rabbit Mesentery", *Circulation Research* **59**, 505–514.

Tangelder, G., Teirlinck, H., Slaaf, D. & Reneman, R. (1985), "Distribution of blood platelets flowing in arterioles", *American Journal of Physiology: Heart and Circulatory Physiology* **17**, H318–H323.

Taylor, C., Draney, M., Ku, J., Parker, D., Steele, B., Wang, K. & Zarins, C. (1999), "Predictive Medicine: Computational Techniques in Therapeutic Decision-Making", *Computer Aided Surgery* **4**, 231–247.

Taylor, R. (1990), "Interpretation of the Correlation Coefficient: A Basic Review", *Journal of Diagnostic Medical Sonography* **1**, 35:39.

Thomson, N., La Celle, P. & Cokelet, G. (1989), "Perturbation of red blood cell flow in small tubes by white blood cells", *Pflügers Archive* **413**, 372–377.

Tortora, G. & Grabowski, S. R. (2001), *Introduction to the human body, 5th edition*, John Wiley and Sons.

Tse, K., Chiu, P., Lee, H. & Ho, P. (2011), "Investigation of hemodynamics in the development of dissecting aneurysm within patient-specific dissecting aneurismal aortas using computational fluid dynamics (CFD) simulations", *Journal of Biomechanics* **44**, 827–836.

VanTeefelen, J., Brands, J., Stroes, E. & Vink, H. (2007), "Endothelial Glycocalyx: Sweet Shield of Blood Vessels", *Trends in Cardiovascular Medicine* **17(3)**, 101–105.

Varghese, S. & Frankel, S. (2003), "Numerical Modeling of Pulsatile Turbulent Flow in Stenotic Vessels", *Journal of Biomechanical Engineering* **125**, 445–460.

Vennemann, P., Kiger, K., Lindken, R., Groenendijk, B., Stekelenburg-de Vos, S., ten Hagen, T., Ursem, N., Poelmann, R., Westerweel, J. & Hierck, B. (2006), "*In vivo* micro particle image velocimetry measurements of blood-plasma in the embryonic avian heart", *Journal of Biomechanics* **39**, 1191–1200.

Vennemann, P., Lindken, R. & Westerweel, J. (2007), "*In vivo* whole-field blood velocity measurement techniques", *Experiments in Fluids* **42**, 495–511.

Vicaut, E. (1995), "Opposite effects of red blood cell aggregation on resistance to blood flow", *Journal of Cardiovascular Surgery* **36**, 361–368.

Weinbaum, S., Tarbell, J. & Damiano, E. (2007), "The Structure and Function of the Endothelial Glycocalyx Layer", *Annual Review of Biomedical Engineering* **9**, 121–167.

Westerweel, J. & Scarano, F. (2005), "Universal outlier detection for PIV data", *Experiments in Fluids* **39**, 1096–1100.

Whitmore, R. (1968), *Rheology of the microcirculation*, New York: Pergamon.

Williams, S., Park, C. & Wereley, S. (2010), "Advances and applications on microfluidic velocimetry techniques", *Microfluid Nanofluid* **8**, 709–726.

Xia, Y. & Whitesides, G. (1998), "Soft Lithography", *Annual Review of Material Science* **28**, 153–184.

Yalcin, O., Wang, Q., Johnson, P., Palmer, A. & Cabrales, P. (2011), "Plasma expander viscosity effects on red cell-free layer thickness after moderate hemodilution", *Biorheology* **48**, 277–291.

Yang, S., Undar, A. & Zahn, J. (2006), "A microfluidic device for continuous, real time blood plasma separation", *Lab on a Chip* **6**, 871–880.

Yazdanbakhsh, K., Lomas-Francis, C. & Reid, M. (2000), "Blood Groups and Diseases Associated With Inherited Abnormalities of the Red Blood Cell Membrane", *Transfusion Medicine Reviews* **114(4)**, 364–374.

Yedgar, S., Kaul, D. & Barshtein, G. (2008), "RBC Adhesion to Vascular Endothelial Cells: More Potent than RBC Aggregation in Inducing Circulatory Disorders", *Microcirculation* **15**, 581–583.

Yen, R. & Fung, Y. (1978), "Effect of velocity distribution on red cell distribution in capillary blood vessels", *American Journal of Physiology: Heart and Circulatory Physiology* **4(2)**, H251–H257.

Yu, P., Balaratnasingam, C., Cringle, S., McAllister, I., Provis, J. & Yu, D.-Y. (2010), "Microstructure and Network Organization of the Microvasculature in the Human Macula", *Investigative Ophthalmology & Visual Science* **51(12)**, 6735–6743.

Zhang, J., Johnson, P. & Popel, A. (2008), "Red blood cell aggregation and dissociation in shear flows simulated by lattice Boltzmann method", *Journal of Biomechanics* **41**, 47–55.

Zhang, J., Johnson, P. & Popel, A. (2009), "Effects of erythrocyte deformability and aggregation on the cell free layer and apparent viscosity of microscopic blood flows", *Microvascular Research* **77**, 265–272.

Zheng, S., Liu, J. & Tai, Y. (2008), "Streamline-Based Microfluidic Devices for Erythrocytes and Leukocytes Separation", *Journal of Microelectromechanical Systems* **17(4)**, 1029–1038.

Zhong, Z., Song, H., Chui, T., Petrig, B. & Burns, S. (2011), "Noninvasive measurements and analysis of blood velocity profiles in human retinal vessels", *Investigative Opthalmology and Visual Science* **52(7)**, 4151–4157.